eman ta zabal zazu

Universidad del País Vasco
Euskal Herriko Unibertsitatea

Development of new eutectic phase change materials and plate-based latent heat thermal energy storage systems for domestic cogeneration applications

Gonzalo Diarce Belloso

Dissertation presented at the University of the Basque Country (UPV/EHU) in fulfillment of the requirements for the degree of PhD in Thermal Engineering of the PhD program of the Department of Thermal Engineering

Under the supervision of:

Dr. Ane Miren García-Romero

Prof. José Mª Pedro Sala Lizarraga

Preamble

With the aim of assisting the reading and understanding of the present PhD dissertation, a brief explanation about its structure and main contents is herein given.

The dissertation starts with a list of the funding sources and collaborations of the thesis. Then, an **index** is provided**,** where the starting page number of each chapter is shown, followed by the nomenclature employed along the document. Afterwards, a **summary** is presented, written in English and in Spanish. It intends to provide the reader with an overall idea of the work carried out. The **seven chapters** that follow make up the main body of the thesis.

Regarding the **content**, the **first chapter** consists of a brief **introduction** on latent thermal energy storage systems that includes the **main objectives** of the thesis and the **methodology** followed to achieve them.

The **second chapter** corresponds to the development of new eutectic mixtures of sugar alcohols for their use as phase change materials. In the **third chapter**, the eutectic mixture formed by sodium nitrate and urea is studied for thermal energy storage purposes. The **fourth chapter** covers the investigation of the erythritol-urea eutectic mixture with the same objective. These chapters correspond to **articles accepted** in peer reviewed journals; however, in order to give uniformity and consistency to the dissertation, their content and format have been adapted to agree with the rest of the document. The bibliographic details of the articles are provided on the initial page of each chapter**.**

After these chapters, dealing with the development of new PCMs, the following chapters present the research carried out to develop the plate-based LHTES system for domestic use with a cogeneration installation. Accordingly, the **fifth chapter** displays the study to develop an overall design methodology for plate-based LHTES systems, while the **sixth chapter** deals with the design, construction and evaluation of a full-scale prototype.

The dissertation finishes with the **seventh chapter,** where the **main conclusions** derived from the research are presented and summarized. A brief analysis of the works required in the future is provided as a final point.

Funding sources and collaborations of the thesis

This thesis has been developed under the framework of a grant from the Research Personnel Training Program awarded by the Department of Education, Universities and Research of the Basque Government (reference no.: BFI-2012-293). Besides, the work has been performed within the ENEDI (Energy in Buildings) research group from the University of the Basque Country (UPV/EHU), which is recognized as a consolidated group by the Basque Government.

The research performed has also been funded by the following projects:

- MicroTES project (ENE2012–38633, FEDER funding included) of the Spanish's Ministry of Economy and Competitiveness (MINECO)
- CogTES project (SA-2012/00329) of the Department of Education, Universities and Research of the Basque Government

Two research stays have been performed in international institutions during the thesis, one of 3 months at the University of Innsbruck (Austria) under the supervision of Prof. Ulrich J. Griesser and another of 10 months at the University of New South Wales (Australia) under the supervision of Dr. Robert Taylor. The latter stay was funded by the Panther Erasmus Mundus exchange program.

In addition, the author of the thesis has actively participated within the SHC/ ECES Task 42/29 research program of the International Energy Agency.

Index of contents

Index of figures

Index of tables

Nomenclature and symbols

Nomenclature	Description	Units
A_{mush}	Mushy zone constant	–
ANF	Present value annuity factor	year $^{-1}$
C_p	Specific heat	kJ/kg·K
e_c	HTF channel thickness	mm
e_{LHTES}	Width of the LHTES system	mm
e_p	Plate thickness	mm
e_{PCM}	PCM thickness	mm
e_w	Wall thickness	mm
f	Liquid fraction	–
g	Standard gravity	m/s^2
h_{conv}	Convection coefficient	W/m^2·K
i	Discount rate of storage capital	–
INC	Investment cost of the system	€
$\dot{m}$	mass flow rate	kg/s
M	Molar mass	g/mole
n	Payback period of the investment	years
n_c	Number of HTF channels	–
n_p	Number of plates	–
N_{cycle}	Number of storage cycles	year $^{-1}$
p	Pressure	bar
$\dot{q}$	Heat flux	W/m^2
$\dot{Q}$	Heat transfer per unit of time	W
R	Ideal gas constant	J/mole·K
REC	Substituted reference energy cost	€/kWh
SC	Installed storage capacity	kWh
SCC_{acc}	Maximum acceptable storage capacity cost	€/kWh
SCC_{real}	Realized storage capacity cost	€/kWh
$S_{PCM-HTF}$	Exchange surface between the PCM and the HTF	m^2
t	Time	s
t_{95}	Time needed to achieve a 95 % discharging energy ratio	s
T	Temperature	°C or K
T_{eut}	Eutectic temperature	°C or K
T_{l}	Liquidus temperature	°C or K
T_m	Melting temperature	°C or K
T_{s}	Solidus temperature	°C or K
$\bar{T}_{s\text{-}l}$	Average phase change temperature	°C or K
$\vec{v}$	Velocity	m/s
V	Volume	m^3
W	Weight	kg or g
w/w	Mass fraction	–
x	Axial coordinate	–
x_i	Liquid mole fraction	–
z	Solid mole fraction	–
ΔH^{sl}	Latent melting enthalpy	kJ/kg
ΔC_p^{sl}	Specific heat difference between solid and liquid phases	kJ/kg·K

Abbreviation	Description
TES	Thermal energy storage
LHTES	Latent heat thermal energy storage
PCM	Phase change material
CHP	Cogeneration
HTF	Heat transfer fluid
DHW	Domestic hot water
DSC	Differential scanning calorimetry
XRD	X-ray diffraction
PDF	Powder diffraction file
KF	Karl Fischer
RH	Relative humidity
HPLC	High performance liquid cromatography
TGA	Thermo-gravimetric analysis

Dimensionless numbers	Description
Bi	Biot number
Fo	Fourier number
Fo_{95}	Single Fourier number for a discharging ratio of 95 %
Nu	Nusselt number
Ra	Rayleigh number
Re	Reynolds number
Ste	Stefan number
X	Dimensionless axial coordinate
θ_{HTF}	Dimensionless temperature of the HTF
θ_{pc}	Dimensionless temperature of the PCM
Ψ	Dimensionless temperature constant
Ψ_{op}	Dimensionless temperature constant (related to the CHP operating temperatures)
Ψ_{pc}	Dimensionless temperature constant (related to the PCM)

Greek symbols	Description	Units
α	Thermal diffusivity	m^2/s
β	Thermal expansion coefficient	K^{-1}
γ^l	Activity coefficient of the liquid phase	–
E	Discharging energy ratio	–
λ	Thermal conductivity	W/m·K
μ	Dynamic viscosity	kg/m·s
ρ	density	kg/m^3
$\bar{\bar{\tau}}$	viscous stress tensor	Pa

Subscripts	Description
eut	Relative to the eutectic composition
high	Relative to the highest operating temperature
HTF	Relative to the heat transfer fluid
i	Relative to each compound in a mixture
inlet	Relative to the inlet section of the LHTES system
low	Relative to the lowest operating temperature
mix	Relative to a binary mixture
outlet	Relative to the outlet section of the LHTES system
PCM	Relative to the PCM
ref	Reference value
w	Relative to wall

Summary

The continuous rise of fossil fuels costs and their decreasing availability, combined with the requirement to reduce carbon emissions, reveal the necessity for more rational and efficient energy use. Buildings are large energy consumers: they are responsible for 40 % of the energy consumption in Europe and almost for 36 % worldwide. Accordingly there is an urgent need of developing new solutions to improve energy efficiency and energy savings.

Cogeneration, also called Combined Heat and Power (CHP), consists in the simultaneous utilization of heat and power from a single fuel or energy source. Due to its high efficiency, cogeneration can play an important role on the reduction of the energy consumption of buildings. However, despite the enormous potential that cogeneration provides, its penetration on the residential and tertiary sector is currently low due to its low economic feasibility.

Previous studies have demonstrated that the integration of thermal energy storage (TES) systems in cogeneration plants could substantially improve this situation. Amongst the different existing TES types, latent thermal energy storage (LHTES) is based on the use of the so-called phase change materials (PCMs), which store heat upon melting and subsequently release it during solidification. LHTES systems are especially suitable for integration in cogeneration plants in buildings where space availability is usually restricted and a high specific storage volume is required. Besides, since LHTES stores and releases the heat at an almost constant temperature, the performance of the plant is improved and the thermal losses are reduced.

As a result of the potential benefits that LHTES systems can provide to the CHP technology, a research line was opened in the ENEDI Research Group of the UPV/EHU, starting with a previous PhD thesis by Dr. Álvaro Campos–Celador. In that work, entitled: *Integration of latent thermal energy storage systems in the design and operation of residential cogeneration plants*, a novel plate-based LHTES system was proposed and its behavior within CHP plants was evaluated by means of simulations.

The thesis rendered promising results and the proposed LHTES system showed good potential; however, different aspects that require further research and development in order to achieve a competitive technology were identified, as follows:

- The specific price of PCMs is higher than the prices of the materials used for the traditional sensible heat thermal energy storage systems, which are usually abundant in nature. There is a clear need of PCMs with reduced cost or with enhanced energy storage capacity
- The low thermal conductivity exhibited by most PCMs limits the charging and discharging thermal power of the systems. Consequently, techniques or solutions to increase the heat exchange surfaces or to enhance the thermal conductivity of the PCM are required. This usually implies a price increment. Accordingly, it is essential to reach a compromise between power and storage capacity and, thus there is a need to develop a methodology able to provide a fast optimization and sizing of the system
- The manufacturing process has to be optimized. Fabrication routes based on the use of commercially available materials and compounds are needed, as well as the use of simple production methods that can be scaled up in order to decrease the fabrication costs

The present PhD thesis is the continuation of the work of Dr. Campos-Celador. Its main purpose is the further enhancement of the proposed LHTES system by means of the investigation of novel solutions to solve the limitations afore described. Accordingly, the following specific objectives were herein defined:

- Investigate new cost-effective eutectic mixtures of PCMs with phase change temperatures and adequate thermophysical properties, suitable for domestic heating and DHW applications
- Develop a simple overall design methodology to provide a fast sizing and optimization tool for plate based LHTES systems
- Design and produce a full-scale plate based LHTES prototype, including the definition of suitable manufacturing routes and the evaluation of the system integrity
- Evaluate the thermal behavior of the full-scale prototype within a CHP pilot plant, perform a complete economical study and propose further improvements of the system

According to these objectives, the research work on cost-effective PCMs started with the study of new binary eutectic mixtures of sugar alcohols for their use as PCMs in the temperature range suitable for heating and domestic how water applications. Sugar alcohols are

widespread materials with melting temperatures between 90 and 200 °C, non–corrosive and non–toxic. They are characterized by a superior volumetric energy capacity and their market price lies within the herein attempted range. However, their melting temperatures are too high to be directly used in LHTES systems for heating and DHW applications. Accordingly, determining potential eutectic sugar alcohol mixtures was a first target. The solid–liquid equilibria of binary systems comprising erythritol, xylitol, and sorbitol were researched in order to determine whether they form eutectic compositions with melting points suitable for the heating and DHW temperature ranges (50 to 90 °C).

The phase diagrams of the mixtures were experimentally established by differential scanning calorimetry (DSC) and X–ray diffraction (XRD). Polarized thermomicroscopy was employed to determine the crystallization rate of both, the pure materials and the eutectic compositions. Additionally, the polymorphic behavior of the pristine materials was assessed.

The results showed that, regarding melting temperature, storage capacity and market price, the studied mixtures are suitable for the intended purpose. Even though the three mixtures were considered interesting for TES purposes, the erythritol–xylitol eutectic composition showed the highest potential due to its superior heat storage ability.

However, the experimental measurements demonstrated that the mixtures presented a low crystallization rate, which limits their use in short-term LHTES systems like that herein proposed. Additionally, the materials show polymorphism and tend to form metastable amorphous states. As a result, further research is needed to enhance the crystallization behavior of the mixtures to be used as PCMs for the intended applications.

In addition, a modeling approach based on thermodynamics was used to predict the solid–liquid equilibrium of the studied mixtures and their melting enthalpies. The simulated results were in good agreement with the experimental results. The modeled and experimental results were used to highlight several practical aspects relevant for the development of new eutectic mixture–based PCMs.

The research on new PCMs continued with the study of the binary mixture composed of sodium nitrate and urea. Urea is a cheap organic compound, widely available and extensively used as a fertilizer. It has a melting temperature of 133 °C, a large melting enthalpy of 220 J/g and a market price around 0.7 €/kg. Unfortunately, it undergoes thermal degradation when

heated above its melting temperature. For this reason, the articles on its use as a PCM agree that urea is not a suitable material for LHTES purposes. However, the use of urea as a component of a binary mixture that melts below that temperature could produce a PCM suitable for LHTES purposes.

Among the possible mixtures, the system formed by sodium nitrate and urea has been proposed in the literature as a eutectic system with one composition suitable for use as a PCM. Sodium nitrate is a widespread inorganic material, which can be currently purchased at approximately 1 €/kg. Previous scientific works reported a eutectic composition composed of 70.5 % (w/w) urea, with a melting temperature of 84 °C and a melting enthalpy of 164 kJ/kg. However, only sparse experimental details were given in the articles and the phase diagram had not been established so far. Moreover, no study on the thermal degradation of the mixture has been reported up to now, which is a critical aspect for the use of this mixture as a PCM.

Accordingly, the phase diagram of the system was experimentally determined by using three complementary methods: DSC, the synthetic visual method and XRD. The main thermal properties and the density of the eutectic composition were studied in detail to evaluate its potential as a PCM. The results showed that the properties are suitable for the intended purpose. The water uptake by the material was also evaluated to gain knowledge of its hygroscopic behavior and XRD measurements were performed to study the formation of new phases or compounds due to the presence of water.

Owed to the thermal degradation underwent by urea upon heating, a preliminary accelerated thermal cycling study comprising 210 cycles was performed to determine the thermal reliability of the mixture. These results were complemented by chromatographic analysis to detect any presence of degradation byproducts.

According to the results, the mixture formed by sodium nitrate and urea shows potential as a PCM in the desired temperature range. Further research focused on the thermal degradation over longer periods of use is encouraged to establish whether the material has a proper lifespan for actual thermal energy storage applications.

The last binary mixture studied as a PCM was comprised by erythritol and urea. To the best knowledge of the author, the analysis of the phase equilibrium of this binary system had been

exclusively carried out by one article, back in 1932. No further related research has been found in the literature.

According to that work, the phase diagram corresponds to a simple eutectic system with a eutectic melting temperature of 78 °C. However, the rest of the key properties for the use of the mixture as a PCM, like the melting enthalpy or the stability against thermal cycling, remain unknown. Besides, the phase diagram was determined upon cooling. Since erythritol shows polymorphism and a noticeable supercooling, these metastable effects could have influenced the results.

Consequently, the phase diagram of the mixture was determined upon heating in order to confirm whether they form a eutectic composition with a melting point suitable for the space heating and DHW temperature range. Additional aspects affecting the phase diagram, such as the polymorphism of erythritol, were also investigated and discussed. The suitability of the eutectic composition as a PCM was also investigated.

The results showed a eutectic composition with a melting temperature of 81.13 °C and a latent melting enthalpy of 248 kJ/kg. The density of the eutectic composition was measured at different temperatures in order to establish the volumetric storage capacity. According to the results and market price, the eutectic mixture formed by erythritol and urea can be a good candidate for use as a PCM for the intended application. However, complex crystallization behavior was noticed. Besides, the results of a preliminary accelerated thermal cycling test showed that further research is required to evaluate the stability of the mixture on longer periods of use.

The study of the urea-erythritol eutectic mixture closes the work dealing with the development of new PCMs on this thesis. Accordingly, the second big objective of the thesis was approached: the development of a simple calculation tool for the overall sizing of plate-based LHTES systems for domestic CHP applications.

To approach this objective a CFD model was developed and experimentally validated to simulate different configurations of the plate-based system. The results were first employed to gain knowledge of the system melting and solidification behavior and subsequently to establish a correlation between the system discharging time and several dimensionless

numbers. These dimensionless numbers depend in turn on the plate thickness, the materials properties and the plant operation parameters.

The results of 86 CFD simulations were adjusted by means of a multiple linear regression analysis to develop the correlation. Then, the correlation was validated against 5 virtual PCMs. The average error of the correlation with respect to the CFD simulations was 2.38 %. Consequently, the developed correlation can be employed confidently for design purposes to determine the discharging time of plate based LHTES systems that operate within the herein considered conditions.

In addition to that correlation, an overall design method for plate based LHTES systems for CHP applications was developed. The method takes into account the remaining constraints of the system and consists of 3 simple steps. It produces a complete sizing of the system without the need of simulations and thus, it noticeably simplifies the design process to develop LHTES systems and decreases the time needed to size them. Besides, with small modifications, it could be easily extended to other applications.

To finish with the research performed in the present thesis, a full-scale plate-based LHTES prototype was designed and built. The above mentioned design methodology was applied to size it. A fabrication procedure was proposed for each component of the prototype. An integrity test of the components was also included, in order to ensure the suitable behavior of seals and welds.

The LHTES prototype was integrated into a micro-CHP pilot plant and tested under representative conditions. RT60, a commercial PCM, was used in these tests. The results were analyzed in terms of the energy stored and the time needed for charging and discharging. The achieved energy density storage was 31 % higher than the energy stored in a water tank with the same volume and temperature operation conditions.

An economic study was performed to evaluate the feasibility of the system. It included the assessment of the LHTES system using the above mentioned new PCMs, based on binary eutectic mixtures of materials, as well as two fatty acids characterized along the work.

The results showed that the cost of the produced prototype (including RT60 as a PCM) was 4.5 times higher than the estimated maximum acceptable costs for the building sector. The same

LHTES system including any of the eutectic mixtures developed in this thesis would reduce the costs to nearby 2 times lower. This reduction is not large enough to achieve the threshold considered competitive for buildings, but it is significant and straightforward. These outcomes reinforce the need of further research on PCMs with enhanced storage capacity. Moreover, they encourage future investigations focused on the improvement of the PCMs already developed in the present PhD thesis.

The use of composite PCMs with enhanced thermal conductivity was also considered in the economic analysis. This can be a solution to increase the economic competitiveness since the number of plates required to form the LHTES system (to achieve the same thermal power output) can be noticeably reduced when high thermal conductivity PCMs are used, and this would strongly decrease the manufacturing cost. A theoretical analysis of the LHTES system using the erythritol-xylitol binary mixture + expanded graphite was performed. This combination would present a cost 3 times lower than the current cost of the prototype with RT60 and close to competitive levels for the building sector. Further research oriented towards the use of PCM composites with enhanced thermal conductivity is therefore recommended.

Resumen

El continuo incremento del coste de los combustibles fósiles, unido a su decreciente disponibilidad y a la urgencia de reducir las emisiones de dióxido de carbono para frenar el cambio climático, ponen de manifiesto la necesidad de desarrollar medidas que promuevan el ahorro energético. Los edificios son grandes consumidores de energía: son responsables del 40 % del consumo a nivel europeo y del 36 % a escala mundial. El desarrollo de nuevas medidas para mejorar la eficiencia energética en edificación resulta por tanto imprescindible en la actual coyuntura mundial.

La cogeneración es una técnica que consiste en la utilización simultánea de calor y electricidad, los cuales son generados a partir de una única fuente de energía. Debido a su alta eficiencia, dicha técnica puede jugar un papel fundamental en la reducción del consumo energético en edificación. Sin embargo, a pesar del enorme potencial existente, el hecho cierto es que la penetración de los sistemas de cogeneración en el sector residencial y terciario es muy baja, debido principalmente a una menor rentabilidad económica de estas plantas en relación a los sistemas de cogeneración industriales.

Estudios previos han demostrado que la integración de sistemas de almacenamiento térmico (TES) en plantas de cogeneración puede mejorar sustancialmente dicha situación. Entre los sistemas TES existentes, los sistemas de almacenamiento térmico latente (LHTES), se basan en el uso de los llamados materiales de cambio de fase (PCMs). Estos materiales absorben energía en forma de fusión, la cual es liberada durante la solidificación. El uso de PCMs permite obtener sistemas con una densidad energética de almacenamiento más elevada que con los sistemas tradicionales. Por tanto, los sistemas LHTES son especialmente apropiados para sistemas en edificación, donde normalmente el espacio disponible para ubicar los equipos es limitado.

A consecuencia de los potenciales beneficios que los sistemas LHTES pueden aportar a la tecnología de cogeneración en edificios, el grupo ENEDI abrió una línea de investigación en dicho campo, que comenzó con la tesis doctoral del Dr. Álvaro Campos-Celador. En dicho trabajo, titulado: *Integration of latent thermal energy storage systems in the design and operation of residential cogeneration plants,* se propuso un sistema LHTES en base a placas, que fue optimizado y evaluado mediante simulaciones numéricas.

Los resultados de dicha tesis fueron prometedores y el sistema LHTES propuesto mostró un elevado rendimiento energético y exergético. Sin embargo, existen aún diferentes aspectos que han de ser evolucionados para conseguir un sistema económicamente competitivo frente a los sistemas de almacenamiento tradicionales, que están basados en tanques de agua. Dichos aspectos son los siguientes:

- El precio de los PCMs es significativamente más elevado que los materiales tradicionalmente empleados en almacenamiento térmico, los cuales son abundantes en la naturaleza. Es necesario desarrollar nuevos PCMs de bajo coste y elevada capacidad de almacenamiento
- Debido a la baja conductividad térmica que los PCMs presentan habitualmente, son necesarias técnicas para la mejora de la transferencia de calor entre el PCM y el fluido caloportador, lo cual implica un aumento del coste de fabricación. Por ello, es esencial alcanzar un compromiso entre potencia de descarga y capacidad y, por tanto, existe una necesidad de desarrollar nuevas metodologías de diseño de sistemas LHTES que sean rápidas, sencillas y fáciles de implementar
- El proceso de fabricación de sistemas LHTES ha de ser mejorado. Es necesario el desarrollo de rutas de fabricación que empleen materiales y productos ya existentes en el mercado, con el objetivo de reducir costes y aumentar la rentabilidad económica de los sistemas

La presente tesis doctoral pretende continuar el trabajo empezado por el Dr. Campos-Celador, y su principal objetivo es la evolución del sistema LHTES propuesto anteriormente mediante la investigación de soluciones novedosas a las limitaciones arriba descritas. En consecuencia, la presente tesis persigue los siguientes objetivos:

- Investigar mezclas eutécticas binarias de materiales para desarrollar nuevos PCMs adecuados para almacenar calor en el rango de temperaturas correspondiente a sistemas de calefacción y agua caliente sanitaria (ACS)
- Desarrollar un procedimiento genérico de diseño de sistemas LHTES para permitir el rápido dimensionamiento de sistemas LHTES y su optimización
- Diseñar y construir un prototipo LHTES a escala real, incluyendo la definición de una ruta de fabricación adecuada y la evaluación del sistema y sus componentes en términos de integridad mecánica

- Evaluar el comportamiento térmico de dicho sistema LHTES en una planta piloto de cogeneración y realizar un estudio económico completo con el fin de proponer futuras mejoras del sistema

Atendiendo a dichos objetivos, el trabajo realizado comenzó con el estudio de mezclas binarias de polialcoholes para su uso como PCMs. Los polialcoholes son materiales con puntos de fusión entre 90 y 200 °C, abundantes, no corrosivos y no tóxicos. Se caracterizan por una alta capacidad de almacenamiento latente y su precio entra dentro del rango definido como adecuado en el presente trabajo. Sin embargo, sus puntos de fusión son muy elevados para su uso directo en sistemas LHTES a temperaturas de calefacción y ACS. Por ello, se estudió el equilibrio sólido-líquido de mezclas binarias compuestas por eritritol, xilitol y sorbitol, con el fin de determinar si forman mezclas eutécticas adecuadas para las temperaturas de calefacción y ACS (entre 50 y 90 °C, aproximadamente).

Los diagramas de fases de las mezclas fueron determinados experimentalmente mediante calorimetría diferencial de barrido (DSC) y difracción de rayos-X (XRD). Las velocidades de cristalización de los materiales puros y de las mezclas fueron estudiadas mediante termomicroscopía óptica. También se evaluó el polimorfismo de los materiales puros.

Los resultados mostraron que, en términos de temperatura de cambio de fase, capacidad de almacenamiento y precio, las mezclas identificadas son adecuadas para el objetivo pretendido. De entre las tres mezclas estudiadas, aquella formada por eritritol y xilitol mostró un mayor potencial, debido a su superior capacidad de almacenamiento.

Sin embargo, los ensayos experimentales demostraron que las mezclas presentan una velocidad de cristalización excesivamente baja, lo cual limita su potencial como PCMs. Además, debido a su polimorfismo, los materiales presentan un comportamiento complejo en cristalización. Por ello, son necesarias investigaciones adicionales para que las mezclas se puedan usar en sistemas LHTES de un modo adecuado.

La investigación en nuevos PCMs prosiguió con el estudio de la mezcla binaria formada por urea y nitrato de sodio. La urea es un compuesto orgánico barato y ampliamente disponible usado principalmente como fertilizante. Presenta una temperatura de fusión de 133 °C, una alta entalpía de 220 J/g y un precio de 0.7 €/kg. Sin embargo, se descompone térmicamente cuando se calienta por encima de su temperatura de fusión. Por ello, todos los artículos que

han estudiado su uso como PCM, concuerdan en concluir que su empleo no es adecuado para el almacenamiento térmico. No obstante, el uso de urea como compuesto en una mezcla eutéctica binaria que funda a una temperatura por debajo de 133 °C, podría dar como resultado un PCM sin el problema de degradación mencionado.

Entre las posibles mezclas que podrían formarse con urea, aquella compuesta por urea y nitrato sódico ha sido propuesta anteriormente en la literatura. Los trabajos previos reportan una temperatura eutéctica de fusión de 84 °C y una entalpía de fusión de 165 KJ/kg. Sin embargo, en dichos trabajos los detalles experimentales son escasos, y el diagrama de fases no ha sido publicado todavía. Más aún, dicho estudios no incluyen una evaluación de la degradación térmica de la mezcla eutéctica propuesta, lo cual supone un aspecto crítico a evaluar en su uso como PCM.

En consecuencia, el diagrama de fases de la mezcla fue determinado en la presente tesis mediante DSC; una técnica experimental denominada “método visual” y difracción de rayos-X. Las principales propiedades térmicas de la composición eutéctica encontrada, así como su densidad fueron evaluadas en detalle para determinar el potencial de la mezcla como PCM. Los resultados mostraron que las propiedades son adecuadas para el objetivo pretendido. Además, se estudió la higroscopicidad de la composición eutéctica, con el fin de evaluar la facilidad de manejo de la mezcla a la hora de producirla. El estudio se completó con un ensayo acelerado de degradación térmica que constó de 210 ciclos de fusión y solidificación.

De acuerdo a los resultados, la mezcla formada por nitrato de sodio y urea muestra potencial para su uso como PCM en la temperatura definida. No obstante, serán necesarias investigaciones adicionales relacionadas con la degradación térmica de la mezcla para confirmar su verdadero potencial como material para almacenamiento térmico.

La última mezcla binaria estudiada a modo de PCM en la presente tesis fue la compuesta por eritritol y urea. De acuerdo a la revisión bibliográfica realizada, dicha mezcla no ha sido previamente estudiada como PCM, a pesar de que existe un artículo del año 1932 en el que su diagrama de fases fue obtenido para otras aplicaciones distintas a la aquí pretendida.

De acuerdo a dicho trabajo, la mezcla es eutéctica y presenta una temperatura eutéctica de fusión de 78 °C. No obstante, el resto de las propiedades fundamentales para su uso como PCM aún no se conocen. Además, en el mencionado artículo, el diagrama de fases se

determinó en enfriamiento, y no en calentamiento. Esto pudo alterar las condiciones de medida, ya que el eritritol presenta un comportamiento polimórfico complejo a la hora de cristalizar. En consecuencia, el diagrama de fases fue establecido en calentamiento en la presente tesis, con el fin de confirmar si existe una composición eutéctica con una temperatura de fusión adecuada para las temperaturas de calefacción y ACS.

Los resultados arrojaron una composición eutéctica con una temperatura de cambio de fase de 81.13 °C y una entalpía de fusión de 248 J/g. La densidad de la mezcla fue medida a diferentes temperaturas con el fin de establecer la densidad de almacenamiento volumétrica. De acuerdo a los resultados obtenidos, la composición eutéctica del sistema es adecuada para su uso como PCM en la aplicación aquí pretendida. Sin embargo, también presenta un comportamiento complejo en cristalización, lo cual dificulta su uso en sistemas LHTES. Además de ello, ensayos preliminares de degradación térmica mostraron que es necesario evaluar la degradación en tiempos más prolongados de uso para confirmar su potencial definitivo.

Después de estudiar la mezcla formada por eritritol y urea, el trabajo relacionado con el desarrollo de nuevos PCMs se dio por finalizado. En consecuencia, se abordó el segundo gran objetivo de la tesis: el desarrollo de una metodología general de dimensionamiento para sistemas LHTES en base a placas integrados en aplicaciones de cogeneración.

Para tal fin, se desarrolló un modelo de dinámica de fluidos computacional (CFD) que fue experimentalmente validado, y con el que se simularon diferentes configuraciones del sistema LHTES. Los resultados fueron empleados inicialmente para comprender mejor el comportamiento en fusión y solidificación del sistema. Posteriormente, se estableció una correlación para calcular el tiempo de descarga del sistema en función de varios números adimensionales. Dichos números, a su vez, dependen del espesor de placas empleado, las propiedades de los materiales y los parámetros de operación de la planta de cogeneración.

Los resultados de 86 simulaciones de CFD se ajustaron mediante análisis lineal multivariante para obtener la correlación, la cual fue validada con los resultados de CFD obtenidos con 5 nuevos PCMs específicamente definidos para dicha tarea. El error promedio alcanzado fue del 2.38 %; por tanto, la correlación desarrollada puede considerarse adecuada para calcular el tiempo de descarga de sistemas LHTES que operen bajo condiciones similares a las definidas en la presente tesis.

Mediante dicha correlación, se desarrolló un método general de dimensionamiento para sistemas LHTES basados en placas. Dicha metodología tiene en cuenta el resto de los parámetros que vienen definidos por la planta de cogeneración donde el sistema LHTES se instala, y consta de tres sencillos pasos. Mediante la misma, se puede dimensionar completamente el sistema sin la necesidad de simulaciones. Por tanto, simplifica sobremanera la etapa de diseño, ahorrando una cantidad de tiempo muy significativa. Además, con pequeñas modificaciones, dicho método podría ser extendido a aplicaciones diferentes a la aquí considerada.

Para finalizar la investigación realizada en la tesis, se diseño y construyo un sistema LHTES a escala real mediante el procedimiento general de diseño arriba descrito. Se propuso una ruta de fabricación para el sistema y cada uno de sus componentes. También se estudió la integridad mecánica de los componentes, con el fin de mostrar su adecuado comportamiento.

El prototipo LHTES se acopló a una planta piloto de cogeneración disponible, y fue ensayado bajo condiciones nominales de operación. Dichos ensayos se realizaron con RT60 a modo de PCM, un material comercial de la casa Rubitherm. Los resultados fueron analizados en términos de energía almacenada y tiempo necesario para carga y descarga. La densidad de almacenamiento obtenida fue un 31 % más elevada que un tanque de almacenamiento de agua con el mismo volumen y bajo condiciones de operación equivalentes.

El estudio se completó mediante un análisis económico para estudiar la rentabilidad del sistema. En el mismo se incluyó también la evaluación del comportamiento teórico del sistema en el caso de que los PCMs empleados fueran las mezclas eutécticas que se han desarrollado a lo largo de la tesis, además de dos ácidos grasos que fueron caracterizados para el trabajo de desarrollo de la metodología general de diseño arriba descrito.

Los resultados económicos mostraron que el actual sistema, con RT60 como PCM, presenta un coste 4.5 veces mayor que el coste estimado como competitivo para el sector de edificación. El mismo sistema LHTES, pero incluyendo cualquiera de las tres mezclas binarias desarrolladas en la tesis reduciría el coste actual a la mitad. Dicha reducción no es suficiente para alcanzar niveles considerados competitivos económicamente; sin embargo, sería una reducción significativa y directa, sin necesidad de modificaciones en el diseño. Esta observación refuerza

la necesidad de desarrollar nuevos PCMs económicamente competitivos y con una capacidad superior de almacenamiento.

El uso de PCMs formados por composites que presenten una mayor conductividad térmica fue también incluido en el estudio económico. Dicha alternativa puede presentar una solución viable para reducir los costes de producción, ya que permitiría reducir el número de placas a usar para conseguir la misma capacidad de descarga. Se realizó un análisis para determinar el coste teórico de un sistema LHTES formado por un PCM compuesto por la mezcla eutéctica de eritritol y xilitol aquí estudiada, combinada con una matriz de grafito expandido. Dicha combinación presentaría un coste cercano al considerado competitivo para el sector de edificación, y 3 veces más bajo que el coste actual del prototipo que incluye RT60. Este resultado permite concluir que es la investigación de sistemas basados en composites con elevada conductividad térmica es por tanto recomendable.

CHAPTER 1: Introduction, objectives and structure of the PhD thesis

ABSTRACT

The present chapter presents the background and motivation of the PhD work performed. The theoretical aspects about cogeneration and thermal energy storage considered relevant for the understanding of the thesis are described. The main objectives and the structure of the dissertation are exposed as well.

1. Introduction

The continuous rise of fossil fuels costs and their decreasing availability, combined with requirements to reduce carbon emissions, reveal the necessity for more rational and efficient energy use. Buildings are large energy consumers: they are responsible for 40 % of the energy consumption in Europe and almost for 36 % worldwide [1]. Accordingy, the Energy Performance of Buildings Directive of the European Union (2010/31/EU, [2]) states the urgency of developing new solutions to improve energy efficiency and energy savings. Those new developments should not only be suitable for the construction of new buildings, but also for the renovation of the existing ones.

Cogeneration, also called Combined Heat and Power (CHP), consists in the simultaneous utilization of heat and power from a single fuel or energy source, at or close to the point of use [3]. The working principle of CHP is schematically shown in Figure 1-1. CHP plants generally convert 75-80 % of the fuel source into useful energy, while modern systems reach efficiencies of 90 % or more. Due to these high values, the current European regulation on energy efficiency (2012/27/EU Directive [4]) includes cogeneration amongst the most efficient energy production processes from fossil fuels. This is reinforced by the Directive 2010/31/EU [2], where cogeneration is claimed to be considered as an alternative of the energy supply both, for individual single building plants and for big district heating plants. Based on these facts, it can be stated that cogeneration can play an important role on the reduction of the energy consumption of buildings.

However, when the information about the number of installed capacities of domestic CHP is analyzed, it can be observed that the current level of penetration is very low. Across EU, in Germany, Denmark or Netherlands, residential CHP is a widespread technology. The penetration on other European countries is presently very low and, accordingly, the CHP heat and electricity generation could at least be double by 2020, as reported in 2007/2008 by the EU Member States [5].

Regarding the specific situation of Spain [6], the overall installed power by 2009 in the tertiary sector (which includes residential and commercial buildings) was 640 MW. This represents approximately 10 % of the existing overall potential [7]. In terms of small-scale CHP applications (plants with an electric power lower than 1 MW, which are mainly focused to

domestic applications), the penetration ratio was 0.38 % of the entire potential. In light of these numbers, it can be stated that presently the ratio of implementation of CHP plants in buildings is poor in spite of the existing high development potential.

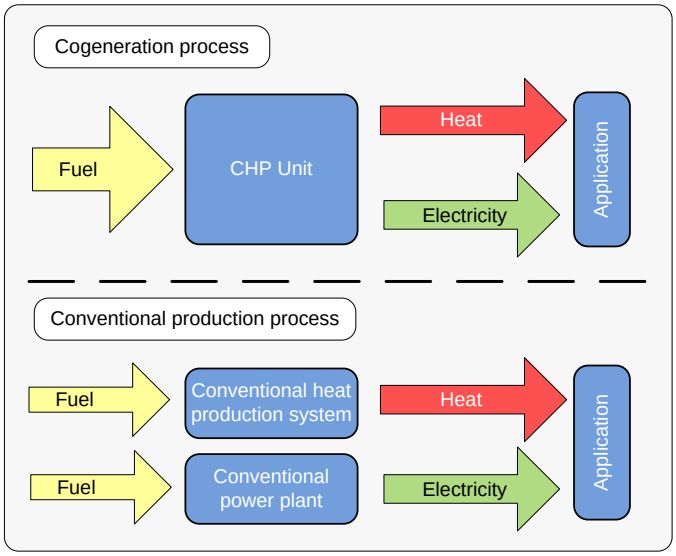

Figure 1-1: Schematic comparison between CHP and conventional production process, adapted from [5]

When the obstacles responsible for this situation are analyzed, it can be inferred that the situation is directly connected with the lower economic feasibility that residential CHP plants offer when compared to the industrial ones. However, while the potential to develop new technical solutions for the industrial sector is limited, domestic CHP is still an almost unexploited sector. The development of techniques to increase the efficiency of residential CHP is viable. This would eventually increase their economic feasibility and, thus, help to improve their integration in the energy mix. The main problems that have to be overcome are the following [5]:

- The thermal energy demand in buildings is highly variable, due to the diary and seasonal dependency of the loads
- The thermal energy demand in buildings is difficult to predict because it is linked to the meteorological conditions and the stochastic demand by the occupants
- The specific power of CHP in building applications is lower than in the industrial sector, and the existing economy of scale makes the bigger devices to be cheaper in comparison with the small ones

Several techniques have been studied up to now to solve these problems. The most relevant are shown in Table 1-1. As it can be seen, the use of Thermal Energy Storage (TES) systems can provide a solution to every problem formerly pointed out. The storage of the excess heat produced and its subsequent release upon demand allows to:

- Stabilize the heat production while the TES system acts as a buffer between the production and the variable consumption
- Decrease the interdependence between the running of the CHP device and the uncertainties of the thermal demand. The store of thermal energy reduces the importance that the gap between peak power and demand has on the production
- Run the system for a higher number of hours, which increases the low economic feasibility of these plants, even those in the small scale-range of power

	Potential solutions				
Existing problems	Running at partial load	Advanced control systems	Centralize the thermal production	Micro-CHP solutions	Thermal Energy Storage Systems
Variable thermal demand	✓				✓
Unpredictable thermal demand	✓	✓			✓
Low specific power			✓	✓	✓

Table 1-1: Evaluation of existing problems and potential solutions for residential cogeneration, adapted from [5]

Accordingly, TES systems can be regarded as an optimum technique to potentiate the growth of CHP for production of heating and domestic hot water (DHW) in buildings. The present thesis deals with the use of latent heat thermal energy storage systems for domestic CHP applications. This specific type of heat storage is described next, along with general theoretical and practical aspects on TES.

2. Thermal Energy Storage: Description of the main aspects

Thermal energy storage can be defined as the temporary storage of thermal energy for its later use, and is considered a key factor for optimizing the operation of CHP plants [8]. The storage is basically independent from the prime mover technology or from the used fuel type.

There are 3 main different ways of storing thermal energy, namely:

- Sensible heat thermal energy storage (SHTES)
- Latent heat thermal energy storage (LHTES)
- Thermochemical thermal energy storage (TCTES)

These types are in turn divided into sort-term and long term storage systems, depending on the time scale. Short term TES systems comprise the thermal energy storage for a time period ranging from hours to a maximum of some few days. Seasonal heat storage ranges from weeks to months. The present work deals exclusively with short-term storage.

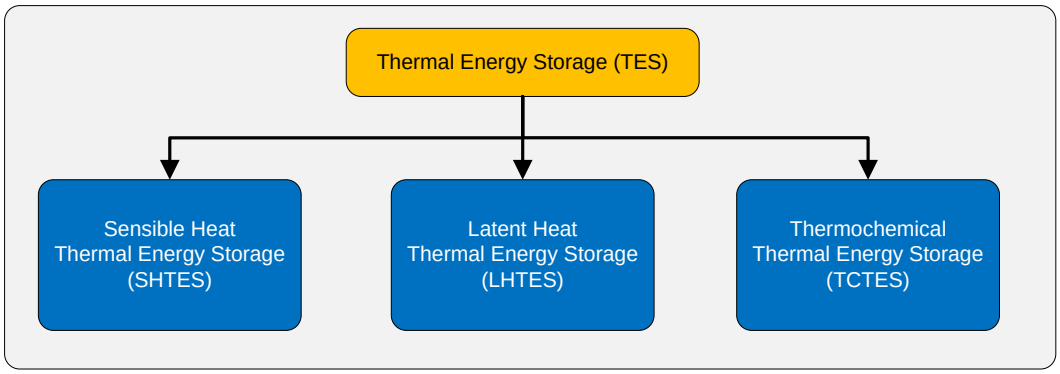

Figure 1-2: Classification of the different types of Thermal Energy Storage (adapted from [9])

Thermochemical thermal energy storage is based on the energy storing or releasing that occurs during reversible chemical reactions or transformations. Common advantages of this mechanism are: high storage energy densities and long storage duration at near ambient temperature [10]. The main drawbacks of these systems are the typical slow velocity of the processes and the difficulty of finding suitable chemical reactions to be widespread used. As a result, presently the technique is at an early stage of development and it cannot be considered as a current alternative to be used in residential CHP applications.

Sensible thermal energy storage is based on the energy storing or releasing that occurs when a certain quantity of mass of a liquid or solid substance varies its temperature under a same initial and final chemical structure [11]. The stored energy is hence directly proportional to the mass of the substance, its heat capacity and the temperature change during the process. The sensible storage materials most commonly employed are rocks, ground, or water. A typical example of SHTES application is the use of domestic hot water storage systems.

Due to its nature, SHTES is an economically feasible technology, robust and reliable. However, it presents two disadvantages: (i) the materials typically used present low heat capacities and,

(ii) it is necessary to have a large change of the system temperature to store enough thermal energy.

Latent thermal energy storage is based on the difference of the internal energy associated to each state on a phase change process. It relies on the storage material absorbing or releasing heat as it undergoes a solid to solid, solid to liquid or liquid to gas phase change or vice versa [12]. The use of the solid-liquid phase change is based on the use of the so-called phase change materials (PCMs), which store heat upon melting and subsequently release it during solidification. The use of PCMs is regarded as a promising technology for domestic applications, due to its relatively high heat storage density with a reasonable simplicity on the handling and operation of the system. These features are especially suitable for applications in the buildings sector [13–19], because:

- Usually, the available space is limited, so the larger storage density allows having smaller storage systems
- The storage at a nearly constant temperature improves the operation of the equipment and reduces the thermal losses
- The shape of the LHTES tanks can adopt different forms and sizes, depending on the requirements. This is unfeasible with traditional hot water SHTES systems, which due to the stratification a cylindrical elongated shape is needed, which implies an inefficient use of the available space
- The latter feature is especially beneficial for CHP devices, which, in the small-scale range of power, are formed by cubic modules (Figure 1-3). A square shaped LHTES can be easily integrated with the CHP modules with a null or small increase of the surface-occupancy

As a result of the potential benefits that LHTES systems can provide to the CHP technology, a research line was started in the ENEDI Research Group of the UPV/EHU by means of a previous PhD thesis performed by Dr. Álvaro Campos–Celador. In that work [5], entitled: *Integration of latent thermal energy storage systems in the design and operation of residential cogeneration plants*, a novel LHTES system based on finned plates was proposed and its behavior within CHP plants was evaluated by means of simulations.

Figure 1-3: View of a WHISPERGEN micro-CHP unit (*left*) and a TECOGEN small-scale CHP unit (*right*)

The thesis rendered promising results and it was concluded that the proposed LHTES system offers a better performance (both considering energy and exergy efficiency) than the traditional hot water SHTES systems, especially due to its easier integration in CHP plants, which increases the efficiency of the latter.

The investigation performed on that thesis was focused on the development of a conceptual design and the work was mainly based on simulations. Accordingly, different aspects require further research and development in order to achieve a competitive technology. Consequently, the present PhD thesis is the continuation of that work [5], and its main objective is the further enhancement of the proposed LHTES system by means of the investigation of novel solutions to solve the limitations therein identified.

The following section will summarize the main features of the storage system proposed in [5]. The reader is referred to the original dissertation for detailed information. The topics covered in that work and the main conclusions attained will also be detailed. Finally, the main shortcomings of the developed LHTES system will be presented, since they are considered the rationale of the present thesis.

3. Design features of the previously developed finned plate-based LHTES system

The main tasks covered by the PhD work performed in [5] are listed next. Those specific topics that are relevant for the present thesis will be briefly discussed on the following subsections.

- Selection of the system configuration and conceptual design:
    - Selection of the materials and components

- Definition of two potential manufacturing routes depending on the production volume (number if units to be produced)

- Optimization of the proposed LHTES system integration within CHP plants
- Simulation of the LHTES system behavior, including the experimental validation of various developed models by means of a small-scale laboratory prototype constructed specifically for that purpose
- Energetic, exergetic and economic evaluation of the proposed conceptual system

3.1. General aspects of the design proposed

An analysis of the available LHTES technologies was first performed in [5]. Three main basic design options exist for solid-liquid LHTES systems, presented in Figure 1-4. Amongst them, the heat exchanger-type storage was selected.

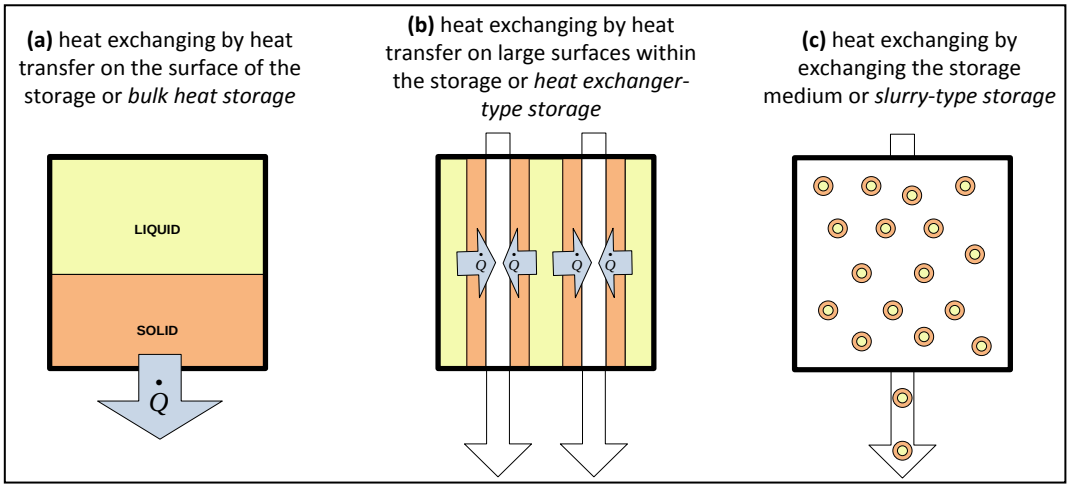

Figure 1-4: Existing LHTES basic configurations [5] (adapted from [20])

Several types of heat exchanger LHTES systems exist, which are mainly defined by the shape of the PCM encapsulation. Although shell-and-tube is the most studied LHTES system type in the literature [17], the flat plate configuration offered several features that are especially advantageous for this application [21], such as:

- High surface to volume ratio, which leads to significant storage and releasing power
- High modularity, because due to the use of single plates as storage units, different storage volumes can be easily approached for different thermal loads, economic frameworks, etc. This can be attained by the simple variation of the number of plates in serial and parallel

- The whole LHTES system presents a rectangular shape which makes an easy integration in CHP plants where the space is a limiting factor
- The shape allows the direct integration of the LHTES system within the CHP module (Figure 1-3), obtaining a “compact pack” that includes the production and storage units and the ancillary systems needed

Accordingly, the base of the LHTES system proposed in [5] was the plate presented in Figure 1-5 (right). The PCM is enclosed inside hollow plates, which should be completely airtight. The plates are arranged upwards on a disposition like that shown on the figure, and the HTF flows in parallel to the largest sides of the plates (*yz* plane in Figure 1-5, left), exchanging the heat with that surface of the plate.

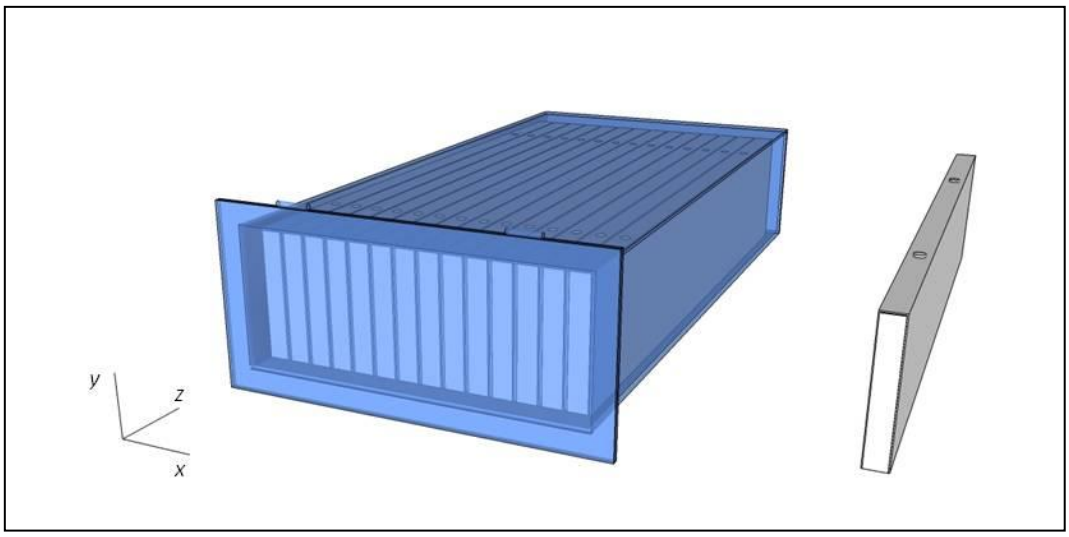

Figure 1-5: Conceptual image of the plate-based LHTES system (left) and detail of a plate (right)

The in-parallel arrangement of the plates, with narrow channels between the plates, forms the channels where the HTF flows through. A compact stack of several in-parallel plates-channels form the basic stack of the LHTES system. Several stacks can be placed in-series and/or in-parallel as well. Therefore, there is no need to use larger plates when large storage volume is required, neither to provide a large number of plates in-series: several compact stacks can be placed in-parallel, piled up or any combination of both. As an example, in Figure 1-6 a LHTES system of 56 plates is presented, where the number of plates in-parallel is 14 and 4 stacks are connected in series (2 placed widthwise and 2 heightwise). In this way, specific designs can be provided for a defined application, adapted to the space availability

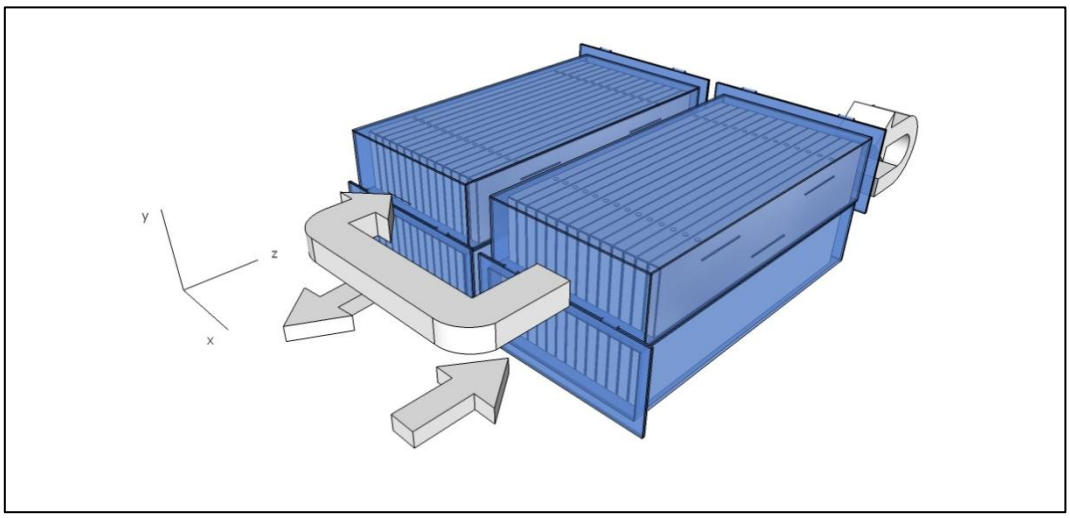

Figure 1-6: Example of plate-based LHTES system with 56 plates divided into 4 stacks

The design originally proposed in [5] included fins inside the plates, in contact with the PCM (see Figure 1-7). The purpose was to increase the foreseen low charging/ discharging rates caused by the low thermal conductivity of typical PCMs [22,23]. Although this is regarded as a suitable solution in the literature, the fabrication costs of the LHTES system increased noticeably. Thus, in the present thesis it was opted to remove the fins from the design.

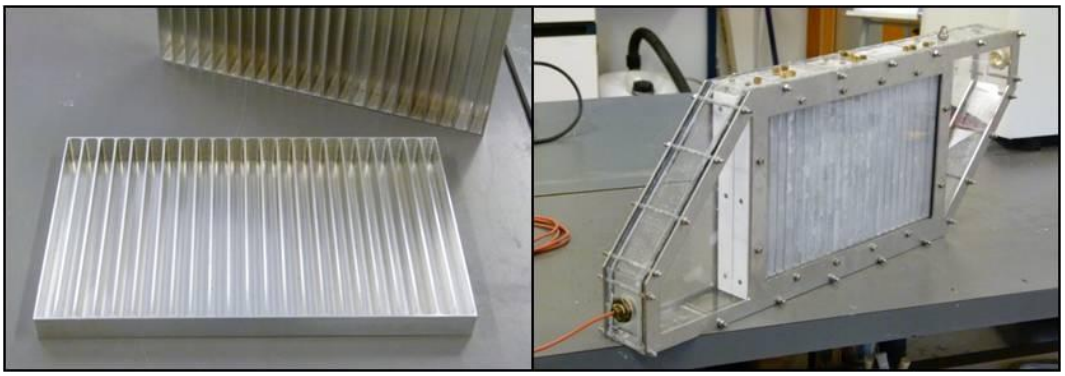

Figure 1-7: Overview of the finned plates used in [5] (left) and the developed laboratory-scale prototype (right)

3.2. Materials selected for the LHTES system

The PCM selected in the PhD previously performed was the commercial paraffin RT60 from Rubitherm GmbH [24]. The desirable requirements for any PCM will be presented in Chapter 2 – Section 1. Amongst them, it was considered that the RT60 presents the following three essential factors for an early research stage like that performed in [5]:

- Phase change temperature (55-61°C) adequate for the involved operation temperatures (which are defined in Section 3.3.2)
- Appropriate thermal behavior and handling, i.e.: stable performance against thermal cycling and no water uptake
- Negligible supercooling

The price of RT60 (from 4 to 6 €/kg depending on the purchased amount) is high for large scale thermal energy purposes [25]; however, it was considered feasible for that research stage. The PCM thermal properties provided by the supplier can be found in [24], while a detailed characterization performed is presented in Chapter 5.

To produce the plates, stainless steel and aluminium alloys were the two candidate materials selected for the system. The small-scale prototype constructed for modeling validation purposes was made of aluminum, while the cost estimation performed considered the properties and cost of the two mentioned material families.

In addition, since the system would be integrated in residential CHP plants, water was selected as the heat transfer fluid (HTF).

3.3. Design considerations of finned plate LHTES systems for CHP

An important part of the work performed in [5], was devoted to the optimization of the integration of the LHTES system in domestic CHP plants. The study defined several design constraints that the developed LHTES system has to meet. The following paragraphs present those constraints that have been relevant for the research carried out in the present thesis.

3.3.1. Plant integration of the LHTES system

Different LHTES system integration choices were discussed in [5]. Amongst them, it was decided that the LHTES system placed after the CHP unit using an in-series arrangement offers the best features for the characteristics of residential applications. The configuration proposed is shown in Figure 1-8. This configuration will be followed in Chapter 6, where a full-scale prototype is designed and tested in a CHP pilot plant.

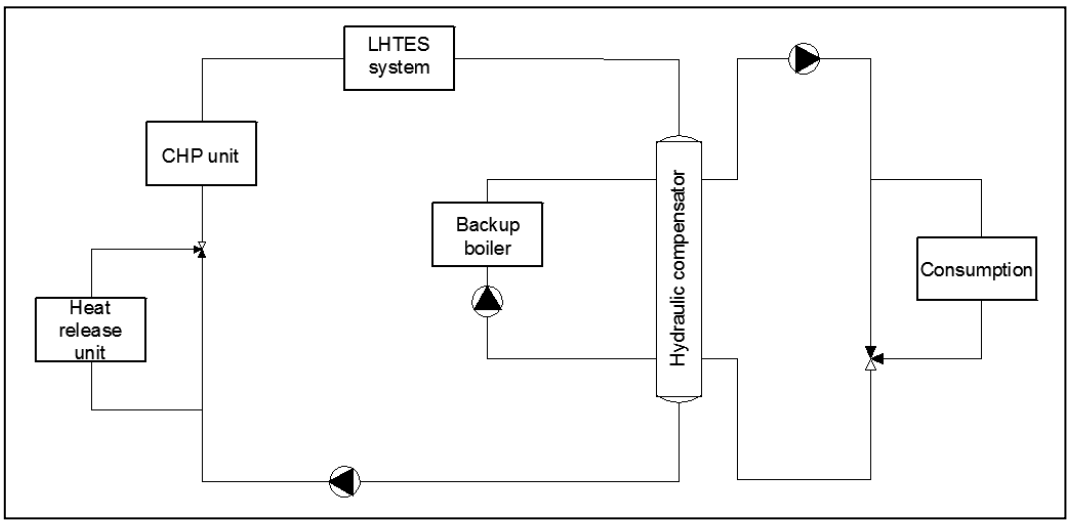

Figure 1-8: Configuration of the LHTES system integration proposed in [5] within a domestic CHP plant

3.3.2. Temperature of the water for charging and discharging of the LHTES

There are two inlet temperatures for the LHTES system, the inlet temperature for charging and the inlet temperature for discharging. A certain CHP design presents two temperature levels, lower and upper, related with the temperature of the HTF exiting and entering the unit. These temperatures correspond to the inlet temperature for the storing process and to the inlet temperature for the discharging, respectively. Their values are linked to the specific CHP unit under consideration. However, it is possible to adapt them in order to get the best performance. Under real operation conditions, variations are expected around these values depending on the dynamics of the plant, but for design purposes they can be considered constant.

An optimization study was performed in [5] to determine the working temperatures of the CHP system that optimized the performance of the LHTES system proposed. A temperature difference between the charging and discharging of 15 °C was chosen, which is usual for residential cogeneration applications. The results showed that the 65-50 °C pair of temperatures was optimum for charging and discharging, respectively, for the RT60 PCM. As the phase change peak of that PCM occurs at 59 °C, even slight variations over the charging-discharging temperature ensured that the peak is covered and the differences in the nominal storage capacity of the so operated LHTES systems are minimized.

3.3.3. Flow regime to be used and its influence on the HTF mass flow rate

An analysis was performed in order to determine the most suitable HTF flow regime to be employed. It was based on a hydraulic modeling and on a simplified analysis of the overall heat transfer problem involved. It was concluded that the developed system should always operate under a laminar regime.

Note that the aforementioned constraints have been described in the present chapter in order to get an overall picture of the system developed in [5]; however, these constraints mainly affect the contents of Chapters 5 and 6 of the present thesis. Thus, for a better reading of the dissertation, they will be again reminded on the corresponding chapters.

3.4. Main tasks and conclusions of the previous PhD dissertation ([5])

After the conceptual design and the integration of the LHTES system were studied in [5], an optimization process was performed in order to estimate the optimal finned-plate LHTES configuration for residential cogeneration plants of different sizes. Two potential fabrication routes were proposed in order to estimate the cost of the LHTES system, which was determined by means of cost estimation models. The performance of LHTES systems with the optimal configuration was compared with the use of conventional hot water TES.

According to the conclusions attained in [5], it can be stated that the plate-based LHTES system proposed presents the following strengths:

- It requires smaller volume than conventional TES systems for a certain storage capacity
- It is modular and can be easily adapted to different applications
- It presents the forecasted effective storage capacity, while in the case of hot water storage tanks it depends on the level of stratification
- Due to its compactness, for the same level of thermal insulation the heat losses to the surroundings are reduced
- It provides a more effective usage of the available space due to its prismatic shape
- It shows an increased efficiency of the plant where it is integrated in comparison with conventional TES systems

In spite of these benefits, the study concluded that the current high cost of the system makes it to be less profitable than conventional TES systems, being economically attractive only for those applications with space limitations. This high cost was attributed to the following factors:

- The specific price of PCMs is comparatively higher than the prices of the materials used for SHTES, which are usually abundant in nature. There is a clear need of PCMs with reduced cost or with enhanced energy storage capacity. This is reinforced with recent literature articles [26], which state that the cost of PCMs should be around 1-2 €/kg
- The low thermal conductivity usually exhibited by PCMs limits the charging and discharging thermal power of the systems. Consequently, techniques or solutions to increase the heat exchange surfaces or to enhance the thermal conductivity of the PCM are required. This usually implies an increase of the price. Accordingly, it is essential to achieve a compromise between power and storage capacity and, thus there is a need to develop a methodology able to provide a fast optimization and sizing of the system
- The manufacturing process has to be optimized. Fabrication routes based on the use of materials and compounds already available in the market and the use of simple production methods that can be scaled up are needed in order to decrease the fabrication costs. Besides, the produced systems should ensure a good integrity for the long life use, preventing problems like the leakage of materials, corrosion, thermal fatigue failures or others

The objectives of the present thesis were defined by taking into consideration all these shortcomings and constraints. They are detailed in the following section, along with the structure of this dissertation.

4. Objectives and structure of the PhD dissertation

The **main objective** of the present thesis is the enhancement of the LHTES system described on the former pages in order to ultimately improve the feasibility and efficiency of energy generation technologies such as domestic CHP plants. According to the shortcomings defined in [5], the following **specific objectives** are sought:

- **Investigate new cost-effective eutectic mixtures of PCMs** with phase change temperatures suitable for heating and DHW applications and adequate thermophysical properties
- **Develop a simple overall design methodology** to provide a fast sizing and optimization tool for plate based LHTES systems
- **Design and construct a full-scale plate based LHTES prototype, including the definition of suitable manufacturing routes** and the evaluation of the system integrity
- **Evaluate the thermal behavior of the full-scale prototype within a CHP pilot plant, perform a complete economical study** and propose further improvements of the system

In addition, the following **side objectives** are pursued. These goals are general and they include also formative aspects, such as:

- Produce innovation and new knowledge on the determination of phase diagrams by means of modeling and experimental complementary techniques in order to develop new PCMs based on mixtures
- Produce innovation and new knowledge on techniques and methodologies to characterize PCMs
- Produce innovation and new knowledge on the modeling of LHTES systems and PCMs and the heat transfer related issues
- Produce innovation and new knowledge on fabrication methods for plate-based LHTES systems and on the integrity of their components that can be applied also to other LHTES types

According to the objectives, the **structure of this document, displaying the research carried out in the thesis,** is described next. The introduction to each chapter includes its own motivations, literature survey and objectives. Also, the initial page of each chapter includes a brief summary of the same.

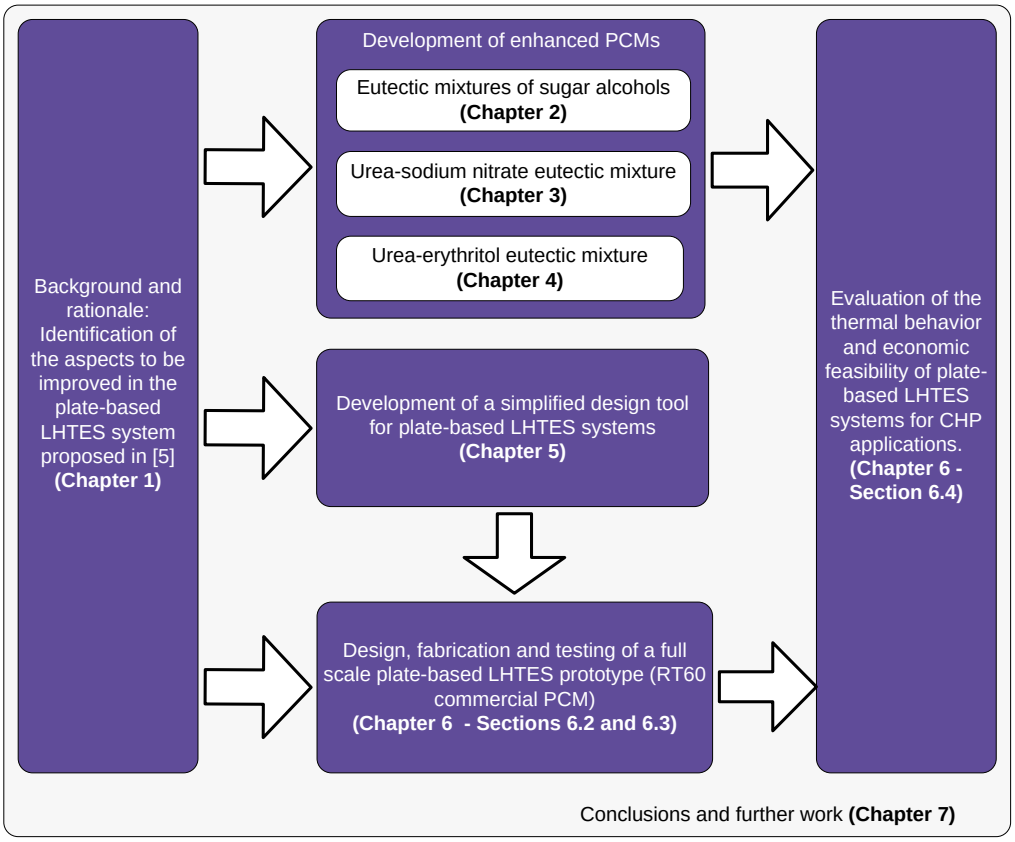

Figure 1-9: Structure of the present document

Chapters 2, 3 and 4 deal with the development of new PCMs based on eutectic mixtures for LHTES systems. These PCMs will be applicable to LHTES systems for space heating and DHW applications in general, not only for domestic CHP appliances. The chapters correspond to articles that have already been published in international scientific journals during the execution of the thesis.

- **Chapter 2** studies **new binary eutectic mixtures of sugar alcohols** for their use as phase change materials (PCMs) in the heating and domestic how water temperature range. The studied mixtures are composed of erythritol and xylitol, erythritol and sorbitol, and xylitol and sorbitol. Their phase diagrams were calculated in order to study whether they form eutectics with melting points suitable for the heating and DHW temperature ranges. The thermal properties and crystallization behavior of those compositions that were found to be suitable were established by several techniques. Additional practical features related to the study of new eutectic-mixture-based PCMs will be also discussed

- **Chapter 3** studies the **binary mixture composed of sodium nitrate and urea** for use as a PCM for the applications involved. The phase diagram of the system was experimentally determined by complementary techniques. A complete characterization of the main thermophysical properties of the eutectic composition was performed in order to evaluate its potential as a PCM. In addition, because urea undergoes thermal degradation upon heating, several tests were performed to investigate the thermal reliability of the mixture. The effects of water uptake were also studied
- **Chapter 4** studies the **binary mixture comprised by erythritol and urea** for its application as a PCM in LHTES systems for heating and DHW applications. This chapter will be also used to assess the suitability of a sequential methodology employed for the development of new eutectic mixture as a PCM. First, a preliminary evaluation performed by means of the modeling of the phase diagram and by hot–stage microscopy is presented. Afterwards, the results are refined with more precise techniques, such as differential scanning calorimetry, the synthetic visual method and X-ray diffraction. The main properties of the eutectic composition will be finally determined. Besides, as performed in Chapter 3, the thermal degradation of the mixture is evaluated by an accelerated thermal cycling test

After these 3 chapters that involve the development of new materials, the subsequent two chapters deal with the development of the system and are related to heat transfer and thermal engineering topics, as follows:

- **Chapter 5** deals with the **development an overall calculation tool for the sizing of plate-based LHTES systems for domestic CHP applications**. A CFD model was developed and experimentally validated to simulate different configurations of the plate-based system. The results were first employed to gain knowledge of the system melting and solidification behavior, and subsequently to establish a correlation that relates the system Fourier number with the Biot and Stefan dimensionless numbers. By means of the obtained correlation the maximum plate thickness as a function of the selected discharging time and the properties of the PCM can be determined without the need of simulations. Finally, considering the remaining constraints of the system, a simplified overall design methodology is proposed. The technique eases the design

process of this kind of systems and decreases the time consumption needed to size them

- In **Chapter 6**, a **full-scale plate-based LHTES prototype is designed, built and evaluated** on a micro-CHP plant under representative conditions. The methodology proposed in Chapter 5 was applied to design it. A fabrication procedure for each component of the prototype is proposed. The chapter includes the testing of the critical components, such as seals and welds, in terms of integrity. A suitable fabrication route is proposed and used to produce the LHTES prototype.

  The produced LHTES prototype was coupled to the micro-CHP plant, where it was tested. **The results are analyzed in terms of, both the total energy storage and the time needed for charging and discharging. Finally, an economic study is performed to evaluate the actual feasibility of the system**. The PCM employed in the experiments was RT60; however, the economical study will include the assessment of the LHTES system using the PCMs developed along chapters 2, 3 and 4 as well as some fatty acids characterized in Chapter 5. In this way, an overall picture of the feasibility of the LHTES system together with the developed materials is attained. This study has also been employed to evaluate further improvements of the system and potential changes or innovations to reduce its cost
- The document ends with **Chapter 7,** where the **main conclusions** are presented and further works are discussed

CHAPTER 2: Eutectic mixtures of sugar alcohols as PCMs for space heating and DHW LHTES systems

Article: Eutectic mixtures of sugar alcohols for thermal energy storage in the 50–90 °C temperature range

Authors: G. Diarce, I. Gandarias, Á. Campos–Celador, A. García–Romero, U.J. Griesser.

Journal: Solar Energy Materials and Solar Cells 134 (2015) 215-226**.**

Year of Publication: 2015

ABSTRACT

This chapter is devoted to the study of new binary eutectic mixtures of sugar alcohols for their use as phase change materials (PCMs) in the temperature range suitable for heating and domestic how water. A brief introduction with general concepts about PCMs has also been included.

The studied mixtures were composed of erythritol and xylitol, erythritol and sorbitol, and xylitol and sorbitol. Their phase diagrams were experimentally established by differential scanning calorimetry and X–ray diffraction. Polarized thermomicroscopy was employed to determine the crystallization rate of both, the pure materials and eutectic compositions. Additionally, the polymorphic behavior of the pristine materials was assessed. The results showed that, with respect to the thermal properties and economic aspects, the produced eutectic compositions are suitable for the intended purpose. Unfortunately, their crystallization rates are noticeably low, which limits their use as PCMs.

A modeling approach based on thermodynamics was used to predict the solid–liquid equilibrium of the studied mixtures and their melting enthalpies. The simulated results were in good agreement with the experimental results. The modeled and experimental results were used to highlight several practical aspects relevant for the development of new eutectic mixture–based PCMs.

1. Introduction

This starting section is divided into two parts. First, a brief introduction of the general aspects of PCMs and their requirements is provided. These requirements are of general application for all type of PCMs and, as a result, they can be extended to the materials developed in Chapters 3 and 4. The second section presents the motivation to study binary mixtures of sugar alcohols.

1.1. General aspects and requirements of PCMs

Solid-liquid phase change materials (PCMs) store thermal energy by means of the latent heat of fusion. The heat is stored upon melting and subsequently released by the solidification of the material. PCMs are able to store up to 7 times more heat per unit volume than common sensible storage materials, such as water, if a 15 °C temperature difference is considered [19]. Besides, they absorb and release heat at a nearly constant temperature. Consequently, their use in LHTES systems is a very interesting alternative to conventional TES solutions, which commonly use water as a storage medium. They allow reducing the storage volume, and improving the operating conditions of the entire system.

According to the literature [12,13,19], the desired thermophysical, kinetic and chemical properties for any PCM are the following:

- Melting and solidification temperatures that match the application
- High energy storage capacity per unit volume at the temperature range involved
- Congruent and reproducible melting and solidification of the PCM for the time scale defined for the application
- High thermal conductivity of both phases
- Reduced supercooling[1]
- High nucleation rate at the temperature range involved
- High crystallization rate at the temperature range involved

[1] Supercooling can be a desirable property depending on the way of using the PCM, because it allows the design of systems where crystallization can be activated "on-demand" by means of an external actuator, such as cold-fingers or others.

- Chemical stability during the life span of the PCM
- No corrosion on the construction materials
- Small volume change on phase transformation
- Low vapor pressure at the operating temperature
- It should be non-toxic, non-flammable and non-explosive to ensure safety
- Should be of abundant supply and low cost

The CHP operation temperatures selected on the dissertation of Campos-Celador [5] were 50-65 °C. However, in order to extend the applicability of the herein studied PCMs, the target temperature range will be 50–90 °C, which is suitable for space heating and domestic hot water (DHW) applications in general. This is also applicable for the PCMs studied in Chapters 3 and 4.

Melting latent heat higher than 150 kJ/kg and a cost lower than 3 €/kg were taken as reference values [19] to proceed on the research carried out in this thesis. Note, however, that the optimum cost strongly depends on the energy density of the material. Thus, these reference values were not considered targets that should be compulsory attained.

Since this study aims at finding new materials or mixtures of materials that can be candidates for the defined temperature range, the rest of the above described requirements (such as the thermal conductivity or others) will not be considered essential at this stage of the research, unless their values blatantly show the PCM unsuitable for the purposes aimed.

1.2. PCMs for heating and DHW applications: brief literature survey and objectives of the chapter

A possible classification of the different families of solid-liquid PCMs is proposed in Figure 2-1. It was performed by combining several classifications provided in different sources [12,13,20]. Amongst the different families, clathrates, salts and metals were discarded for the present study since they are suitable for temperature ranges different to those herein involved [27]. In addition, hydroxides were not considered due to their difficult handling and questionable safety behavior [28].

Regarding the materials from the remaining families suitable for the required temperature range, several studies have shown that fatty acids like stearic acid and palmitic acid, present

the required thermal properties [29]. However, the current market price of stearic acid is approximately 7–12 €/kg, while the price of palmitic acid is 8.5–11 €/kg [30,31]. These prices are considered too high for domestic applications.

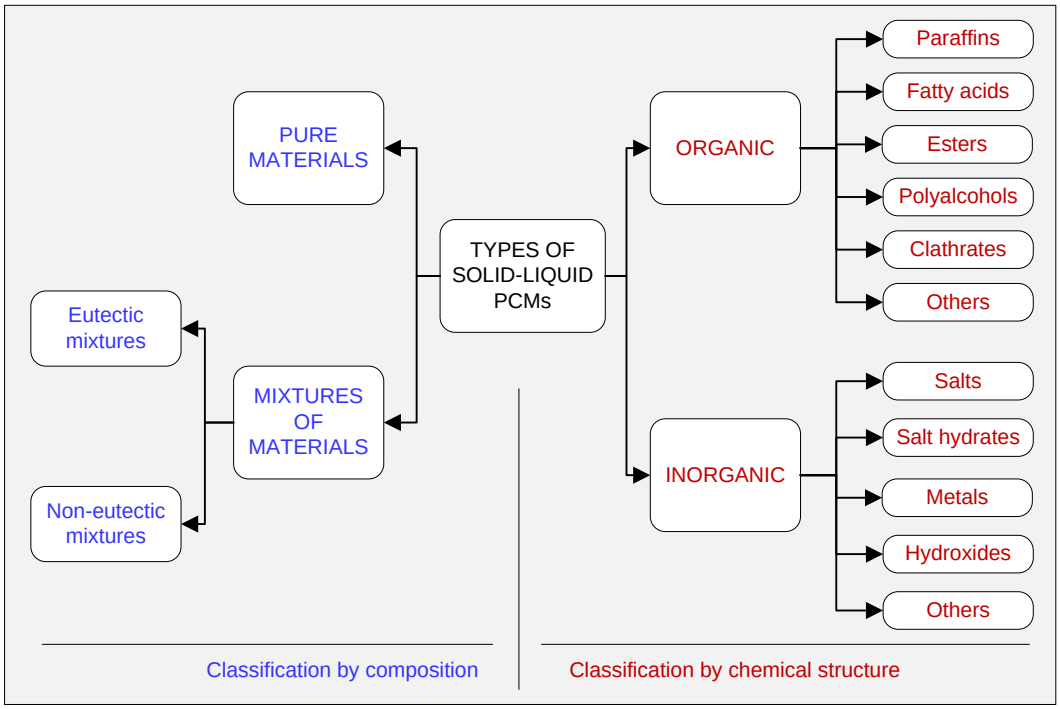

Figure 2-1: Classification of solid-liquid PCMs according to their chemical structure and to their composition

Several hydrated salts have also been identified as potential PCMs within this temperature range. Among them, sodium acetate trihydrate is a potential candidate for heating and DHW applications [32] due to its large melting enthalpy, which ranges from 226 to 264 kJ/kg [13,33]. From an economic point of view, it could be a suitable option, because it has a price of approximately 3 €/kg [31]. However, it shows phase segregation during thermal cycling, which makes necessary the use of solutions to avoid that undesirable effect. Furthermore, it shows a large supercooling, which could be an additional drawback depending on the application [34].

Several authors have aimed to improve the thermal behavior of this material [35–37] and proposed technical solutions that resulted in an enhanced stability of the PCMs. Nonetheless, the studied methods involved the modification of raw materials with additives, which could increase the PCM cost and, depending on the amount of additives, decrease the storage ability noticeably.

Sugar alcohols (so called polyalcohols or polyols) are potential candidates to be used as PCMs. They are widespread materials with melting temperatures between 90 and 200 °C [25], non–corrosive and non–toxic [18]. Although they present several drawbacks in their application as PCMs, such as polymorphism, severe supercooling and tendency to form amorphous metastable phases upon cooling, they are characterized by a superior volumetric energy capacity. Besides, their market price is between 1 and 6 €/kg, which lies within the attempted range. Furthermore, as mentioned in recent literature [38], they have not been sufficiently studied until now.

Accordingly, the present chapter deals with the use of sugar alcohols as PCMs for space heating and DHW applications. Erythritol, xylitol and sorbitol were considered as candidates[2], since they are widespread compounds and present reasonable market prices (see Section 2.1).

Note that the pristine materials do not show a phase change temperature within the 50-90 °C temperature range required (see Section 2.1). Accordingly, their binary mixtures were studied, in order to determine whether they form eutectic PCMs suitable for the aimed purpose.

Based on the presented literature survey, four objectives are sought in the present chapter:

- The first objective aims to determine solid–liquid equilibrium of binary systems comprising erythritol, xylitol, and sorbitol in order to study whether they form eutectics with melting points suitable for the heating and DHW temperature ranges. The main thermal properties of the mixtures will also be established
- The second objective is to study the crystallization behavior of the pure materials and of the selected mixtures. It is known that approaches such as the application of proper temperature ranges [39] or the addition of seeds [40] could effectively nucleate the desired polymorph of a material. The same occurs with the reduction of the supercooling effect, for what solutions as using nucleating agents [41] or electric fields [42] have been successfully applied in PCMs. Therefore, this study is focused on evaluating the crystallization rate of the materials because it can be considered the

[2] The polyols mannitol and galactitol were initially considered as candidates, but the results, presented in [164], showed that none of them formed suitable eutectics for the intended application when mixed with the other three sugar alcohols. This was confirmed by two articles published after this work was concluded ([165,166]); therefore, they were excluded from the dissertation for the sake of brevity.

limiting factor for all properties affecting the crystallization of a PCM. Additionally, the polymorphism of the pure materials will be discussed, in order to get an overall picture of the crystallization behavior of the concerned compounds

- The third objective is to evaluate the feasibility of a thermodynamics–based modeling approach for the prediction of phase diagrams of the selected mixtures. Until the present, the search for new mixture–based PCMs has been commonly performed by trial–and–error experimental procedures, which are time consuming and sometimes unfeasible. The modeling of solid–liquid equilibrium of mixtures can be a suitable way to predict the thermal behavior of potential LHTES materials
- The final objective of the chapter is to gain knowledge on practical features related to the study of new eutectic-mixture-based PCMs. Experimental measurements will be used to highlight aspects related to the feasibility of using differential scanning calorimetry (DSC) to determine phase diagrams. Additionally, the employed modeling approach will be used to set up some relevant aspects linked with the theoretical limits that eutectic mixtures can show when are aimed to be used as PCMs

2. Experimental methods and theoretical considerations

The experimental aspects are explained in this section, as well as the model employed to calculate the phase diagrams. Note that the experimental part of this work was performed during the research stay of the author at the University of Innsbruck (Austria). Thus, the characterization apparatus and methods employed differ from those employed in Chapters 3 and 4.

2.1. Materials employed and their thermal properties

Erythritol, xylitol and sorbitol were the compounds selected for the study. The main characteristics of the used materials can be found in Table 2-1. Thermal properties were determined by DSC using the procedure described in Section 2.3. The binary mixtures investigated were the following: erythritol–xylitol, erythritol–sorbitol and xylitol–sorbitol.

2.2. Preparation of the binary mixtures for the experimental determination of the phase diagrams

The most appropriate way to prepare mixtures for the determination of phase diagrams is to carry out a prior melting and solidification of the samples [43]. However, the sugar alcohols evaluated in this study undergo polymorphism and vitrification upon cooling, rendering the prior melting and solidification approach unsuitable in the present case. As a result, physical blends were prepared by gentle mixing, using the following procedure.

Compound	Brand	Purity	ΔH^{sl} (kJ/kg) [a]	Molecular weight (g/mol)	Melting (onset) temperature (°C) [a]	ΔC_p^{sl} (kJ/kgK) [a]	Market price (€/kg) [b]
Xylitol	Alfa Aesar	99 %	240.1	152.15	92.7	0.9	5.5
Erythritol	Alfa Aesar	99 %	333.7	122.11	118.7	1.1	3.7
Sorbitol	Sigma Aldrich	99.5 %	153.0	182.17	93.2	1.3	0.8

Table 2-1: Properties of the pure materials employed in the study.
[a] Measured by DSC.
[b] Market price for the bulk material obtained from [25], not for the reagents used in the study.

The pure materials were ground by mortar and pestle and sieved through a 125 μm diameter sieve to remove large grains. Karl Fischer titration measurements (C20 Coulometric KF Titrator from Mettler Toledo) were performed at that point to ensure negligible water content. Batches of 200 mg mixtures were then prepared from these pure materials. The prepared batches had compositions separated by an approximate 0.1 molar ratio to cover the entire composition range of each phase diagram (note that fewer batches were prepared for the xylitol–sorbitol system, as detailed in Section 3.2).

To produce each batch, materials were weighed on a Mettler Toledo AT250 Balance (accuracy ± 0.03 mg) and added to a mortar. A small amount of diethyl ether was poured to facilitate mixing between components. This volatile solvent partially dissolves components and, therefore, helps to form potential new phases [43]. Then, both components were gently mixed

by pestle for 5 min. The addition of diethyl ether and the mixing procedure were repeated three times for each batch. Mixtures were stored in closed glass vials until their properties were measured. Samples which contained sorbitol were kept in a desiccator with phosphorus pentoxide to prevent moisture gain due to its hygroscopic nature [40].

2.3. Differential Scanning Calorimetry

DSC was employed to determine the thermal properties of the pure materials and to construct the phase diagrams of the binary mixtures. A power–compensation Perkin–Elmer DSC 7 was employed. The employed calibration and experimental characteristics used were:

- Temperature calibration performed with benzophenone and caffeine
- Heat flow calibration carried out using indium
- Sample weight: 4 to 6 mg (± 0.0005 mg), weighed by a Mettler UM3 Ultra–microbalance
- Aluminum sealed crucibles, volume: 30 μL
- Purge gas: dry nitrogen (99.999 % pure)
- Heating rate: 1 K/min

The justification for the selected heating rate[3] and a detailed procedure on the construction of phase diagrams from DSC thermograms are discussed in Sections 3.1 and 3.2, respectively.

Melting enthalpies were determined by the integration of the phase transition peak of the thermograms. An integral tangential interpolated baseline was employed. Therefore, melting enthalpies reported throughout the chapter only account for latent heat.

2.4. Polarized thermomicroscopy

Hot–stage polarized microscopy, also called polarized thermomicroscopy, was used to evaluate the feasibility of the DSC to determine the liquidus temperature of a phase diagram (Section 3.1). It was also employed to measure the crystallization rate of the pure materials and their

[3] Note that the DSC normalized method that will be used in Chapter 3 – Section 2.6 could not be applied for the mixtures involved in the present chapter, due to their low crystallization rate and polymorphism (see Section 3.3).

eutectic mixtures (Section 3.3). Additionally, it was applied to understand the polymorphic behavior of the pure materials, by performing heating and cooling measurements at variable rates. More details about this technique can be found in ref. [43].

The apparatus employed was a Linkam LTS350 model equipped with a TP92 controller. Photomicrographs were recorded with an Olympus DP71 camera attached to an Olympus BX-50 microscope. The specific methods followed for each type of experiment are described next.

2.4.1. Procedures for the determination of liquidus temperatures of the mixtures

A sample of approximately 1 mg was placed on a glass slide and protected by a cover slide. The material was carefully positioned together to ensure that one unique droplet would form during the melting process. The glass slide was then placed onto the hot–stage and heated to a temperature one degree above the eutectic temperature of the system. In this way, a mixture comprising solid crystals within a liquid phase was obtained.

The sample was held at this temperature for 15 min to reach thermal equilibrium. If crystals were observed within the melt after that period, the temperature was raised 1 °C, and the sample was isothermally heated for another 15 min. This process was repeated until all crystals melted and the material was completely in a liquid phase. The temperature at this point was the liquidus temperature.

2.4.2. Methodology for the evaluation of the crystallization rate

A sample of approximately 1 mg was placed onto a glass slide and protected by a cover slide. The material was then heated 10 °C above its melting temperature and subsequently cooled to room temperature. No recrystallization was noticed upon cooling because of the tendency of the materials to form metastable phases (except pure erythritol, which recrystallized readily, as detailed in Section 3.3). The sample was placed on the slide such that the melt was in contact with edges of the cover slide. Seeds of the original material were then added to the edge to trigger crystallization. For the specific case of sorbitol, seeding was performed at different predetermined temperatures to obtain the desired polymorph for each case (see Section 3.3.1).

The prepared sample was then placed on the hot–stage microscope, which had been preheated to the temperature at which the crystallization rate was to be measured. Micrographs were taken periodically to monitor the crystal growth. The rate was calculated by measuring the distance from the edge to the crystallization front for each micrograph. After each experiment was finished, the sample was melted again to confirm that the polymorphic form that had been measured was the desired form.

2.5. X-ray diffraction

In addition to DSC measurements, X–ray diffraction (XRD) measurements were carried out to investigate solid phases of the binary mixtures. Diffraction patterns were obtained with a PANalytical X'Pert PRO diffractometer operated in the transmission mode. The conditions used were the following:

- Cu–K$\alpha_{1,2}$ radiation source (wavelength 0.15419 nm) with focusing mirror
- Tube voltage of 40 kV and tube current of 40 mA
- Step size of 0.013 °2θ in the angular range of 2 to 40 °2θ with 40 s per step
- Measurements were performed at ambient temperature

2.6. Modeling of the phase diagrams. Theory and calculations

An approach based on the Gibbs excess energy was adopted to model the solid–liquid behavior of the studied mixtures. In this section, only the employed equations are shown for the sake of brevity. The detailed deduction of the equations is provided in Appendix A. A thorough explanation of the theoretical background behind the methodology can also be consulted in reference books from chemical thermodynamics, such as ref. [44].

The Schoeder–Van Laar equation (Eq. 2-1) was employed to calculate the temperature–composition phase diagrams of the systems. There, x represents the mole fraction in the liquid phase; γ^{l} is the activity coefficient of the liquid, which denotes the deviation from an ideal mixture; ΔH^{sl} represents the enthalpy of fusion of the pure compound; T_m is the melting temperature of the pure compound; T is the temperature of the system and R is the ideal gas constant. The subscript i represents each compound in the system.

$$x_i\gamma_i^l = exp\left((\Delta H_i^{sl}/RT_{mi})\ ((T - T_{mi})/T)\right) \quad \text{Eq. 2-1}$$

Eq. 2-2 was used to predict the resultant enthalpies of the eutectic compositions at the eutectic temperature ($\Delta H_{mix}^{sl\,(T\,eut)}$). There, ΔC_p^{sl} is the difference between the specific heat of the solid and liquid state and T_{eut} accounts for eutectic temperature. The remaining nomenclature is the same used in Eq. 2-1.

$$\Delta H_{mix}^{sl\,(T\,eut)} = \sum_i x_i(\Delta H_i^{sl} + \Delta C_{p\,i}^{sl}\,(T_{m\,i} - T_{eut})) \quad \text{Eq. 2-2}$$

Two options were adopted to determine the activity coefficients of the liquid phase (γ^l). On the one hand, an approach based on group contribution methods was employed. The specific procedure used was the Modified UNIFAC model [45], which is detailed in Appendix A. On the other hand, systems were assumed to form an ideal mixture. For those cases, the activity coefficients equal unity. The equations were implemented in Matlab (MathWorks, Inc. [46]) and solved by means of a self-developed code.

3. Results and discussion

Some theoretical considerations needed for the interpretation of the results are described first in this section. Then the experimental diagrams determined are presented, followed by a part dealing with the crystallization behavior of the materials. The section finishes with a discussion on the theoretical determination of the phase diagrams.

3.1. Relationship between a DSC thermogram and the experimental liquidus temperature of a phase diagram

DSC is one of the most common techniques used to determine experimental phase diagrams. However, it is a dynamic method, and a phase diagram represents an equilibrium state. Therefore, the interpretation of the DSC data to construct an accurate phase diagram is yet a matter under study. This section aims to gain knowledge about this aspect. The analysis will be focused in eutectic–type phase diagrams. Some theoretical remarks that must be considered before the analysis of the results are provided next.

3.1.1. DSC thermograms of eutectic mixtures and problems related to the accurate determination of the liquidus temperature by DSC

Within a eutectic phase diagram, two types of physical transitions can be distinguished. Accordingly, the DSC thermogram of any composition different from the eutectic one will show two main peaks [47], as it can be visualized in Figure 2-2.

The first peak[4] corresponds to the melting of the eutectic part of the material. This transition is invariant and thus occurs at a fixed temperature for any composition of the binary mixture. Consequently, it can be defined by the extrapolated onset temperature (hereinafter termed onset temperature) of the DSC peak (see Figure 2-3). The second peak of the thermogram will be a broad endothermic effect, caused by the solution of the remaining solid component in the melt. Within a phase diagram, this transition is defined by the liquidus temperature. Since this temperature represents the ending of a phase change, the onset temperature cannot be used to define it. A different singular point of the thermogram must be used.

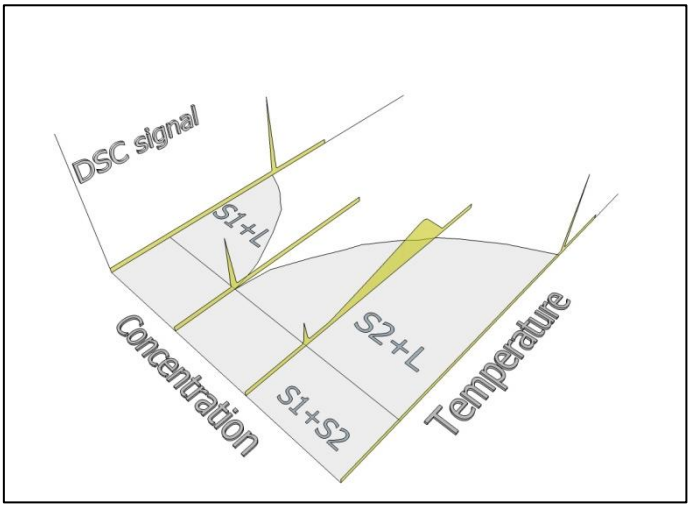

Figure 2-2: Representation of the type of DSC signal expected for different compositions within a eutectic binary phase diagram

A possible approximation could be the use of the maximum temperature of the peak [47], as depicted in Figure 2-3 (squared orange point). However, this temperature represents the value of the plate temperature when the energy exchange is maximum, which does not necessarily

[4] The herein included description corresponds to the construction of the phase diagram upon heating, which is indeed recommended in order to avoid uncertainties related to metastable phases or to supercooling effects.

correspond to the end of the melting [48]. The endset temperature does not either represent the end of fusion (squared blue point).

As suggested by [48], the end of a melting transition can be physically related to the inflection point of the decreasing portion of a DSC peak (hereinafter termed inflection temperature and represented by a squared green point in Figure 2-3). Thus, the liquidus temperature of mixtures in eutectic systems could be calculated in this way. However, the inflection temperature is dependent on the heating rate. A heating rate low enough to ensure thermal equilibrium within the sample must be determined.

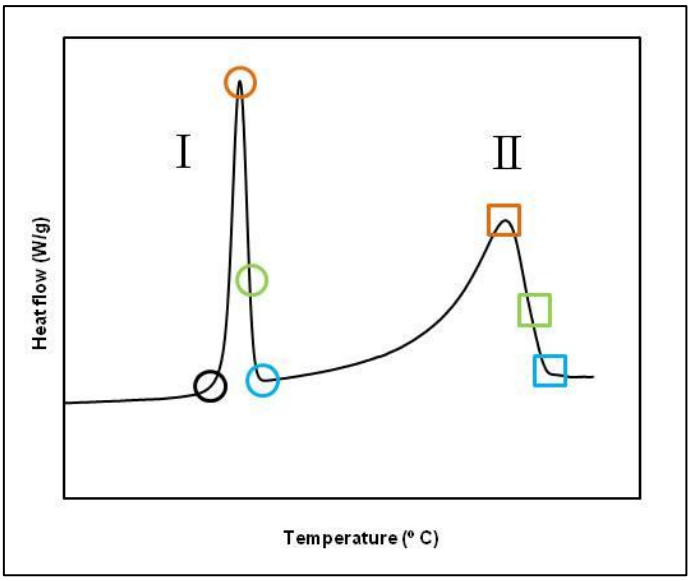

Figure 2-3: DSC thermogram of a composition different from the eutectic of the erythritol-xylitol binary mixture. Peak I: melting of the eutectic part. Peak II: melting of the remaining solid component. Singular points: black point, onset temperature; orange points, peak temperatures; green points, inflection temperatures and blue points, endset temperatures

3.1.2. Determination of the liquidus temperature: Comparison of results obtained by polarized thermomicroscopy and DSC

Measurements were performed by polarized thermomicroscopy to study the suitability of the DSC inflection temperature to define the liquidus temperature and to confirm that the DSC heating rate employed in the present study (1 K/min) was low enough to ensure thermal equilibrium. Although it is possible to use polarized thermomicroscopy to determine the liquidus temperature of every composition, the optimization of the DSC method was attempted because complete automation can be achieved with this technique.

Experiments were performed following the procedure described in Section 2.4.1. Mixtures of several compositions of the erythritol–xylitol and erythritol–sorbitol systems were measured. The results were compared with the inflection temperatures and with peak maximum temperatures obtained by DSC at 1 K/min. These results are shown in Table 2-2.

Erythritol-xylitol system			
$X_{xylitol}$	Melting temperature thermomicroscopy (ºC)	Maximum peak temperature DSC (ºC)	Inflection temperature DSC (ºC)
0.45	106.0	99.0	105.0
0.21	114.0	110.0	114.8
Erythritol-sorbitol system			
$X_{Sorbitol}$	Melting temperature thermomicroscopy (ºC)	Maximum peak temperature DSC (ºC)	Inflection temperature DSC (ºC)
0.18	115.0	111.5	113.6
0.29	110.0	106.9	109.7

Table 2-2: Determination of the liquidus temperature of the binary mixtures studied; comparison between DSC and polarized thermomicroscopy (X accounts for molar fraction)

The difference between the liquidus temperature determined by thermomicroscopy and that calculated using the inflection temperature of DSC measurements showed an absolute maximum difference of 1.4 °C, with an average difference of 0.9 °C. Conversely, the average difference between the peak maximum temperature and that measured by thermomicroscopy was 4.4 °C.

According to the results, it can be stated that, under a heating rate of 1 K/min, and using samples of approximately 5 mg, the inflection temperature of the DSC peak can be used to determine the end of a melting transition. In contrast, the maximum peak temperature is not a suitable approach under the applied conditions. Consequently, the inflection temperature will be the criterion employed in the present chapter to establish the liquidus temperature of experiment-derived phase diagrams.

3.2. Experimental determination of phase diagrams of mixtures. Evaluation of thermophysical properties and economical aspects of the eutectic compositions

Experimental phase diagrams of binary mixtures comprising erythritol–xylitol, erythritol–sorbitol and xylitol–sorbitol were determined by DSC. Thermal measurements were complemented by XRD experiments. The obtained results are discussed below.

3.2.1. Erythritol–xylitol binary system

The DSC thermograms obtained for the erythritol–xylitol mixture are shown in Figure 2-4. All studied compositions exhibited two endothermic peaks, except for samples with compositions close to their eutectic mixtures. The first peak was always found at a fixed temperature. The temperature of the second varied with the composition; as the composition approached 100 % of one component, the second peak became larger, and its inflection temperature approached that of the pure component. From these results, it can be inferred that the phase diagram of the erythritol–xylitol system corresponds to a simple eutectic type.

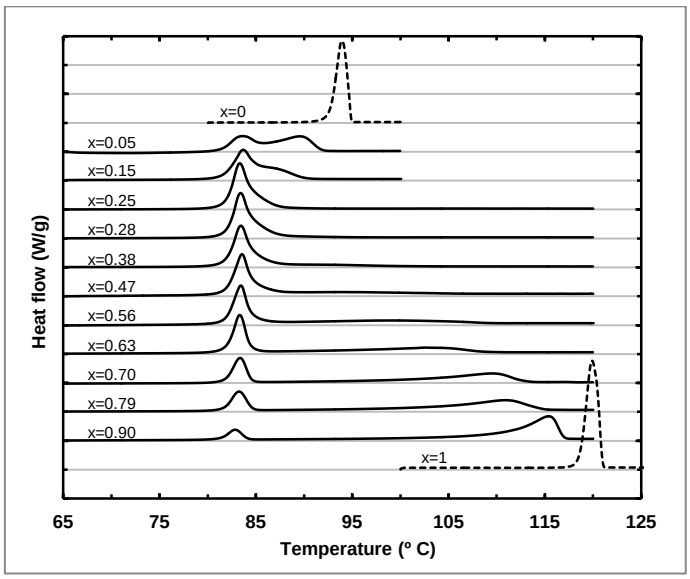

Figure 2-4: DSC thermograms obtained for the erythritol–xylitol system; molar ratios referred to erythritol are presented numerically next to each thermogram

This conclusion was confirmed by XRD measurements. Samples of each prepared composition were measured by this technique to complement DSC results. Diffraction patterns of the pure compounds were also obtained. Experimental patterns of the pure compounds were compared with simulated patterns of crystal structures and with available data in the literature [40,49,50]. The results were in agreement with both sources.

As an example, diffractograms of pure erythritol, pure xylitol, and a mixture comprising 0.67 and 0.33 molar ratios of erythritol and xylitol, respectively, are shown in Figure 2-5. It can be seen that the diffractogram of the mixture shows the sum of reflections present on each of the pure compounds. Neither new reflections nor disappearing ones were observed. Similar behaviors were observed in diffractograms of the other studied compositions. Therefore, it can

be concluded that no new phase was formed on the solid state, and the phase diagram of the mixture is a simple eutectic type.

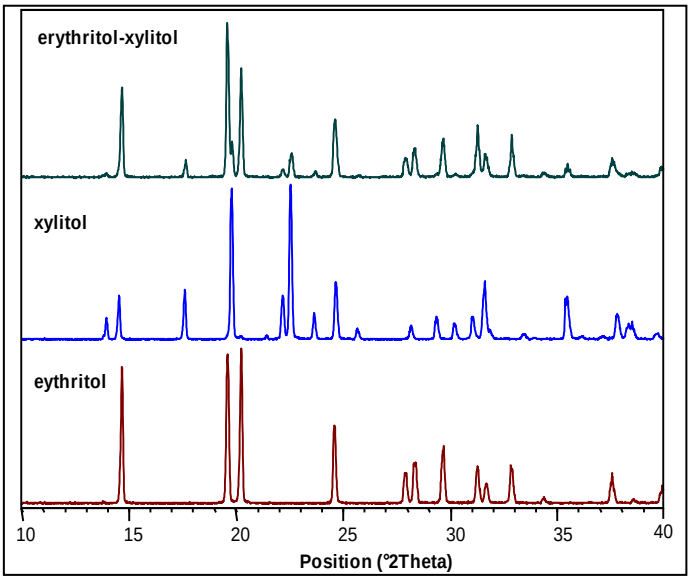

Figure 2-5: XRD diffractograms for pure erythritol, pure xylitol and a mixture comprised by 0.67 molar ratio erythritol and 0.33 molar ratio xylitol

The experimental phase diagram was constructed starting from the DSC thermograms shown in Figure 2-4. The results are depicted in Figure 2-6. Three different singular DSC temperatures extracted from the thermograms were used to produce this figure. First, the inflection temperature of the second endothermic peak of each mixture was used to determine the experimental liquidus temperatures. Second, the inflection temperatures of the first endothermic of the thermogram of each mixture were used to determine the eutectic temperature. Finally, the onset temperature of the first endothermic was also depicted because, for certain compositions, a partial overlap of the first and the second endothermic peaks turned out unfeasible the evaluation of the inflection temperatures of the first endothermic.

According to the results, the eutectic composition of the system was found at an approximately 25 % erythritol molar ratio[5], which is equivalent to the 21 % mass ratio. Its

[5] Because the phase diagram was determined by DSC, it is not possible to provide a numerical value of the uncertainty of the determined eutectic composition.

eutectic melting temperature was 83.9 °C[6]. The melting enthalpy of the eutectic mixture was found to be 248.7 J/g. The determined thermal properties are summarized in Table 2-3 (along with the properties of the determined eutectic compositions of the other two systems, discussed in Section 3.2.2, and with the estimated market prices of the determined eutectic compositions).

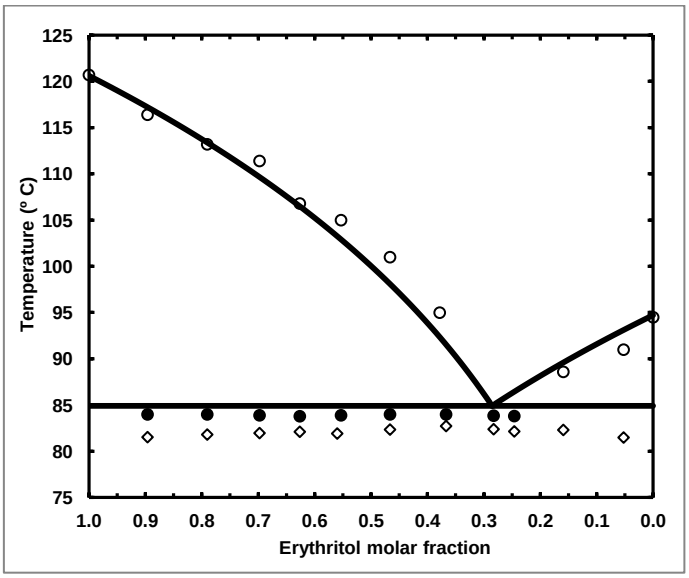

Figure 2-6: Proposed phase diagram for the erythritol–xylitol system (O–Experimental inflection temperature of the 2nd endothermic (liquidus temperature); ◇–Experimental onset temperature of the 1st endothermic; ●–Experimental inflection temperature of the 1st endothermic; — Predicted equilibrium temperatures using the Modified Unifac model)

The melting temperature of the erythritol–xylitol eutectic mixture can be considered suitable for LHTES systems for heating and DHW applications. Regarding the enthalpy, it can be stated that the material shows a large storage capacity compared with other known PCMs. The market price was estimated from the prices of the pure compounds (see Table 2-1), and calculated using mass fractions of the components. It was found to be approximately 5.2 €/kg. It can be slightly high for domestic applications, but this could be compensated with the large energy density offered by the material.

Consequently, considering the thermal properties and economic aspects of the eutectic mixture, the material could be suitable for the objectives sought. Unfortunately, as discussed

[6] The erythritol-xylitol eutectic mixture was afterwards studied in [162,166] as a part of a extensive study on sugar alcohols for TES. The results attained in those references agree with the eutectic composition and thermal properties herein achieved.

in Section 3.3, the studied mixture exhibits a low crystallization rate, which limits its use as a PCM.

3.2.2. *Erythritol–sorbitol and xylitol–sorbitol binary systems*

DSC results for the erythritol–sorbitol and xylitol–sorbitol mixtures indicated a simple eutectic phase diagram. Thermograms for the respective systems are presented in Figure 2-7 and Figure 2-8. Experimental phase diagrams are correspondingly shown in Figure 2-9 and Figure 2-10. Only three compositions were analyzed for the xylitol–sorbitol system because it has already been studied elsewhere [51]. XRD results showed that no new phase was formed in the solid state. Therefore, both systems can be regarded as simple eutectic type mixtures.

Binary System		Type of phase diagram obtained	Composition of the eutectic mixture (referred to compound 1)		Eutectic onset temperature (ºC)	Eutectic inflection temperature (ºC)	Eutectic melting enthalpy (kJ/kg)	Estimated prize of the mixture (€/kg)
1	2		Molar ratio	Mass ratio				
Erythritol	Xylitol	Eutectic	0.25	0.21	82.2	83.9	248.7	5.2
Erythritol	Sorbitol	Eutectic	0.30	0.22	81.0	86.6	172.8	1.5
Xylitol	Sorbitol	Eutectic	0.52	0.47	67.0	74.6	169.6	3.0

Table 2-3: Experimental thermal properties and market price of the determined eutectic compositions

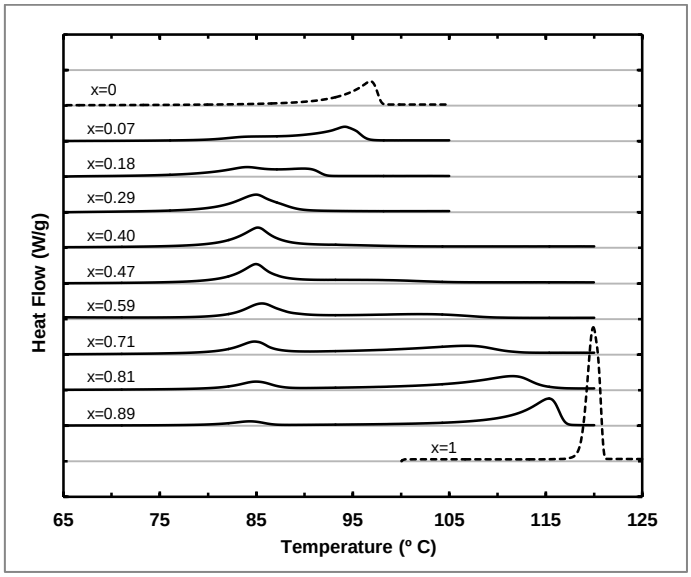

Figure 2-7: DSC thermograms obtained for the erythritol–sorbitol system; molar ratios referred to erythritol are presented numerically next to each thermogram

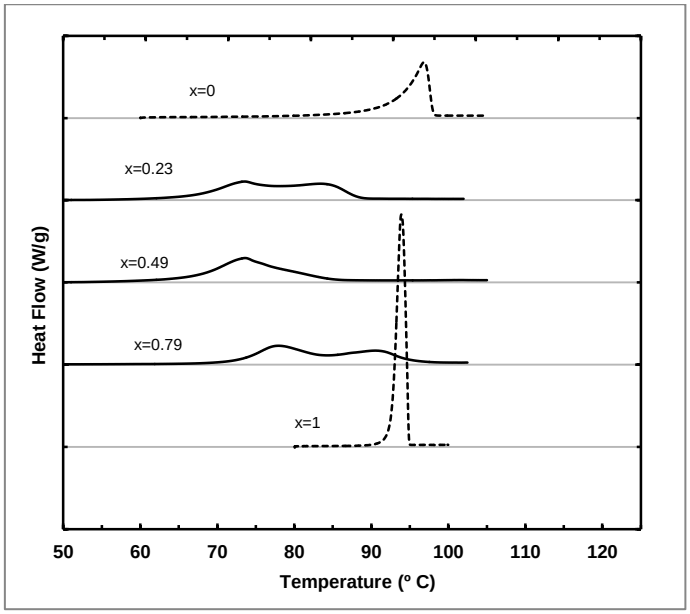

Figure 2-8: DSC thermograms obtained for the xylitol–sorbitol system; molar ratios referred to xylitol are presented numerically next to each thermogram

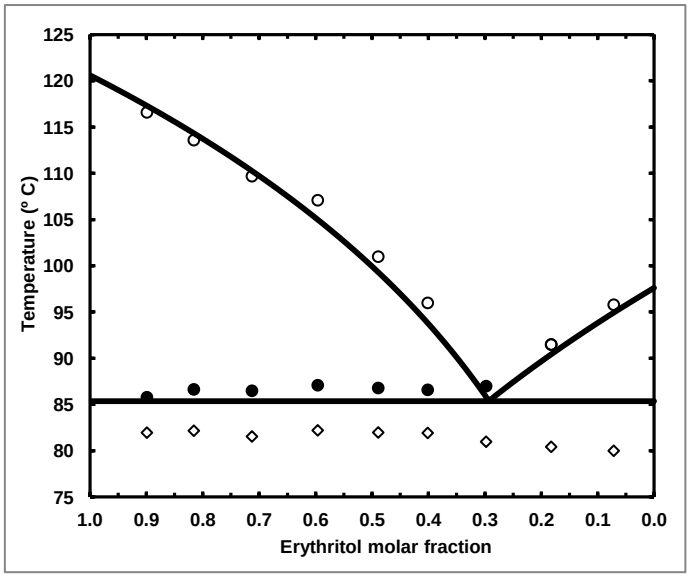

Figure 2-9: Proposed phase diagram for the erythritol–sorbitol system (O–Experimental inflection temperature of the 2nd endothermic (liquidus temperature); ◇–Experimental onset temperature of the 1st endothermic; ●–Experimental inflection temperature of the 1st endothermic; — Predicted equilibrium temperatures using the Modified Unifac model)

The erythritol–sorbitol eutectic composition was found at a erythritol molar ratio of 0.30 (equivalent to a 0.22 mass ratio). Its melting temperature was 86.6 °C. The mean difference between the onset and inflection temperatures of the first endothermic was 5 °C. This denotes that the melting process occurred through a wider range of temperatures than in the erythritol–xylitol mixture. This effect can likely be attributed to the presence of impurities in the pure sorbitol, whose melting transition also occurred in a broad range of temperatures.

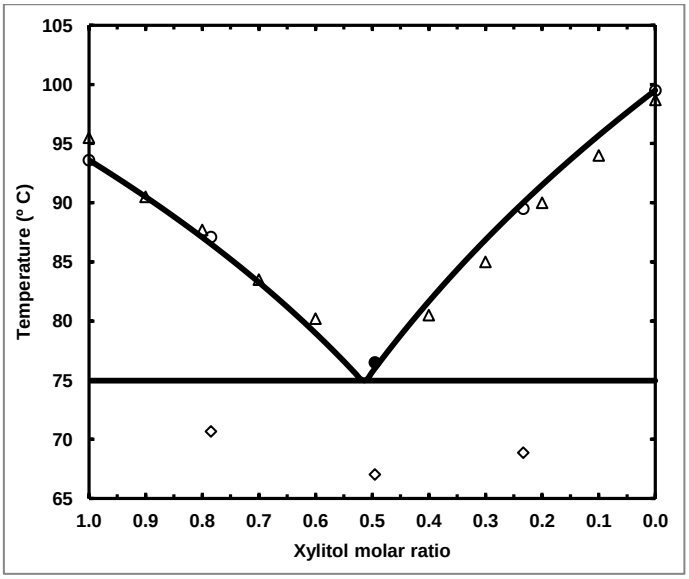

Figure 2-10: Proposed phase diagram for the sorbitol–xylitol system (O–Experimental inflection temperature of the 2nd endothermic (liquidus temperature); △–Experimental liquidus temperature values published by [51];◇–Experimental onset temperature of the 1st endothermic; ; ●– Experimental inflection temperature of the 1st endothermic; — Predicted equilibrium temperatures using the Modified Unifac model)

The melting enthalpy of the eutectic composition was 172.8 J/g. Its current market price is approximately 1.5 €/kg.

The xylitol–sorbitol eutectic composition was found at a xylitol molar ratio of 0.49 (equivalent to a 0.45 mass ratio). The melting temperature was 74.6 °C, which was lower than the previous two mixtures. The difference between the onset and inflection temperatures of the first endothermic for the eutectic composition was 9 °C. Additionally, the onset temperatures of the different measured compositions showed a difference of 3 °C. This could be interpreted as a sign of the formation of a new solid phase. However, the XRD patterns did not show signs of any new structure in the solid state. These dissimilarities would not have a direct effect on the selected application; thus, a deeper analysis was unnecessary. The melting enthalpy of the mixture was 169.6 J/g, and the price of the resultant mixture is approximately 3 €/kg.

In light of these results, according to their thermal properties and economic features, the erythritol–sorbitol and xylitol–sorbitol eutectic compositions could be suitable for the application. However, their enthalpies are within the same range, or even slightly lower, than other materials used as PCMs at the intended temperatures, such as paraffins and fatty acids. Additionally, both compositions present low crystallization rates, which limits their use as PCMs. This will be discussed in Section 3.3.

3.3. Crystallization behavior of the materials

The crystallization behavior of the pure materials and eutectic mixtures of the erythritol–xylitol and erythritol–sorbitol systems were evaluated by polarized thermomicroscopy (procedure detailed in Section 2.4.2). Measurements were also performed to understand the polymorphic behavior of the pure compounds.

3.3.1. Crystallization behavior of the pure compounds

Pure erythritol showed a very fast crystal growth rate, i.e., an instantaneous crystallization. This made rate quantification by the proposed methodology unfeasible because the samples completely recrystallized before they were placed on the microscope. However, this is a positive feature because if the material is used as a PCM, the heat will be released instantaneously.

Regarding polymorphism, according to the published literature, erythritol can crystallize to two polymorphic structures, form I and form II, which melt at 119 and 104 °C, respectively [49]. Under the cooling conditions employed for the preparation of the samples (quench cooling down to room temperature), erythritol crystallized forming the metastable polymorph: form II. When the samples were subsequently heated from room temperature, form II transformed to form I. This transition occurred between 70 and 90 °C, depending on the heating rate applied. A micrograph taken while the transformation was happening is shown in Figure 2-11. This behavior agrees with results published elsewhere [49].

Pure xylitol presented a low crystallization rate, and its nucleation was only promoted when seeds were added to the sample. Regarding polymorphism, xylitol has two known structures with melting points of 94 and 61 °C [50]. Under the thermal conditions employed in the present study, observations with the microscope revealed no formation signs of the metastable structure (melting point: 61 °C).

The results obtained for the xylitol crystallization rate are shown in Figure 2-12. Several micrographs taken at different times are illustrated in Figure 2-14 (both Figure 2-12 and Figure 2-14 also show the results for the erythritol–xylitol eutectic composition). As seen in Figure 2-12, the rate profile of xylitol shows a maximum at 70 °C. The crystallization rate at that

temperature is 10.6 mm/h. The crystallization rates for xylitol agree with the data published in the literature [52,53].

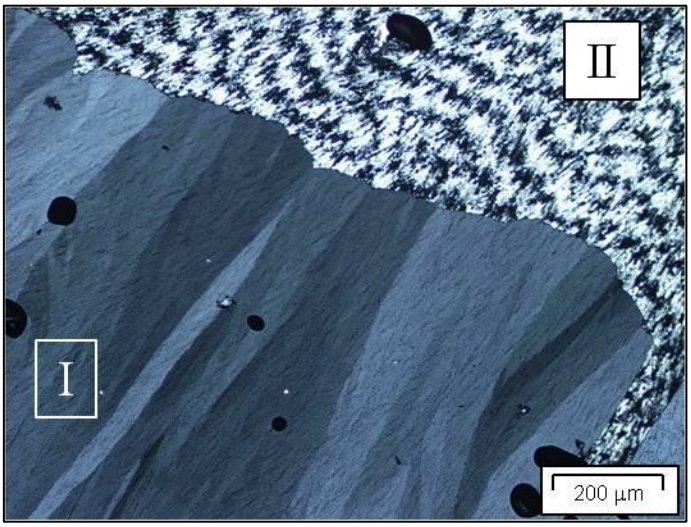

Figure 2-11: Micrograph showing the two polymorphs (I and II) of erythritol

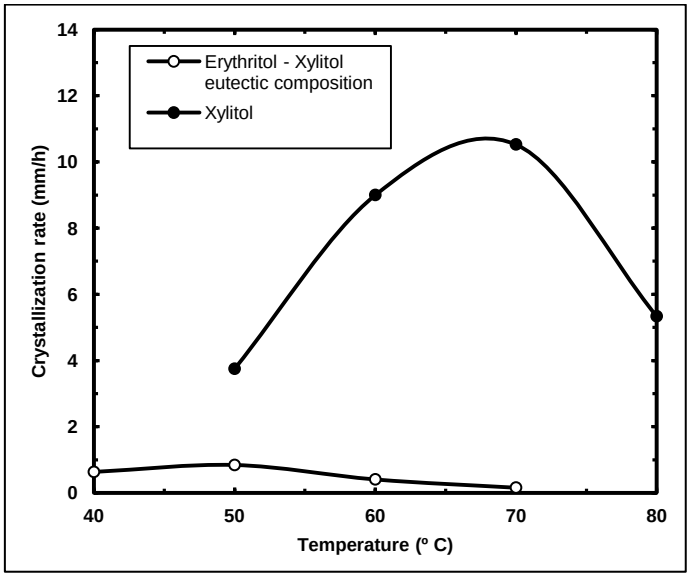

Figure 2-12: Measured crystallization rates for the pure xylitol and for the erythritol–xylitol eutectic composition

Pure sorbitol can crystallize to seven different polymorphic forms and one hydrated form [40]. The published melting temperatures of the different polymorphs range from 47 to 100 °C. The different crystal structures can be obtained by seeding the melt at certain temperatures, as stated by [40].

In the present study, samples of the alpha, beta and gamma forms were prepared by seeding the supercooled melt at different predefined temperatures (the nomenclature followed is the

one proposed by [40]). The crystallization rate results for each structure are shown in Figure 2-13. All polymorphs showed a maximum crystallization rate at 80 °C. At this temperature, the maximum crystallization rate of the alpha form was 1.4 mm/h; the beta form showed a maximum crystallization rate of 1.8 mm/h, and the gamma form presented a noticeably lower maximum crystallization rate of 0.06 mm/h.

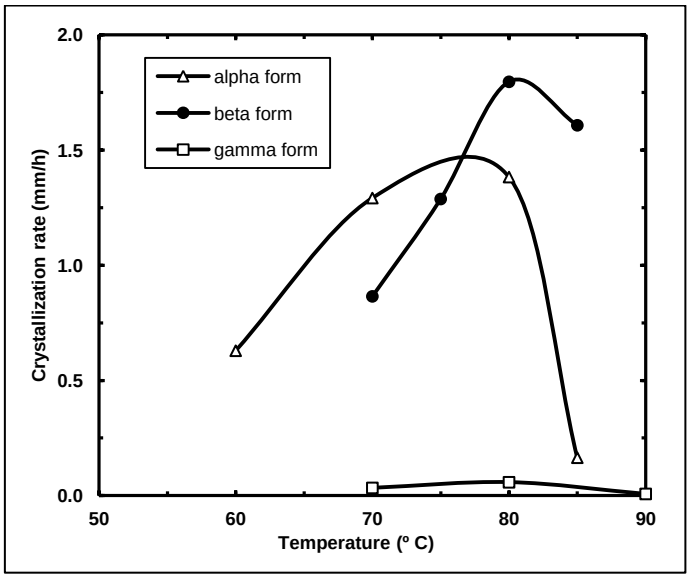

Figure 2-13: Measured crystallization rates for the different polymorphic forms of pure sorbitol

3.3.2. Crystallization behavior of the eutectic compositions

The crystallization rate of the erythritol–xylitol eutectic composition measured at different temperatures is shown in Figure 2-12. Several micrographs taken at different times are illustrated in Figure 2-14. There, the eutectic nature of the mixture can be noticed from the alternate growth of the crystals. Seeds can be also observed at the left side of the pictures of the eutectic mixture. The results for the erythritol–sorbitol eutectic composition are shown in Figure 2-15.

It is remarkable that the eutectic materials showed a crystallization rate noticeably lower than those of the pure compounds of the mixtures. The erythritol–xylitol eutectic mixture showed a maximum crystallization rate of 0.8 mm/h at 50 °C[7], while the erythritol–sorbitol system

[7] These results agree with those published afterwards by [53], where the crystallization rate of erythritol, xylitol and their eutectic mixture were measured by optical microscopy and infrared thermography.

showed a maximum rate of 0.034 mm/h at 60 °C. Therefore, the maximum crystallization rate of the erythritol–xylitol mixture was 13 times lower than the maximum rate of pure xylitol. Meanwhile, the maximum growth rate on the erythritol–sorbitol mixture was 2 times lower than that of pure sorbitol.

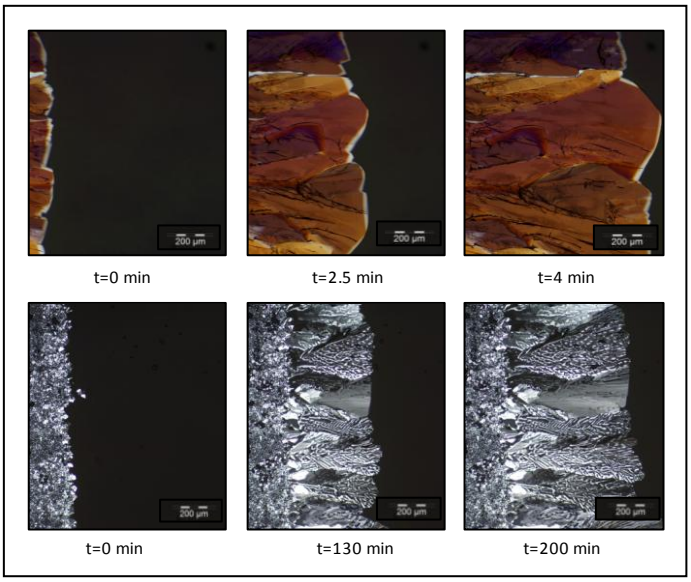

Figure 2-14: Micrographs taken during the crystallization rate measurements at different times. Pure xylitol is shown above. The erythritol–xylitol eutectic composition is presented below

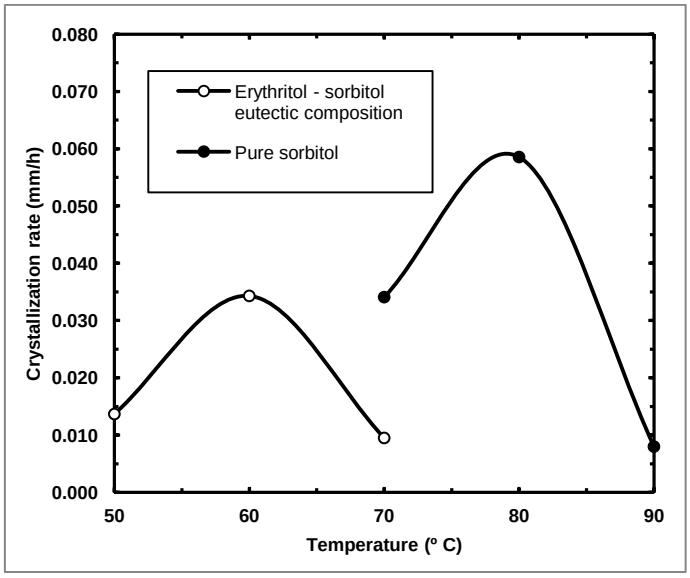

Figure 2-15: Measured crystallization rates for the pure sorbitol and for the erythritol–sorbitol eutectic composition. The polymorphic form of the sorbitol was the gamma form.

This crystallization behavior could be explained by a mechanism proposed by Winegard et al. [54], where any eutectic growth begins with the nucleation of one of the phases. This phase would grow until the surrounding liquid becomes enriched in other components. As a result of

the increased concentration, the second component also nucleates. At that point, there are two possibilities: first, the two initial crystals may grow side–by–side; second, there may be alternate nucleation of the two phases. When the first possibility occurs, the growth rate of the eutectic crystals is greater than that of the pure components. When the second possibility occurs, the growth rate of the eutectic crystals is lower than those of the pure components, which was observed in the systems studied in this paper.

The crystallization mechanism of eutectic mixtures affects the development of potential new eutectic–based PCMs because, depending on the given case, the resultant crystallization rate could be higher or lower than that of the pure compounds. Presently, the mechanism of eutectic solidification is debated [55], and the factors enabling one system to crystallize by one of the two options presented here are still unclear.

Organic eutectic systems following both behaviors have been reported in the literature, regardless of the nature and type of components forming the mixture. For instance, the naphthalene–phenanthrene [56] and β naphthol–vanillin [57] eutectic systems show a lower crystallization rate than their pure compounds. Conversely, the α naphthol–vanillin system [57] presents a rate higher than those of its pure materials. Further research on eutectic crystallization mechanisms are needed to understand the crystallization behavior of new eutectic–based PCMs.

The results revealed that the low crystallization rate of the studied eutectic mixtures limits their use as PCMs for short term applications because a fast release of heat is required. A different possibility would be the use of these compounds for seasonal storage. This application requires longer storage and release periods (on the order of several months), and these compounds could be used for storing significant amounts of thermal energy if larger heat exchange surfaces are employed in the storage unit. In any case, further studies on the crystallization behavior of the mixtures are required[8].

[8] After the content of the present chapter was published, a crystallization mechanism based on bubbling was proposed to promote a fast crystallization of the erythritol-xylitol eutectic mixture. The method was developed within the SAMSSA project of the FP7 European program [167]. Although the method was proven to be effective, its implementation within the plate-based LHTES system proposed in the present thesis was considered unfeasible without a complete redesign of the system.

3.4. Theoretical prediction of phase diagrams by thermodynamic modeling

The simulated results were compared with the experimental data to validate the model. The model was used to understand the influence that the properties of the pure materials had on eutectic binary systems.

3.4.1. Comparison between experimental and predicted phase diagrams

Simulations using the adopted modeling approach were carried out to predict solid–liquid equilibrium of the studied mixtures. The two approaches used to calculate the liquid activity coefficients (the Modified UNIFAC method and the ideal mixture assumption; see Section 2.6), rendered differences smaller than 0.1 °C, for both the eutectic and liquidus temperatures. As a result, the studied mixtures can be considered ideal mixtures from a thermodynamic point of view.

The predicted values and experimental results of eutectic temperatures and the melting enthalpies for the eutectic compositions are summarized in Table 2-4. In the case of the erythritol–xylitol system, the absolute difference between the predicted and the experimental eutectic melting temperatures was 1.0 °C; for the erythritol–sorbitol system was 1.3 °C and for the xylitol–sorbitol system 0.4 °C.

Dissimilarities between the experimental and predicted eutectic compositions were not quantified because exact eutectic compositions cannot be determined by the methods employed in this study. Nonetheless, the predicted and experimental liquidus temperatures were in good agreement with each other, as can be visualized in Figure 2-6, Figure 2-9 and Figure 2-10. Similarly, the prediction of melting enthalpies agreed with experimentally determined values. Based on these results, it can be concluded that the employed modeling approach is suitable for the intended purposes.

Binary System		Experimental eutectic temperature (ºC)	Predicted eutectic temperature (ºC)	Experimental melting enthalpy (kJ/kg)	Predicted melting enthalpy (with ΔC_p^{sl}) (kJ/kg)	Predicted melting enthalpy (neglecting ΔC_p^{sl}) (kJ/kg)
1	2					
Erythritol	Xylitol	83.9	84.9	248.7	247.9	262.8
Erythritol	Sorbitol	86.6	85.3	172.8	169.8	191.8
Xylitol	Sorbitol	74.6	75.0	169.6	169.2	192.6

Table 2-4: Comparison between predicted and experimental results for the eutectic compositions of the systems studied

The importance of taking into account the influence of the specific heat variation term between the solid and liquid phases (i.e., ΔC_p^{sl}) for predicting enthalpies should be addressed. Usually, the influence of the ΔC_p^{sl} is neglected in modeling studies [44] because experimental values for the pure compounds are not always available and because the influence of this parameter on the prediction of equilibrium temperatures is usually not significant. However, as seen in Table 2-4, absolute errors up to 23.4 J/g (xylitol–sorbitol system; relative error: 14 %) were observed in the prediction of melting enthalpies when the term was neglected. Therefore, for typical thermal properties of PCMs in the intended temperature range (ΔC_p^{sl} between 0.5 and 1.5 J/g and melting enthalpies between 150 and 250 J/g), relative errors between 10 and 20 % would be observed if the term was ignored.

3.4.2. Influence of properties of the pure materials on resultant binary eutectic systems

The model served to gain knowledge about the relationship between properties of the pure components forming the mixture and expected properties of the formed eutectic system. This knowledge can be used to define mixtures potentially interesting to be used as PCMs, without the need to perform an experimentally intensive work.

According to Eq. 2-1, and if the influence of the activity coefficient is neglected (which is a suitable assumption in the present case, as shown in Section 3.4), it can be shown that when an eutectic system is formed by two high melting enthalpy compounds, the liquidus line of the phase diagram is flatter[9]. As a result, if the aim is to produce a eutectic mixture with a high depression of the melting temperature (with respect to the pure compounds), it is not

[9] Note that the enthalpy is calculated in the model in kJ/mol. In this situation, the materials with the same molar mass are compared. Compounds with low molar mass will lead to steep liquidus lines, while compounds with high molar mass will render flattered liquidus lines.

recommended to use two materials with high melting enthalpies. In contrast, using materials with moderate melting enthalpies will render large depressions on the resultant eutectic melting temperature. This corresponds to steeper liquidus lines on the phase diagram. However, the obtained melting enthalpy will be low. This is especially the case when the value of the ΔC_p^{sl} term is significant.

Another interesting conclusion is related to the expected composition of eutectic mixtures. When the component with the highest melting temperature is also the component with the highest melting enthalpy, the eutectic composition will be rich in the compound with the lowest melting point. In these cases, the eutectic melting temperature and the melting enthalpy will be very close to those of that compound, which, in the limit case, would render a monotectic phase diagram. These considerations explain the low melting enthalpy of the eutectic composition in the erythritol–sorbitol system.

The ΔC_p^{sl} value is another practical feature to be considered in the search of new eutectic–based PCMs. Most materials used as PCMs have higher C_p in the liquid state than in the solid state. In this case, the ΔC_p^{sl} contribution is negative in relation to the melting enthalpy of the formed eutectic mixture. In these cases, and if the contribution of the excess enthalpy is omitted, the greater the depression of the eutectic melting point on the phase diagram, the lower the melting enthalpy of the mixture. Consequently, eutectic mixtures that show a melting temperature noticeably lower than the pure compounds forming the mixture are likely to show a low melting enthalpy. The aforementioned observations can be extended to any eutectic mixture with a behavior close to ideality (i.e., $\gamma' \cong 1$), and they can be used as guidelines when determining new eutectic mixtures to be used as PCMs.

4. Conclusions of the chapter and further work

Three new binary mixtures of sugar alcohols comprising erythritol, sorbitol and xylitol were studied for LHTES applications in the heating and DHW temperature ranges. Solid–liquid phase diagrams of the systems were experimentally established, and each showed a simple eutectic type phase diagram.

Eutectic compositions underwent melting temperatures of 83.9, 86.6 and 74.9 °C, for the erythritol–xylitol; erythritol–sorbitol and xylitol–sorbitol systems, respectively. Regarding the

heat storage ability, the erythritol–xylitol eutectic composition showed the largest melting enthalpy of 248.7 J/g. Meanwhile, melting enthalpies for the erythritol–sorbitol and xylitol–sorbitol eutectic compositions were found to be 172.8 and 169.6 J/g, respectively. Regarding melting temperatures and enthalpies and market prices, the mixtures studied are suitable for the intended purpose.

However, experimental measurements performed by polarized thermomicroscopy showed that the mixtures presented a low crystallization rate, which limits their use in short-term LHTES systems. Additionally, the materials show polymorphism and tend to form metastable amorphous states. As a result, further research is needed to enhance the crystallization behavior of the mixtures if they are to be used as PCMs.

A thermodynamics–based modeling approach was employed to predict solid–liquid equilibrium of binary systems. Equilibrium temperatures and melting enthalpies obtained from simulations were in good agreement with experimental results. Therefore, the method could be used for the prediction of new PCMs made of binary eutectic mixtures.

The importance of taking into account the specific heat capacity difference between the solid and liquid phases to correctly predict melting enthalpies of the mixtures was highlighted. The model was additionally used to observe that, theoretically, the larger the melting enthalpies of the pure compounds that form a eutectic binary system, the lower the depression in the melting enthalpy of the resultant eutectic composition.

CHAPTER 3: The sodium nitrate-urea eutectic mixture as a PCM for heating and DHW LHTES systems

Article 1: The sodium nitrate-urea binary mixture as a phase change material for medium temperature thermal energy storage. Part I: Determination of the phase diagram and main thermal properties

Authors: G. Diarce, E. Corro-Martínez, L. Quant, Á. Campos–Celador, A. García–Romero.

Journal: Solar Energy Materials and Solar Cells**.**

Year of Publication: 2016

Article 2: The sodium nitrate-urea binary mixture as a phase change material for medium temperature thermal energy storage. Part II: Accelerated thermal cycling test and water uptake behavior of the material Determination of the phase diagram and main thermal properties

Authors: G. Diarce, E. Corro-Martínez, Á. Campos–Celador, A. García–Romero, J.M. Sala.

Journal: Solar Energy Materials and Solar Cells**.**

Year of Publication: 2016

ABSTRACT

This chapter studies the binary mixture composed of sodium nitrate and urea for use as a phase change material in LHTES systems for heating and DHW applications. This mixture is characterized by its highly competitive cost (1 €/kg).

The phase diagram of the system was experimentally determined via DSC, the synthetic visual method and XRD. The main thermal properties and the density of this composition were studied in detail to evaluate its potential as a PCM. The results showed that the properties are suitable for the intended purpose. The water uptake by the material was evaluated to gain knowledge of its hygroscopic behavior. XRD measurements were performed to study the formation of new phases or compounds due to the presence of water.

In addition, because urea undergoes thermal degradation upon heating, a preliminary accelerated thermal cycling study comprising 210 cycles was performed to determine the thermal reliability of the mixture. These results were complemented by chromatographic analysis to detect any presence of degradation byproducts.

According to the results, the mixture formed by sodium nitrate and urea shows potential for use as a PCM in the desired temperature range. Further research focused on thermal degradation over longer periods of use is encouraged to establish whether the material has a proper lifespan for actual thermal energy storage applications.

1. Introduction

The need for research to find more efficient and cheap PCMs has been described in the introductory section of Chapter 2, where this need is stressed on the case of LHTES systems to be used in heating and DHW applications. So far, materials as paraffins [26]; fatty acids like stearic and palmitic acid [29,58,59] and salt hydrates such as sodium acetate trihydrate [37,60,61] have been addressed in the literature as good candidates to be used for the intended temperature range. However, each of them show specific drawbacks that restraint their application as PCMs. As a consequence, according to the state-of-the-art, further research is still needed to develop new PCMs in the desired temperature range, with increased storage capacities, and economically competitive.

Amongst the low-cost candidates which are potentially suitable to produce PCMs, urea is a cheap organic compound that is widely available and extensively used as a fertilizer [62]. It has a melting temperature of 133 °C, a large melting enthalpy of 220 J/g [63] and a market price between 0.5 and 1 €/kg [64,65]. Unfortunately, it undergoes thermal degradation when heated above its melting temperature [66–68]. For this reason, the articles on its use as a PCM [63,69,70] agreed that urea is not a suitable material for LHTES purposes. However, the use of urea as a component of a binary mixture that melts below that temperature could produce a PCM suitable for LHTES purposes.

Among the possible mixtures, the system formed by sodium nitrate and urea was reported as a eutectic system with one composition suitable for use as a PCM [71,72]. Sodium nitrate is a widespread inorganic material that is also commonly used as a fertilizer; it is employed as a thermal storage material at higher temperatures in concentrated solar thermal plants [73,74], and it can be currently purchased at approximately 1 €/kg [64].

The mentioned articles [71,72] reported a eutectic composition composed of 70.5 % (w/w) urea, with a melting temperature of 84 °C. However, no experimental details were provided, and neither the phase diagram nor the melting enthalpy was established. The melting enthalpy was evaluated later in [75], in a work that studied several binary eutectic mixtures formed by urea and other compounds. The eutectic composition proposed in the article was composed of 70.88 % (w/w) urea, and the reported experimental melting enthalpy was 164.46 kJ/kg. Nevertheless, only sparse experimental details were given, and no study on the thermal

degradation of the mixture was reported, which is a critical aspect for the use of this mixture as a PCM.

Until now, to the best knowledge of the author, only one article dealt with thermal cycling of the sodium nitrate-urea mixture, published by Kamimoto et al. [70] in 1984. These researchers studied the thermal degradation of urea and several mixtures formed by urea and other compounds using DSC and Thermo-gravimetric Analysis (TGA). They reported that the samples of the sodium nitrate-urea system did not crystallize during their experiments, even when cooled to room temperature, and therefore, they did not report any related conclusions. Based on the TGA results from other eutectic mixtures containing urea, they suggested that the thermal stability of urea is not improved when it forms part of a eutectic mixture. However, the experimental conditions (open crucibles) employed on that study might have been too severe for the objective herein proposed. Moreover, the maximum temperature on the experiments was considerably higher than the targeted temperature range in the current work. As a result, their conclusions could not be extrapolated to the application sought in this work.

Consequently, the information on thermal degradation available in the literature is related to pure urea. As abovementioned, this compound has been studied as a PCM by several authors [63,69,70], who concluded that it is not a suitable material for TES purposes due to its poor stability in thermal cycling. However, all of these studies used maximum experimental temperatures of 140 °C or higher because the melting point of pure urea is 133 °C. Accordingly, the conclusions reached in those articles cannot be extrapolated to the eutectic mixture involved in the current work, which would undergo a maximum operating temperature noticeably lower when used for the herein intended applications.

In addition to these studies, several works devoted to the use of urea for the reduction of NO_x emissions in diesel engines [67,68,76,77] studied the degradation processes at temperatures below 133 °C. According to these works, the decomposition of urea at temperatures below its melting point is nearly negligible. However, the specific temperature at which the decomposition process begins remains unclear.

Several authors claimed that the degradation of pure urea below its melting temperature is insignificant [66] while others have concluded that minor degradation can be observed even at

100 °C [67]. Moreover, the latter suggested that the presence of water could catalyze the degradation to occur at temperatures even lower. This observation introduces moisture as an additional factor for consideration. In any case, it is remarkable to stress that all of the sources concluded that the degradation is not important below 133 °C. Therefore, an insignificant or low degradation of the urea eutectic mixtures might be expected when working at a temperature around or below 90 °C. Nevertheless, it must be taken into account that any thermal decomposition is not only influenced by the absolute temperature of the system, but also by its state of aggregation at that temperature. According to previously published articles [71,72] the sodium-nitrate-urea eutectic mixture is foreseen to melt around 84 °C, and thus, its thermal degradation in the liquid state at that temperature could be different than the decomposition experienced by pure solid urea at the same temperature. This hypothesis has yet to be confirmed.

As a result, it can be stated that although the sodium nitrate-urea binary mixture has been addressed as a eutectic system with potential use as a PCM, the phase diagram of the mixture, its eutectic composition and its main physical properties remain uncertain. Moreover, its thermal stability is yet to be studied. Accordingly, the following objectives are sought in the present chapter of the thesis:

- First, it is aimed to determine the phase diagram of the sodium nitrate-urea system in order to confirm the presence of a eutectic composition with a phase change temperature suitable for the intended applications. Several complementary techniques have been used for this purpose, and special efforts were made to avoid any influence of thermal degradation and/or water content on the results obtained
- Second, the main physical characteristics of the eutectic composition found suitable for its use as a PCM will be evaluated in detail, including: melting and solidification temperatures and enthalpies, supercooling degree, storage capacity at the intended temperature range, density of the solid and the liquid phases and volume expansion during phase change

  Based on these properties, the suitability of the composition proposed as a PCM is discussed and compared to other PCMs available at the intended temperature range. Note that thermal conductivity, although a relevant property for any PCM, was considered out of the scope of the research at the present stage

- Third, a preliminary evaluation of the thermal stability of the eutectic composition found will be accomplished. To this end, an accelerated thermal cycling study was performed using DSC, and complemented by HLPC measurements to detect formation of potential degradation byproducts. The thermal cycling behavior of the mixture has also been compared with that of the pure urea, in order to ascertain whether the degradation is solely related to the maximum temperature reached by the material or if the state of aggregation of urea plays a significant role in the process
- Finally, the influence of the water content on the thermal behavior of the mixture has been assessed because, as shown in [67], this factor can influence the production, handling and use of the PCM. For this purpose, coupled DSC-TGA, XRD, High Performance Liquid Chromatography (HPLC) and KF titration measurements have been employed

Altogether, the presented objectives intend to create a complete picture of the suitability of the mixture for its use as a PCM. It is worth noting that, unlike Chapters 2 and 4, no predictive model was employed herein to calculate the theoretical phase diagram of the system. The modeling of inorganic compounds (i.e.: sodium nitrate) is a time consuming task, more difficult than in the case of organic compounds. As a result, it was considered more appropriate to focus the efforts on the experimental determination of the phase diagram and the suitable characterization of the mixture. The modeling of inorganic compounds might be considered in further research.

2. Experimental methods and theoretical considerations

The experimental conditions employed in the work were selected to avoid any influence of thermal degradation during preparation (and measurement) of the samples. Equally, for the determination of the phase diagram, attempts were made to avoid any water uptake, since the materials involved are hygroscopic, and this property could affect the results. As a consequence, certain of the involved procedures were more complex than those commonly found in the literature. Therefore, the present chapter includes an exhaustive explanation of each set-up and procedure, especially for the procedures that differed from those typically described in the literature.

2.1. Materials used

Analytical grade urea and sodium nitrate were purchased from Panreac Química S.L.U., with a purity of 99 %. Their main thermal characteristics are shown in Table 3-1. Note that the market price there given is from technical grade materials acquired from Quimidroga S.A. [64]. These materials were also analyzed by DSC and the thermal properties showed no significant differences.

Compound	Brand	Purity	ΔH^{sl} (kJ/kg) [a]	Molecular weight (g/mol)	Melting onset temperature (ºC) [a]	Market price (€/kg) [b]
Urea	Panreac Química	99 %	243.2	60.06	133.3	0.7
Sodium nitrate	Panreac Química	99 %	172.7	85.00	302.9	1.2

Table 3-1: Properties of the pure materials employed in the study.
[a] Measured by DSC.
[b] Market price for the bulk material obtained from [64], not for the reagents used in the study.

2.2. Differential Scanning Calorimetry (DSC)

DSC was used to determine the thermal properties of the pure materials; investigate the phase diagram; evaluate the behavior of the composition proposed as a PCM, and perform the accelerated thermal cycling measurements. In this Section 2.2 the common specifications of the DSC employed are detailed. The procedures for the sample preparation and temperature programs applied for each test will be explained in the subsequent Sections 2.5.2, 2.6 and 2.8. The apparatus used was a Mettler Toledo DSC1, with the following calibration/ characteristics:

- Both heat flow and temperature calibrations performed with gallium and indium
- Zinc was used to check heat flow and temperature calibration at higher temperatures when the pure sodium nitrate was measured
- Sealed aluminum crucibles of 25 µl were used
- Dry nitrogen (99.999 % pure) was employed as a purge gas

The phase change enthalpies were determined by integration of the phase transition peaks of the thermograms. Accordingly, the enthalpies reported throughout the chapter consider only latent heat unless otherwise indicated. An integral tangential interpolated baseline was used for this purpose.

The uncertainty for the temperature measurements can be considered ± 0.2 °C under the conditions applied, while the uncertainty for the enthalpy determination accounts for 5 % of the measured value.

2.3. Determination of the water content of the materials

Karl Fischer titration (KF titration) was performed to determine the water content of the samples. A KF-31 coulometric titration system from Mitsubishi Chemical was used for this task. The estimated accuracy of the device for the experimental conditions underwent in this chapter was ± 0.01 % (w/w) of the total water content of each sample.

2.4. High Performance Liquid Chromatography (HPLC) measurements

HPLC was used to detect and quantify the potential formation of degradation byproducts during those sample preparations that involved prior melting (Sections 2.5.2 and 2.6). In addition, it was used to identify and quantify the presence of degradation byproducts before and after accelerated thermal cycling measurements (see Section 2.8.1 for experimental details). Based on the literature [66–68], the measurements were focused on the detection of traces of biuret and cyanuric acid because these are the main thermal degradation byproducts reported at the applicable temperatures.

Measurements were performed on an Agilent Technologies 1200 Series HPLC system with a 6410 Triple Quad mass spectrometer and MassHunter software equipped with electrospray ionization (ESI) as the ion source and operating in positive and negative modes. The main features are provided next:

- Column used: SeQuant® ZIC-HILIC 3.5 µm/150 x 4.6 mm (the guard column contained the same packing material)
- Mobile phase used for chromatographic separation: 15:85 (aqueous/organic)
- Aqueous phase: ammonium formate in water (10 mM)
- Organic phase: acrylonitrile (ACN)/water (95:5) with 10 mM ammonium formate in composition and flow rate isocratic mode at a flow rate of 0.7 ml/min
- Column temperature during the run: 30°C
- Injection volume: 5 µL

For the mass spectrometer conditions, monitoring of urea and its potential degradation byproducts (biuret and cyanuric acid [66,67]) was performed using a triple quadrupole mass spectrometer equipped with an electrospray ionization interface.

For detection and quantification, nitrogen was used as nebulizer and desolvation gas. The following ESI source conditions were applied:

- Nebulizer gas flow: 11 L/min
- Gas temperature: 350 °C
- Nebulizer pressure: 50 psi
- Capillary voltage: 3200 V in positive mode and 3500 V in negative mode

The electrospray ionization was set to positive mode for urea and biuret and negative mode for cyanuric acid. The fragmentor values were optimized to maximize the intensity of the protonated molecular species of urea and biuret and for deprotonated molecular species of cyanuric acid. The mass spectrometer was operated in the MS2 SIM mode to monitor the corresponding ionized species. The selected ions were m/z 61 for urea, m/z 104 for biuret and m/z 128 for cyanuric acid.

2.5. Evaluation of the phase diagram of the mixture

Several techniques and methodologies are valid for the determination of phase diagrams. However, each of these options has limitations, and as a result, no phase diagram can be considered fully reliable until it has been assessed by at least two independent methods [78,79].

In this work, three complementary procedures were chosen. The first two procedures, i.e.: the synthetic visual method and DSC measurements, were based on thermal analysis. The synthetic visual method is a precise technique used to determine the liquidus line of the system [80,81]. However, due to thermal degradation of urea, only a portion of the phase diagram could be studied using this method. Moreover, this method is not suitable for the determination of solidus lines.

Thus, DSC measurements were performed to establish the solidus line of the phase diagram, and to construct a Tammann plot [82,83] that enabled precise establishment of the eutectic composition previously inferred by the liquidus line. A specific DSC sample preparation method was followed that covered the entire composition range of the phase diagram. Finally, XRD was used to study the crystalline structure of the materials. Each procedure is explained in the following sections.

2.5.1. Synthetic visual method

The liquidus line of the phase diagram was measured using the so-called synthetic visual method [80,81]. In this procedure, the melting process of a sample is visually observed by the researcher while its temperature is monitored. This method shows three relevant advantages in comparison to DSC for the determination of the liquidus line[10]: i) samples in the order of grams can be measured; ii) the samples are stirred during the measurements, and iii) the heating rate can be extremely low without sensitivity losses. These working conditions prevent any thermal and/or compositional gradient within the sample, while the use of a slow enough heating rate leads to ascertain the end of melting with smaller uncertainty than in the DSC

The apparatus employed is described first in this section along with the operation conditions and temperature programs used. Then, tests performed to verify the heating rate employed in the measurements will be detailed.

2.5.1.1. Description of the system and operation conditions

As no commercial devices are available for the synthetic visual method, nor standardized procedures for its implementation, a self–tailored experimental assembly was built. It is schematically shown in Figure 3-1 and described next.

The main component of the setup is the reactor, a tailor-made glass container including an outer jacket. The sample is placed in its inner vessel, which is subsequently closed using a screwed Teflon plug made to assure air tightness. The outer jacket is used to heat or cool the sample using a heat transfer fluid (HTF) and is connected to a programmable thermostatic bath (Grant GP200-R3 model, ± 0.02 °C temperature uncertainty) through two insulated hoses. The bath is computer controlled by specific software.

A magnetic stirrer is used to homogenize the sample in order to avoid any temperature or compositional gradient in the material during the experiment. The temperature of the sample is monitored through a T-type thermocouple (± 0.5 °C uncertainty). Temperature data are

[10] This method was not available during the research stay of the author at the University of Innsbruck, where the experimental results of sugar alcohols were performed. Accordingly, DSC was used in Chapter 2 to determine the liquidus line of the mixtures, which can be also a suitable method.

recorded and stored into a data acquisition system (34921A model, Agilent Technologies) with a simultaneous temperature display that allows real time visualization of the temperature of the sample.

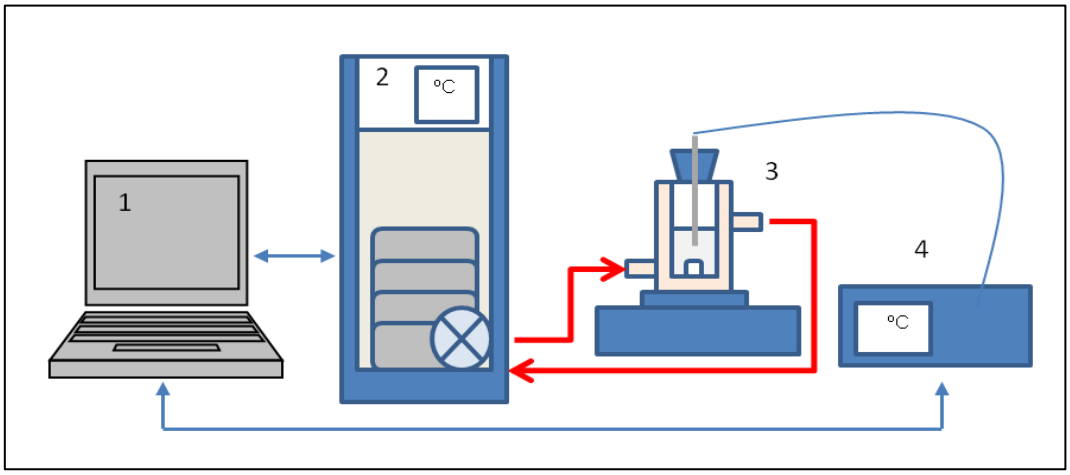

Figure 3-1: Schematic view of the experimental set-up for the synthetic visual method. 1) Computer, 2) thermostatic bath, 3) monitored glass reactor and magnetic stirring system and 4) data acquisition system

To prepare the samples, the pure materials were first sieved through a 400 μm diameter sieve to remove large grains. KF measurements were performed to control the moisture content of these materials. All results showed water contents of less than 0.2 %, which was considered suitable for the objectives sought. The materials were weighed (± 0.02 mg) according to the desired composition and introduced into the reactor. Each sample reached a total mass of 16 g. The magnetic shuffler was inserted into the reactor, and the sample was mixed with a spatula to ensure intimate contact between the pure compounds.

At that point, the HTF flow through the outer jacket was switched on. Its temperature was fixed at a predefined value above the eutectic temperature and below the liquidus line (this temperature was obtained from preliminary tests). When the eutectic portion of the sample began to melt, the magnetic stirrer started to rotate. Thus, a sample composed of a melt with solid suspended particles was obtained. The temperature of the HTF was held constant until the sample reached thermal equilibrium. For this purpose, two conditions had to be met: i) a temperature difference between the HTF and the sample of less than 1 °C, and ii) no further changes in the temperature of the sample (i.e., the temperature remained stable for 5 min within a 0.1 °C interval).

At that moment, the temperature of the HTF was submitted to a linear heating ramp of 0.1 K/min. This heating rate has been considered to guarantee quasi-static equilibrium conditions, as explained in the following paragraph. The evolution of the sample was visually examined until no solid particles remained in the melt, meaning that the liquidus temperature had been reached.

2.5.1.2. Verification of the heating rate employed

A systematic method was applied to determine a measurement rate that assured that the quasi-static equilibrium conditions required to determine a phase diagram [78] were always attained. This procedure consisted of determining the liquidus temperature of the same specific composition several times, using each time a heating rate lower than the previous repetition (usually halving it). When two consecutive measurements showed a liquidus temperature difference within the uncertainty of the thermocouple (± 0.5 °C), it was assumed that quasi-static equilibrium was reached. This heating rate was used for the measurements on the remainder of the compositions.

The composition selected for the repeated measurements was 75 % (w/w) urea and 25 % (w/w) sodium nitrate. Heating rates of 0.5, 0.25 and 0.1 K/min were applied. The results showed that a rate of 0.1 K/min was suitable for the conditions in this study. Note that this quasi-static equilibrium depends on the size of the crystals, the construction and design of the jacketed reactor and other factors (materials physical properties). As a consequence, the rate used herein should not be extrapolated to experimental conditions different from those used in this research. Nevertheless, the methodology proposed to determine the adequate heating rate can be used to determine the adequate heating rate for each material and the particular experimental setup and conditions.

The experimental reproducibility of the setup built for the synthetic visual method was assessed by reproducing the same experiment five times with two different compositions on different days (10 fresh samples in total). The results showed a standard deviation of 0.05 °C for each composition, and thus, the reproducibility of the method was considered suitable for the objectives of this work.

2.5.2. DSC measurements performed to construct the Tammann plot and to determine the solidus line of the phase diagram

To establish the eutectic composition of the phase diagram, a Tammann plot of the system was constructed. This is a widely known method [82] based on the application of the lever rule to phase diagrams. It relies on the fact that, if the enthalpy associated with the eutectic phase change is measured for different compositions of a binary eutectic system, then the maximum enthalpy value will occur at the eutectic composition. The enthalpy value of the eutectic part of the each composition will descend linearly from that maximum until they become zero at the left and the right endpoints of the eutectic line.

Because the variation of the eutectic enthalpy is linear, the results can be easily adjusted to linear correlations at each side of the eutectic composition. These correlated lines can be employed to find precisely the eutectic composition at the point where they merge with each other, which results in a significantly simpler and straightforward determination of the eutectic point in comparison to the extrapolation from the liquidus line of a phase diagram, where the trend is not linear.

Moreover, information on the solid miscibility of the system can also be obtained from the Tammann plot. If the phase diagram is a simple eutectic system with negligible solid solubility, the zero enthalpy of the obtained lines will occur at the extremes of the phase diagram (x=0 and x=1). Otherwise, the zero enthalpy of the line will occur at the compositions on the extremes of the eutectic line of the phase diagram. Additional details of the Tammann plot and related fundamentals are given in refs. [82,83].

DSC was used to measure the eutectic melting enthalpies of the mixtures. Samples were prepared directly within the DSC crucibles to minimize errors in the composition resulting from sampling from larger batches. To do that, the required amount of each component was weighed (± 0.001 mg) and placed in the crucible. Then the crucible was closed.

This procedure was performed inside a globe box (330 ABB model, Plas-Labs, Inc.) with a relative humidity (RH) of 5 %, in order to ensure that the materials did not undergo any water uptake from the atmosphere, and that the air enclosed inside the crucible was not humid. Eleven different compositions were selected to cover the entire range of the phase diagram.

Each composition was prepared and measured in duplicate to assure reproducibility. In total, 22 samples were measured.

Commonly, the study of a phase diagram involves prior complete melting and solidification of each sample before measurements are performed. However, in this case, those compositions with a liquidus line above the melting point of pure urea (133 °C) would undergo thermal degradation. More specifically, HPLC preliminary tests showed signs of degradation starting at 115 °C. Thus, it was decided to pre-melt the samples to a temperature below 115 °C but above the potential eutectic temperature observed in the literature (84 °C) [71,72]. The temperature program used is illustrated in Figure 3-2.

The procedure began at 20 °C, and the sample was heated at 4 K/min up to 110 °C. This assured complete fusion of the eutectic part in all samples and, in certain compositions, total melting occurred as well (samples with a liquidus temperature below 110 °C). Next, the sample was cooled to 20 °C at 10 K/min to solidify it. Finally, the sample was heated to 135 °C at 2 K/min. Isothermal segments of 5 min were included between each dynamic ramp. The last dynamic segment was used to obtain the eutectic melting enthalpy for construction of the Tammann plot. The thermograms obtained using these measurements were also used to construct the solidus line of the phase diagram, as described in Section 3.1.2.

To ensure that this procedure avoided thermal degradation of urea, certain samples were submitted only to prior melting and solidification segments and were subsequently analyzed by HLPC. No degradation byproducts were found in any of the samples. Therefore, it was concluded that the preparation method was suitable for assessment of the entire composition range of the phase diagram without any interference from thermal degradation.

2.5.3. X-Ray diffraction (XRD) measurements for the study of the phase diagram of the mixture

To gain knowledge about the solid crystalline phases present in the phase diagram of the mixture, XRD measurements were performed. The samples were prepared following the same melting and solidification procedure applied for the production of batches of DSC samples described in Section 2.6. Two types of experiments were performed and are described next. This technique was also used for the study of the water uptake of the PCM; the experimental conditions applied for this purpose will be presented in Section 2.9.2.

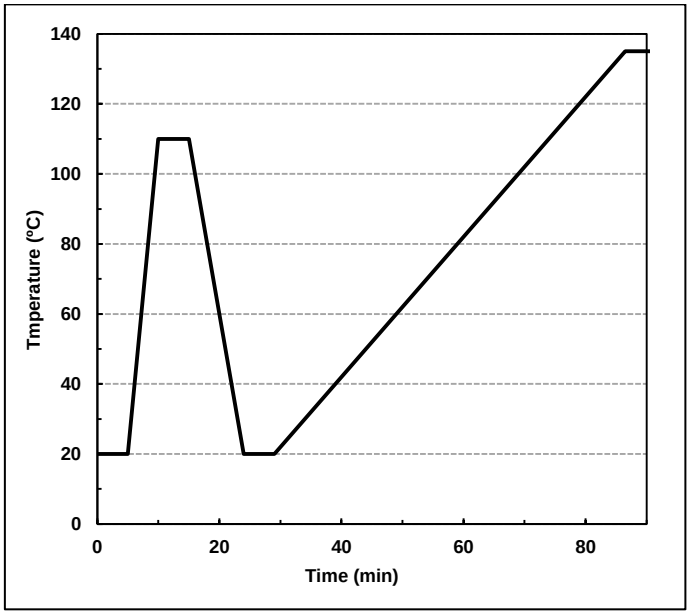

Figure 3-2: DSC temperature program applied for the determination of the eutectic melting enthalpies for construction of the Tammann plot

2.5.3.1. XRD tests at ambient temperature

XRD measurements at ambient temperature were carried out for qualitative identification of the phases present in the mixture. These measurements were performed to study the crystalline phases involved in the phase diagram of the mixture (Section 3.1.4). The diffraction patterns were collected using a Philips X'pert Pro automatic diffractometer under the following operation conditions.

- Cu–K$\alpha_{1,2}$ radiation source (wavelength 1.5418 Å)
- Tube voltage of 40 kV and tube current of 40 mA in theta-theta configuration using a secondary monochromator
- PIXcel solid-state detector (active length in 2θ 3.347 °)
- Data were collected from 10 to 80° 2θ (step size = 0.026 ° and time per step = 120 s)

Identification of the solid phases present in the mixture was performed using the Powder Diffraction File (PDF) database. The PANalytical X´Pert High Score program was used for identification and Miller indexing of all observed maxima.

2.5.3.2. High-temperature XRD experiments

High-temperature XRD experiments were performed to quantify the cell parameters of the mixture at different temperatures. This procedure made possible the study of the presence of any miscibility in the solid phases (see Results Section 3.1.4 for a complete explanation). Diffractograms were collected on a Bruker D8 Advance diffractometer, under the conditions detailed next:

- Cu tube radiation source (wavelength 1.5418 Å)
- Tube voltage of 30 kV and tube current of 20 mA
- Vantec-1 PSD detector
- Anton Parr HTK2000 high-temperature furnace
- Data were collected from 15 to 60 ° 2θ (step size = 0.033 ° and time per step = 0.1 s)

Data sets were recorded at 30, 60 and 76 °C. Four diffractograms with 5 minutes of delay between each were collected at each isothermal segment to assure that the sample had reached thermal equilibrium.

To quantify the cell parameters of the mixture, a full profile fitting of the XRD patterns was performed. This is a procedure commonly used to extract precise information on the position, intensity, width and shape of each individual peak in the diffraction pattern [84]. To do it, the FullProf software [85] was used. In the analysis, the unit cell parameters of peak shape (pseudo-Voigt), background, systematic 2θ shift, overall isotropic displacement, U,V,W half-width parameters for the profile function and asymmetry parameters were calculated. No structural model was applied.

2.6. Determination of the thermal properties of the composition selected as a PCM

A eutectic composition was found at 71.25 % (w/w) urea and 28.75 % (w/w) sodium nitrate (as described in Section 3.1). DSC measurements were performed to establish its phase change temperatures and enthalpies. For this purpose, the DSC normalized procedure developed under the framework of the SHC/ ECES Task 42/29 research program of the International Energy Agency (IEA) was applied. The details of the method can be found in [86,87].

A heating and cooling rate of 1 K/min was found suitable according to the preliminary measurements. The maximum and minimum temperatures of the program were 95 and 10 °C with isothermal segments of 5 min between each consecutive ramp. An integration range between 60 and 92 °C was used to determine the melting latent heat.

To produce each sample, a batch of approximately 2 g was first prepared using a melting and solidification procedure. To this end, the materials were weighed (± 0.02 mg) according to the chosen composition, and placed into a glass vial that was subsequently closed with a hermetic screwed plug. The vial was immersed into a glass beaker filled with glycerin as a heating fluid. A Pt-1000 probe placed in the glycerin bath and connected to a hot stirring plate (Mr Hei End model, Heidolph Instruments GmbH, ± 0.2 °C temperature uncertainty) was used to control the temperature of the glycerin. The temperature of the bath was held constant at 95 °C under stirring with a magnetic shuffler. Another magnetic shuffler was also placed into the glass vial to homogenize the sample.

When the material was completely melted (after approximately 15-20 min), an aliquot was extracted and placed onto an aluminum sheet. After this aliquot solidified, a sample of approximately 10 mg was taken from it. This sample was weighed (± 0.001 mg), placed into a DSC crucible and hermetically sealed with a crucible sealing press.

All steps were performed inside a glove box (330 ABB model, Plas-Labs, Inc.) under a dry air atmosphere (3 to 5 % RH at every moment) to avoid moisture uptake. The relative humidity was monitored continuously using a thermohygrometer (608 H2 model, Testo AG). All samples displayed less than 0.1 % (w/w) water presence measured by KF titration (Section 2.3). Moreover, HLPC results confirmed that no degradation byproducts were present in the samples. The remainder of the abovementioned aliquot was used to obtain samples for XRD.

2.7. Density measurements of the composition proposed as a PCM

The density of the composition selected as a PCM (71.25 % (w/w) urea and 28.75 % (w/w) sodium nitrate, as described in Section 3.1) was determined in the solid phase at 25 °C, and in the liquid phase at 89, 93 and 103 °C. All measurements (for both the solid and the liquid phases) were duplicated to assure reproducibility.

Both determinations were based on the well-known Archimedes´ principle. The density of the solid was obtained from the difference between the weight of a sample of PCM immersed in a fluid of a known density and its weight in air. A Sartorius ED224S scale (± 0.1 mg) with an YDK01LP density determination kit was used for this purpose.

The kit consisted of a metallic structure assembled to the scale with a flat plate holder on the top and a skimmer on the bottom. It also included a glass beaker to hold the fluid, which was placed on an auxiliary platform and thus not leaned on the scale. To perform the measurements, a solid sample of approximately 2 g was produced following a melting and solidification procedure and was weighed first in air using the flat holder on the top. Subsequently, the sample was placed on the skimmer, immersed in vegetable oil with a known density (0.913 g/cm^3) and weighed under these conditions.

Eq. 3-1 was used to calculate the density of the solid, where $W_{s,a}$ and $W_{s,fl}$ are the weights (g) of the solid sample in air and immersed in the fluid, respectively; ρ_{fl} is the density of the fluid used (0.913 g/cm^3); and ρ_a is the density of the air at 25 °C and a pressure of 1 atm (0.00184 g/cm^3).

$$\rho_{solid\ sample} = \left({W_{s,a}(\rho_{fl} - \rho_a)} \Big/ {(W_{s,a} - W_{s,fl})} \right) + \rho_a \qquad \text{Eq. 3-1}$$

The density of the liquid PCM was also determined using the scale and abovementioned kit. In this case, a calibrated glass teardrop with a known volume (10 cm^3) was first weighed in air. Next, the PCM was placed into a double-jacketed glass beaker coupled to a thermostatic bath (Grant GP200-R3 model, ± 0.02 °C temperature uncertainty) and melted. This beaker was placed on the auxiliary platform abovementioned. The temperature of the PCM was maintained at the desired level with the help of a Pt-100 probe that was connected to the thermostatic bath. At that point, the suspended teardrop was immersed in the liquid PCM and weighed. Eq. 3-2 was used to calculate the density of the liquid. There, $W_{b,a}$ and $W_{b,s}$ are the weights (g) of the volume-known body in air and immersed in the molten sample, respectively, and V_b is the volume (cm^3) of the body.

$$\rho_{liquid\ sample} = \left({}^{(W_{b,a} - W_{b,fl})}/_{V_b} \right) \qquad \text{Eq. 3-2}$$

2.8. Evaluation of the thermal reliability of the materials

DSC was used to perform the accelerated thermal cycling studies of the materials. The apparatus and calibration employed were the same presented in Section 2.2.

2.8.1. Accelerated thermal cycling of the sodium nitrate-urea eutectic mixture

Based on the results that will be presented in Section 3.1.3, the eutectic composition formed by 71.25 % (w/w) urea and 28.75 % (w/w) sodium nitrate was selected. To produce the DSC samples, the melting and solidification procedure detailed in Section 2.5.2 of this Chapter was followed. However, instead of preparing the samples inside the globe box with a low RH, it was decided to prepare the sample and close the crucible under laboratory ambient conditions with a RH of 32 %. This was done to evaluate the sample under conditions that apply in a potential large-scale production process, without the use of any box or room with a controlled atmosphere.

The DSC temperature program applied for the accelerated cycling test is shown in Figure 3-3. It was defined based on the actual operation temperatures that the PCM would undergo in a storage application. The maximum temperature of the program was set to 95 °C, which assured complete melting of the sample at each cycle. However, the minimum temperature of the program had to be defined by considering that the mixture shows supercooling at this stage of development[11] (see results Section 3.2.2). As a consequence, the minimum temperature of the cycling program was set to 10 °C to allow the material to crystallize at every cycle at the cooling rate selected. The heating and cooling rates of the program were set to 3 K/min. Isothermal segments of 5 min were applied after each heating and cooling ramp to homogenize the temperature of the sample before the subsequent step.

[11] The author is aware that supercooling can be a problem for the material to be used as a PCM; however, this drawback should be addressed after the mixture shows good thermal reliability, i.e., at a further stage of development.

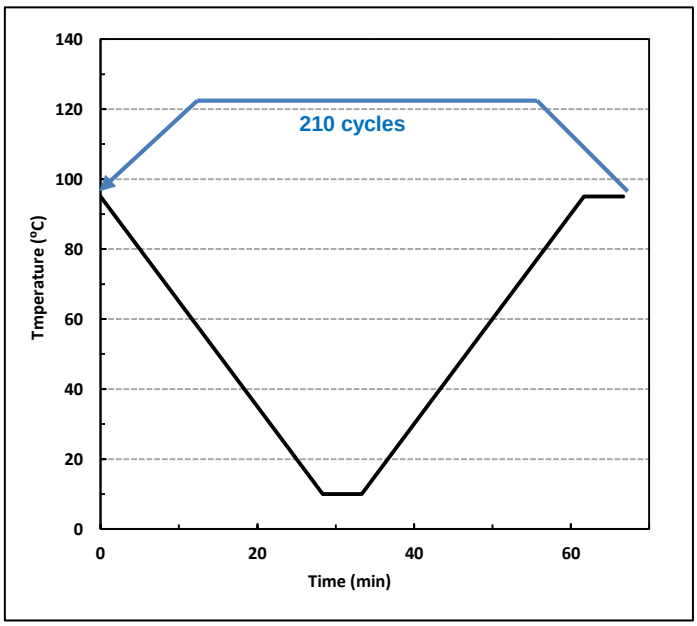

Figure 3-3: DSC temperature program applied for the accelerated thermal cycling measurements

Each experiment consisted of 210 complete thermal cycles, which was considered sufficient for this stage of the research. Potential mass loss during the experiment was periodically monitored although sealed crucibles were used. For this purpose, the DSC test was paused periodically, always when the sample was in the solid state, and the sample crucible was weighed (± 0.001 mg) before the test was resumed.

For fair comparison of the melting and solidification enthalpies, the integration limits were placed at the same temperatures for every cycle, i.e.: between 60 and 92 °C during heating and between 85 and 20 °C during cooling. The wider integration temperature range upon cooling was chosen because of the supercooling effect, which resulted in a different crystallization temperature in each cycle.

2.8.2. Accelerated thermal cycling of pure urea

Pure urea was also cycled via DSC. The maximum temperature of the program was 140 °C, and the minimum temperature was set to 30 °C with consideration of the supercooling of this material. The heating and cooling rates of the program were set to 3 K/min. Isothermal segments of 5 minutes were applied after each heating and cooling ramp. In this case, the measurement was terminated after 100 cycles because the thermal degradation at that point was significant and sufficient for comparison with the eutectic mixture (see Section 3.4.3).

2.9. Water uptake behavior of the composition selected as a PCM

Two experimental methods were used to evaluate the water uptake behavior coupled TGA/ DSC and XRD. They are detailed in the subsequent sections.

2.9.1. Coupled Thermogravimetric Analysis and Differential Scanning Calorimetry (coupled TGA/DSC) for the evaluation of water uptake of the PCM

Coupled TGA/DSC was used to study the influence of the water content on the thermal behavior of the eutectic mixture (71.25 % (w/w) urea and 28.75 % (w/w) sodium nitrate). The device used was a Mettler Toledo TGA/DSC 1, using the following characteristics:

- Both heat flow and temperature calibrations were performed with indium
- Mass calibration was carried out using standard calibrated weights
- Sealed aluminum crucibles of 25 μl were used
- Pierced lids were employed to allow water to volatilize during the measurements
- Dry nitrogen (99.999 % pure) was employed as a purge gas

The temperature program used went from 20 to 135 °C at a 3 K/min heating rate. Isotherms of 5 min before and after the dynamic ramp were performed. A blank curve with an empty crucible was performed prior to each measurement, and was subtracted afterwards from the sample signal.

Two different types of samples were prepared and are referred to as *dry* samples and *hydrated* samples throughout this chapter. The *dry* samples were prepared following the melting and solidification procedure previously detailed in Section 2.5.2. The process was performed inside a globe box (330 ABB model, Plas-Labs, Inc.) under an atmosphere with a RH of 3-4 %. The water content of these samples was determined by KF titration, which resulted in a 0.1 % (w/w) water content value. The samples were maintained inside the globe box prior to measurement.

The *hydrated* samples were obtained starting from the batch of *dry* samples. For this purpose, the moisture content of the globe box was increased until a RH of 55 % was achieved. The samples remained under this atmosphere for 3 days until they were introduced to the

crucibles and closed under the noted RH. KF measurements of samples prepared under these conditions rendered a water content of 7 % (w/w).

2.9.2. X-ray diffraction measurements for water uptake of the PCM

XRD measurements were performed to investigate the influence of the water content on the crystalline phases of the system. The samples were obtained from the batches prepared for the coupled TGA/DSC measurements described in Section 2.9.1. They were transported from the globe box to the XRD apparatus inside hermetic vials that had been closed inside the globe box. The measurements were performed immediately after each vial was opened to minimize the influence of any external moisture on the diffraction room.

The diffraction patterns were collected at ambient temperature with the Philips X'pert Pro automatic diffractometer described in Section 2.5.3.1, using the same measurement conditions.

3. Results and discussion

This section is divided into four parts. First, the results for the phase diagram are presented; second, the thermal properties of the composition selected as a PCM are detailed; third, the water uptake behavior of the system is analyzed and, finally, the thermal reliability of the eutectic composition is assessed.

It is important to remark on the significant influence that the experimental conditions had on the measurements performed. Variables such as relative humidity content, sample preparation temperatures and/or type of container used (open or closed) were shown to have noticeable influence on the results. This information should be borne in mind if any of the experiments presented are reproduced in further investigations. Besides, the obtained results should be restricted to experimental conditions that assure circumstances similar than those herein attained.

3.1. Studies on the phase diagram of the sodium nitrate-urea mixture

3.1.1. Determination of the liquidus line of the system

The liquidus line of the phase diagram was determined using the synthetic visual method. Because urea undergoes thermal degradation, only the portion of the phase diagram where the liquidus line stays below 115 °C was studied. This was the temperature at which the HLPC measurements began to show signs of degradation. Therefore, the compositional interval evaluated ranged from 67.50 to 82.50 % (w/w) urea. Nine different compositions were evaluated in this range and each composition was measured in duplicate. Thus, a total of 18 different samples were studied. The results obtained are presented in Figure 3-4.

A eutectic system can be inferred according to the shape of the obtained portion of the phase diagram. The diagram shows a congruent melting composition near 71 % (w/w) urea with a melting temperature of approximately 86 °C. The reproducibility of the measurements was suitable, as extracted from the results for the duplicated samples, which showed negligible differences.

This partial liquidus line obtained was not sufficient to establish the entire phase diagram. In addition, the synthetic visual method is not suitable for precise determination of the solidus line of a system. Thus, DSC measurements were performed to establish the solidus line of the phase diagram and to determine the exact composition of the eutectic mixture via construction of the Tammann plot. These results are detailed next.

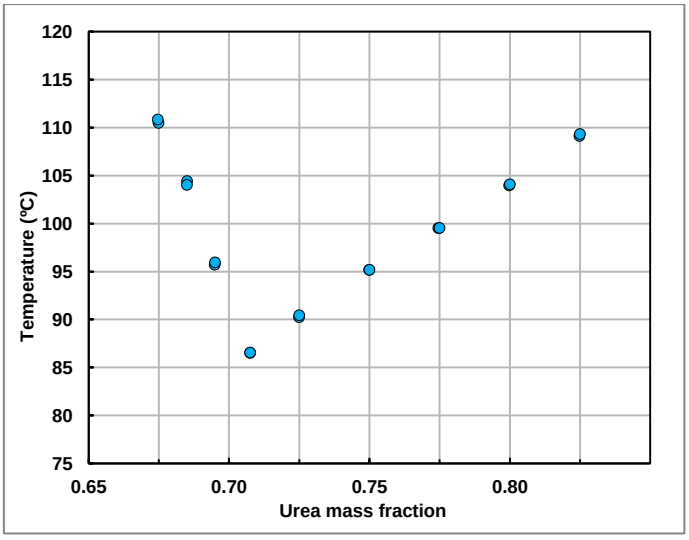

Figure 3-4: Results for the liquidus line temperatures of the mixture from the synthetic visual method (diagram focused only on the compositions under study)

3.1.2. DSC measurements: Assessment of the shape of the thermograms and determination of the solidus line of the system

The shape of the DSC thermograms was first appraised to gain knowledge of the type of phase diagram involved. Certain thermograms are illustrated in Figure 3-5 as examples. Every composition showed an endothermic peak near 86 °C. Based on the theory behind the interpretation of DSC thermograms for eutectic binary mixtures (see Chapter 2 or refs. [78,88] for additional information), the presence in every composition of a first peak that occurs at a fixed temperature can be attributed to a eutectic transition. The melting onset temperature of each first endothermic was evaluated to construct the solidus line. The average value of the onset of the peaks was 85.8 °C, being the minimum and the maximum values 84.8 and 86.5 °C, respectively.

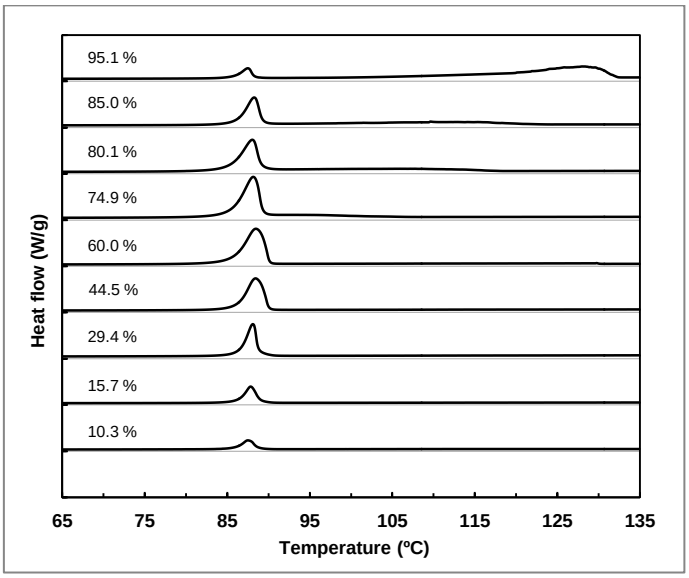

Figure 3-5: DSC thermograms for the measurements performed to construct the Tammann plot of the mixture. Mass percentages referred to urea are presented numerically next to each thermogram

A second endothermic was also observed in those compositions between 71.25 % (w/w) and 100 % (w/w) urea and became larger as the composition approached 100 % urea. This second peak typically corresponds to the solution of the remaining solid in the melt [88], and can be used to estimate the liquidus line of the phase diagram. For the current work, because the synthetic visual method is more precise for this purpose, only the results obtained from this technique will be considered; however, the shape of the DSC thermograms with this second peak again suggest a eutectic system. Note that the second peak was not observed in the samples with compositions below 71.25 % (w/w) urea because the DSC temperature program

was terminated at 135 °C to avoid thermal degradation (see Section 2.5.2); for those compositions, the liquidus line would be located above 135 °C.

3.1.3. Construction of the Tammann plot and determination of the eutectic composition of the system

To construct the Tammann plot, the melting enthalpy of each first endothermic peak in the DSC thermograms was evaluated and represented as a function of the composition. The results are shown in Figure 3-6. As can be observed, the melting eutectic enthalpies form two ascending lines that start from the extremes of the composition values and extend until they reach a maximum at a certain composition. This shape of the Tammann plot suggests a eutectic phase diagram.

To determine the specific eutectic composition, the points were adjusted to a linear correlation using the least squares regression. The correlation coefficients (Pearson's R) were 0.997 and 0.994, and thus, the adjustment was considered acceptable. The lines obtained from the regression crossed at a composition of 71.25 % (w/w) urea and 28.75 % (w/w) sodium nitrate.

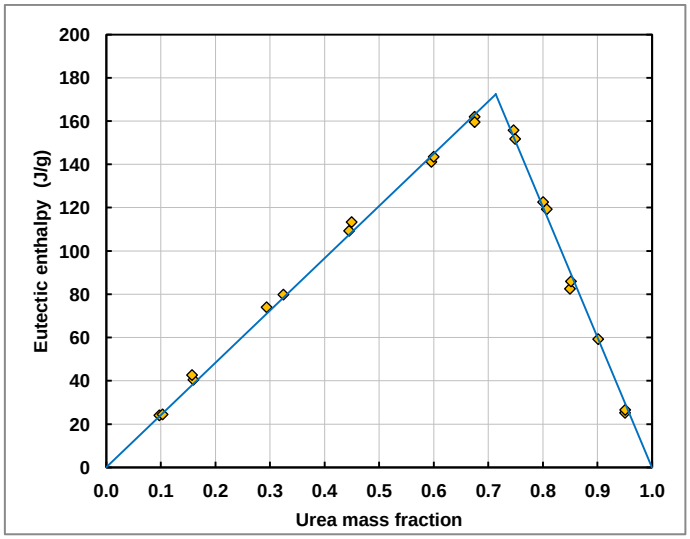

Figure 3-6: Results for the Tammann plot of the mixture obtained by DSC (orange diamonds). The linear regression performed is represented as a continuous blue line

Note also that the adjusted lines of the plot reached an enthalpy value of 0 J/g at the extremes of the compositional axis (urea mass fraction=0 and urea mass fraction=1). This observation corresponds to a situation in which the solubility at the extremes of the phase diagram is

negligible, and thus no significant miscibility between the two compounds should be expected in the solid state.

To obtain a complete picture of all results presented thus far, the results of the Tammann plot are presented in Figure 3-7 together with those obtained from DSC for the solidus line and those achieved for the liquidus line as determined by the synthetic visual method. A simple eutectic phase diagram can be clearly inferred from the figure. Moreover, the eutectic composition inferred by the liquidus line agrees with that obtained from the representation of the Tammann plot. As a consequence, the mixture formed by 71.25 % (w/w) urea and 28.75 % (w/w) can be treated as the eutectic composition of the sodium nitrate-urea system, and this was the composition selected as a PCM.

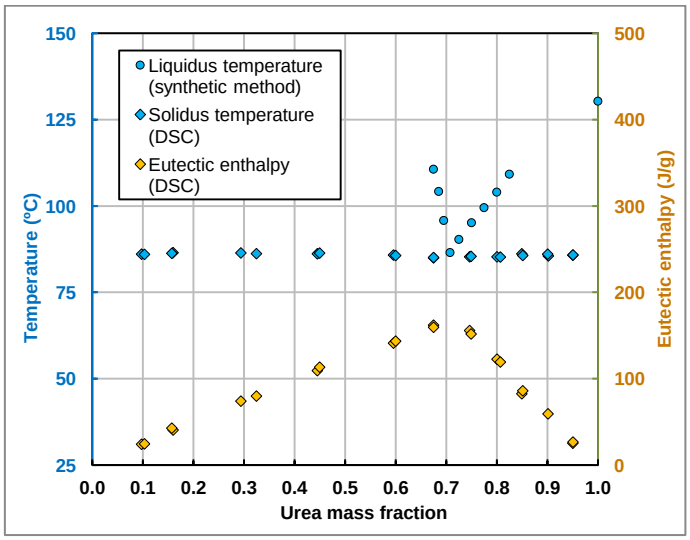

Figure 3-7: Combined results of the liquidus line of the sodium nitrate-urea system obtained from the synthetic visual method (blue circles), the onset temperatures from DSC (blue diamonds) and the eutectic enthalpies (orange diamonds) determined from DSC for the Tammann plot

3.1.4. XRD analysis of the crystalline phases in the phase diagram

Two different types of XRD measurements were performed: ambient temperature XRD tests and variable temperature XRD analysis.

3.1.4.1. Results of ambient temperature XRD measurements

To confirm the results obtained from thermal analysis, the crystalline structure of the system was studied using XRD experiments. The composition formed by 71.25 % (w/w) urea and 28.75 % (w/w) sodium nitrate was first evaluated. A preliminary identification of the solid phases present in the mixture was performed using the Powder Diffraction File (PDF) database. The

XRD data were in agreement with urea [$CO(NH_2)_2$ - (PDF Ref. code: 01-073-3118)] and sodium nitrate [$Na(NO_3)$ - (PDF Ref. code: 04-007-5274)]. The identification of the peaks in the diffraction pattern obtained is illustrated in Figure 3-8.

All peaks on the diffractogram correspond either to those of the pure urea (dark blue) or to sodium nitrate (light blue). The two peaks of the diffractogram that were not indexed to urea or to sodium nitrate correspond to the diffraction from the platinum sample holder.

Two additional compositions were evaluated by XRD, one composed of 75 % (w/w) urea and 25 % (w/w) sodium nitrate and another formed by 69.5 % (w/w) urea and 30.5 % (w/w) sodium nitrate. The same pattern was obtained in both situations (although the sample formed by 69.5 % urea had to be submitted to thermal treatment, as detailed below).

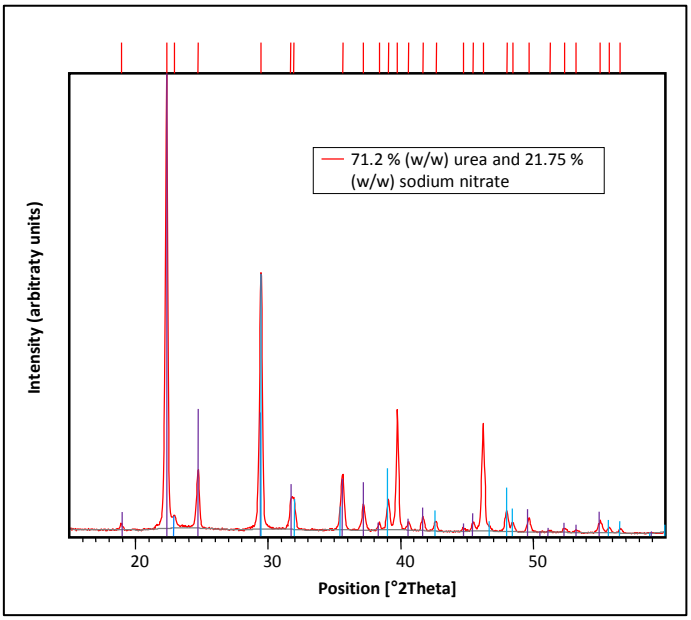

Figure 3-8: Identification and Miller indexing of the composition formed by 71.25 % (w/w) urea and 28.75 % (w/w) sodium nitrate (light blue lines correspond to sodium nitrate miller indices and dark blue lines indicate the indices of urea)

According to the XRD analysis for phase diagrams [89], any composition of a eutectic system produces a diffractogram composed solely by the sum of the peaks of the phases forming the eutectic system, as herein occurred. Thus, these results corroborate those attained from thermal analysis and confirm that the phase diagram formed by sodium nitrate and urea is a eutectic type.

3.1.4.2. Results of variable temperature XRD measurements

To study the presence of any solid miscibility at the extremes of the phase diagram, variable temperature XRD measurements were performed at 30, 60 and 76 °C. For this investigation, the composition with 71.25 % urea (w/w) was evaluated. The theory behind phase diagrams states that in a 2-phase region, if any solid miscibility occurs between the pure compounds, it might vary with temperature [78]. According to this observation and because the atoms of each component diffuse within the structure of the other, the cell parameters of each phase present in the system should vary following an inverse relationship, i.e., one phase should increase its cell volume with temperature while the other one should decrease.

To determine the cell parameters of the sample at each temperature, a full XRD profile fitting was performed following the procedure explained in Section 2.5.3. The experimental and the calculated data were in agreement, as illustrated in Figure 3-9.

The specific cell parameters obtained are presented in Table 3-2 together with the crystal system and space group of each compound. As shown, the parameters for both phases increased slightly as the temperature rose. This behavior was attributed to the thermal expansion of the solid, but it would be inconsistent with any solid miscibility variation in the system. As a consequence, the results indicate no significant solid miscibility in the phase diagram. This observation is consistent with the results attained from the Tammann Plot.

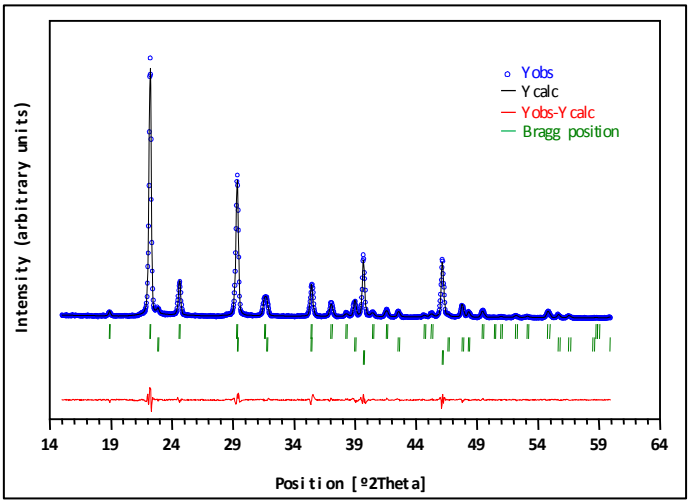

Figure 3-9: X-ray diffraction profile fitting for the eutectic composition measured at 60 °C. Blue circles denote experimental points (Y obs) while the black continuous line is the calculated profile (Y calc). The theoretical peak Bragg positions (green vertical sticks) and the difference lines (Yobs-Ycalc) are shown at the bottom of the figure

	Sodium nitrate (Å) (rhombohedral, R-3 c)			Urea (Å) (tetragonal, P-421 m)		
Temperature (ºC)	**a**	**b**	**c**	**a**	**b**	**c**
30	5.067	5.067	16.831	5.645	5.645	4.700
60	5.067	5.067	16.898	5.666	5.666	4.703
76	5.071	5.071	16.930	5.678	5.678	4.705

Table 3-2: Unit cell parameters (Å) of both components of the sample formed by 71.25 % (w/w) urea and 28.75 % (w/w) sodium nitrate at different temperatures

3.1.5. Formation of metastable phases

It is required to report that a new phase different from urea and from sodium nitrate was detected in certain XRD samples. This event occurred in the diffraction measurements at room temperature of mixtures composed of 69.5 % (w/w) urea and 30.5 % (w/w) sodium nitrate that were prepared as described in Section 2.6. The diffractogram obtained is shown in Figure 3-10.

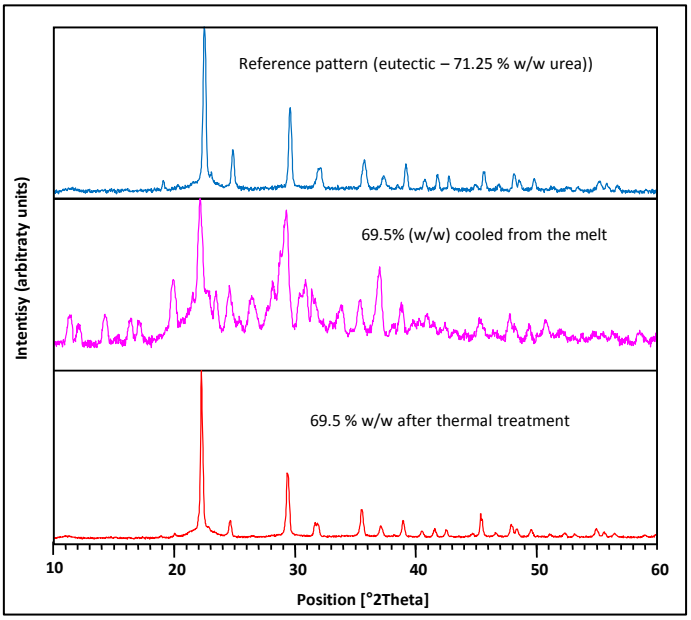

Figure 3-10: XRD comparison of the sample composed of 69.5 % (w/w) before and after the thermal conditioning procedure. The diffractogram of the eutectic sample (above) is shown as a reference

The diffraction peaks corresponding to urea and sodium nitrate remained, but several new maxima appeared at different angles. No successful pattern identification was achieved for this new phase/compound using the PDF database. The appearance of a new phase did not match with the results obtained in the study thus far and were inconsistent with a simple eutectic phase diagram. Thus, a large probability existed that the unknown compound could be a metastable phase formed during the solidification that took place upon preparation of the samples.

To evaluate this case, the sample was submitted to thermal treatment. It was melted and maintained at 80 °C under stirring until it solidified. In this manner, crystallization occurred without any supercooling (see Section 3.2 for supercooling of the material). Moreover, the solidified sample was held at 80 °C for 3 days to activate diffusion and to promote the formation of the equilibrium phases of the system. After this treatment, the sample was slowly cooled and measured again by XRD at room temperature. The results showed a diffractogram composed of pure urea and sodium nitrate (Figure 3-10, lowest part). Therefore, it was concluded that the phase observed was a metastable form that appeared under high crystallization rates.

Moreover, the formation of the metastable phase was accompanied by a noticeable change in the habit of the crystals formed. When the metastable form crystallized, needle-shaped

crystals were obtained (long fibers), but this formation did not occur when the stable form crystallized. It is also noteworthy that the metastable phase did not form in hypereutectic compositions (i.e., greater than 71.25 % (w/w) urea content). As a result, an abrupt change was noted in the crystallization behavior of mixtures with urea content greater than 71.25 % (w/w). This observation suggests that formation of the metastable phase is promoted by the proeutectic precipitation of the nitrate-rich phase, which forms solely in hypoeutectic compositions, and it reinforces the theory that the eutectic composition is formed with 71.25 % (w/w) urea.

Finally, it must be noted that this metastable phase does not affect the use of the eutectic composition as a PCM because this phase will not form under the usual cooling rates used for TES applications, as demonstrated in the Section 3.2.

3.2. Thermal properties and density of the composition proposed as a PCM: Potential of the mixture for TES applications

The main thermal and physical characteristics of the eutectic composition in the sodium nitrate-urea system were characterized to determine its feasibility as a PCM for thermal storage applications. The mixture selected was that obtained from the Tammann plot and formed by 71.25 % (w/w) urea and 28.75 % (w/w) sodium nitrate.

3.2.1. Melting onset temperature and latent melting enthalpy

DSC measurements were performed to establish the calorimetric properties of the chosen composition. The measurements were performed following the procedure defined in [86,87] with a measurement rate of 1 K/min. The results for the heat flow are shown in Figure 3-11.

The shape of the thermogram showed only one clean peak during both melting and solidification processes. Thus, it can be stated that the material melts congruently. This congruent behavior was reproducible for repeated thermal cycles, as it will be shown in Section 3.4.1. The melting onset temperature obtained for the composition studied was 85.0 °C, and its melting latent heat was 172.0 J/g.

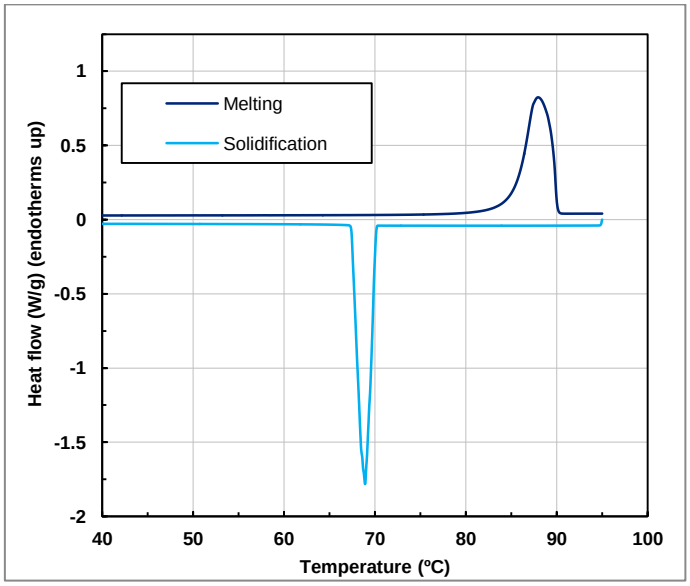

Figure 3-11: DSC results (heat flow vs. temperature) for the eutectic composition (71.25 % (w/w) urea)

3.2.2. Crystallization behavior and assessment of supercooling

Upon solidification, the sample showed supercooling (Figure 3-11). For the experimental conditions applied, the onset crystallization temperature of the material was 70.1 °C. Besides, the crystallization enthalpy was 163.3 J/g.

It is known that supercooling is a stochastic effect, influenced by experimental conditions such as sample mass and cooling rate, among others [41]. Thus, additional measurements were performed to evaluate dependency on the cooling rate. For this purpose, three fresh samples of approximately 10 mg were submitted to subsequent cooling ramps at 0.5, 2, 4 and 8 K/min (each sample was melted again between each cooling ramp). The results are shown in Figure 3-12.

As shown, no clear correlation between the cooling rate and the supercooling can be determined from the attained results. Only the measurements performed at 8 K/min showed a clear tendency towards higher supercooling, as expected. For lower cooling rates, it can only be stated that all samples crystallized between 70 °C and 30 °C. As a result, the minimum supercooling observed was 15 °C. This degree of supercooling could be a problem for the material to be used as a PCM, however, it could be expected to be reduced if a larger mass is employed [41]. Besides, to avoid it the use of nucleating agents could be investigated. Nevertheless, this step should be only undertaken at a future stage of development, after the proper lifespan of the mixture has been completely confirmed.

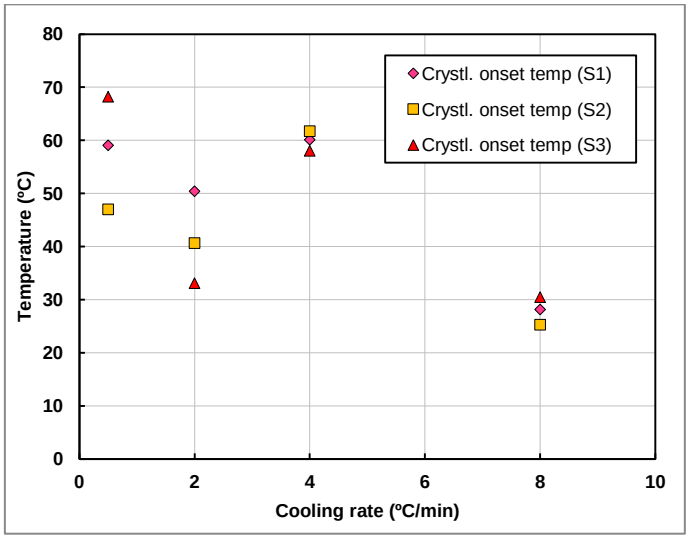

Figure 3-12: Crystallization onset temperatures for 3 samples (S1, S2 and S3) of the PCM at different cooling rates

3.2.3. Energy storage of the eutectic PCM

When a PCM is used in a LHTES system, the actual storage capacity of the material is defined by the sum of the sensible and latent storage heats in the working temperature range of the intended application. This storage capacity can be extracted from the enthalpy vs. temperature curve, which covers both sensible and latent heat. In this study, the defined working temperature interval was 75 to 90 °C. This gap can be considered representative of the operating conditions for domestic microcogeneration devices [90].

The results are shown in Figure 3-13. Within the temperature range selected, the enthalpy stored upon melting was 203 J/g, which represents the maximum storage capacity of the PCM in that range. Water shows a storage ability of 63 J/g in the same interval. Therefore, the PCM could store 3.2 times more energy per mass unit than water for the intended application.

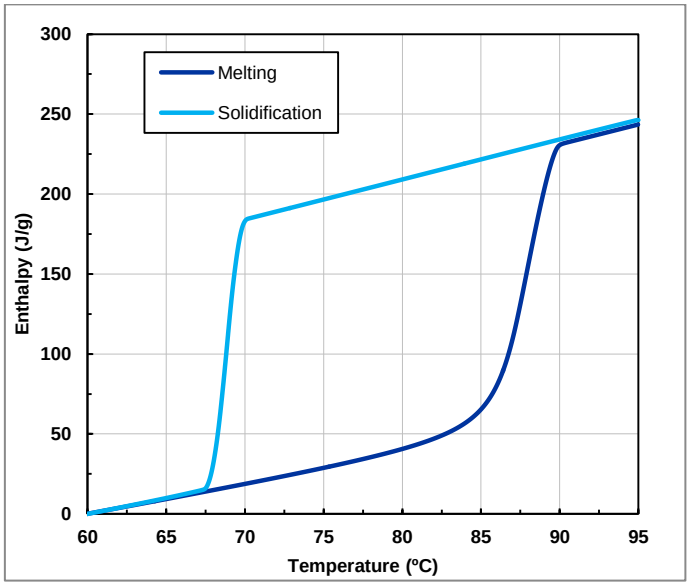

Figure 3-13: Enthalpy vs. temperature (DSC results) for the eutectic composition (71.25 % (w/w) urea) obtained from integration of the DSC heat flow values (Figure 3-11)

3.2.4. *Specific weight of the eutectic composition as a function of temperature and volume expansion during phase change*

The specific weight (density) of the eutectic composition as a function of temperature is shown in. From the specific weight values at different temperatures in the liquid state, a thermal expansion coefficient of $9 \cdot 10^{-4}$ K^{-1} was obtained. Moreover, from the density change between the solid (25 °C) and the liquid (89 °C) it was inferred that the material expands on melting and shrinks on solidification, undergoing a volume expansion of 4.1 %.

	Solid		Liquid	
Temperature (ºC)	25	89	93	103
Specific weight (g/cm^3)	1.480	1.423	1.419	1.405

Table 3-3: Determined values of specific weight (density) of the eutectic composition as a function of temperature

3.2.5. *Volumetric energy density of the PCM, current price and comparison with other PCMs*

The volumetric energy density was used to compare the thermal characteristics of the proposed eutectic mixture with other known PCMs. To calculate this value, only the latent melting enthalpy (without the sensible contribution) was considered because most values available in the literature consider only latent heat. As a result, using the value obtained for the liquid density at 89 °C, and the latent melting enthalpy of 172.0 J/g, a volumetric energy density of 245 MJ/m^3 was obtained.

This value is slightly lower than the storage densities of known PCMs based on salt hydrates for the temperature range involved, which are typically comprised between 250 – 400 MJ/m^3 [13]. However, it is at the same level than the values usually handled for fatty acids such as stearic or palmitic acid [29], and is larger than the values of paraffins (120-200 MJ/m^3) [13]. Moreover, the market price of the proposed eutectic material is around 0.9 €/kg [64], which is highly competitive in the current market situation. This value is in the same range as that of salt hydrates [91] and well below that of fatty acids and paraffins.

To summarize, all of the determined properties of the eutectic material are listed in Table 3-4. It can be affirmed that, according to its energy storage capacity, melting temperature and current market price, the proposed PCM is a suitable option for TES applications at the heating and DHW temperature range.

Property	Value
Melting onset temperature (°C)	85.0
Melting latent enthalpy (kJ/kg)	172.0
Solidification onset temperature (°C)	70.1[a]
Solidification latent enthalpy (kJ/kg)	163.3[a]
Energy storage capacity between 75 and 90 ºC (kJ/kg)	203
Solid density at 25 ºC (kg/dm^3)	1.48
Liquid density at 89 ºC (kg/dm^3)	1.42
Thermal expansion coefficient in the liquid state	$9 \cdot 10^{-4}$
Volume expansion upon melting (%)	4.1
Volumetric latent melting energy density (MJ/m^3)	245
Market current price (€/kg)	0.9

Table 3-4: Summary of the properties of the eutectic composition proposed as a PCM.
[a] Properties affected by supercooling, they are thus limited to the experimental conditions herein applied.

3.3. Influence of the water content on the material

After the main thermophysical properties were assessed, studies were performed to understand the influence of the water uptake in the melting and crystallization behavior of the material. KF titration, coupled TGA/DSC, HPLC and XRD measurements were used for this purpose.

3.3.1. Coupled TGA/ DSC results: Influence of water content on the thermal properties of the material

A *dry* sample (prepared under a 4 % RH atmosphere, KF measurements = 0.1 % water content) and a *hydrated* sample (prepared under a 55 % RH atmosphere, KF measurements = 7 % water

content) were prepared following the procedure explained in Section 2.3 and evaluated using coupled TGA/DSC. An additional *dry* sample obtained from the same batch was also measured by HPLC, and no signs of biuret or cyanuric acid were noted. Thus, the samples did not undergo any thermal degradation due to the preparation procedure. The coupled TGA/ DSC results are shown in Figure 3-14.

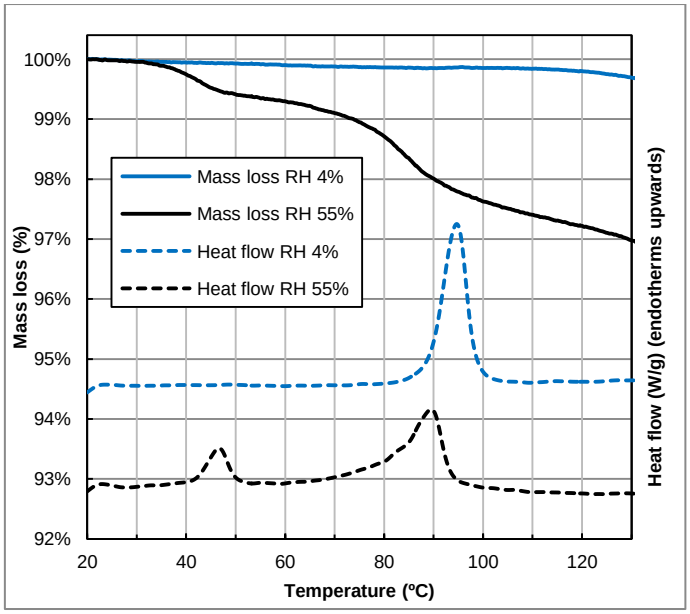

Figure 3-14: Coupled TGA and DSC heating results of samples prepared under an atmosphere with 4 % RH (*dry* sample, 0.1 % water content, blue lines) and 55 % RH (*hydrated* sample, 7 % water content, black lines)

As observed, the heat flow signal of the samples showed clear differences. The *dry* sample produced a thermogram formed by one clear melting peak with a melting onset temperature of 85 °C and a melting latent enthalpy of 170 J/g. These results are equivalent to those obtained previously by DSC (Figure 3-11).

In contrast, the *hydrated* sample presented a thermogram formed by two endothermic peaks. The first peak was a low enthalpy transition of nearby 10 J/g that took place at 42 °C. The second peak was a wide endothermic peak with a melting onset temperature at 70 °C. The latent enthalpy of the *hydrated* sample was obtained from the simultaneous integration of the two peaks of the thermogram in Figure 3-14 and showed a value of 140 J/g.

For the mass loss results, both samples presented different behaviors. The *dry* sample showed a negligible weight decrease trend until it reached 115 °C. By that point, the mass loss had reached 0.1 %, which corresponded with the water content originally present in the sample. At this temperature, the sample was completely melted, as the endset temperature of the

melting peak of the heat flow curve occurred at 100 °C. At a temperature higher than 115 °C, the mass loss rate increased. This last mass loss could not be related to water because it had already been eliminated from the sample at lower temperatures; thus, it was attributed to an initial stage of the thermal degradation of urea[12].

In contrast, the TGA curve of the *hydrated* sample displayed several steps. A first stage of mass loss was noted at approximately 40 °C, where the weight of the sample was reduced by 0.6 %. This event corresponded with the first endothermic peak observed in the heat flow curve for the same sample. After that point, the signal remained approximately stable until a second mass loss stage was observed between 70 and 90 °C. This step agreed with the temperature of the second endothermic that occurred in the heat flow signal, which corresponded to the melt of the sample. During this stage, the total mass loss reached 2 % of the sample weight. Thus, a 5 % of water remained in the material even after it was completely melted (remind that the initial water content of the *hydrated* sample was 7 %). Beyond this point, the weight loss continued, following a constant trend until the measurement finished at 135 °C. This last mass loss step was attributed to a combined process of water release with formation of initial thermal degradation byproducts.

According to the temperature and enthalpy of the first endothermic observed in the heat flow curve of the *hydrated* sample, and because it corresponded clearly with the first mass loss process registered, it was concluded that the transition was due to the release of adsorbed water. However, only a portion of the original water content was released after this first step. This observation indicated that the remaining amount of water was not only adsorbed superficially but was included in the structure of the sample as a new phase or compound. This conclusion can explain why the onset temperature, the enthalpy and the shape of the second peak of the *hydrated* sample were different than those of the melting peak of the *dry* sample. This hypothesis was subsequently confirmed by the XRD results (see Section 3.3.2).

[12] It should be noted that the objective of these measurements was to compare the behavior of a *dry* and a *hydrated* sample, and thus the experimental conditions (heating rate, pierced crucible lid used, etc.) were defined for that purpose. As a consequence, the results should not be used to conclude that the degradation of the *dry* material starts at 115 ºC because this would vary noticeably depending on the experimental conditions.

Based on these results, it can be concluded that water uptake clearly affects the thermal behavior of the proposed eutectic PCM. Therefore, water uptake should be avoided during any potential production process, handling and/or use of the PCM. To this end, the driest possible atmosphere should be maintained. However, although no explicit tests were included in this work for the sake of brevity, it was observed that the water uptake was not critical if the samples were prepared under an atmosphere of 35 % RH or below.

This conclusion can be extracted from the samples that will be used in Section 3.4 for thermal cycling measurements. A difference of 7 J/g was registered between the initial melting enthalpy of that sample (prepared under 32 % RH) and the *dry* samples measured in this section. Moreover, the initial melting onset temperature in the thermal cycling experiment was 1.4 °C lower than that measured for the *dry* samples. These differences were related to the higher water content of the sample used for thermal cycling; however, the thermal properties of that sample were still considered suitable for its use in LHTES applications.

3.3.2. *XRD measurements: Influence of water content on the crystalline structure of the material*

The *dry* and *hydrated* samples were also evaluated by XRD to study their solid crystalline structure, and the results are shown in Figure 3-15. The 2θ diffraction angles depicted in the figure correspond to the range from 10 ° to 45 ° in order to present a clearer view of the zone of interest.

The *dry* sample (S1) can be observed in the upper part of the diffractogram. Its pattern showed only those peaks from pure sodium nitrate and urea, as in Section 3.1.4. These results indicated that the sample was formed solely by a eutectic mixture of the pure materials. In contrast, the diffractogram of the *hydrated* sample (S2), depicted in the middle of the illustration, displayed noticeable differences. The peaks of urea and sodium nitrate were still present in the diffractogram, but several new peaks appeared. This difference was especially noticed at low diffraction angles, from 10 ° to 20 ° 2θ, where 6 new clear maxima were found.

Pattern identification of the new peaks was attempted using the PDF database. No agreement was found with any possible degradation byproduct that could have been formed, i.e., biuret, cyanuric acid or others. The results were neither in agreement with any of the compounds that potentially could have contaminated the sample during preparation or handling. They did not

either match the metastable phase described in Section 3.1.5. Thus, the most likely cause of the new peaks was the formation of new unknown phases due to the presence of water.

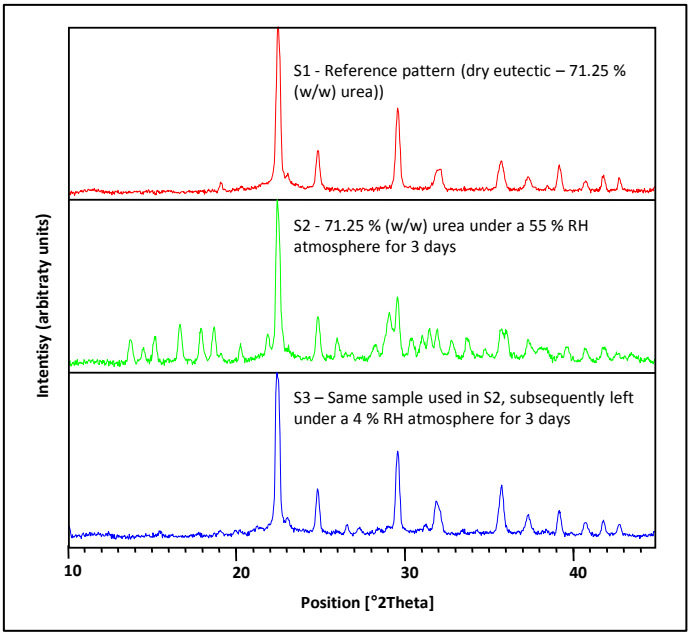

Figure 3-15: Comparison of XRD results from samples with different water content

To confirm this possibility, the *hydrated* sample that was measured by XRD was inserted again into the globe box under a RH of 4 % for a period of 3 days. After that time, the sample was measured again by XRD. As shown in the lowest portion of Figure 3-15 (S3), the peaks previously displayed in the *hydrated* sample had disappeared. This reversibility would not be observed if the new phase was caused by any permanent thermal degradation or by any contamination of the sample. Additional measurements were performed with a sample composed of 75 % (w/w) urea and 25 % (w/w) sodium nitrate, and the same pattern was observed. Thus, it was concluded that the new peaks were caused by the presence of water.

These differences observed in relation to the original diffractogram were too significant to be caused merely by water adsorbed at the surface of the material or even by the presence of a new solid solution. According to the literature [78], these effects should only produce a displacement of the positions of the peaks of the original diffractogram, small intensity modifications for the reflections, or the appearance of small new signals caused by a potential symmetry change, due to the presence of adsorbed (or diffused, in the case of a solid solution) water molecules in the crystalline network. Thus, it was concluded that the pattern corresponds to a new compound formed by water and urea and/or sodium nitrate. This

interpretation agreed with the results previously suggested from the coupled TGA/DSC measurements.

The objective of this chapter was the study of the influence of the water content on the thermal behavior of the mixture, which was accomplished, and therefore, the identification of this new compound is beyond the scope of this work. However, this point could be relevant for applications other than thermal energy storage.

3.4. Accelerated thermal cycling of the mixture: DSC and HPLC results

The results of the thermal degradation studies of the eutectic composition are discussed throughout this section.

3.4.1. DSC thermal cycling results for the sodium nitrate-urea eutectic mixture

The latent melting enthalpies of the sodium nitrate-urea eutectic mixture during thermal cycling are shown in Figure 3-16 together with the crystallization enthalpy. For the sake of clarity, only the results of one of every three cycles are presented in the figure, although every cycle was evaluated during the analysis. The mass loss of the sample throughout the experiment was negligible, and therefore, it has not been included in the discussion of the results.

In the illustration, it can be observed that the melting enthalpy was stable during the number of cycles performed, although it must be mentioned that a minor constant decrease was noticed as the number of thermal cycles increased. The melting enthalpy average value was 165.1 J/g. The maximum melting enthalpy measured was 165.5 J/g and was attained at the 3rd cycle, whereas the minimum value was 163.6 J/g and was reached at the 208^{th} cycle. This resulted in a reduction of 1.2 % of the original melting enthalpy after 210 cycles.

The evolution of the melting onset temperatures is illustrated in Figure 3-17 together with the results for the crystallization onset temperatures. No decreasing trend was found in the results. The maximum onset temperature recorded was 83.66 °C, and the minimum was 83.34 °C. This difference is nearly within the accuracy of the DSC apparatus used (± 0.2 °C), and thus, it can be considered negligible.

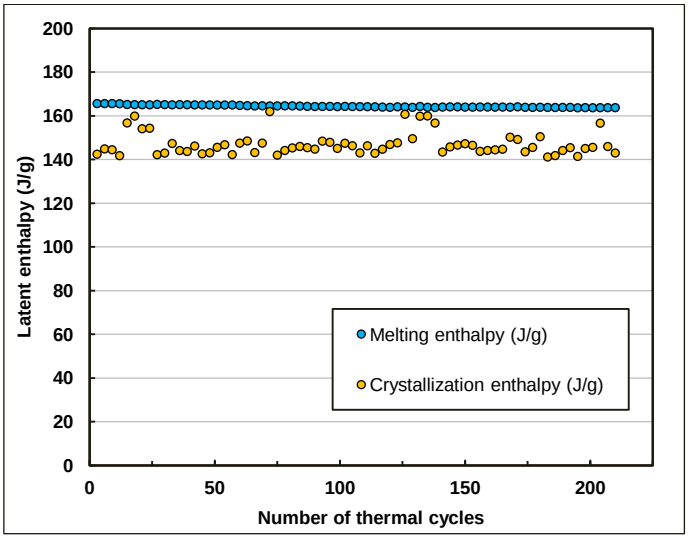

Figure 3-16: Melting and crystallization enthalpy of the eutectic mixture during thermal cycling measurements

The crystallization enthalpy (Figure 3-16) did not show any decreasing tendency, although a certain dispersion of the values was observed throughout the test. This observation was related to the supercooling registered at each cycle. As extracted from Figure 3-17, the values of the crystallization temperature during the thermal cycles were grouped into two temperature levels.

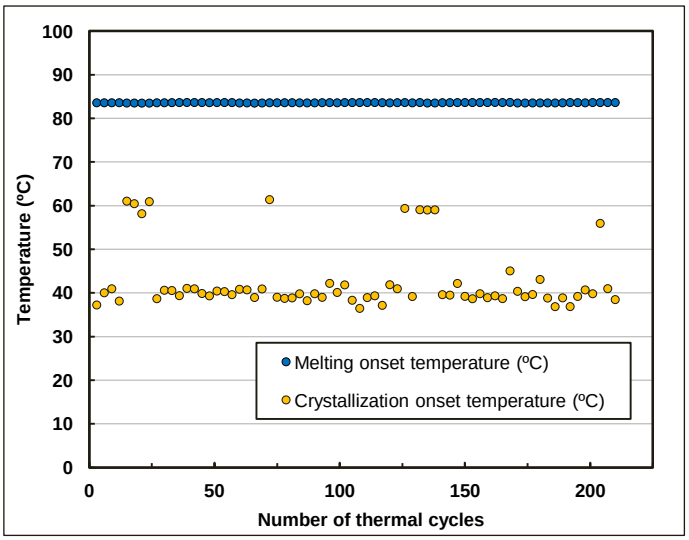

Figure 3-17: Melting and crystallization onset temperatures for each thermal cycle performed

In 173 out of the 210 cycles performed, the crystallization onset temperature was between 36.5 and 45.1 °C (average: 39.5 °C; typical deviation: 1.39 °C). In these cases, the crystallization enthalpy was between 139.2 and 150.4 J/g (average: 145.2 J/g; typical deviation: 2.2 J/g). In the remainder of the cases (37 cycles), the crystallization onset temperature was higher,

between 51.6 and 73.6 °C depending on the cycle (average: 60.0 °C; typical deviation: 4.6 °C). In those cases, the crystallization enthalpy was between 154.1 and 165.0 J/g (average: 158.9 J/g; typical deviation: 2.8 J/g). These enthalpy values were closer to the values measured upon melting (165.1 J/g).

The difference between the melting and the crystallization enthalpy determined during the thermal cycling is related to the measuring procedure applied, in which only the latent heat was computed in the evaluation procedure and not the total enthalpy evolution during the cycle. With respect to the behavior of the crystallization onset temperatures, no decreasing trend was found, although as commented, the results showed additional dispersion due to the random nature of supercooling [41].

To complement the results, the evolution of the shape of the DSC melting thermograms for the eutectic mixture is shown in Figure 3-18. As observed, the shape of the heat flow signal remained constant during the test. No new thermal events or transitions or peaks appeared while the material was subjected to the thermal cycles. The onset temperatures were maintained constant, as discussed above. Only a minor decrease of 0.5 °C was noticed in the endset temperatures of the thermograms. This change was small, and it was thus considered negligible for the objectives of this research work.

3.4.2. HPLC results: Evaluation of the presence of degradation byproducts in the eutectic mixture before and after the thermal cycling test

In addition to the DSC results, the presence of degradation byproducts was assessed using HLPC analysis. A sample of the starting batch (cycle 0^{th}) was evaluated to ensure no degradation byproducts were caused by the preparation procedure. The HPLC did not detect any trace of biuret and/or cyanuric acid in the starting material.

The sample submitted to thermal cycling was also evaluated after the measurements were finished. In this case, the presence of 0.4 % (w/w) biuret was detected in the sample. The formation of this minor amount of biuret was not sufficient to affect the thermal behavior of the sample during thermal cycling, as discussed during the previous section. However, this detection could suggest the starting point of a thermal degradation process. Further research

should be performed to study the evolution of the formation of byproducts during longer periods of use.

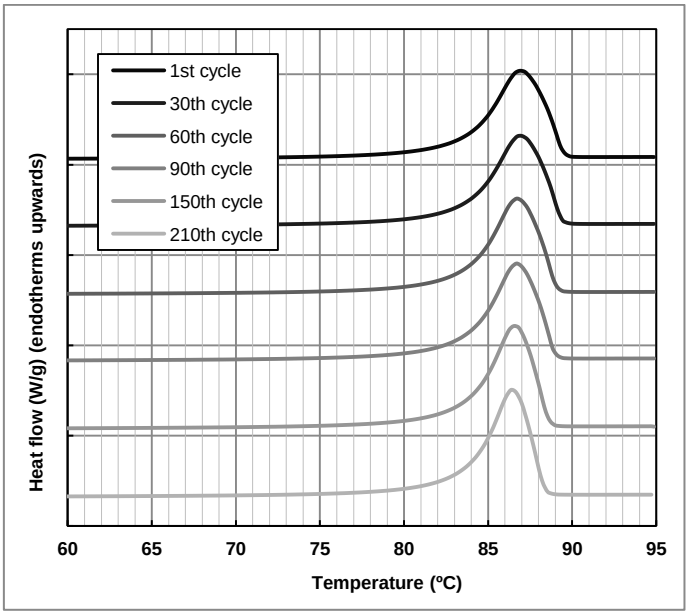

Figure 3-18: Evolution of the melting DSC thermograms relative to the thermal cycles performed

3.4.3. Comparison of the thermal cycling behavior of the eutectic composition and pure urea

The degradation of pure urea in the liquid state above 133 °C is well known. Nevertheless, the melting point of a eutectic mixture where urea is one eutectic phase is lower than the melting point of the pure compound. Because any thermal degradation is a kinetic-driven process, it can be expected to be influenced by the absolute temperature. Thus, the degradation of urea above the melting point of the eutectic mixture herein proposed (85 °C) would be expected to be lower than its degradation at 133 °C. However, it could also occur that the state of aggregation has also influence on the degradation. If this is the case, then the degradation of urea in the liquid state within a eutectic mixture would also be significant even at temperatures lower than 133 °C, and thus, its use in a eutectic mixture would not enhance its thermal reliability. This possibility was suggested by [70].

To evaluate this situation, the melting temperature and enthalpy results of the sodium nitrate-urea eutectic mixture attained during the thermal cycling test were compared with those of pure urea, in order to determine the relevance/irrelevance of the state of aggregation of urea on its degradation. To ensure that the experiments were as comparable as possible, the maximum temperatures of the thermal cycles were defined to reach a maximum temperature

that was approximately 10 °C above the melting temperature (95 °C for the eutectic mixture; 140 °C for the pure urea measurements). The time at the maximum temperature of each cycle was 5 min for both cases. The results are shown in Figure 3-19.

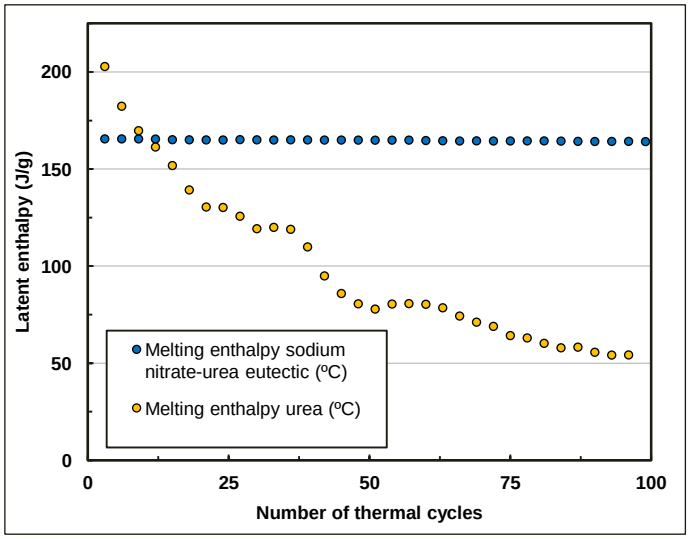

Figure 3-19: Melting enthalpy of the sodium nitrate-urea eutectic composition and of the pure urea during thermal cycling

As observed, the evolution of the pure urea melting enthalpy and the melting enthalpy of the mixture showed completely different patterns. As commented in the previous section, the eutectic mixture maintained its melting behavior constant during the test. In contrast, pure urea showed a clear decreasing trend starting from the beginning of the thermal cycling process, and its initial enthalpy of 243 J/g decreased to 50 J/g after 100 cycles. This decrease represents a reduction of the 79 % of the original latent melting enthalpy.

Moreover, the shape of the thermograms varied noticeably. With the increasing number of cycles, the main melting peak was displaced to lower temperatures. In addition, new endothermic peaks appeared at lower temperatures. From these results, it was concluded that the thermal degradation of liquid urea is greatly dependent on the temperature. This observation supports the possibility for its use as a component of eutectic PCMs that operate at maximum temperatures lower than 133 °C. The implications of this observation are commented in the following section together with the results presented during this chapter and suggestions for future works.

3.4.4. Conclusions related to the thermal stability of the sodium nitrate-urea eutectic mixture and further works

The results presented throughout Section 3.4 demonstrate that the thermal properties of the eutectic mixture during the accelerated thermal cycling test remained stable and displayed negligible changes. Moreover, it was shown that the thermal behavior of the eutectic mixture along the working temperature range is clearly improved in relation to that of the pure urea near its melting temperature. These outcomes, together with the suitable thermal and economical properties presented in Section 3.2, led to conclude that the eutectic material proposed has potential for use as a PCM. Therefore, further investigations on this eutectic material are encouraged to assess the thermal stability of the material for longer periods of use. Future research could be also performed to investigate the thermal behavior of eutectic mixtures of urea with other compounds that render melting temperatures within the application intended.

In future works on the thermal stability, however, it is important to remark that investigation should not rely exclusively on accelerated thermal cycling measurements. The accelerated thermal cycling test by DSC was found suitable for this initial stage of research because it is a quick and straightforward methodology for PCMs. However, because the thermal degradation of urea is driven by its reaction kinetics, the time that the material remains at the maximum operation temperatures can noticeably affect the results. During an accelerated cycling test, the permanence at high temperature is short for each cycle (on the order of minutes), whereas under actual operating conditions, this time would last for several hours. Therefore, even if an accelerated thermal cycling measurement of 5000 cycles is performed, the results could not be extrapolated to 5000 cycles in an actual application.

A methodology suitable for establishing the degradation kinetics of the eutectic mixture is required to predict its long-term behavior under the maximum operating temperature. This procedure should combine not only calorimetric evaluation methods but also complementary techniques that allow assessment of the structural changes that take place during the degradation process, such as HLPC, XRD, FTIR (Fourier Transform Infrared Spectroscopy) or others. Moreover, the conditions of the test (sample size, closed environment, etc.) should be representative of actual LHTES systems. This type of research is necessary before the material

can be validated for use as PCM for long-term applications, where it must endure several years of actual operating conditions in a real LHTES system.

4. Conclusions of the chapter and further work

The binary system composed of sodium nitrate and urea was studied for thermal energy storage systems in heating and DHW applications. The main conclusions are summarized next.

The solid–liquid equilibrium of the system was determined using three complementary techniques: the synthetic visual method, DSC and XRD. The experimental results showed a eutectic phase diagram, with negligible solid miscibility along the whole composition range. The eutectic composition was formed by 71.25 % (w/w) urea and 28.75 % (w/w) sodium nitrate and melted at 85.0 °C. This was the composition selected as a PCM.

The XRD results showed the presence of a new metastable phase for compositions rich in sodium nitrate that was formed depending on the crystallization conditions. No successful pattern identification was found in the PDF database. After thermal treatment, this new phase disappeared, thus confirming its non-equilibrium nature. This potential metastable phase or compound did not have influence in the application of the eutectic composition as a PCM.

The composition proposed as a PCM was studied in detail using DSC. The density of the material was also measured. The results rendered a volumetric energy density of 245 MJ/m3. This value is close to the storage capacities of stearic or palmitic acid and is larger than the values for paraffins in the temperature level considered. The market price of the proposed eutectic material is 0.9 €/kg, which is competitive. According to the energy storage capacity, melting temperature and price, the PCM studied is suitable for TES applications at the intended temperature level.

To complement the results, the influence of the water uptake was studied. Coupled TGA/DSC results showed that *hydrated* samples, prepared under a 55 % RH, presented a thermal behavior clearly different from that of *dry* samples, prepared under an atmosphere of 4 % RH. The XRD results suggested that the water presence in the *hydrated* sample forms a new unidentified compound in the system, which coexists with the phases of the pure urea and sodium nitrate to form a ternary mixture. These remarks should be taken into consideration in a further production process of the material.

The thermal stability of the eutectic mixture was evaluated using an accelerated thermal cycling test that comprised 210 thermal cycles. Under the experimental conditions applied, the melting enthalpy of the mixture underwent a minor reduction, while the crystallization enthalpy maintained a stable trend. Negligible changes were noted for the melting and crystallization onset temperatures. The shape of the DSC thermograms during the test revealed no signals of new transitions or peaks, although a minor decrease in the melting endset temperature was observed.

The presence of degradation byproducts was assessed using HLPC analysis. Traces of biuret and cyanuric acid were monitored. The results showed a quantity of 0.4 % (w/w) of biuret after the 210 thermal cycles. This amount is not relevant, although it could denote signs of the start of a potential degradation process.

The thermal cycling behavior of the eutectic material was compared with that of the pure urea at a maximum temperature 10 °C above both of their respective melting temperatures. After 100 cycles, pure urea showed a great reduction of its original latent melting enthalpy. Moreover, the shape of the thermograms varied noticeably, displaying new endothermic peaks at lower temperatures. It was concluded that the thermal stability of the proposed eutectic PCM at its potential operation range (below 90 °C) is clearly improved relative to that of the pure urea at its melting temperature (133 °C).

As a main conclusion, the sodium nitrate-urea eutectic mixture proposed shows potential for use as a PCM for LHTES systems at the heating and DHW temperature range. Further research is required to evaluate the thermal stability of the mixture for long periods of use and under conditions representative of actual applications.

CHAPTER 4: The erythritol-urea eutectic mixture as a PCM for heating and DHW LHTES systems

Article: Determination of the phase diagram and main thermophysical properties of the erythritol–urea eutectic mixture for its use as a phase change material.

Authors: G. Diarce, L. Quant, Á. Campos–Celador, J.M. Sala, A. García–Romero.

Journal: Solar Energy Materials and Solar Cells.

Year of Publication: 2016

ABSTRACT

This chapter deals with the study of the binary system comprised by erythritol and urea. It is the last chapter of the thesis related to the development of new PCMs for heating and DHW applications.

A sequential methodology was employed to evaluate the suitability of the mixture as a PCM. First, a preliminary evaluation was performed by means of the modeling of the phase diagram and by hot–stage microscopy. Afterwards, the results were refined with more precise techniques, such as DSC, the synthetic visual method and XRD.

The results showed a eutectic composition with a melting temperature of 81.13 ºC and a latent melting enthalpy of 248 J/g. The density of the eutectic composition was measured at different temperatures in order to establish the volumetric storage capacity. The properties are suitable for the aimed applications. The current market price of the mixture is nearby 2.4 €/kg, which can be regarded as reasonable. However, complex crystallization behavior was noticed. A preliminary accelerated thermal cycling test was also performed.

According to the results, the eutectic mixture formed by erythritol and urea can be a good candidate for use as a PCM in medium temperature range applications. Further research is required to evaluate the stability of the mixture on longer periods of use. The methodology employed has proven to be adequate for the development of new eutectic PCMs.

1. Introduction

As stated in previous chapters, the cost of PCMs is still hindering the ultimate expansion of commercial LHTES systems [26]. As demonstrated in Chapter 3, urea can be considered as a potential low–cost PCM candidate when forming part of eutectic systems that work at temperatures below its melting temperature (134 °C). This allows reducing its thermal degradation upon heating [63], thus increasing its life span. Nonetheless, the number of articles dealing with urea based eutectic mixtures for TES purposes is scarce [71].

Erythritol can be considered a feasible candidate to form a binary eutectic system with urea. Erythritol, a widespread material with a melting temperature of 119 °C, a noticeably high melting enthalpy of 340 J/g and a current market price nearby 3.7 €/ kg [25] was already studied in Chapter 2. As mentioned there, this material has recently arisen a notable interest as a PCM due to its large phase change enthalpy, as it can be extracted from the numerous articles published during the latest years [92–95]. However, to the best knowledge of the author, the analysis of the phase equilibrium of the binary system formed by erythritol and urea was exclusively carried out by ref. [96] back in 1932. No further related research have been found in the literature.

According to [96], the phase diagram corresponds to a simple eutectic system with a eutectic melting temperature of 78 °C. However, the rest of the key properties for the use of the mixture as a PCM, like the melting enthalpy or the stability against thermal cycling, remain unknown. Besides, the phase diagram was determined upon cooling and, as cited in the literature [49,88] and shown in Chapter 2, erythritol shows polymorphism and a noticeable supercooling. Thus, these metastable effects could have influenced the results. It is therefore necessary to determine the phase diagram upon heating in order to confirm or modify the previously reported results. According to these conditions, three main objectives are sought in the present chapter:

- The first objective aims to determine the phase diagram of the mixture formed by erythritol and urea upon heating in order to confirm whether they form a eutectic composition with a melting point suitable for the space heating and DHW temperature range. Additional aspects affecting the phase diagram, such as the polymorphism of

erythritol and others will be also investigated and discussed, as they can influence the use of the potential eutectic mixture as a PCM

- The second objective is to evaluate the suitability of the eutectic composition as a PCM. The phase change enthalpy and the specific weight of the material have been established in order to calculate its volumetric storage capacity. A preliminary thermal cycling test was performed to compare the thermal stability of the eutectic mixture with that of the pure urea. This is a key feature, because urea degrades when it is heated above its melting temperature.

  Based on all these properties, the suitability of the mixture is discussed and compared with other PCMs available in the literature. Note that the thermal conductivity, although a relevant property for any PCM [36], is considered out of the scope of the research at the present stage
- The last objective of the chapter is to gain knowledge on the systematic determination of phase diagrams and the thermophysical properties of PCMs through complementary techniques. The need to develop suitable PCM characterization methods has been highlighted in several recent articles [79,87,97,98]. As a result, a sequential methodology was employed in this work to evaluate the suitability of the mixture as a PCM.

  This procedure started using fast techniques to achieve an initial an initial estimation of the potential of the eutectic composition as a PCM. It was done by means of numerical modeling of the phase diagram and by hot–stage microscopy. The latter is carried out by the use of an experimental technique called contact preparation method, typically employed in the field of pharmacology [43]. The obtained results are then refined with more precise techniques, such as DSC, the synthetic visual method [99] and XRD. In addition to reporting the results of the study performed with the erythritol–urea system, this chapter aims at offering detailed information of the methodology employed

It is worth noting that the erythritol-urea system was the last binary mixture studied during this PhD thesis and thus, the methodology employed gathers all the knowledge gained along the study of the previous binary systems presented in Chapters 2 and 3. This is the reason why the emphasis on the characterization techniques is included on this chapter and not on the previous ones.

2. Experimental methods and theoretical considerations

First in this section, the materials employed and their main thermal characteristics are presented in Section 2.1. The general specifications of DSC measurements are presented in Section 2.2. Each experimental methodology employed is presented starting from Section 2.3. They will be described in detail, and following the same sequence employed in the sequential process formerly described.

2.1. Materials employed and their thermal properties

In order to promote the reproducibility of the results and to avoid uncertainties derived from impurities, analytical grade materials were employed. Table 4-1 gathers their most important characteristics. The thermal properties included in that table were measured via DSC.

Compound	Supplier (analytical grade)	Purity	Melting onset temperature (ºC) [a]	Latent melting enthalpy (kJ/kg) [a]	Molar mass (g/mole)	Market price (€/kg) [b]
Erythritol	Alfa Aesar	99 %	118.7	333.7	122.11	3.7
Urea	Panreac	99 %	133.3	243.7	60.06	0.7

Table 4-1: Properties of the raw materials employed in the study.
[a] Measured by the author by means of DSC.
[b] Market price for bulk technical grade materials obtained from [25] (erythritol) and [64] (urea), not for the reagents used in the study.

2.2. Differential scanning calorimetry (DSC)

DSC was used to determine the following features required in this chapter:

- The thermal properties of the raw materials (melting temperature and enthalpy)
- The thermograms of the mixtures evaluated in the erythritol–urea system (which enabled the determination of the solidus line of the phase diagram and the Tammann plot)
- The melting temperature and enthalpy of the eutectic composition found
- The accelerated thermal cycling test of the materials

The common specifications of the DSC employed and the calibration used are those detailed in Chapter 3 - Section 2.2. The procedures for the sample preparation and temperature programs applied for each specific test performed will be explained in the subsequent Sections 2.5.1 and 2.8 of the present chapter.

2.3. Modeling of the phase diagrams. Theory and calculations

To model the phase diagram of the mixture, the approach based on the Gibbs excess energy presented in Chapter 2 – Section 2.6 was applied. The Schoeder–Van Laar equation (Eq. 2-1) was employed to calculate the temperature–composition phase diagrams of the systems. The detailed explanation of the theory behind the model can be found in Appendix A, or consulted in [44].

In Chapter 2, the Modified UNIFAC method [45] was employed to evaluate the activity coefficients of the liquid phases (γ^{l}). However, this approach was found unsuitable for the present case because none of the structural groups available made possible to form urea from the sum of smaller group contributions. As a consequence, it was opted to use the Pharma Modified UNIFAC [100]. The equations involved are the same than those employed for the Modified UNIFAC, but the values of the parameters used are different. These values are provided in ref. [101], along with a detailed description of the theory behind the model.

The Pharma Modified UNIFAC model includes urea amongst its structural groups [100], but its interaction parameters with alkanes and/or with alcohols have not been yet published. A suitable alternative approach comprised the modeling of urea as a combination of acetamide and a NH_2 group.

The parameters for acetamide (main group 40, subgroup 101 [100]) are available in the literature, but the parameters for the NH_2 group are not. Therefore, the parameters of the CH_2 group (main group 1, subgroup 2 [100]) were used instead. This assumption was considered suitable bearing into mind the similar size and structure of both NH_2 and CH_2 functional groups, and that the main objective of the simulation was to obtain a preliminary estimation of the composition and temperature of the eutectic mixture. In addition, the system was modeled assuming to form an ideal mixture. For the latter approach, the activity coefficients equal unity [44].

2.4. Evaluation of the phase diagram by hot–stage polarized microscopy (polarized thermomicroscopy)

The second step in the procedure was an evaluation by means of hot–stage polarized microscopy [43]. This technique is widely used to investigate the melting and crystallization behavior of pharmacological compounds and polymers. It has also been employed for the

determination of phase diagrams in varied chemical applications, like industrial separation and purification processes. However, it has been rarely used to determine properties of materials for thermal energy storage purposes (see [88,102] as examples). The hot–stage apparatus employed in this chapter was the same presented in Chapter 2 - Section 2.4.

A specific method to prepare and evaluate the samples, known as the contact method preparation, was applied. No article using this procedure for the determination of new eutectic PCMs has been found in the literature; therefore, a detailed explanation of the procedure is provided next. A comprehensive description of this preparation technique can be also found in ref. [103].

2.4.1. The contact method preparation

This method is suitable to determine the type of phase diagram formed by two compounds by performing one single experiment [103]. The experimental procedure starts placing a cover slip onto a glass slide. Some crystals of the compound with the highest melting temperature (urea in this case) are placed on the glass slide at one edge of the cover slip (right side, for example). The slide is then heated up until the crystals melt and the liquid is drawn by capillarity into the space between the slide and the cover slip. The amount of substance has to be enough to fill in about the half of the cover slip. The slide is then cooled down until the material solidifies.

Then, some crystals of the low temperature compound (erythritol in this case) are placed on the opposite edge of the cover slip (left side, in this case). The slide is again heated to melt the second compound and spread it until the liquid fills in the remaining space below the cover slip. In the contact zone, the liquid component will dissolve a part of the solid component, thus forming a mixing zone. The solidification is then promoted by cooling the slide down. At that point, the sample is ready to be evaluated.

The particular feature of the so prepared sample is that the mixing zone contains all the mixtures represented on the phase diagram, graded from one edge of the cover slip to the opposite one. Therefore, the type of phase diagram formed by the two original compounds can be recognized by observing the processes occurring in this area. To do so, the sample is gradually heated up on the hot–stage, while its evolution is monitored by means of an optical microscope. As illustrative examples, the expected behavior of 3 theoretical types of binary

systems formed by two generic compounds (A and B) are detailed next, accompanied by Figure 4-1 [103] .

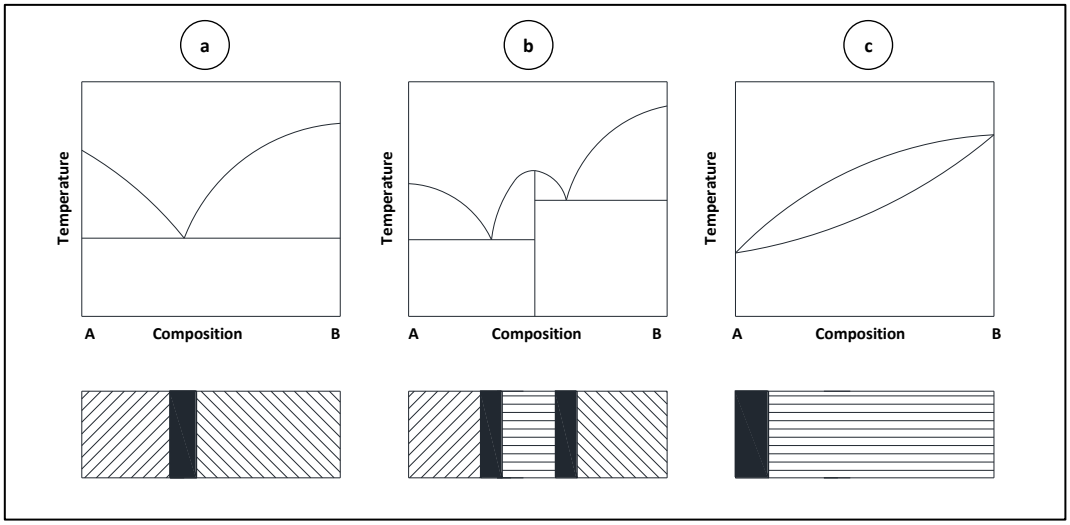

Figure 4-1: Different examples of theoretical binary phase diagrams (above) and their corresponding expected result for samples prepared by the contact method (below): (a) simple eutectic, (b) eutectic system with compound formation and (c) isomorphous system

When the materials form a simple eutectic system (Figure 4-1 (a)), melting will first take place at the eutectic temperature in the mixing zone. This melting will result into a unique stripe that will be seen black under the polarized light of the microscope, due to the amorphous (liquid) nature of the melt. The crystals of the pure materials will remain in the visual field at both sides of that black stripe. The eutectic temperature will be identified as the temperature where the continuous dark stripe appears in the field.

No additional significant transitions will be observed as the temperature is further raised, except that the black area will grow in size, until the temperature reaches the melting point of the compound with the lowest melting temperature. At that point, the part of the visual field occupied by that compound will become dark. Finally, the whole sample will turn into dark when the temperature of the hot–stage attains the melting temperature of the remaining compound.

In Figure 4-1 (b), a eutectic system involving addition compound formation with congruent melting behavior is shown. In this case, when the sample is heated on the hot–stage, a first dark stripe will appear at the lowest eutectic temperature. While the temperature is increased, an additional vertical stripe will appear on a different place, which will correspond to the second (higher temperature) eutectic system. The crystals of the congruent melting compound

will remain between both vertical dark stripes, and they will melt when the hot–stage reaches the melting temperature of this compound. Eventually, each pure component of the sample will correspondingly become dark when the respective melting points are attained.

The last case shown in the illustration (Figure 4-1 (c)) corresponds to an isomorphous system, where complete miscibility in the solid state occurs. In this kind of phase diagram, the first black stripe will be observed when the temperature of the hot–stage reaches the melting point of the pure compound with the lowest melting temperature. This vertical stripe will form on one of the extremes of the visual field. As the temperature is gradually increased, the black portion will be extended steadily towards the space occupied by the rest of the sample. The sample will become completely dark when the melting temperature of the remaining pure compound is reached.

2.5. Experimental determination of the phase diagram by thermal analysis methods

On the preliminary evaluation, comprised by the modeling of the phase diagram and its analysis by the contact method preparation, it was confirmed that the mixture involved formed a simple eutectic phase diagram with a melting temperature suitable for the objective aimed (as will be shown in Section 3.1.2). As a result, an accurate determination of the phase diagram was required.

For that purpose, DSC measurements were performed in order to extract information from the outline of thermograms of samples with different compositions. This served to construct the Tammann plot [82] that allowed determining the precise eutectic composition of the system and to establish the corresponding solidus (eutectic) temperature. Additionally, the liquidus line was established by the so-called synthetic visual method. Theoretical remarks and details of these techniques, as well as the performed experiments, are given next.

2.5.1. Assessment of the shape of the thermograms, determination of the solidus line of the system and Tammann plot of the mixture

In order to define the experimental conditions for the DSC experiments carried out to obtain the thermograms for different compositions, two important constraints inherent to the materials were considered.

The first constraint was the polymorphism exhibited by erythritol, which can crystallize to two crystal structures, Form I and Form II (see Chapter 2 or refs. [49,88]). Form I is the equilibrium structure, which melts at 119 °C, while Form II is a metastable structure that melts at 104 °C. Upon cooling, erythritol tends to crystallize to the metastable polymorph, Form II. However, according to the literature [49], if the material is quenched down to a temperature below its glass transition (-44 °C), when the sample is subsequently heated up, crystallization of Form I can be achieved [13].

The second constraint was the thermal degradation of urea at high temperature. Commonly, the procedure to study a phase diagram by means of DSC involves the complete melting and solidification of each sample before the measurements are performed. However, this could cause partial thermal degradation of urea and therefore affect the results. Thus, based on the HPLC results attained in Chapter 3 [99,104], it was decided to pre–melt the samples to a temperature above the eutectic and below 115 °C. This guaranteed that for every composition prepared, the sample became to a semisolid state where (at least) the eutectic portion of the sample was melted.

This procedure does not ensure the total miscibility of the sample, and thus it is only suitable to establish the solidus line of the phase diagram and to produce the Tammann plot of a simple eutectic type phase diagram. This fact was confirmed by the hot-stage microscopy results (Section 3.1.2), whose samples were prepared by a method that guaranteed complete miscibility (see Section 2.5.2). Thus, it can be ensured that the method employed to prepare the DSC samples was valid for the objectives sought.

Taking into account these two constraints, the DSC samples were prepared following the next procedure. Batches of approximately 2 g were produced first, with compositions separated by an approximate 0.1 mass ratio in order to cover the entire compositional range of the phase diagram. To prepare each batch, the pure compounds were weighted (Ohaus Discovery scale, ± 0.02 mg accuracy) according to the desired composition, and placed into a glass vial. The vial

[13] The author is aware that this behaviour can be a drawback for the application of the material as a PCM, however the potential solutions will be the subject of future research works in the case that the material shown sufficiently suitable features for its use as a PCM

was subsequently hermetically closed, and immersed into a stirred glycerin bath at 90 °C (temperature controlled by a Pt–1000 probe) for 25 min.

At this temperature, the samples were formed by a liquid part and a solid portion (or fully liquid on those compositions with liquidus temperature below 90 °C). The vial was extracted from the bath and left to cool down under the room environment, while stirring with a spatula. When the material reached ambient temperature, the bulk sample was removed from the vial and gently ground for 5 minutes by mortar and pestle. This process caused the crystallization of the erythritol portion of the batch to Form I, and homogenized the product. To prepare each DSC sample, around 10 mg of material were weighted (± 0.02 mg) and placed in a crucible. The DSC temperature program used is schematically depicted in Figure 4-2.

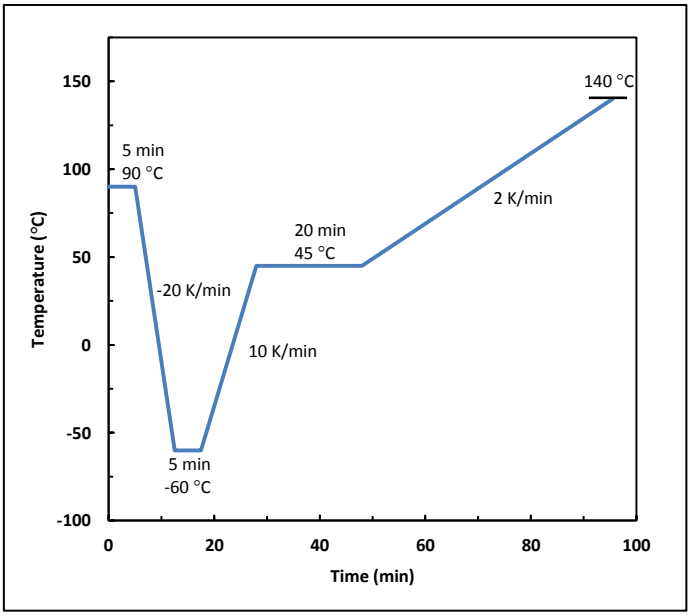

Figure 4-2: Heating program employed for the DSC measurements performed to study the phase diagram

The program started with a prior melting of the eutectic part of the sample at 90 °C for 5 min, in order to achieve a good contact between the sample and the crucible (at this temperature all the samples will have a significant liquid percentage, then ensuring good contact between the crucible and the material under study). The following quick cooling ramp to -60 °C led to the glass formation on the erythritol, instead of crystallization.

After 5 minutes at -60 °C, the sample was heated until 45 °C and maintained at this temperature for 20 min. This long soaking stage had the purpose to promote the crystallization of erythritol Form I, aided by the presence of the remaining seeds that did not melt at 90 °C.

Finally, the sample was heated from 45 to 140 °C at 2 K/min. This was the segment used for the analysis of the thermograms.

The heating rate employed in the last part ensured a good sensitivity to determine the heat flow of the DSC while it was slow enough to discriminate the two characteristic peaks obtained on the thermograms of the mixtures corresponding to non–eutectic compositions of binary eutectic systems [88]. Each measurement was duplicated (two fresh samples of each composition were measured following the same conditions) to assure reproducibility.

To establish the eutectic composition of the phase diagram, a Tammann plot of the system was constructed [82]. This method was already detailed in Chapter 3 - Section 2.5.2 and consists of representing the enthalpy associated with the eutectic phase change for different compositions of a binary system. In the present work, to evaluate the eutectic melting enthalpy for each composition, the melting enthalpy of the first peak of each thermogram was calculated by the integration of the heat flow signal, as detailed in Section 2.2.

2.5.2. The synthetic visual method

In order to establish the liquidus line of the system, the so–called synthetic visual method [80,81] was used. The self–tailored experimental assembly detailed in Chapter 3 - Section 2.5.1 was used for the present chapter. More details can be also found in ref. [99].

Due to the thermal degradation underwent by the urea, only the portion of the phase diagram where the liquidus line remains below 115 °C was studied [99]. Accordingly, the compositions assessed ranged from 30.0 to 85.0 % (w/w) erythritol. Eleven different compositions were evaluated within this range. The total sample mass employed for each measurement was around 15 g. The heating rate selected for the dynamic heating ramp was 0.01 K/min, defined according to the procedure presented in Chapter 3 - Section 2.5.1 in order to guarantee that the quasi–static equilibrium conditions were met.

2.6. X-ray diffraction (XRD) measurements

In order to complement the thermal analysis with the study of the solid crystalline phases present in the mixture, XRD measurements at ambient temperature were performed. The diffraction patterns were collected by a Philips X'pert Pro automatic diffractometer, using the configuration presented in Chapter 3 - Section 2.5.2.1.

A sample formed by 54.9 % (w/w) erythritol and 45.1 % (w/w) urea was assessed. This was the eutectic composition found, as it will be shown in Section 3.1.4. The samples were extracted from the batches prepared for DSC measurements described in Section 2.5.1.

The identification of the solid phases present in the mixture was performed using the Powder Diffraction File (PDF) database. The PANalytical X´Pert High Score program was used for identification and Miller indexing of all observed maxima.

2.7. Determination of the specific weight of the eutectic composition

With the aim of establishing the volumetric energy density of the eutectic PCM proposed, the specific weight (density) of the eutectic mixture was established. The composition selected was 54.9 % (w/w) erythritol and 45.1 % (w/w) urea (see Section 3.1.4). Its density was determined in the solid phase at 25 °C, and in the liquid phase at 95, 100 and 105 °C. All the measurements were duplicated to assure reproducibility.

Both determinations (specific weight of a solid and specific weight of a liquid) were based on the Archimedes principle. The Sartorius YDK01LP density determination kit presented in Chapter 3 - Section 2.7 was used for that aim. More details of both the specific procedure and the experimental set–up can be found in that Chapter 3 and in ref. [99].

2.8. Accelerated thermal cycling measurements by DSC

In order to evaluate the thermal degradation of the mixture, an accelerated thermal cycling test was performed by means of DSC. The eutectic composition (54.9 % (w/w) erythritol and 45.1 % (w/w) urea) was evaluated, and the results were compared with those of pure urea already shown in Chapter 3 - Section 3.4.3.

For the eutectic mixture, the temperature program executed at each cycle is shown in Figure 4-3. The maximum temperature of the thermal cycling program for the eutectic mixture (90 °C) was defined bearing into mind the operation conditions of a potential LHTES system where the PCM would be used [21]. The cooling rate and the minimum temperature of the cycles were defined considering that erythritol shows polymorphism. The use of a method that promoted the crystallization of Form I of erythritol within the mixture was used, as detailed in Section 2.5.1.

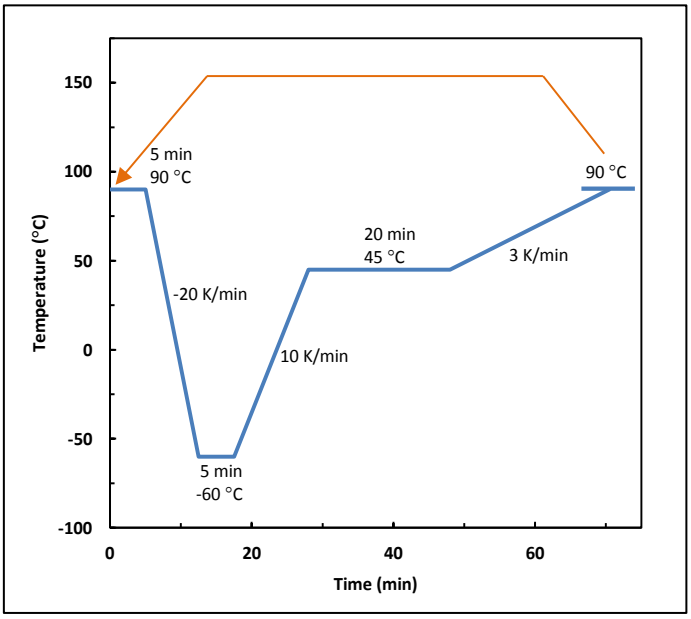

Figure 4-3: Temperature profile of each cycle repeated on the DSC to study the thermal degradation of the eutectic composition

The tests for each material were comprised by 85 melting and solidification cycles. This was considered suitable to cope with the purpose of comparing the behavior of the eutectic mixture with that of the pure urea (as will be shown in the results section).

3. Results and discussion

3.1. Experimental determination of the phase diagram of the mixture

The results will be presented and discussed following the afore-presented methodology, starting from the preliminary methods for a fast initial estimation of the phase diagram of the system, to more complex techniques to refine the results.

3.1.1. Theoretical prediction of phase diagrams by thermodynamic modeling

The phase diagram of the system was calculated using the model explained in Section 2.3. The activity coefficients were obtained by assuming an ideal mixture and by the Pharma UNIFAC approach. The results of the calculated phase diagrams are displayed in Figure 4-4, along with the experimental results obtained.

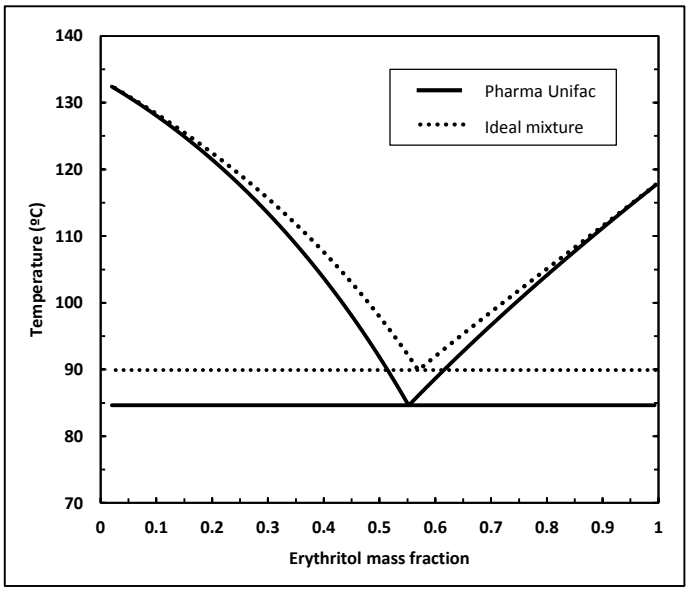

Figure 4-4: Phase diagram of the erythritol–urea system predicted by means of the activity coefficients calculated with the Pharma UNIFAC approach and with the ideal mixture approach, and experimental results for the liquidus and solidus temperatures of the phase diagram obtained by the synthetic visual method and DSC, respectively

As it can be seen, the results for the Pharma UNIFAC approach rendered a calculated phase diagram with a eutectic temperature at 85 °C and a eutectic composition formed by 55.2 % (w/w) erythritol and 44.8 % (w/w) urea. The results for the ideal modeling approach showed a eutectic melting temperature of 90 °C and a eutectic composition formed by 57.1 % (w/w) erythritol and 42.9 % (w/w) urea.

According to these results, the melting temperature of the eutectic composition potentially formed would be within the range required for the intended applications [21]. This was confirmed by the results attained by the contact preparation method, as detailed next. The comparison between the modeled phase diagram and the experimental results will be discussed in Section 3.1.6.

3.1.2. Preliminary evaluation of the erythritol–urea system by hot stage microscopy

To confirm the results obtained by modeling, the contact method was employed. The results are shown in Figure 4-5.

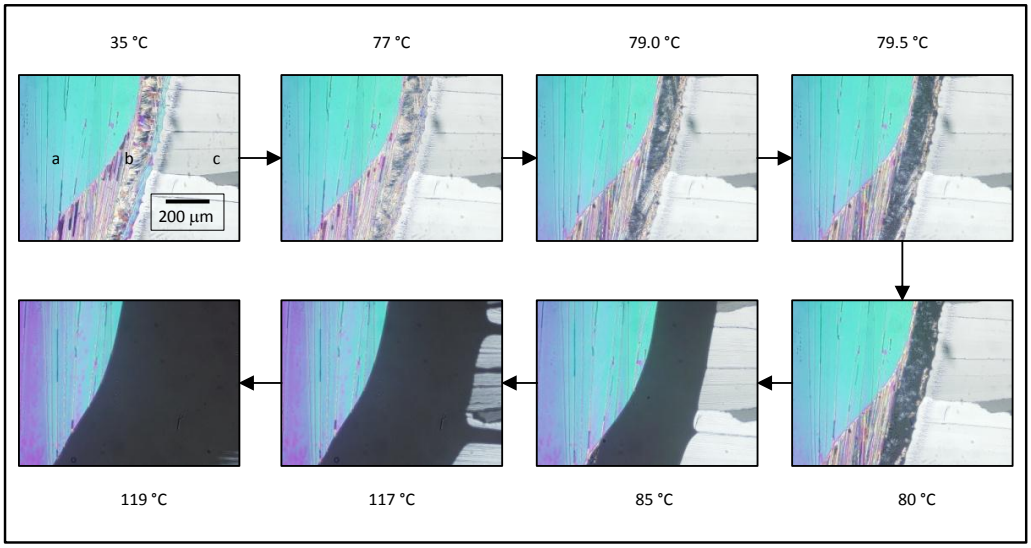

Figure 4-5: Micrographs showing the phase diagram evolution by hot–stage microscopy using the contact method preparation

On the upper left corner of Figure 4-5, the micrograph of the sample at 35 °C is depicted. At that temperature, the whole sample was in the solid state. Three different zones can be distinguished: on the left hand, marked by the letter *a*, pure urea is found; on the right hand, denoted by *c*, pure erythritol is placed and, finally, on the middle of the image, distinguished by *b*, the mixing zone is located. As it can be observed, this mixing zone remained completely solid until a temperature of approximately 79 °C was attained.

At that point, the mixing zone started to melt and a clear dark stripe was formed on the image. When the sample reached 85 °C, the mixing zone disappeared completely, and only pure erythritol and urea remained in the system. The sample maintained its shape until the temperature approached the melting temperature of the pure erythritol, 118 °C. When the sample reached 119 °C, the portion occupied originally by this material became dark; meaning is complete melting. Finally (although not depicted in the Figure), above 133 °C, the lasting portion of urea disappeared from the visual field.

According to the theory behind the contact method preparation [103], the presence of a unique mixing zone between the two pure compounds, and its melting at a clear unique temperature, suggest that the binary system formed by erythritol and urea is a eutectic type. From the results attained, it was concluded that the mixture showed a melting eutectic temperature suitable for medium temperature TES. The estimated eutectic temperature,

between 79 and 85 °C, agreed with the melting temperature calculated through modeling (Section 3.4).

Note that these measurements did not aim to obtain an accurate eutectic transition temperature. This was performed through the precise determination of the phase diagram, as shown next.

3.1.3. Results of the solidus and liquidus lines of the phase diagram

DSC was employed to gain additional knowledge about the solidus line involved. The different thermograms obtained are shown in Figure 4-6. Every thermogram evaluated presented two endothermic peaks. The first one occurred at a fixed temperature for every composition (around 81 °C, as specified in the following paragraph).

As explained in Chapter 2, this pattern can be attributed to a presence of an invariant phase transition, i.e. a eutectic point [47,82,88]. The temperature of the second peak varied with the composition: as the composition approached 100 % of one component, the second peak became larger, and its peak temperature approached that of the pure component. This behavior can be attributed to the solution of the remaining solid component in the melt. The shapes of the thermograms obtained suggest that the phase diagram involved is a eutectic type.

The solidus temperature for each composition was determined from the melting onset temperatures of the thermograms shown in Figure 4-6. An average value of 81.13 °C was attained, while the minimum and the maximum melting onset temperatures were 80.8 and 81.4 °C, respectively. The results for each solidus temperature can be visualized in Figure 4-7. They are also provided numerically in Table 4-2.

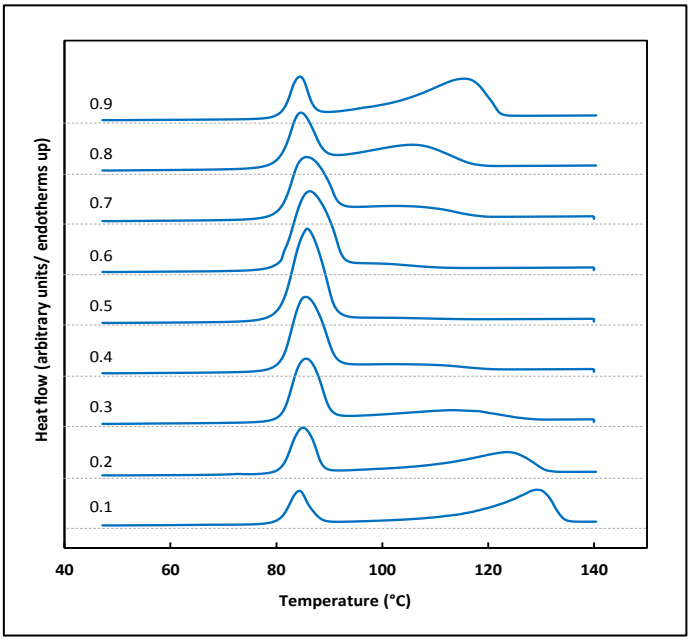

Figure 4-6: DSC thermograms obtained for the erythritol–urea system; mass ratios referred to erythritol are presented numerically next to each thermogram

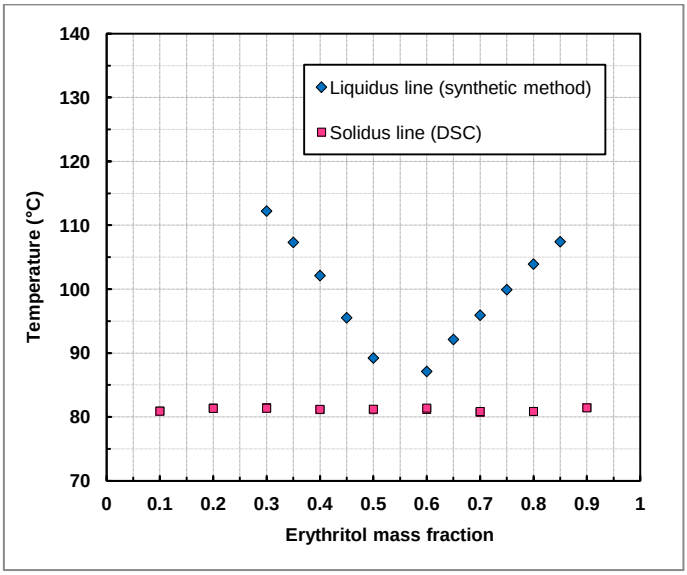

Figure 4-7: Experimental results for the liquidus and solidus temperatures of the phase diagram obtained by the synthetic visual method and DSC, respectively

In Figure 4-7 and Table 4-2 the results for the liquidus temperature of the system obtained by the synthetic visual method are represented as well. Note that the results for the liquidus line of the system could have also been obtained by the DSC thermograms, as explained in [88]; however, the synthetic visual method is a method more reliable for that purpose; thus, only the results obtained by means of it were taken into account in the present chapter.

Erythritol mass fraction	Liquidus temperature (ºC)	Eutectic temperature (ºC)
0.10	_	80.9
0.20	_	81.3
0.30	112.2	81.4
0.35	107.3	_
0.40	102.1	81.2
0.45	95.5	_
0.50	89.2	81.2
0.60	87.1	81.3
0.65	92.1	_
0.70	95.9	80.8
0.75	99.9	_
0.80	103.9	80.8
0.85	107.4	_
0.90	_	81.4

Table 4-2: Experimental results obtained for the liquidus and solidus temperatures of the erythritol-urea system

Based on the shape obtained for the liquidus line of the phase diagram and the solidus line established by DSC, a eutectic composition placed between 50 % and 60 % (w/w) erythritol was inferred. However, these results were not sufficient to establish precisely the eutectic composition. Notice that, as the sample composition approached the eutectic composition, the semi–solid interval becomes smaller and, under these circumstances the measurements with the synthetic visual method are difficult. A good approximation of the eutectic composition could have been obtained by means of a manual extrapolation of the results, i.e.: joining the points by hand; however this approach would have not been based on any physical meaning. Therefore, a Tammann plot was constructed to determine the specific eutectic composition of the eutectic mixture. The results are discussed next.

3.1.4. Determination of the Tammann plot of the system

To build the Tammann plot, the eutectic melting enthalpy for each sample was determined by the integration of the heat flow signal of the first endothermic peaks shown in Figure 4-6. Each result was then represented as a function of its composition. The resulting plot is shown in Figure 4-8.

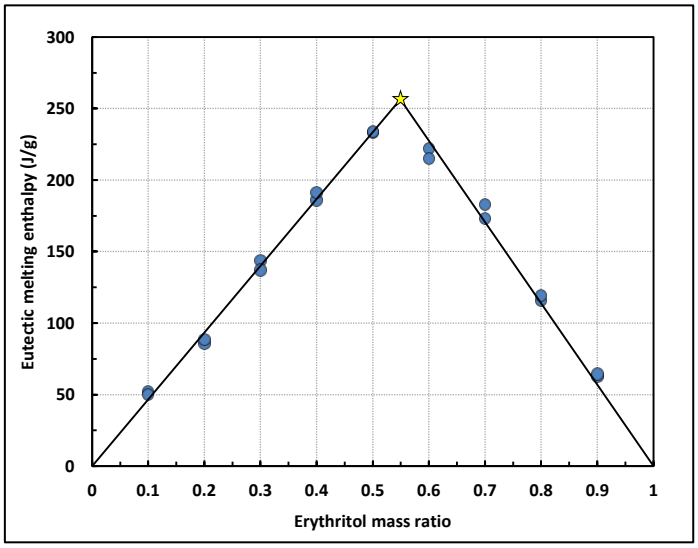

Figure 4-8: Tammann plot of the erythritol–urea system (blue dots). The two linear regressions are represented as continuous lines. The eutectic composition obtained is marked with a yellow star

As it can be observed, the eutectic melting enthalpy increased on the compositions between 10 and 50 % (w/w) erythritol, and decreased on the compositions between 60 and 90 % (w/w) erythritol. In order to find out the exact value, the experimental results were adjusted to two linear correlations, one for the compositions between 10 and 50 % (w/w), and another one for those compositions between 60 and 90 % (w/w) erythritol.

The linear correlation coefficient (Pearson's R) found for each line took values of 0.9961 and 0.9833, respectively, which can be considered a good adjustment. The two adjusted lines crossed to each other at a composition of 54.9 % (w/w) erythritol and 45.1 % (w/w) urea. This value was defined as the eutectic composition of the system. In addition, it was observed that the adjusted lines took a value of zero enthalpy at the extremes of the phase diagram (x=0 and x=1). This corresponds to negligible solid miscibility between the compounds involved.

3.1.5. XRD results of the crystalline phases of the system

The crystalline structure of the material was studied by XRD experiments. The composition formed by 54.9 % (w/w) erythritol and 45.1 % (w/w) urea was assessed. The identification of the solid phases present in the mixture was performed by means of the Powder Diffraction File (PDF) database. The obtained experimental XRD data agreed with erythritol (Form I) [$C_4H_{10}O_4$ – (PDF ref. code: 00–033–1665)] and urea [$CO(NH_2)_2$ – (PDF ref. code: 01–073–3118)]. The diffraction pattern obtained is illustrated in Figure 4-9.

The patterns of the pure erythritol and urea reagents employed in the work were also measured, and they are shown in the mentioned Figure 4-9 for comparison with the eutectic compound. All the peaks on the XRD pattern matched either to those of pure erythritol or pure urea. No new compound or phase is formed when these materials are combined in a binary mixture. Therefore, these results confirm those reached by the thermal analysis: the phase diagram formed by erythritol and urea is a eutectic system.

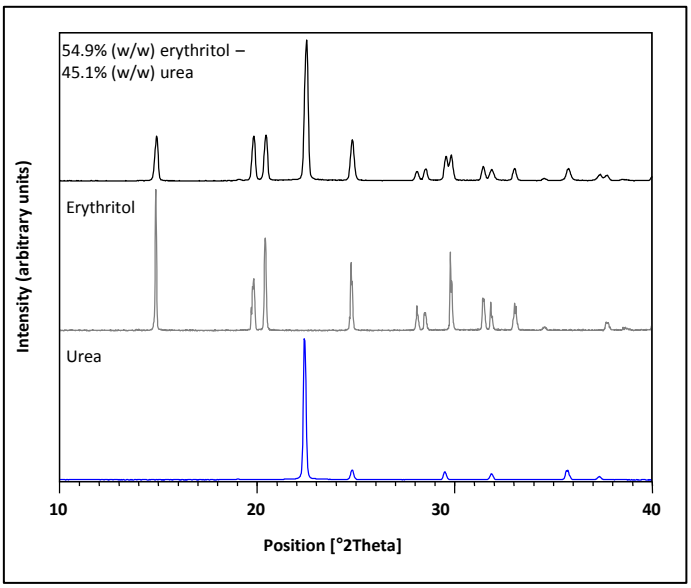

Figure 4-9: XRD diffractograms of pure erythritol, pure urea and a mixture comprised by 54.9 % (w/w) erythritol and 45.1 % (w/w) urea

3.1.6. Agreement between the experimental and numerical results; phase diagram proposed and comparison with previously published results

After the phase diagram of the mixture was established, the results previously obtained by modeling were compared with the experimental ones, in order to evaluate the suitability of the model employed. All these results can be found in Figure 4-10.

As it was discussed in Section 3.1.1, the calculated eutectic composition through the Pharma Modified UNIFAC approach rendered a value of 55.2 % (w/w) erythritol and 44.8 % (w/w) urea. The composition attained by means of the experimental measurements was formed by 54.9 % (w/w) erythritol and 45.1 % (w/w) urea. Thus, the agreement was suitable in terms of the eutectic composition.

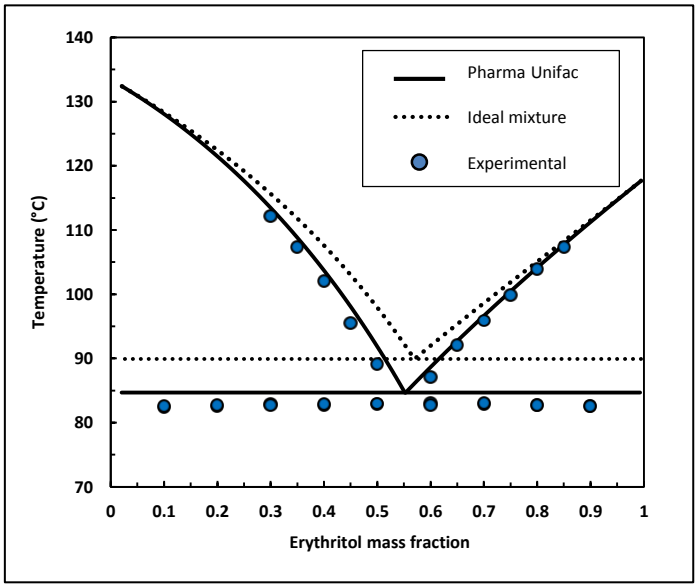

Figure 4-10: Comparison between the modeled and experimental phase diagram of the erythritol–urea system

Regarding the eutectic melting temperature, the model rendered a value of 85 °C, while the experimental values showed a melting temperature of 81.13 °C. This difference can be partially explained from the fact that the criterion adopted to define the experimental melting temperature was the onset melting temperature. This criterion is suitable for making the DSC results comparable between them [87], but is more representative of the beginning of a melting process, which is not the equilibrium melting temperature. Instead of the onset melting temperature, the use of the peak temperature or the inflection temperature [88] would be closer to the temperature predicted by the model. However, as demonstrated previously in the literature [47,48], these criteria present a dependence on the heating rate, as follows: the larger the heating rate, the greater the peak and/or inflection temperatures recorded upon melting. Thus, they were not considered appropriate for the present study. In any case, the temperature agreement can be regarded as suitable for the purposes herein aimed.

The results attained with the ideal model, i.e.: a eutectic melting temperature of 90 °C and a eutectic composition formed by 57.1 % (w/w) erythritol and 42.9 % (w/w), showed larger differences with the experimental results. This is an expected pattern, due to the differences between the molecules of the two materials involved in the mixture, which lead the mixture to show a non-ideal behavior.

As a summary of the results presented so far, the proposed phase diagram is shown in Figure 4-11, where the Tamman plot has also been adjoined. There, it can be seen the suitable agreement between the experimental and the calculated (Pharma UNIFAC) liquidus lines. Besides, it can be observed the good agreement between the calculated eutectic composition and the value obtained from the adjustment of the experimental Tammann plot. As a conclusion, according to all the different methods employed, the phase diagram proposed in this work for the erythritol–urea binary system can be regarded as a simple eutectic type, with a eutectic composition of 54.9 % (w/w) erythritol and 45.1 % (w/w) urea, and a eutectic melting onset temperature of 81.13 °C.

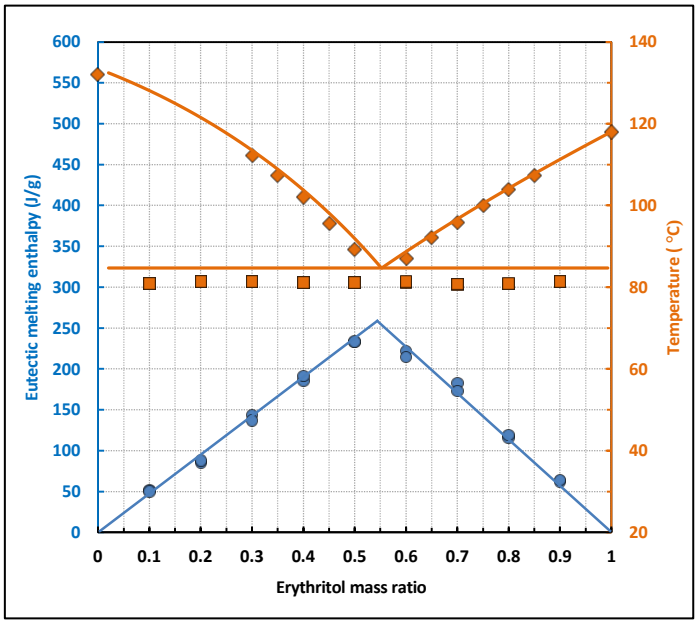

Figure 4-11: Proposed phase diagram for the erythritol–urea system. The liquidus line experimentally obtained by the synthetic visual method (orange diamonds), the solidus line experimentally determined by DSC (orange squares), the calculated phase diagram by the Pharma UNIFAC approach (orange lines), the experimental Tamman plot (blue circles) and the linear correlations for the Tamman plot results (blue lines)

The literature survey presented in this work rendered only one article dealing with this mixture [96]. The information published in that article presents certain differences with the results herein reported. The eutectic composition of the system reported in [96] was formed by 46.6 % (w/w) erythritol and 53.4 % (w/w) urea, with a eutectic temperature of 78 °C.

A difference of 8.3 % (w/w) in composition cannot be considered due to a reasonable experimental bias, while the eutectic temperature, 3.1 °C lower that the melting onset temperature value determined in this work, seems also high to be deemed as reasonable experimental error. These differences could most likely be explained by the fact that, in [96],

the phase diagram was studied upon cooling, which could have influenced the results due to the noticeable supercooling of erythritol. Besides, polymorphism of this compound could also have affected the results attained on the mentioned article. In any case, not enough experimental explanations were included in it to outcast a conclusive analysis.

3.2. Evaluation of thermophysical properties and economical aspects of the eutectic composition

The melting enthalpy of the eutectic composition was determined from the DSC measurements. The specific weight of the liquid and solid phases was established in order to determine the volumetric storage capacity of the eutectic material. Besides, the cost of the PCM was calculated. Using these three criteria, the eutectic composition was compared with other PCMs available in the literature.

3.2.1. Experimental determination of the specific weight of the eutectic composition

The results for the specific weight (density) of the eutectic composition have been gathered on Table 4-3.

	Solid		Liquid	
Temperature (ºC)	25	95	100	105
Specific weight (g/cm^3)	1.333	1.282	1.279	1.276

Table 4-3: Specific weight measured for the erythritol-urea eutectic composition at different temperatures

The analysis of these results led to the calculation of the thermal expansion coefficient on the liquid state of $4.7 \cdot 10^{-4}$ K^{-1}. In addition, from the density change between the solid (25 °C) and the liquid (95 °C) it was observed that the material expands upon melting and shrinks on solidification. The volume expansion underwent was 4.0 % of the volume occupied in the liquid state.

3.2.2. Latent melting enthalpy, volumetric storage density and economical considerations of the eutectic composition proposed as a PCM

For the calculation of the volumetric energy density, only the latent melting enthalpy (without the sensible contribution) was considered because most values available in the literature consider only latent heat. The eutectic composition (54.9 % (w/w) erythritol and 45.1 % (w/w)

urea) was measured by DSC and a latent melting enthalpy of 248 J/g was obtained. Thus, considering the determined liquid density at 95 °C: 1.282 g/cm^3, the proposed eutectic mixture shows a volumetric storage capacity of 318 MJ/ m^3.

If this value is compared with other PCMs available in the literature that are based on the use of raw materials, the density storage attained is at the same range than the values for salt hydrates for the temperatures involved, which are commonly comprised between 250–400 MJ/m^3 [91]. It provides a higher energy storage capacity than the PCMs based on paraffins or fatty acids [26].

The eutectic mixture proposed was besides compared with PCMs based on salt hydrates specifically commercialized for thermal storage purposes and already obtainable in the market. For that, the commercial PCMs S89 and S83 from PCM Products company [105] were taken as representative examples. According to the data published by the suppliers, these PCMs provide energy densities of 234 and 226 MJ/m^3, respectively. Therefore, the energy storage density of the eutectic PCM herein proposed is higher than that provided with these commercialized PCMs.

The current market price of the proposed eutectic material was calculated from the market price of the raw materials. According to [25], erythritol can be purchased at nearby 3.7 €/kg, while urea can be found at 0.72 €/kg [64]. As a result, the estimated cost of the eutectic mixture resulted to be 2.4 €/kg. This value is slightly higher than bulk salt hydrates [91] but well below than fatty acids and paraffins. Therefore, it can be regarded as a reasonable price in the current PCM market situation.

3.3. Accelerated thermal cycling behavior of the eutectic composition

The evolution of the melting temperature and the melting enthalpy of the erythritol–urea eutectic mixture during the thermal cycling test were compared with those of pure urea, in order to determine the relevance/irrelevance of the state of aggregation of urea on its degradation. The evolution of the melting onset temperatures of the eutectic mixture and of pure urea are shown in Figure 4-12.

After 85 cycles, the melting onset temperature of the eutectic mixture decreased in 0.63 °C. Even though the DSC temperature program was defined to avoid the crystallization of the

metastable Form II of erythritol, in Figure 4-12 it can be seen that this polymorph crystallized 6 times out of 85 cycles. This drove the mixture to crystallize on those cycles at a melting onset temperature of 71 °C. Regarding the thermal behavior of pure urea, a clear decrease in the onset temperature from 133 to 120 °C was noticed after only 40 cycles. Afterwards, the onset temperature remained constant.

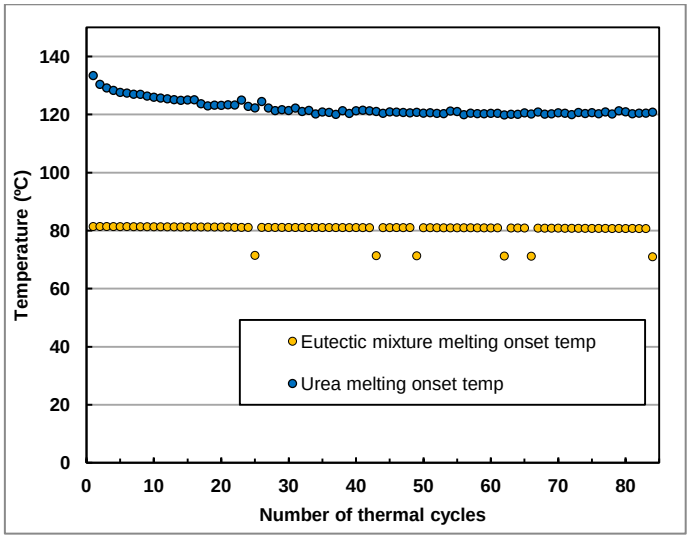

Figure 4-12: Evolution of the melting onset temperatures of the eutectic mixture erythritol–urea and of pure urea during the thermal cycling test

The behavior of the latent melting enthalpy of both compounds is depicted in Figure 4-13. After the 85 thermal cycles, the enthalpy of the eutectic mixture was reduced 9 J/g. This represents a decline of 3.6 % in relation to the original melting enthalpy. Those cycles where the portion of erythritol crystallized as Form II, the enthalpy of the mixture displayed a value of 190–195 J/g. In relation to the heat of fusion of urea, it decreased from 235.7 J/g to 58.4 J/g after 85 cycles. This represents a decrease of 75 % of the original latent heat.

In addition to the evaluation of the melting enthalpy and melting temperature, the DSC thermograms for the eutectic mixture from cycles no. 1, 20, 40, 60 and 80 are compared in Figure 4-14. It can be seen that the outline of the curves remained constant during the thermal cycling performed; no new peaks or thermal events were noticed. Conversely, the shape of the thermograms registered for the pure urea varied noticeably. With the increasing number of cycles, the main melting peak was displaced to lower temperatures, and new endothermic peaks appeared at lower temperatures, increasing its relative intensity with the number of cycles.

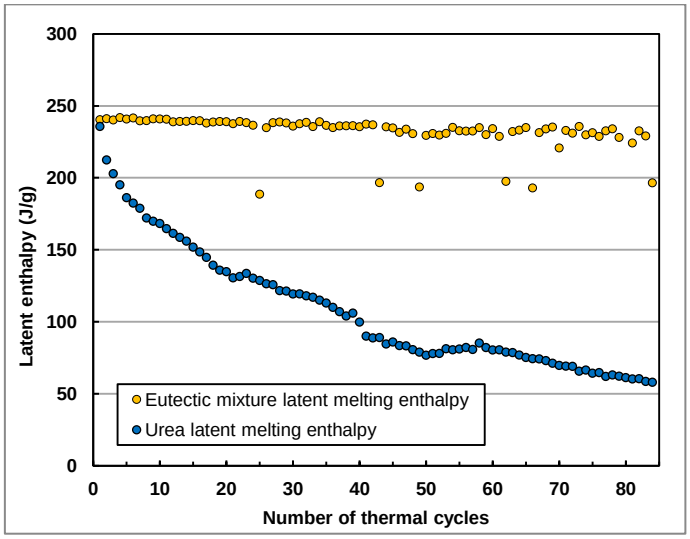

Figure 4-13: Evolution of the latent melting enthalpy of the eutectic composition and of the pure urea during thermal cycling

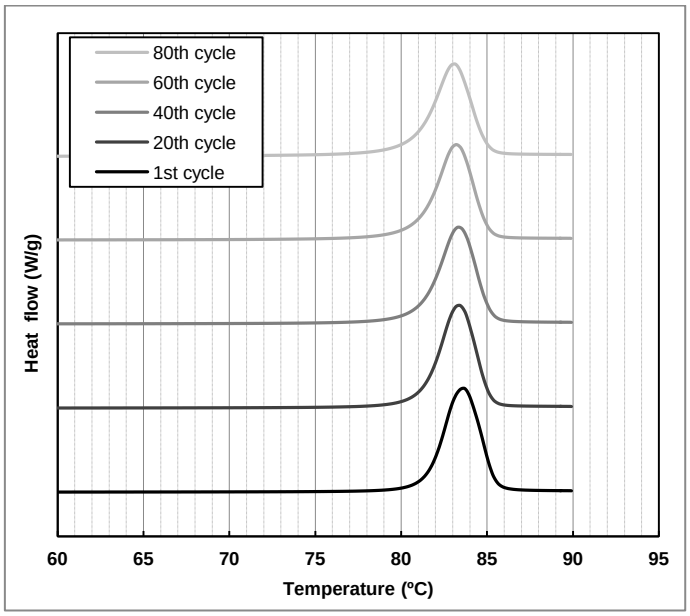

Figure 4-14: Evolution of the melting DSC thermograms of the eutectic mixture during the thermal cycling test

As a consequence from the result obtained, it can be stated that the thermal properties of the eutectic composition remained stable after 85 thermal cycles. In contrast, pure urea showed a noticeable decrease on its performance and a clear degradation and formation of byproducts. Therefore, it can be deduced that the thermal degradation of liquid urea is greatly dependent on the temperature.

This trend agrees with the results attained in Chapter 3 for the accelerated thermal cycling test of the sodium nitrate-urea eutectic mixture. The results attained in both chapters reinforce the

possibility of the use of urea as a component of eutectic PCMs that work at maximum temperatures below 133 °C.

4. Conclusions of the chapter and further work

The binary system formed by erythritol and urea was studied for its use as a PCM in thermal energy storage systems for heating and DHW applications. The solid–liquid equilibrium of the system was assessed by means of a systematic procedure, which has proven to be adequate for the determination of phase diagrams, and can be used for the development of new eutectic PCMs.

The experimental results attained showed that the binary system involved forms a simple eutectic phase diagram. A eutectic composition was found at 54.9 % (w/w) erythritol and 45.1 % (w/w) urea, with a melting onset temperature of 81.13 °C. A volumetric energy density of 318 MJ/m3 was obtained. The price of the proposed eutectic material was estimated at 2.4 €/kg. According to the energy storage capacity, melting temperature and price, the PCM studied is suitable for TES purposes at the intended temperature level.

Preliminary thermal cycling tests performed showed that after 85 thermal cycles the enthalpy of the eutectic mixture was reduced 3.6 % in relation to the original melting enthalpy. In contrast, pure urea showed a decrease of 75 % of its initial storage ability. This demonstrated that the thermal degradation of liquid urea is greatly dependent on the temperature, and allowed concluding that its decomposition rate will be lower when forming part of a eutectic PCM that operates at maximum temperatures below 133 °C.

Further works specifically focused to evaluate the stability of the mixture on longer periods should be performed before it is confirmed that it can be employed as a PCM. Since urea undergoes a thermal decomposition, the investigation should not rely exclusively on accelerated thermal cycling measurements (as discussed in Chapter 3 – Section 3.4.4). The potential thermal degradation of erythritol should also be taken into consideration. Finally, solutions to the complex crystallization behavior of erythritol should be developed before the material can be used in commercial systems.

CHAPTER 5: Development of a simplified overall methodology for the sizing of plate based LHTES systems for domestic CHP plants

ABSTRACT

After studying the urea-erythritol eutectic mixture, the work dealing with the development of new PCMs was considered finished. Accordingly, this chapter faces the second big objective of the thesis: the development of a simple calculation tool for the overall sizing of plate-based LHTES systems for domestic CHP applications.

To approach this objective a CFD model was developed and experimentally validated to simulate different configurations of the plate-based system. The results were first employed to gain knowledge of the melting and solidification behavior of the system and subsequently to establish a correlation to correlate the discharging time of the system with several dimensionless numbers. By means of the obtained correlation the maximum plate thickness can be determined as a function of the selected discharging time and the properties of the PCM without the need of simulations. Finally, considering the remaining constraints of the system, a simplified sizing methodology was proposed. The technique eases the design process of this kind of systems and decreases the amount of time needed to size them.

1. Introduction

As described in Chapter 1, the main goal of this PhD dissertation is the development of the plate-based LHTES system for domestic CHP applications designed in a previous PhD thesis of Campos-Celador [5]. The system consists of rectangular PCM filled-in-plates vertically positioned, which are arranged in parallel to make up a heat exchanger between the HTF and the contained PCM.

One of the main challenges to be faced when developing new LHTES systems is the design and sizing of the system. LHTES systems are normally designed according to a specific storage capacity and to a charging and discharging power. For a given storage capacity this is equivalent to define specific charging and discharging time requirements for each application. The PCMs commonly used at the herein involved temperatures have low thermal conductivities, between 0.2 and 0.7 W/m·K [13], which limits the charging and discharging velocity. This velocity can be increased by several means such as including fins within the encapsulation plates[14] [90], or using composites that combine PCMs with additional materials to increase the thermal conductivity [22,23]. Unfortunately, these solutions raise the cost of the system, which is, up to date, one of the main drawbacks that limit the commercial deployment of LHTES devices. Therefore, it is necessary to develop systems and materials with minimum possible technological processing [25].

In terms of fabrication, the most straightforward solution to increase the charging/ discharging rate of plate-based LHTES systems consists of increasing the heat exchanger surface. This can be achieved by the reduction of the thickness of the plates. However, this is a conflicting solution, because the storage capacity is simultaneously decreased due to a reduction of the amount of PCM. As a result, storage capacity and charging/discharging time are interrelated concepts and the optimization of the system requires a compromise between them.

The ability to succeed on that objective largely depends on the availability of models that allow a fast sizing and accurate simulation of LHTES systems. However, the analysis of the heat and mass transfer mechanisms in a solid-liquid phase change problem is a complex task because

[14] The LHTES system previously designed by Campos-Celador included fins inside the plates. However, an ulterior analysis recommended removing the fins from the design in order to increase the economic feasibility of the system.

the location of the melting front is unknown and it forms simultaneously part of the problem and the solution. As a result, large efforts have been performed over the last years to develop suitable models for LHTES systems [17]. The models developed include analytical, experimental and numerical approaches. A survey of some relevant articles regarding numerical models specifically focused on rectangular geometries resembling the herein involved solution were thoroughly reviewed in [16,17]. The main features are briefly discussed next.

Regarding the analytical approaches, only few solutions are available in a closed form due to the complexity of the phase change problem [16]. These are mainly for one-dimensional cases of infinite or semi-infinite regions with simple initial and boundary conditions and constant thermal properties. Under these conditions, these exact solutions usually take the form of functions of the single variable ($x/t^{1/2}$) and are known as similarity solutions. A collection of similarity solutions and references can be found in [106]. Due to the simplifications usually adopted to formulate these solutions, these models fail to accurately predict the behavior of those LHTES systems that present complex geometries, or include with non-homogeneous materials.

The mentioned shortage can be overcome by numerical methods. Models such as finite differences and finite volumes offer great potential for solving problems of moving boundaries [107]. Due to the complexity of the involved equations, most available solutions are based on one- or two-dimensional systems that use fixed grids. Traditionally, these models assume that the problem is conduction controlled; however, this approach is not able to accurately predict the melting rate, or to track the complex motion of the solid–liquid interface in every moment during the phase change. Recently, the effect of natural convection has been started to be included in numerical studies [17]. Unfortunately, this requires detailed codes that are unsuitable for optimization purposes, where fast and versatile models are needed.

Even though the literature dealing with the modeling of plate-based LHTES is profuse, most of the articles are essentially focused on the development of models that lead to a deeper understanding of the melting and solidification processes or on the study of the charging/discharging process of a specific LHTES system. To the best knowledge of the author, there is a clear lack of studies focused on the development of methodologies suitable for designing and optimizing plate-based LHTES systems capable of defining a broad range of plan

configurations in a systematic and easy way. This reduces the commercialization potential of the existing market ready LHTES products, since the economic and technical performance of the LHTES system relays in the suitability of the dimensions and the design to the requirements posed by the application.

According to the identified needs, the main goal of this chapter is to develop an overall fast and systematic calculation tool for the sizing of plate-based LHTES systems. The structure of the work performed is presented on Figure 5-1.

The process starts with the development of a CFD model that will be experimentally validated. The model is first used for the simulation of the charging and discharging time of a plate with 3 different commercial PCMs. Several values of the plate-thickness were simulated, as well. The objective of this activity is to gain knowledge on the involved heat transfer problem and on the influence of natural convection on the system.

Subsequently, the main goal of the chapter is faced: the development of a simplified correlation suitable to reliably calculate the discharging time as a function of the plate thickness, the PCM properties and the operation constraints of the application. In this way, the straightforward calculation of the maximum plate thickness capable to provide a desired discharging thermal power can be attained. To do so, the discharging time of the system was calculated by means of a detailed CFD model for 15 virtual PCMs and variable plate thickness values.

Finally, the developed correlation is combined with the rest of the requirements that constrain the system, to define the overall design methodology. These requirements are fixed by the application where the LHTES system will be installed: a domestic CHP plant.

Before proceeding with the chapter, it has to be remarked that the developed correlation has been calculated exclusively for discharging because this is the process considered limiting for design purposes [5]. This is owed to the particular operation procedure of the involved application, domestic CHP plants, where the energy production usually occurs in a scheduled way during certain hours of the day and, accordingly, the charging of the LHTES system can be accommodated to that schedule. In addition, the discharging process depends on the user behavior, which cannot be predicted. Besides, it has to be considered that the heating and DHW consumptions require a high power in relation to the charging process.

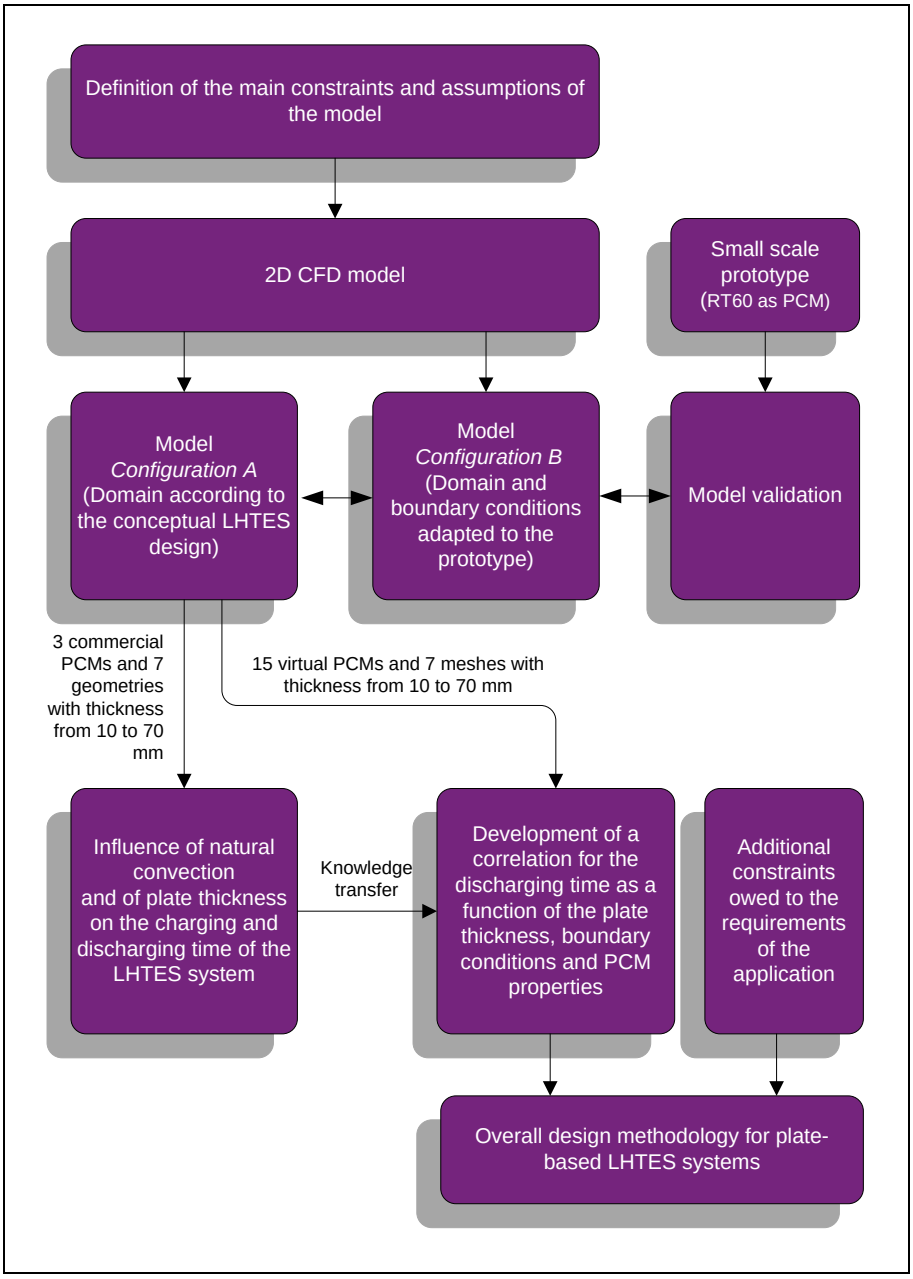

Figure 5-1: Flowchart of the study and development performed along the chapter

2. Numerical models and experimental methods

The conceptual design developed in [5] consists of a plate-based system where the PCM is enclosed within the plates. The plates are vertically positioned and the HTF flows in between them, exchanging heat with the plates' largest surfaces. The plates are arranged in parallel and they can also be arranged in series to finally form a modular LHTES system. A 3D schematic illustration of a system with an arbitrary selected configuration of 14 plates in parallel is depicted in Figure 5-2 (a). A top view of the system is shown in Figure 5-3.

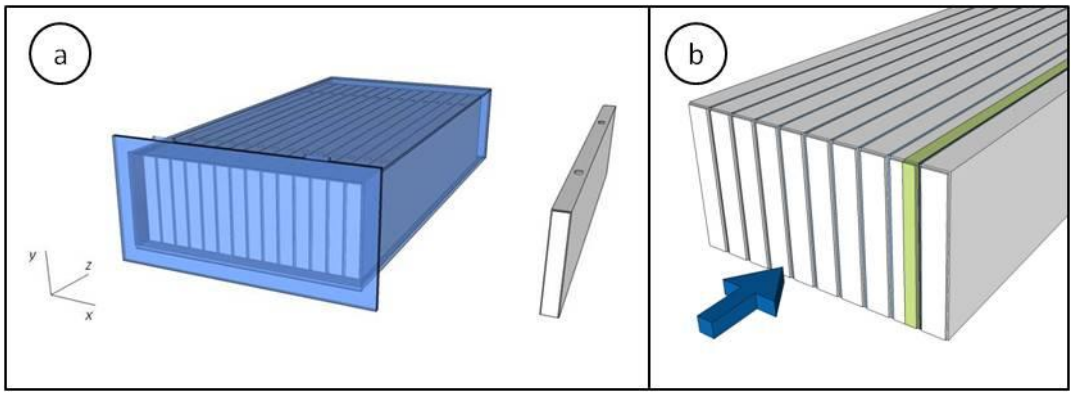

Figure 5-2: a) Schematic representation of a LHTES system consisting of 14 plates in parallel. A detail of one plate is depicted on the right; b) Sketch showing plates in parallel, with half a plate and half a HTF channel highlighted in yellow

Figure 5-3: Top view of a LHTES system consisting of 14 plates in parallel. The arrows represent the water flow direction. 1) water inlet, 2) inlet collector, 3) heat exchange area, 4) outlet collector, 5) water outlet. The yellow rectangle represents the domain covered by the developed laboratory-scale prototype (Section 2.5)

To define the model, the heat transfer problem involved was first analyzed. According to the geometry, two assumptions were adopted to produce the model:

- The modeled domain can be reduced to half a plate and half a HTF channel (Figure 5-2 (b)). This was assumed based on symmetry aspects, because each plate in the system is placed between two water channels
- The heat transfer problem was regarded as two-dimensional through the *x* and *y* axis of Figure 5-2 (b). This assumption is backed by the fact that the temperature gradients in the charging and discharging process occur in this plane. Altough the gradients through the *y* axis could be also neglected following the same assumption, this effect

was included in the analysis to account for the potential convection effects, considering that the additional computational efforts required were assumable. The supposition is besides supported by the results of Campos-Celador [5] for similar plate-based LHTES systems with a length lower than 10 m and relies on the value of the Biot number of the HTF to the PCM herein involved [108]

The following additional assumptions were also employed to produce the model, based on the operational system constraints (summarized in Chapter 1 and previously defined in [5]) :

- The thickness of the channels for the HTF is 2 mm
- The HTF flow regime is laminar
- The heat transfer within the HTF is one-dimensional along the *x* axis (in Figure 5-2) and the convection effect is included by analytical correlations for laminar flow.
- The plates are made of aluminum alloy
- Water is used as a HTF
- The thermophysical properties of the materials are constant with temperature, except for the effective specific heat (see Section 2.4)
- The PCM motion in the liquid state is laminar (assumption justified according to the Rayleigh number values involved [109])

In addition, it was considered that the modeling code to be used should be:

- Able to include natural convection within the PCM
- Versatile, to simulate different geometries and configurations
- Reasonably fast, to enable the simulation of a large number of cases in order to obtain abundant results to develop a simplified correlation

As a result of the abovementioned features, a 2D CFD modeling approach was selected. The ANSYS Fluent 15.0 CFD commercial software [110] was employed, run on a high performance computing cluster to reduce the simulation time [111]. The modeled domain comprised half a plate and half a HTF channel. The applied boundary conditions were based on the above mentioned assumptions.

The details of the model are provided next. Note that several terms employed throughout this section will correspond to specific terminology employed by ANSYS Fluent. Their meaning and

descriptions can be consulted in the User's Manual of the CFD package [110], available online. The description of the prototype constructed for validation purposes is provided in Section 2.5.

2.1. Domain, boundary conditions and developed meshes

The created geometries were grouped into two different configurations, introduced next. The details of each one are provided on the subsequent sections.

- *Configuration A*: This was the main configuration. It was employed to evaluate the charging and discharging time of the LHTES system for several plate thickness and different PCMs, i.e.: to develop the simplified correlation
- *Configuration B*: It was exclusively used to validate the CFD model against experimental results, due to some particular characteristics of the prototype

2.1.1. Configuration A: Domain, boundary conditions and meshes

The *configuration A* was based on the conceptual LHTES system design. It was used to assess the charging and discharging time for several plate thickness and different PCMs. Seven geometries with different thickness were constructed under this configuration (the thickness values are defined below). The domain and boundary conditions are depicted in Figure 5-4.

2.1.1.1. Domain of configuration A

The model was comprised exclusively by the PCM subdomain, defined as a fluid zone[15]. The aluminum wall between the PCM and the water in the actual system (Figure 5-2) was not included in the model. This decision was supported by preliminary simulations, which showed that the aluminum could be neglected due to its high thermal conductivity in comparison with the PCM.

2.1.1.2. Boundary conditions of configuration A

The upper and lower walls were considered adiabatic. The right side (relative positions according to Figure 5-4) was defined as a symmetry wall, since the domain covers half of a plate. Hence, the heat exchange between the PCM and the HTF was exclusively given trough

[15] When the enthalpy-porosity method in ANSYS Fluent is used, any material that changes phase is treated as a fluid. The solidification is computed by means of the momentum equation (see Section 2.2.2).

the left wall. The heat transfer was modeled by the Newton equation for convection [109], which is shown in Eq. 1.

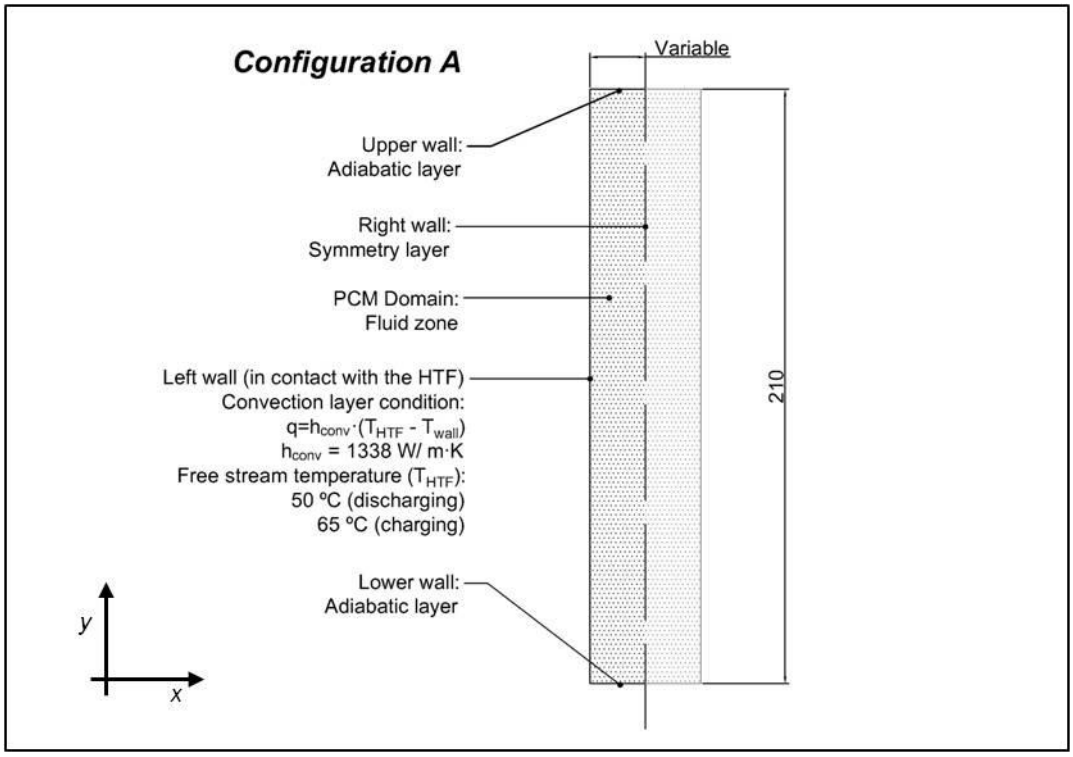

Figure 5-4: Representation of the modeled geometry and boundary walls for the *configuration A* (used for the discharging time studies). Dark lines represent the domain modeled (half a plate). The shadowed zone represents the rest of the plate. Dimensions are in mm

$$\dot{q} = h_{conv}(T_{HTF} - T(0)_{PCM}) \qquad \text{Eq. 5-1}$$

There, T_{HTF} accounts for the free stream temperature of the water, with a constant value of 50 °C upon solidification and of 65 °C upon melting. The term $T(0)_{PCM}$ represents the temperature of the PCM-HTF interface, which was calculated for each cell as part of the solution of the CFD domain. Finally, h_{conv} is the convection heat transfer coefficient, with a value of 1204 W/m^2·K. It was calculated by means of the analytical Nusselt value for forced convection under laminar regime[16]: 8.235 [109].

[16] Laminar regime is an operational requirement of the developed LHTES design

2.1.1.3. Meshes of configuration A

Seven geometries with variable thickness were created under *configuration A*. Their dimensions were based on the sizes of the commercially available aluminum extruded profiles [112], according to the fabrication procedure defined in Chapter 6.

The plate thickness values (*x* axis in Figure 1) considered were 10, 20, 30, 40, 50, 60 and 70 mm. Accordingly, since half plates were simulated, the thickness of the built meshes ranged from 5 to 35 mm.

The inclusion of a variable height values in the study was discarded since its effect on the involved heat transfer is usually assumed as negligible or of very low impact. This can be extracted from analytical correlations for natural convection within rectangular enclosures [113]. Moreover, this would drastically increase the number of simulations to be performed.

As a result, a single height of 210 mm was considered. This height is slightly larger than the height of commercially available hollow-box type profiles suitable to provide PCM plates of the above defined thicknesses [112]. Accordingly, it was intentionally selected as a conservative scenario regarding the natural convection effects within the PCM. It is foreseen that the height of commercial profiles used in an actual system will be lower and thus the influence of natural convection will be less significant. This is important by the time of applying the simplified correlation developed in Section 3.3, because it neglects natural convection effects.

The mesh configuration comprised a mapped grid with orthogonal quadrilateral cells. The detailed view of the top part of the mesh for the geometry with a half thickness of 5 mm is shown in Figure 5-5. A refined boundary layer was created beside the wall in contact with water, where larger temperature and velocity gradients are expected. The cells adjacent to that wall presented a size of 0.0125x0.125 mm (referred to the *x* and *y* axis in Figure 5-5, respectively). The size of the cells along the *y* direction was constant for the whole mesh: 0.125 mm. The size of the cell sides along the *x* axis gradually increased as the cells were distanced from that wall, according to a growth factor of 1.1 until a size of 0.125x0.125 mm was achieved. This was the maximum cell size and it can be considered the representative size as well. It was selected according to a mesh sensitivity analysis, which will be discussed in Section 3.1.1.

As a result of the formerly explained dimensions, the number of elements in the meshes ranged from 92400 cells for the mesh with 5 mm half thickness (minimum), to 519120 cells for the mesh with a half thickness of 35 mm (maximum).

The properties of the PCMs combined with this *configuration A* are detailed in Section 2.4.

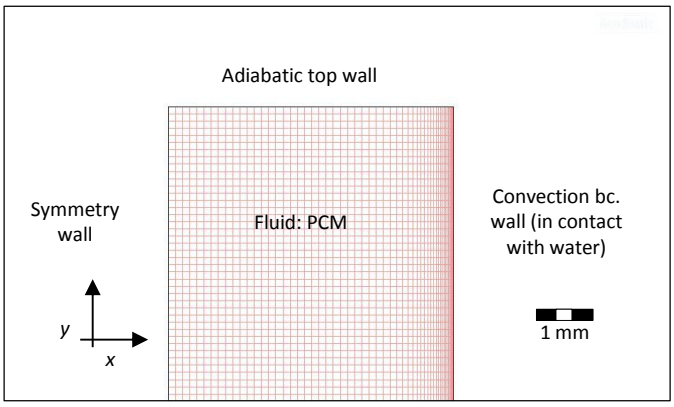

Figure 5-5: Detail of the upper part of the mesh with half thickness of 5 mm under *configuration A*

2.1.2. Configuration B: Domain, boundary conditions and mesh

The *configuration B* was exclusively built for validation purposes. It was similar to the *configuration A* described above, although some modifications were included due to particular features of the constructed prototype. The PCM was RT60 (Section 2.4) since that was the only material employed in the prototype. The characteristics of the modeled domain and the boundary conditions are depicted in Figure 5-6.

2.1.2.1. Domain of configuration B

In this case, the aluminum walls were included within the meshed domain. This was done because in the prototype (see Section 2.5), due to the high thermal conductivity of the aluminum, the encapsulation acts as a thermal bridge between both sides of each plate and heat is also transferred to the PCM from the outer side. Thus, the heat transfer for each plate cannot be regarded as symmetric.

Accordingly, two sub-domains were defined: the PCM as a fluid and the aluminum as a solid. Note that there was no upper aluminum meshed wall in the model, because it was not present in the LHTES prototype.

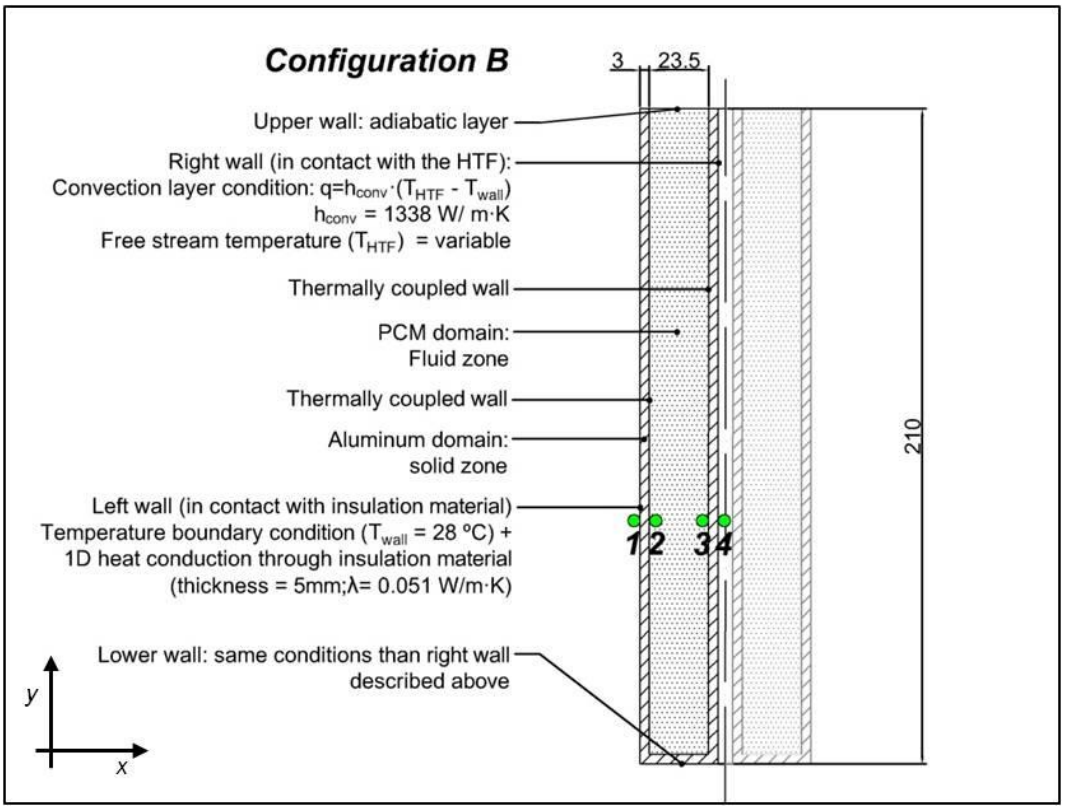

Figure 5-6: Representation of the modeled geometries and boundary walls of the *configuration B* (used for the model validation). Dark lines represent the domain modeled (one plate of the prototype). The shadowed zone represents the additional plate present in the prototype. Green circles represent the location of the thermocouples used in the experimental tests. Dimensions are in mm

2.1.2.2. Boundary conditions of configuration B

The PCM and the aluminum sub-domains were thermally coupled by the walls placed in between them (termed as *shadow walls* in ANSYS Fluent). Regarding the boundary walls placed at the outer part of the domain, the upper and the lower sides were considered adiabatic.

The heat between the PCM and the HTF was exchanged trough the right wall exclusively. The heat transfer was modeled by the Newton equation for convection (Eq. 5-1); however, unlike the case of *configuration A*, the water free stream temperature (T_{HTF}) was variable along time due to the boundary conditions applied in the experiments with the prototype (see Section 3.1.2). This temperature was included in the model by means of a user defined function (UDF) [110].

The left side was in contact with the outer insulation material. The heat transfer was modeled by solving the 1D heat conduction equation in the direction normal to the wall (approach

termed *thin-wall* in ANSYS Fluent). The imposed outer wall temperature was 28 °C, obtained from the experimental tests. The thickness of the insulation material was 5 mm and presents a thermal conductivity of 0.051 W/m·K, data supplied by the prototype manufacturer [114].

2.1.2.3. Mesh of configuration B

One mesh was built under this *configuration B* with a height of 210 mm and a total thickness (PCM+aluminum) of 29.5 mm (see Figure 5-6). The grid configuration and the size of the cells was equivalent to that employed in the configuration *A*.

The employed governing equations, numerical schemes and convergence criteria were the same for both geometry configurations, *A* and *B*. They are described along the following subsections.

2.2. Governing equations

CFD modeling involves the solution of the continuity, momentum and energy conservation equations for every cell in the domain at every time step. The well-known enthalpy-porosity method [115,116] was used to model the melting and solidification process of the PCM. A summary of the applied equations is shown next. The nomenclature corresponds to that provided at the beginning of the dissertation; thus, only those terms of the equations that need an additional explanation will be defined along the text. The detailed deduction of the equations can be consulted in ref. [110].

2.2.1. The energy equation

The effective specific heat formulation of the energy conservation equation was employed. In this method, the PCM is treated as a material with variable C_p as a function of temperature [117,118]. The effective C_p data against temperature for each PCM are obtained by DSC trough a methodology that involves two steps. First, the experimental DSC curve (heat flow rate vs. temperature) is obtained. This is then divided by the heating rate (K/min) and by the PCM mass (mg) used in the DSC experiment to obtain the effective C_p curve vs. temperature. This curve includes both the sensible and the latent heat of the PCM. The data are implemented in the ANSYS Fluent software as a piecewise-linear function [110]. The energy equation used is shown in Eq. 5-2.

$$\frac{\partial(\rho C_p T)}{\partial t} + \nabla.\left(\rho\vec{v}C_p T\right) = \nabla.(\lambda\nabla \mathrm{T}) \qquad \text{Eq. 5-2}$$

2.2.2. The momentum equation

The general form of the momentum transport equation is shown in Eq. 5-3 [108]. The source term, S, accounts for the velocity reduction of the fluid due to the increasing porosity of each cell as defined in Eq. 5-4. There, the constant ε is a small number with a default value of 0.001 to prevent division by zero [110]. The parameter A_{mush} reflects the mushy zone morphology and describes how steeply the velocity is reduced to zero while the PCM solidifies. A value of 10^5 was selected [119]. The source term S is also a function of the liquid volume fraction, f, which is in turn computed as a function of the temperature by means of the lever rule, as defined in Eq. 5-5.

$$\frac{\partial(\rho\vec{v})}{\partial t} + \nabla(\rho\vec{v}\vec{v}) = -\nabla p + \nabla(\bar{\bar{\tau}}) + \rho g + S \qquad \text{Eq. 5-3}$$

$$S = \frac{(1-f)^2}{f^3 + \varepsilon}\vec{v}A_{mush} \qquad \text{Eq. 5-4}$$

$$\begin{cases} f = 0 & \text{if } T < T_s \\ f = \dfrac{T - T_s}{T_l - T_s} & \text{if } T_s \le T \le T_l \\ f = 1 & \text{if } T > T_l \end{cases} \qquad \text{Eq. 5-5}$$

The natural convection within the PCM was modeled by means of the Boussinesq approximation [109,110]. Besides, the viscous stress tensor ($\bar{\bar{\tau}}$) was adapted to incompressible fluids. The flow regime of the PCM in the liquid state was considered laminar, based on the typical maximum Rayleigh numbers involved in every geometry [109]. As a result, the final version of the momentum equation employed is represented in Eq. 5-6.

$$\rho_{ref}\left(\frac{\partial\vec{v}}{\partial t} + \vec{v}\nabla\vec{v}\right) = -\nabla p + \nabla(\mu\nabla^2\vec{v}) + \rho_{ref}g - \rho_{ref}\beta(T - T_{ref})g + S \qquad \text{Eq. 5-6}$$

2.2.3. The continuity equation

The continuity equation for incompressible flows was employed to meet the mass conservation within the domain [108]. This is shown in Eq. 5-7.

$$\nabla \vec{v} = 0 \qquad \text{Eq. 5-7}$$

2.3. Numerical schemes, convergence criteria and initial simulation conditions

The used numerical schemes, convergence criteria and algorithms are summarized in Table 5-1. They were selected according to the recommendations given by ANSYS Fluent [110] and also based on the own-previous knowledge of the CFD code. Some specific features that need an extended explanation are described next:

- The numerical convergence of the model was checked by means of the scaled numerical residuals of all computed variables. For additional convergence verification, the temperature and velocity magnitudes were monitored on several points of the domain at each iteration
- An adaptive time stepping method was used for the simulations. In this approach the size of the time-step changes as the calculations proceeds. The simulations start with a minimum time-step size, which value is defined by the user. The size of each subsequent time-step is automatically calculated based on a truncation error associated with the time integration scheme. If the truncation error is smaller than a specified tolerance, the size of the time-step is increased; if the truncation error is greater, the time-step size is decreased. More details about the algorithm used by Fluent to estimate the truncation error are given in ref. [120]

The flow field was initialized before each simulation started. The initial conditions of the domain are presented in Table 5-2. It was assumed that the plate started the process from a fully charged or discharged state. Accordingly, the temperature of all the cells was set at 50 °C for charging simulations, with the free stream temperature of the HTF (T_{HTF} in Eq. 5-1) at 65 °C. The opposite configuration was used for discharging.

The achievement of the 100 % storage or release of energy is unfeasible in practice for the system proposed because the PCM temperature approaches assimptotically to the HTF inlet temperature. Thus, the criterion defined to evaluate the behavior of the system is the time

needed to store or release 95 % of the total thermal capacity of the system (referred hereinafter to as 95 % energy ratio). The general assumption behind this criterium is that the marginal increase of stored energy above this percentage implies an excessive increase of the required time.

Item	Selection or value used	Remarks
Solver	Pressure-based double-precision	_
Pressure-Velocity coupling method	PISO	Highly recommended for all transient flow calculations
Pressure interpolation schemes	PRESTO	Second order schemes for pressure are incompatible with the enthalpy-porosity approach
Spatial discretization schemes	Second-order upwind for momentum and energy equations.	_
Time stepping method	Adaptive	_
Transient formulation scheme	1st order	Second-order schemes are incompatible with adaptive time stepping in ANSYS Fluent.
Minimum time-step size	10^{-4} seg	The size was maintained constant at least for the first 10 time-steps. A small time-step was used at the beginning to minimize the error, because the highest heat flux values occurred always at the beginning of the simulations due to the large temperature gradients inside the system at the initial stages.
Maximum time-step increase	1.05 times the previous value	
Maximum time-step	Variable for the different geometries. Selected based on the plate thickness	It ranged from 10 seg for a half thickness of 5 mm, to 300 seg for a half thickness of 35mm.
Continuity residual value	10^{-4}	The value chosen assured that the mass-imbalance error was less than 0. 2 % of the net flux through the domain.
Velocity residual value	10^{-6}	The validity of this value was confirmed by monitoring the velocity magnitudes on several points of the domain at each iteration
Energy residual value	10^{-9}	The validity of this value was confirmed by monitoring the temperature on several points of the domain at each iteration
Computational facilities used for the simulations	Leonardi high performance computing cluster within the Faculty of Engineering of the University of New South Wales (UNSW) [111]	The typical configuration used employed a node with four physical AMD Opteron 2.20 GHz processors, each having 12 cores (48 cores used in total) and 96 GB of physical memory
Time needed to complete the simulations (h)	From 1 to 15	The time depends on the thickness of each case-study, on the PCM employed and on the under-relaxation factors applied

Table 5-1: Numerical schemes, convergence criteria and algorithms used for the model

Process	Temperature of the PCM (and aluminum in *configuration B*) (ºC)	Free stream temperature of the HTF (T_{HTF} in Eq. 5-1) (ºC)	PCM velocity (m/s)	Absolute pressure of the domain (bar)
Charging	50	65	0	1.013
Discharging	65	50	0	1.013

Table 5-2: Initialization values employed for the flow field

2.4. Selected materials and their thermophysical properties

Water acted as HTF and aluminum was selected as the material for the plates. Their properties are shown in Table 5-3. Since the model did not include any HTF sub-domain, the water properties were used only for the calculation of the heat transfer coefficient at the convection

boundary wall (Eq. 5-1). The aluminum properties were exclusively used in the geometry *configuration B*.

Material	Density (kg/ m^3)	Cp (kJ/kgK)	Thermal conductivity (W/mK)	Viscosity (kg/ms)
Water	998.2	4.182	0.59	0.001003
Aluminum	2719	0.87	202.4	_ [a]

Table 5-3: Thermophysical properties used for HTF (water) and aluminum
[a] Solid material (property does not apply)

The PCMs used can be gathered into two groups. On the first group, 3 materials commercially available were chosen to gain knowledge about the melting and solidification processes with real PCMs. On the second group, 15 virtual PCMs with variable properties were defined in order to perform the parametrical analysis carried out to establish the simplified correlation to determine the discharging time of the system (see Section 3.3.2).

2.4.1. Properties of the commercial PCMs employed: RT60, stearic acid and palmitic acid

For the selection of the commercial PCMs the following requirements were considered [13,15,20]:

- Melting temperature between 50 and 65 °C
- Energy storage higher than 150 kJ/kg for the total operation temperature range
- Stability in relation to the thermal cycling and easy handling (i.e.: no phase segregation; no thermal degradation and non-hygroscopic behavior)
- A market price below 6 €/kg

According to these constraints, RT60, stearic acid (referred to as SA hereinafter) and palmitic acid (referred to as PA hereinafter) were selected as PCMs. RT60 is a paraffin wax from the company Rubitherm GmbH [24], that was already used in the previous PhD work by Campos-Celador [5] (See Chapter 1). SA and PA are two fatty acids [29], technical grade purity (70 % purity for SA and 80 % purity for PA), supplied by Quimidroga S.A. [64].

Laboratory grade (99 % purity) SA and PA were also acquired [121] and characterized. Even though they showed an energy storage capacity around 30 % higher than the technical grade products, their price was above 500 €/kg, which completely discarded their use as PCMs in commercial systems. Hydrated salts were initially considered as candidates, due to their high

storage density [91]; however, they were discarded for the present work due to their common thermal stability problems and hygroscopicity.

The thermal characteristics of the 3 materials (RT60, PA and SA) were measured by DSC in order to obtain the effective C_p vs. temperature curves used as inputs in the CFD model. The apparatus used was a Mettler Toledo DSC1, using the calibration configuration detailed in Chapter 3 - Section 2.2.

The effective C_p vs. temperature curves were obtained by derivation of the enthalpy vs. temperature. The standardized PCM characterization procedure developed under the IEA Task 24 - Annex 29 was used to perform the measurements [86,87]. A heating and cooling rate of 1 K/min was selected according to the methodology. The minimum and maximum temperatures of the program were 35 and 75 °C with isothermal segments of 5 min between each consecutive heating/cooling ramp.

The values attained for the 3 PCMs upon solidification are shown in Figure 5-7 to Figure 5-9. The temperature interval presented in the figures range from 40 to 70 °C. Nevertheless, only those data corresponding to the interval 50 - 65 °C were needed in the model. PA and SA showed hysteresis in their behaviour and thus slightly different curves were obtained upon melting. Consequently, those simulations performed for charging (see Section 3.2.1) included the melting curves instead of the solidification ones. These curves they will be ommited for the sake of brevity. The solidus and liquidus temperatures used are marked in the mentioned figures and were also obtained from the DSC measurements.

PA showed only one peak upon solidification. Conversely, SA and RT60 showed an additional transition at a temperature below the main solidification peak. This was likely attributed to the purity of the materials, especially in the case of the SA, whose composition included a 30 % of impurities.

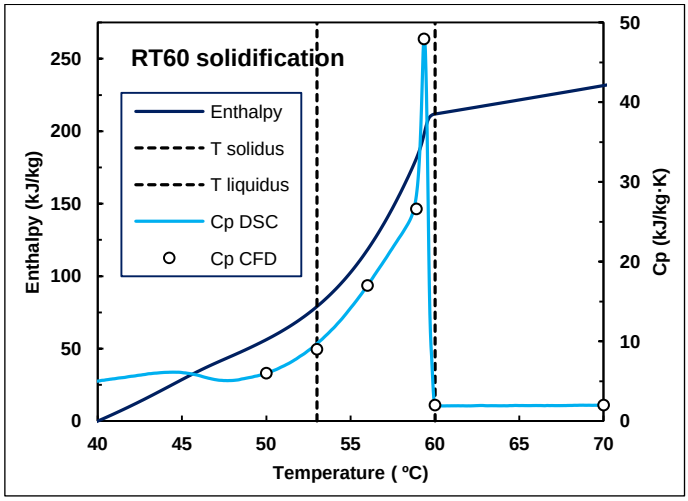

Figure 5-7: Enthalpy vs. temperature plot and effective Cp vs. temperature plot for RT60 upon solidification (measured by DSC)

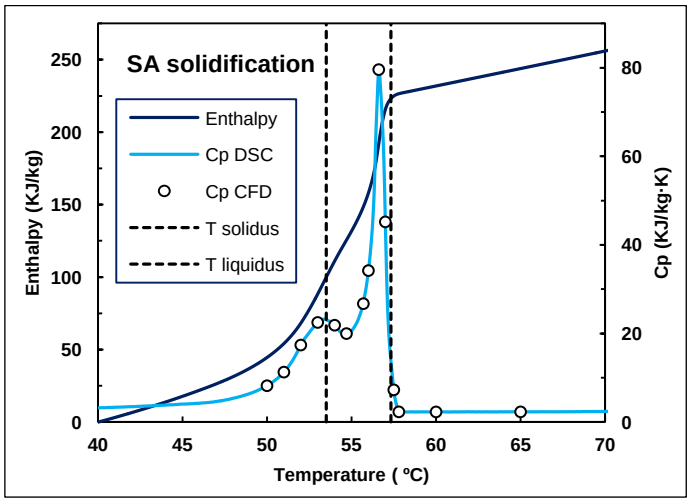

Figure 5-8: Enthalpy vs. temperature plot and effective Cp vs. temperature plot for stearic acid upon solidification (measured by DSC)

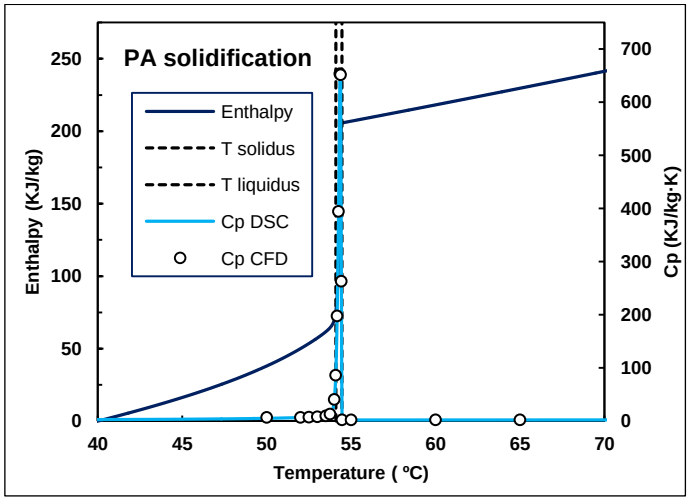

Figure 5-9: Enthalpy vs. temperature plot and effective Cp vs. temperature plot for palmitic acid upon solidification (measured by DSC)

The rest of the thermophysical properties included in the model were considered constant in relation to the temperature (in the working temperature range). Their values are shown in Table 5-4.

Material	Density [a b] (kg/ m^3)	Solidus temperature (ºC) [b]	Liquidus temperature (ºC) [b]	Enthalpy stored between 50 and 65 ºC (kJ/kg) [b]	Thermal conductivity (W/m K) [c]	Viscosity (kg/ms) [c]	Thermal expansion coefficient (1/K) [b]	Market price (€/kg) [c]
RT60	782	53	60	167.6	0.2 [24]	0.0285 [24]	0.001	3-6 [24]
PA	852	54.1	54.45	196.3	0.16 [29]	0.00764 [29]	0.00078	1.5 [64]
SA	850	53.5	57.3	203.8	0.17 [29]	0.00731 [29]	0.00084	1.9 [64]

Table 5-4: Thermophysical properties of the commercial PCMs employed in the 2D CFD model. [a] Evaluated at 65 ºC, calculated from the thermal expansion coefficient. [b] Values determined from own experimental characterization. [c] Values from the literature

The density of the 3 PCMs was measured by the method detailed in Chapter 3 - Section 2.7 and corresponds to a temperature of 65 °C, assuming that the LHTES system would be filled-in with the liquid PCM at that temperature. This is a relevant feature, because the PCM mass present in the model is calculated from this density value and the volume of the domain. The thermal expansion coefficient was calculated from the density experimental measurements as well.

The solidus and liquidus temperatures were obtained from the above mentioned DSC measurements. The viscosity of the materials and their thermal conductivity were obtained from the literature. The references are provided next to each value in Table 5-4.

2.4.2. Properties of the virtual PCMs defined for the parametrical study

The 15 virtual PCMs employed to establish the simplified correlation were defined based on the findings achieved through the simulation results of the 3 commercial PCMs (discussed in Section 3.2). Therefore, their description will be performed in the subsequent Section 3.3.2.

2.5. Description of the small-scale prototype developed for the validation of the CFD code

A laboratory-scale prototype of the LHTES system employed in order to validate the CFD model with experimental data. It was designed and manufactured in cooperation with TSM S.L. [122] and Dikoin S.L. [114]. Its construction served to gain knowledge for the further fabrication of the full-scale prototype that will be faced in Chapter 6. A sketch of the prototype is depicted in Figure 5-10.

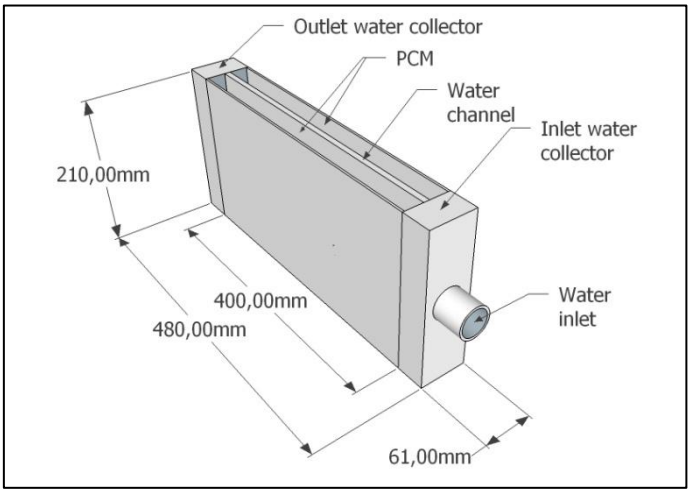

Figure 5-10: Sketch of the constructed laboratory-scale LHTES prototype

It consists of a single 2 mm HTF channel placed between two rectangular enclosures where the PCM was confined. These enclosures, 23.5 mm thick, correspond to two halves PCM plates. The prototype, therefore, would be equivalent to a 1 channel – 2 (half) plates LHTES system (see colored area in Figure 5-3). Two empty spaces that acted as water collectors were included in order to achieve a good hydraulic distribution, one at the inlet and another at the outlet. The material used in the construction was aluminum, with a wall thickness of 3 mm. The total mass of PCM RT60 used was 3.0 kg. The dimensions of the system can be visualized on Figure 5-10.

PCM temperatures were recorded at the inner and outer sides of the enclosure, at a height of z=7.5 cm (3 cm below central plane) and at the central transversal plane to the channel (see

marks 1, 2, 3 and 4 on Figure 5-6, corresponding to one thermocouple each one). Attached T-type thermocouples (± 0.5 °C uncertainty) were used, connected to a data acquisition system (Agilent Technologies - 34972A model). The prototype was insulated by a 5 cm thickness polymeric foam (0.051 W/m·K). A petcock was placed on the inlet collector to purge the air out of the system. All these elements can be appreciated on the pictures shown on Figure 5-11.

The HTF temperature program during the measurements was controlled by a programmable thermostatic bath (Lauda Proline RP845C, ± 0.01 °C uncertainty). The experimental conditions employed in the tests are presented in Section 3.1.2, along with the measurements results.

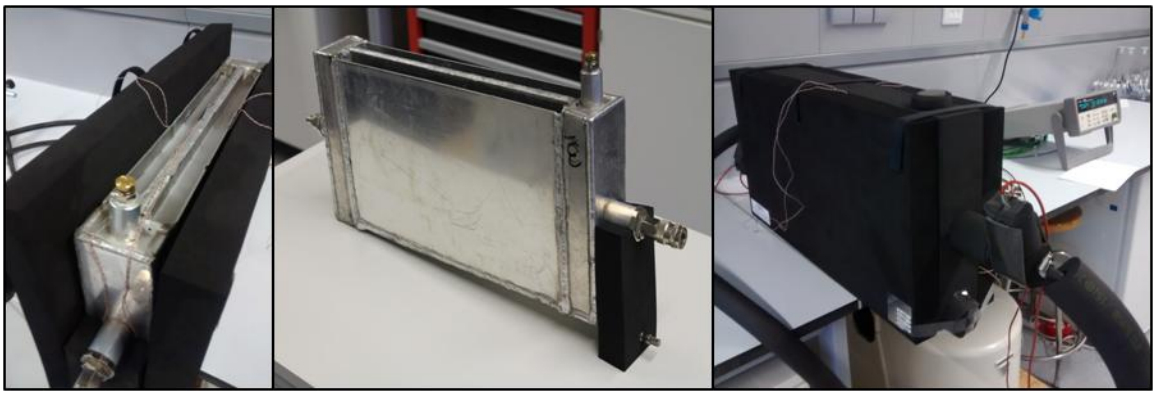

Figure 5-11: Images of the laboratory-scale LHTES prototype

3. Results and discussion

The section on results is divided into four parts, as follows:

- CFD model validation (Section 3.1)
- Simulations with commercial PCMs to gain knowledge about the thermal behavior of the system and about the influence of natural convection (Section 3.2)
- Simulations for the development of a simplified correlation for the estimation of the discharging time (Section 3.3)
- Proposal of an overall design methodology (Section 3.4)

3.1. Validation of the developed CFD model

Before the simulations were performed the model was validated. To do so, the mesh numerical uncertainty was established and the results of a simulation were compared with the experimental tests produced with the prototype.

3.1.1. Determination of the numerical uncertainty of the mesh

A verification procedure was performed to prove that the obtained results were independent from the mesh employed. The numerical uncertainty resulting from the domain spatial discretization was quantified by means of the Grid Convergence Index method (GCI method). The details about the calculation procedure can be found in [123]. The steps are the following ones:

- Define a representative cell or mesh size
- Select three significantly different sets of grids and run simulations to determine the values of key variables important to the objective of the simulation study
- Calculate the apparent order of the method
- Calculate the extrapolated values for the key variables selected
- Calculate the fine grid convergence-index, which will represent the numerical uncertainty of the finest mesh employed

The thinnest geometry (5mm half thickness under *configuration A*) was selected as the worst-case scenario, due to the expected higher relative speed of the melting front. Three different meshes were built, with cells of side-length 0.125, 0.35 and 0.5 mm respectively. The solidification process of the PA was simulated for each mesh. The time needed to achieve a 95 % of discharging ratio was chosen as the key variable.

The fine-grid convergence index [123] was estimated. This represents the difference of the results in comparison to the results that would be obtained using a mesh with theoretical cell size 0 (and hence with no discretization errors). The results showed a negligible relative error of 0.003 % for the finest mesh (cell-side size 0.125 mm). As a consequence, the mesh was considered suitable for the purposes aimed in this work.

3.1.2. Validation of the model against experimental results

The results obtained in the simulations were compared to experimental data in order to validate the model. Solidification results were employed in the comparison since this is considered the limiting stage of the process for the LHTES application involved. Experimental measurements were performed with the LHTES prototype described in Section 2.5. Two different type of tests were performed, because the velocity of the PCM solidification front

depends on the type of boundary conditions applied [124]. The temperature profiles of the tests can be seen in Figure 5-12. The tests are described next:

- First test: a temperature lineal ramp for the water inlet was applied by means of the thermal bath. For this purpose, the water entering the LHTES system followed a temperature program that decreased linearly from 65 to 50 °C in 2h 25 min (0.1 K/min)
- Second test: the water entering into the LHTES system followed a parabolic temperature inlet condition. The temperature program of the thermal bath decreased from 65 to 50 °C in 3.25 h under the parabolic profile shown in Figure 5-12

The measurements finished when the inlet water temperature reached 50 °C. Both tests were performed in duplicate, obtaining the same temperature profiles.

The validation criterion used was the temperature difference between the experimental and simulated temperatures at the point measured by the probe number 2 (according to the nomenclature in Figure 5-6). This probe is the most critical of all the employed probes owed to its position. The results are depicted on Figure 5-12.

The simulation results agree with the experimental results, as Figure 5-12 clearly demonstrates. The quantitative differences are presented on Table 5-5. The average results are within the uncertainty range of the used thermocouples (± 0.5 °C). In light of the results, it can be concluded that the model is capable of reproducing the PCM solidification and can be used for the simulation of the LHTES system.

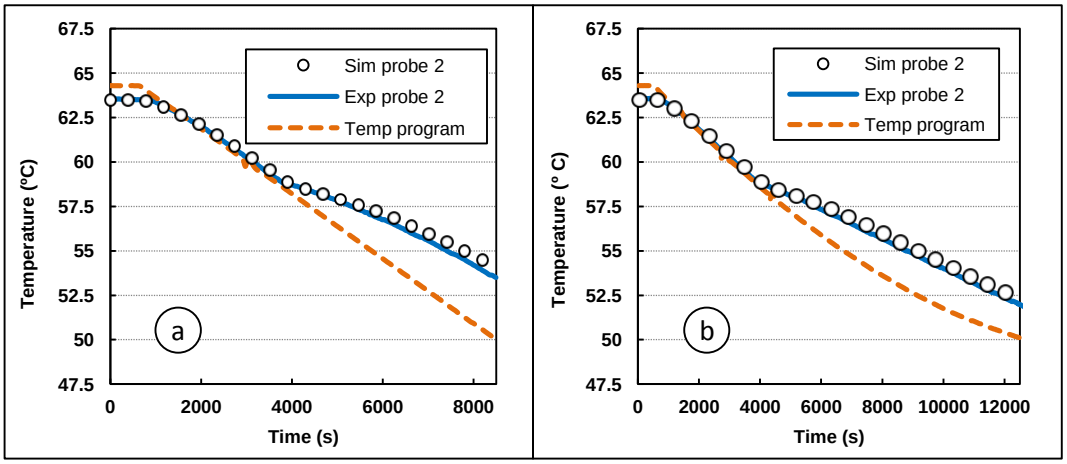

Figure 5-12: Experimental vs. simulated results with the 2D CFD model: a) ramp temperature inlet condition; b) parabolic temperature inlet condition

Boundary condition (temperature program type)	Average temperature difference (exp vs. sim)	Maximum temperature difference (exp vs. sim)
Constant temperature program (Test 1)	0.19 °C	0.60 °C
Parabolic temperature program (Test 2)	0.20 °C	0.36 °C

Table 5-5: Average and maximum temperature difference between the experimental and simulated temperatures at the control point selected for validation

3.2. Characterization of the charging and discharging time as a function of the plate thickness and influence of the natural convection

After the model was validated, the simulations for the analysis of the system behavior were performed. Three commercial PCMs (RT60, PA and SA) were simulated, using seven plate thicknesses with each material: 10, 20, 30, 40, 50, 60 and 70 mm. The main objective was to understand the system discharging behavior as a function of the plate thickness, in order to learn how to proceed with the further simplified correlation to be developed. In addition, it was intended to characterize the influence of natural convection on the system. Therefore, not only the discharging but also the charging[17] process was analyzed in order to attain an overall knowledge of the process. The system was considered completely charged/ discharged when a 95 % energy ratio was stored/ released.

[17] The author is aware that the model was not validated upon melting; however, the conclusions about charging were mainly based on trends and not on quantitative results. A high accuracy is not essential for such an approach and thus the validation was not considered crucial.

The results of the charging and discharging time for the 3 PCMs are shown in Figure 5-13. For each PCM, the discharging time was higher than the charging time for every plate thickness. This confirms one of the hypothesis that backed up the selection of the discharging process as the limiting stage that must be considered to design these systems (as suggested in [5], and explained in Section 1).

Figure 5-13 indicates that the charging times for all the PCMs showed a linear relationship as a function of the plate thickness, while the trend for the discharging time was parabolic. This trend can be better appreciated in Figure 5-14, where the regression adjustments were added for the PA results. The observed tendencies suggest that natural convection affects differently upon melting and solidification, which will be confirmed in the following sections.

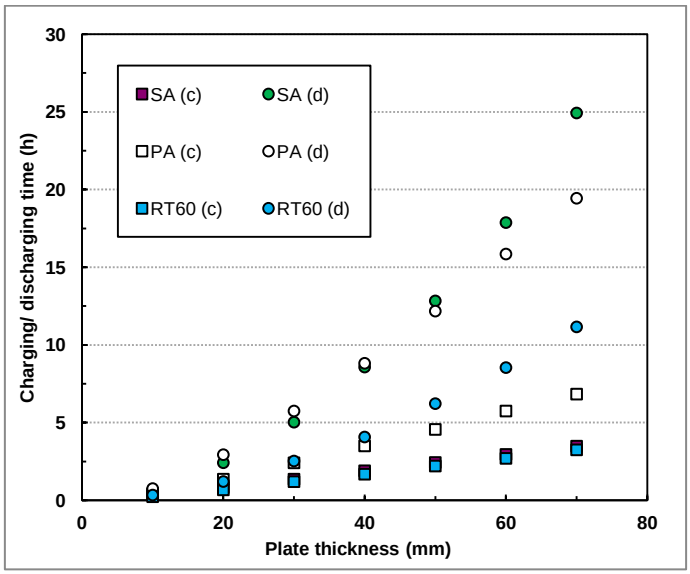

Figure 5-13: Simulated charging and discharging time (95 % energy ratio) for the LHTES system as a function of the plate thickness for 3 real PCMs

3.2.1. *Influence of natural convection upon charging*

To study the relevance of natural convection on melting, simulations neglecting the natural convection within the liquid PCM were also performed. To do that, the density of the PCM was defined as constant instead of using the Boussinesq approximation in the momentum equation (Section 2.2 - Eq. 5-6). The charging results corresponding to RT60, considering and neglecting natural convection are presented in Figure 5-15.

A noticeably different behavior can be observed when natural convection is neglected. As it can be seen, the trend of the charging time results versus plate thickness becomes parabolic,

likewise the solidification tendency attained when natural convection was included (Figure 5-14).

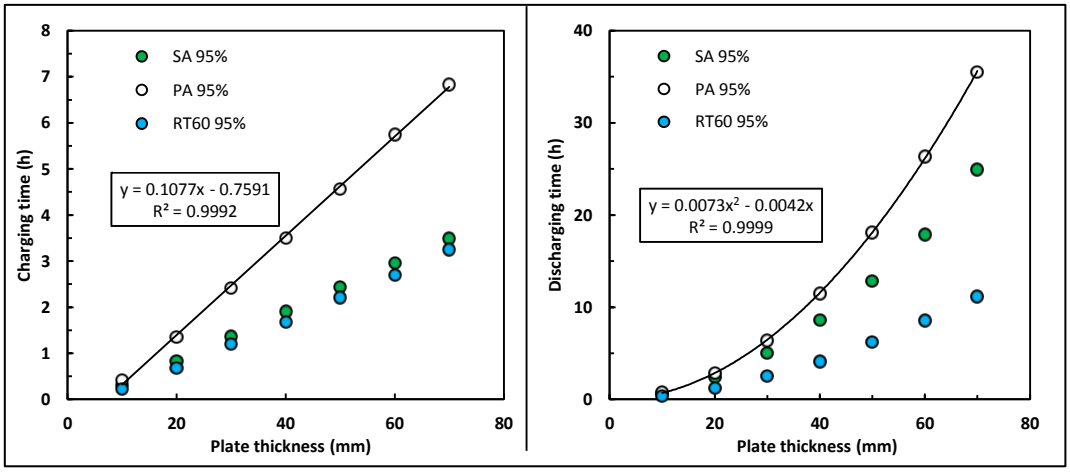

Figure 5-14: Simulated charging time (left) and discharging time (right) of the LHTES system for 3 real PCMs, for a 95 % energy ratio

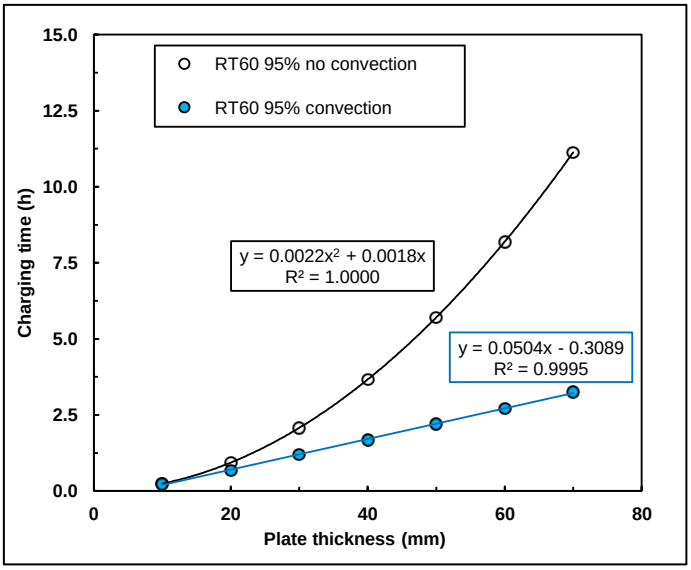

Figure 5-15: Charging time for the RT60 as a function of the plate thickness for simulations with and without natural convection within the PCM

The charging results considering and neglecting natural convection are provided in Table 5-6 (along with the discharging results). Errors up to 243 % are introduced if the effect of natural convection is neglected on the modeling of the system (Table 5-6). Moreover, the larger the plate thickness, the higher the error attained, as foreseen and explained by the influence of the Rayleigh number on natural convection within PCMs [125,126]. A similar behavior was found for PA, where errors up to 210 % were attained when natural convection was neglected.

	charging time (h) - RT60 95 % energy ratio			discharging time (h) - RT60 95 % energy ratio		
PCM thickness (mm)	Convection	No convection	Relative error	Convection	No convection	Relative error
70	3.25	11.13	243 %	11.16	14.84	33 %
60	2.70	8.20	203 %	8.54	10.99	29 %
50	2.21	5.71	159 %	6.22	7.64	23 %
40	1.68	3.67	118 %	4.08	4.97	22 %
30	1.20	2.08	73 %	2.53	2.85	13 %
20	0.68	0.94	39 %	1.21	1.32	9 %
10	0.23	0.24	5 %	0.34	0.37	11 %

Table 5-6: Charging and discharging time needed for a 95 % energy ratio as a function of the plate thickness for RT60: results with natural convection considered in the model and results without natural convection

The results indicate that neglecting convection upon melting is unsuitable depending on the case. This outcome, although not directly related with the main objective of the chapter, is relevant for the modeling of LHTES systems in general, because neglecting the natural convection inside the PCM is a modeling approach traditionally adopted in PCM-related research [17].

On the other hand, when the convection is taken into account, the linear trend shown by the results opens the possibility of developing a simplified correlation to model the melting behavior of plate-based LHTES systems upon melting. This can be faced in future works for applications where the charging process could be the limiting stage, like for instance solar systems where the heat has to be stored under constrained periods and the loads is distributed through the whole day.

3.2.2. *Influence of natural convection upon discharging*

The consideration of the natural convection on discharging has a relevant influence on the simplified correlation to be developed because the theoretical formulation of the heat transfer problem involved (Section 3.3.1) will be different if the effect is included or not.

Simulations of the discharging process neglecting natural convection within the liquid PCM were performed. The discharging time as a function of the plate thickness follows a parabolic trend in both situations, as shown in Figure 5-16 for RT60, either when natural convection is considered as well as when it is neglected. This indicates a low influence of natural convection upon solidification.

As shown in Table 5-6, the results for RT60 indicate that the maximum error upon discharging when convection is neglected is 33 %, attained when a 70 mm thickness is used. That thickness value (70 mm) is not suitable for real use due to the extremely high discharging time needed (11.2 h). The error for 30 mm plate thickness, or narrower plates, can be considered more representative of the reality. The errors on those cases are nearby 11 %. Even lower values were obtained in simulations using PA as PCM.

These errors, or differences, can be significant or not depending on the objective. In the case herein involved, since the principal aim consists on the development of a fast design methodology for LHTES systems, an extreme accuracy is not considered essential. Accordingly, neglecting natural convection within the PCM upon solidification was assumed as a reasonable approach for the theoretical formulation of the simplified correlation. This will be discussed in the following Section 3.3.

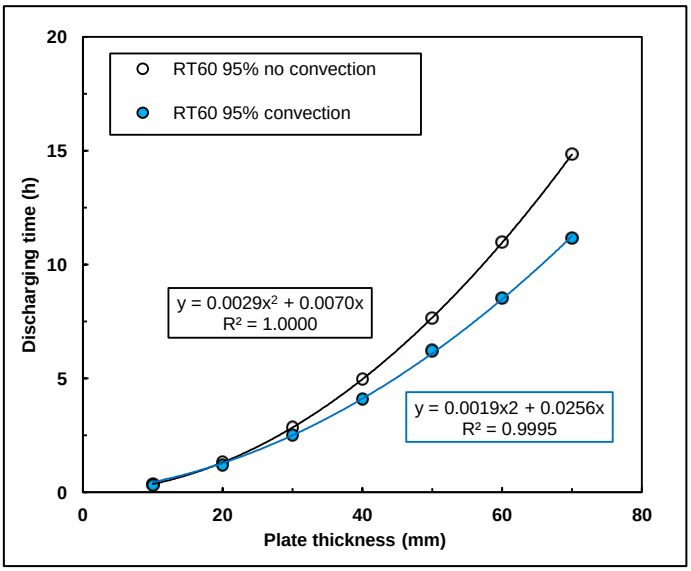

Figure 5-16: Discharging time needed for a 95 % energy ratio as a function of the plate thickness for the RT60 PCM: results considering the natural convection in the model and neglecting it

On the other hand, as it can be extracted from Table 5-6, the influence of natural convection upon melting is noticeably higher than on solidification. This difference allows drawing a general observation that is not directly related with the aims intended in the chapter, but is relevant for the selection of the optimum PCM phase change temperature to be employed in LHTES systems in general, as follows:

When a PCM is selected for a specific application it is accepted that the phase change temperature has to be placed between the highest and the lowest operation temperatures of

the system [13,15,33]. It is also well known that the relative position of this phase change temperature within the operation range will influence the charging and discharging time.

Accordingly, a commonly adopted solution is the selection of a PCM with a phase change temperature centered within that operation range because it is assumed that this will render equal charging and discharging times (provided that the PCM presents no hysteresis). That would happen if natural convection effects were negligible, or if natural convection has the same effect during the melting and the solidification processes.

However, it has been demonstrated that natural convection has a noticeably higher influence upon melting than upon solidification. As a result, a PCM with a phase change temperature centered in the operation temperature range will typically show a faster melting process and a slower solidification. Thus, when similar charging and discharging times are desirable, the phase change temperature to be selected has to be closer to the highest operation temperature. The exact phase change temperature within the interval should be determined based on the relative influence of the natural convection for each case.

Such a study, although out of the scope of this PhD dissertation, is commendable for the near future because most of the related literature includes the need of a "suitable" phase change temperature amongst the requirements of the PCM, but recommendations on the relative position of the phase change temperature within the operation interval are rarely given. Besides, the outcomes would optimize the exergetic performance of the system since a phase change temperature closer to the highest operation temperature would result in higher outlet temperatures along the discharging process [127].

After this broad study on the general behavior of the system and on the influence of the natural convection, the development of a simplified correlation to estimate the discharging time of the system is faced, considered to be the major task of the chapter.

3.3. Development of a simplified correlation to estimate the discharging time of plate-based LHTES systems

In order to develop the simplified correlation, a theoretical formulation of the heat transfer problem was first performed to identify which dimensionless numbers can be employed to solve the problem involved. Afterwards, 15 virtual PCMs were defined and CFD simulations were performed. The discharging time results obtained were adjusted by regression to get the

exponents and coefficients of the dimensionless numbers involved in the correlation. Finally, to validate the correlation, simulations with five additional PCMs were carried out and their results were compared with those obtained from the correlation.

3.3.1. *Theoretical formulation of the heat transfer problem: identification of the dimensionless numbers*

In order to identify the dimensionless numbers involved in the heat transfer problem, a theoretical analysis was carried out following a procedure equivalent to that proposed in ref. [128]. Like in the case of the above described CFD model, the domain consisted of a half-plate section transverse to the water flow direction (*xy* plane in Figure 5-2). In view of the results presented on Section 3.2, the heat transfer through the PCM was assumed conduction-driven. Besides, it was assumed that the heat conduction mainly occurs through the plate wall in the *x* direction.

As a consequence, the one-dimensional transient heat conduction equation [109] was considered suitable for the evaluation of the system. It is presented in Eq. 5-8. The term S computes the absorption or release of latent heat during the phase change (Eq. 5-9). The symbols presented throughout this subsection agree with the nomenclature provided at the beginning of the dissertation.

$$\rho C_p \frac{\partial T}{\partial t} = \lambda \frac{\partial^2 T}{\partial^2 x} + S \qquad \text{Eq. 5-8}$$

$$S = \rho \Delta H^{sl} \frac{\partial f}{\partial t} \qquad \text{Eq. 5-9}$$

With the aim of analyzing the impact of the parameters involved in the equation, a dimensionless form of Eq. 5-8 was deduced. To do that, the dimensionless numbers presented from Eq. 5-10 to Eq. 5-14 were defined. In the Fourier number (Eq. 5-11), *L* is the thickness of PCM (e_{pcm}), and α accounts for the thermal diffusivity. The Stefan number was defined as the ratio of sensible heat over the latent heat, being ΔT assumed to be 1 °C [128]. In Eq. 5-12, x represents the axial coordinate.

Stefan number: $Ste = \frac{C_p \Delta T}{\Delta H^{sl}}$ (where $\Delta T = 1\ °C$) Eq. 5-10

Fourier number: $Fo = \frac{\alpha_{PCM} t}{L^2}$ (where $L = PCM\ thickness\ (e_{pcm})$) Eq. 5-11

$$X = \frac{x}{e_{pcm}}$$ Eq. 5-12

$\theta_{pc} = \frac{T - T_s}{T_l - T_s}$ (where $T_s = solidus\ temperature;\ T_l = liquidus\ temperature$) Eq. 5-13

$\Psi = \frac{\Delta T}{T_l - T_s}$ (where $\Delta T = 1\ °C$) Eq. 5-14

Replacing the required terms of Eq. 5-8 by the herein defined dimensionless parameters renders the expression presented in Eq. 5-15.

$$\left(1 - \frac{\Psi}{Ste}\frac{\delta f}{\delta \theta_{pc}}\right)\frac{\delta \theta_{pc}}{\delta Fo} = \frac{\partial^2 \theta_{pc}}{\partial X^2}$$ Eq. 5-15

In addition, the convection boundary layer between the PCM and the HTF (see Figure 5-4) was described by the Eq. 5-16.

$$\lambda \frac{\partial T(0,t)}{\partial x} = h_{conv}(T_{HTF} - T(0)_{PCM})$$ Eq. 5-16

As performed with Eq. 5-8, the dimensionless groups involved in Eq. 5-16 were identified to rearrange the equation in its non dimensional form. They are shown from Eq. 5-17 to Eq. 5-20.

$$Bi = \frac{h_{conv} L_{Bi}}{\lambda_{pcm}}$$ Eq. 5-17

$$\Psi_{op} = \frac{T_{high\ HTF} - T_{low\ HTF}}{T_l - T_s}$$ Eq. 5-18

$$\Psi_{pc} = \frac{T_s - T_{HTF}}{T_l - T_s}$$ Eq. 5-19

$$\theta_{HTF} = \frac{T_{HTF} - T_{low\ HTF}}{T_{high\ HTF} - T_{low\ HTF}}$$ Eq. 5-20

Substituting these dimensionless numbers in Eq. 5-16, the formula shown in Eq. 5-21 is reached.

$$\frac{\delta\theta_{pc}(0,t)}{\delta X} = Bi\{[\theta_{HTF}(t)\,\Psi_{op} + \Psi_{pc}] - \theta_{pc}(0,t)\}$$ Eq. 5-21

The attempted correlation is aimed to be used to estimate the discharging time of the process. Accordingly, since *Fo* represents the dimensionless time of the process, an expression that correlates the *Fo* number with the rest of the dimensionless numbers involved was sought. Based on the dimensionless form of the involved equations (Eq. 5-15 and Eq. 5-21), the *Fo* number can be expressed as a function of the rest of the parameters in the way shown in Eq. 5-22.

$$Fo = {\alpha_{PCM} t}\Big/{e_{pcm}}^2 = f(Ste\,, Bi, X, \theta_{pc}, \theta_{HTF,}\, \Psi, \Psi_{op}, \Psi_{pc})$$ Eq. 5-22

The *Fo* number as defined in Eq. 5-22 is time-dependent along the discharging process. However, since the correlation sought is aimed to be used for design/sizing purposes, the variable wanted to be calculated is the time needed to achieve a complete discharging of the system. As described in Section 2.3, the system is considered fully discharged when a 95 % energy ratio is released. As a result, a single *Fo* number (Fo_{95}) is proposed, shown in Eq. 5-23. There, t_{95} is the time needed to achieve a 95 % discharging energy ratio.

Thus, Fo_{95} is referred to the completed process and thus it does not depend on those dimensionless groups that in Eq. 5-22 are related with the dynamic nature of the process, i.e.: X, $\theta_{pc}$and θ_{HTF}. Based on this, Eq. 5-24 shows the relation of Fo_{95} with the formerly identified dimensionless numbers.

$$Fo_{95} = {\alpha_{PCM} t_{95}}/{e_{pcm}{}^2} \qquad \text{Eq. 5-23}$$

$$Fo_{95} = f(Ste\,, Bi, \Psi, \Psi_{op}, \Psi_{pc}\,) \qquad \text{Eq. 5-24}$$

The parameters that characterize all the dimensionless numbers included on the proposed expression (Eq. 5-24) are broken down in Table 5-7. As it can be observed, all the items needed to calculate *Fo$_{95}$* are completely defined by either the properties of the PCM, the properties of the HTF or parameters that are constrained by the operation conditions of the application (domestic CHP for the case involved).

As a result, the proposed *Fo$_{95}$* number can be used for the calculation of the discharging time as a function of the plate thickness, the materials properties and the plant operation parameters. Accordingly, a parametrical study to determine the exact relation of the *Fo$_{95}$* with the rest of dimensionless number was performed. Before proceeding with the results of the study, the properties of 15 virtual PCMs were defined. They are detailed next.

3.3.2. Definition of 15 virtual PCMs to develop a correlation for the Fo number

According to the constraints discussed in the previous section, 15 virtual PCMs were defined, together with the following thermal properties: melting temperature, melting enthalpy, density, specific heat and thermal conductivity. In the case of the melting temperature, two different parameters were varied: the average melting temperature (which was obtained from the mean value of the solidus and liquidus temperature), and the melting temperature range (calculated from the difference from the latter two temperatures).

The values for the properties were selected based on literature values [12,13,26,33,91] of existing PCMs at the temperature range involved. The first step comprised the definition of the

maximum and minimum values of each property to be employed in the study, which are shown in Table 5-8. Those values that need an explanation are discussed next.

Dimensionless number	Parameters involved	Dependency of the parameters involved
Ste	C_p	PCM property
	ΔH^{sl}	PCM property
	ΔT	Defined as 1 °C
Bi	$h_{conv} = \frac{Nu \cdot 2 \cdot e_{HTF\ channel}}{\lambda_{HTF}}$	Nu =8.235 (laminar flow requirement – Section 2) λ_{HTF}= Property of the HTF $e_{HTF\ channel}$= channel thicnkess of the HTF (fixed to 2 mm due to constraints of the application – Section 2)
	$L_{Bi} = \frac{V_{PCM}}{S_{PCM-HTF}} = \frac{e_{PCM}}{2}$	e_{PCM}= thickness of the PCM. (this is the variable to be optimized as a function of the discharging time)
	λ_{pcm}	PCM property
Ψ	T_l	PCM property
	T_s	PCM property
	ΔT	Defined as 1 ºC
Ψ_{op}	$T_{low\ HTF}$	Defined by the application (50 ºC in the case involved)
	$T_{high\ HTF}$	Defined by the application (65 ºC in the case involved)
	T_l	PCM property
	T_s	PCM property
Ψ_{pc}	$T_{low\ HTF}$	Defined by the application (50 ºC in the case involved)
	T_l	PCM property
	T_s	PCM property

Table 5-7: Break down of the parameters that characterize all the dimensionless numbers involved in the expression proposed for the *Fo number* (Eq. 5-24)

The lowest thermal conductivity (0.162 W/mK) was chosen based on the value of PA, which presented the lowest value of the 3 real PCMs previously studied. The maximum value of the thermal conductivity is 2 W/mK, which is achievable only by the use of PCM composites; however, even though the use of composite-PCM lies out of the scope of this PhD work, it was considered interesting to extend the range of application of the correlation to PCM composites. The lowest density, again, had the same value of PA, 852 kg/m^3, while the highest one, 1500 kg/m^3, can be considered typical for inorganic compounds like hydrated salts for the temperature range involved.

Property	Thermal conductivity (W/mK)	Cp (kJ/kg K)	Latent phase change enthalpy (kJ/kg)	Average phase change temperature (ºC)	Phase change temperature range (ºC)	Density (kg/m^3)
Minimum value	0.162	1.5	100	53.75	0.5	852
Maximum value	2	3	200	62.25	4	1500

Table 5-8: Minimum and maximum values of the properties that defined the virtual PCMs

According to the selected the minimum and the maximum values, each PCM was defined. The resultant virtual PCMs are listed in Table 5-9 along with their thermophysical properties. The effective C_p vs. temperature curve, used as an input in the CFD model (Section 2.4.1), was

obtained from the enthalpy vs. temperature curve, which was in turn constructed from the corresponding thermal properties of each PCM.

The thermal expansion coefficient and the viscosity were adopted from the PA values: 0.00078 K^{-1} and 0.00764 kg/m·s, respectively. These values were employed for all the virtual PCM materials because these properties are relevant in natural convection but not on the thermal diffusion that dominates the process in solidification. Since the formulation of the heat transfer problem was based on a conduction-driven situation, the significance of these properties was foreseen to be irrelevant.

The values of the dimensionless numbers resulting for each PCM simulated are also presented in Table 5-9. Note that the *Bi* and *Fo* numbers depend also on the plate thickness, and thus different values were obtained for each PCM, as many as the number of different thickness values simulated. For the sake of brevity, only the minimum and the maximum values are shown in the table for these two dimensionless numbers.

ID PCM	ΔH_{sl} (kJ/kg)	C_p (kJ/kgK)	λ (W/mK)	T_s(°C)	T_l (°C)	$\overline{T}_{s\text{-}l}$ (°C)	T_s - T_l (°C)	ρ (kg/m^3)	*Fo* min	*Fo* max	*Bi* min	*Bi* max	*Ste*	Ψ	Ψ_{op}	Ψ_{pc}	Property varied with this PCM
1	150	2.3	0.162	63	61.5	62.25	1.5	852	0.72	0.8	37	260	0.015	0.67	10	7.7	
2	150	2.3	0.162	59	57.5	58.25	1.5	852	0.92	1.03	74	260	0.015	0.67	10	5	
3	150	2.3	0.162	54.5	53	53.75	1.5	852	1.61	2.1	37	260	0.015	0.67	10	2	Melting temperature
4	150	2.3	0.162	60	56	58	4	852	0.83	1.1	37	260	0.015	0.25	3.8	1.5	
5	150	2.3	0.162	57	55	56	2	852	1.01	1.33	37	260	0.016	0.50	7.5	2.5	
6	150	2.3	0.162	53.5	53	53.25	0.5	852	2.34	2.51	37	260	0.015	2.00	30	6.0	
7	100	2.3	0.162	59	57.5	58.25	1.5	852	0.67	0.79	37	260	0.023	0.67	10	5	Melting enthalpy
8	200	2.3	0.162	59	57.5	58.25	1.5	852	1.14	1.35	37	260	0.012	0.67	10	5	
9	150	2.3	0.5	59	57.5	58.25	1.5	852	0.98	1.21	12	84	0.015	0.67	10	5	
10	150	2.3	1	59	57.5	58.25	1.5	852	1.03	1.21	6	42	0.015	0.67	10	5	Thermal conductivity
11	150	2.3	2	59	57.5	58.25	1.5	852	1.09	1.79	3	21	0.015	0.67	10	5	
12	150	2.3	0.162	59	57.5	58.25	1.5	1500	0.84	1.07	37	260	0.015	0.67	10	5	Density
13	150	2.3	0.162	59	57.5	58.25	1.5	1200	0.92	1.02	74	223	0.015	0.67	10	5	
14	150	1.5	0.162	59	57.5	58.25	1.5	852	1.47	1.57	74	223	0.009	0.67	10	5	C_p
15	150	3	0.162	59	57.5	58.25	1.5	852	0.76	0.79	74	223	0.021	0.67	10	5	

Table 5-9: Thermophysical properties of the virtual PCMs defined for the study

3.3.3. Simplified correlation to estimate the system discharging time

Simulations with the above defined fifteen virtual PCMs were performed in order to determine the precise relation of the Fo_{95} with the rest of dimensionless numbers presented in Eq. 5-24. The time required to achieve a 95 % discharging ratio was the variable under analysis.

The simulations were planned for 7 different thickness values (10 to 70 mm) per PCM. However, only 3 different thickness values were simulated for PCMs 13, 14 and 15 to reduce the time consumption. This was considered valid as it was observed that 3 points were enough to study the influence of each variable. Besides, only four cases were run for the PCM 6 and six cases for the PCM 2 and PCM 12, instead of seven. As a result, 86 different cases were simulated.

In order to develop the sought correlation, a multiple linear regression analysis of all the data available was performed. This technique allows the study of the relationship between one continuous dependent variable from two or more independent variables [129]. It fits a line through a multi-dimensional cloud of data points. The general form of the multiple linear regression is shown on Eq. 5-25.

$$y = a_0 + a_1 x_1 + a_2 x_2 + \ldots + a_n x_n \qquad \text{Eq. 5-25}$$

To attain a final expression where the independent variable is related with the product of the exponentials of the independent variables, a logarithmic transformation was applied to Eq. 5-25, as shown in Eq. 5-26. The natural logarithm of the Fo_{95} number was considered as the dependent variable. The natural logarithms of the remaining dimensionless numbers (Eq. 5-24) acted as independent variables.

Applying logarithmic properties, Eq. 5-26 was rearranged to reach the expression presented in Eq. 5-27. The coefficients *a0*, *a1*, etc. represent the exponents for each dimensionless number. The constant *C* is obtained by means of the transformation shown in Eq. 5-28.

$$Ln\,Fo = a_0 + a_1 Ln\,Ste + a_2 Ln\,Bi + a_3 Ln\,\Psi + a_4 Ln\,\Psi_{op} + a_5 Ln\,\Psi_{pc} \qquad \text{Eq. 5-26}$$

$$Fo_{95} = C\ Bi^{a_1} Ste^{a_2}\ \Psi^{a_3}\ \Psi_{op}^{a_4}\ \Psi_{pc}^{a_5}$$ Eq. 5-27

$$C = e^{a_0}$$ Eq. 5-28

The multivariable analysis was performed by means of the MS excel software. This software gives certain regression statistics to evaluate the fitting degree between the data and the calculated linear regression equation. A brief explanation of each term is given next [129].

- Multiple R: It is the correlation coefficient, which indicates how strong the linear relationship is. A value of 1 means a perfect positive relationship and a value of zero means no relationship at all. It is the square root of R squared (see below)
- R squared (R^2): This is the *Coefficient of Determination* or *Pearson´s R*. It gives an indication about how many points fall on the regression line. For instance, a value of 0.8 indicates that 80 % of the values of the dependent variable (*y*) are explained by the independent variables employed (x_1, x_2…x_n)
- Adjusted R square (Adjusted R^2): This parameter adjusts the aforedescribed R squared (R^2) to the number of terms in a model. This is the parameter that has to be employed when more than one dependent variable is employed, like the case involved. While R^2 assumes that every single variable explains the variation in the dependent variable, the adjusted R^2 indicates the percentage of variation explained only by the independent variables that actually affect the dependent variable. The adjusted R^2 will penalize the addition of independent variables that do not fit the model, which helps to identify which are significant and which are not
- Standard Error: It represents the average distance that the observed values fall from the regression line. The smaller the values are, the better the model is, since the observations will be closer to the regression line

In addition to the abovementioned parameters, the p-value was used to evaluate the statistical significance of each independent variable included in the regression equation. The p-value tests the null hypothesis of each variable. A value lower than 0.05 indicates that the null hypothesis for that independent variable can be rejected, and therefore, that the variable has statistical significance.

The multiple regression adjustment was performed including all the dimensionless numbers defined in Eq. 5-24. The obtained correlation is shown in Eq. 5-29.

$$Fo_{95} = 0.25\, Bi^{-0.10} Ste^{-0.78}\, \Psi^{0.89}\, \Psi_{pc}^{-0.67} \qquad \text{Eq. 5-29}$$

The exponent obtained for the dimensionless temperature Ψ_{op} was zero; thus, it was taken out of the equation. This is an expected behavior because in the present case the working temperatures of the HTF were constrained by the CHP plant and they had the same values for all the simulations performed (65 and 50 °C). Therefore, Ψ_{op} was redundant with Ψ under the imposed constraints. Note however that this parameter would, presumably, have influence under different HTF operation temperatures, and thus should not be discarded in further studies on the topic.

The *adjusted Pearson's R* obtained for the correlation was 0.976, which can be considered a good fit for the aims sought. This indicates that 97.6 % of the data are explained by the resultant correlation. The p-values for all the variables included in the equation (Eq. 5-29) were lower than $1 \cdot 10^{-16.}$ This means that the null hypothesis can be neglected for all of them and thus each of them has actual influence on the equation.

The adjustment of the correlation can be visualized in Figure 5-17. The discharging time obtained by means of the correlation was compared with those obtained by means of the original CFD simulations. The average error was 3.5 %.

The correlation given in Eq. 5-29 uses the time needed to achieve 95 % discharging ratio of the system. This value is considered representative of a complete discharge of the system and thus can be employed for design purposes. However, it was considered of interest to analyze the influence of the discharging ratio (E) on the correlation. This variable was included in the formula as an additional dimensionless number. A multivariable analysis was performed by including the discharging time calculated for three different discharging ratios: 98, 95 and 85 %. Accordingly, 258 data were used to fit the correlation.

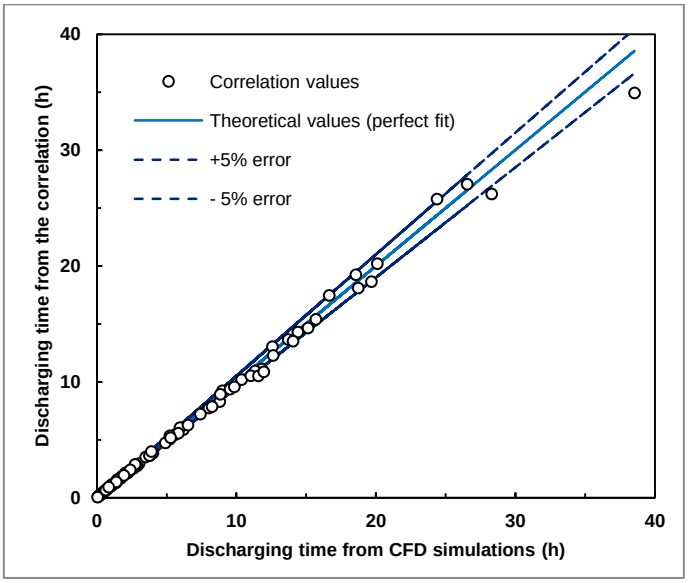

Figure 5-17: Comparison of the discharging time of the LHTES system calculated by the simplified correlation vs. the values calculated by CFD simulations

The resulting expression can be found in Eq. 5-30. The *adjusted Pearson´s R* value was high, with a value of 0.972. The comparison of the parameters and exponents of the two correlations and the range of validity in terms of discharging ratio are shown in Table 5-10.

The exponents of the new correlation present values similar to those attained for the correlation when the 95 % discharging energy ratio is used. The constant *C* is slightly different on both cases. The average error between the discharging time obtained through the correlation and the CFD theoretical results was 4.52 %. The use of this new correlation (Eq. 5-30) would allow evaluating the effect of a potential increase of the thermal output power of the LHTES system as a consequence of a partial sacrifice of the storage capacity.

$$Fo_{85-98} = 0.30\, Bi^{-0.11} Ste^{-0.78}\, \Psi^{0.89}\, \Psi_{pc}^{-0.65} E^{2.9} \qquad \text{Eq. 5-30}$$

	Discharging ratio validity range	Value of the constant	Values of the exponents of the dimensionless numbers					Adjusted Pearson´s R	Mean relative error
Correlation	**%**	***C***	***Bi***	***Ste***	***Ψ***	***Ψpc***	***E***	R	%
1 (Eq. 5-29)	95	0.25	-0.10	-0.78	0.89	-0.67	_	0.976	3.51
2 (Eq. 5-30)	85 to 98	0.30	-0.11	-0.78	0.89	-0.65	2.9	0.972	4.52

Table 5-10: Comparison of the parameters and exponents of the two correlations and the range of validity in terms of discharging ratio

In order to validate the Fo_{95} correlation (Eq. 5-29), five new PCMs were defined, starting from combinations of thermal properties different to those employed for the 15 virtual PCMs used to correlate the data.

The new PCMs were defined in a way that they covered a similar Fo_{95} range than previously covered by the 15 PCMs (shown in Table 5-9). Simulations were performed with the 2D CFD model to calculate the time needed to achieve a 95 % of discharge energy ratio. The discharging time was also calculated by means of the developed simplified correlation (Eq. 5-29). The results achieved are shown in Table 5-11, along with the physical properties of the 5 PCMs.

Good agreement was attained between the discharging time results obtained by the CFD simulations and the correlation. The maximum error attained was 4.8 %, achieved with the PCM C2 and a thickness of 40 mm. The *Fo* number for this PCM is close to the maximum value of *Fo* covered by the correlation and, as a result, it can be considered the worst-case scenario. The average error between the results attained by the CFD simulations and the correlation for the 15 simulations performed (3 thickness values x 5 PCMs) was 2.38 %. Consequently, the correlation developed can be employed confidently for design purposes to determine the discharging time of plate based LHTES systems that operate under the constraints defined troughout the chapter and within the above mentioned *Fo* number range.

PCM	PCM thickness (mm)	Thermal conductivity (W/mK)	C_p (kJ/kgK)	Density (kg/m^3)	Latent enthalpy (kJ/kg)	Average melting temp (ºC)	Thermal diffusivity (m^2/s)	*Bi* number	*Ste* number	Ψ	Ψ_{pc}	*Fo* number (obtained from the correlation)	Discharging time obtained with the correlation (h)	Discharging time obtained from CFD (h)	Relative discharging time error
C1	20	1	2.3	852	100	58.25	5.10E-07	11.0	0.159	0.67	5.00	0.88	0.193	0.191	0.9 %
	30	1	2.3	852	100	58.25	5.10E-07	15.8	0.159	0.67	5.00	0.85	0.417	0.407	2.6 %
	40	1	2.3	852	100	58.25	5.10E-07	20.2	0.159	0.67	5.00	0.83	0.724	0.693	4.4 %
C2	20	0.162	2.3	1500	200	54.25	4.70E-08	67.9	0.047	0.67	2.33	2.09	4.947	5.010	1.3 %
	30	0.162	2.3	1500	200	54.25	4.70E-08	97.5	0.047	0.67	2.33	2.01	10.722	10.540	1.7 %
	40	0.162	2.3	1500	200	54.25	4.70E-08	124.9	0.047	0.67	2.33	1.96	18.583	17.740	4.8 %
C3	20	0.2	2.3	1300	150	58.25	6.69E-08	55.0	0.111	0.67	5.00	1.04	1.733	1.710	1.3 %
	30	0.2	2.3	1300	150	58.25	6.69E-08	79.0	0.111	0.67	5.00	1.00	3.755	3.720	1.0 %
	40	0.2	2.3	1300	150	58.25	6.69E-08	101.1	0.111	0.67	5.00	0.98	6.509	6.460	0.8 %
C4	20	0.4	2.3	1000	115	56.25	1.74E-07	27.5	0.110	0.67	3.67	1.11	0.710	0.693	2.5 %
	30	0.4	2.3	1000	115	56.25	1.74E-07	39.5	0.110	0.67	3.67	1.07	1.539	1.503	2.4 %
	40	0.4	2.3	1000	115	56.25	1.74E-07	50.6	0.110	0.67	3.67	1.04	2.668	2.580	3.4 %
C5	20	0.4	2.3	1000	115	56.25	1.74E-07	27.5	0.110	0.67	3.67	1.11	0.710	0.693	2.5 %
	30	0.4	2.3	1000	115	56.25	1.74E-07	39.5	0.110	0.67	3.67	1.07	1.539	1.503	2.4 %
	40	0.4	2.3	1000	115	56.25	1.74E-07	50.6	0.110	0.67	3.67	1.04	2.668	2.580	3.4 %

Table 5-11: Properties of the virtual PCMs employed to test the validity of the developed correlation

3.4. Overall design methodology for plate based LHTES for domestic CHP applications

After the correlation to determine the discharging time was defined, the development of an overall design method for plate based LHTES systems was approached. The herein proposed procedure is specifically focused on CHP applications, but with small modifications it could be easily extended to other technologies. On the present case, the discharging process was considered the limiting step; however, on other applications charging could be the restraining process. A schematic diagram of the process is depicted on Figure 5-18.

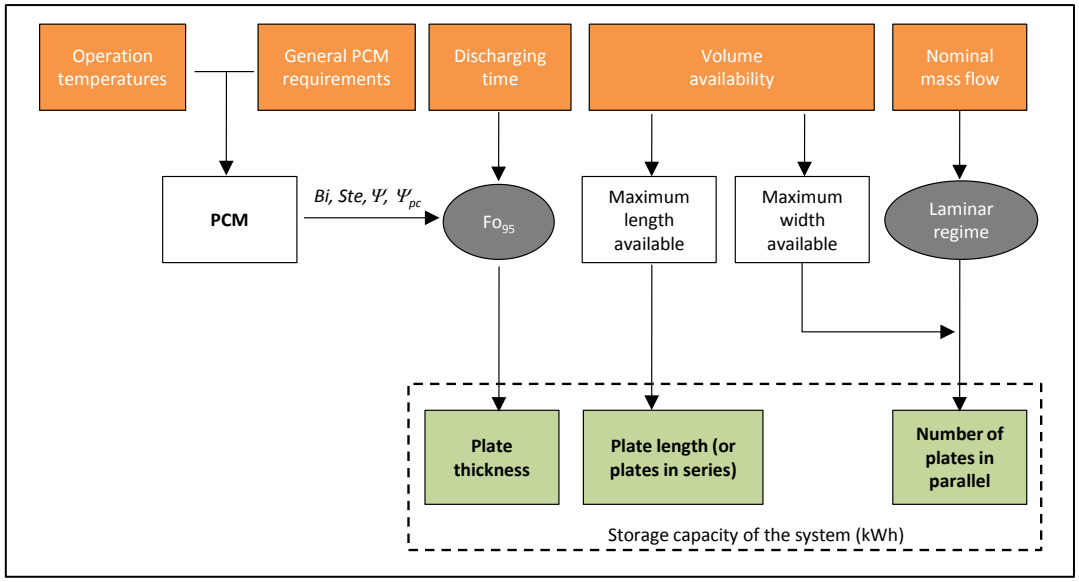

Figure 5-18: Schematic overview of the design methodology proposed

The method is based on the constraints shown in orange on Figure 5-18. Amongst them, the operation temperatures and the nominal mass flow are fixed by the CHP plant [5]. The PCM requirements are well known and widely available in the literature [13,20]. The discharging time is defined by the forecasted user-consumption profile.

The remainder constraint is the volume availability. It is important to remark that the proposed methodology assumes that a limited volume is available due to the domestic nature of the application. Accordingly, it is considered that the maximum volume available will be equivalent to the size of a household appliance (approximated dimensions: 600 mm deep; 600 mm wide and 850 mm high). Thus, the objective of the methodology is to maximize the storage capacity of a system that fits in the defined volume and is able to provide the thermal

power required to achieve the discharging time previously calculated from the user demand profile.

There is an additional constraint to be added to those shown on Figure 5-18: the plates where the PCM is enclosed are constructed from extruded commercial hollow profiles of rectangular section [112]. This choice has the aim to optimize the manufacturing procedure (see Chapter 6) and therefore the commercial availability will constrain the thickness and height of the plates to those sizes available in the market.

Based on these constraints, the overall design method is comprised by three main steps, which are detailed next.

3.4.1. Determination of the plate thickness

The determination of the maximum plate thickness to be used is the most important step. It will be calculated based on the simplified correlation developed in Section 3.3. To do so, a maximum acceptable discharging time has to be first defined ($t_{95\,max}$), which is estimated for each case depending on the forecasted user-consumption profile.

Then, one or more PCMs are chosen according to the requirements present in the literature [20]. The maximum plate thickness will be influenced by the PCM selected; thus, the design process has to be accomplished for each PCM considered. The best choice will depend on the evaluation criteria chosen for the design (energy density, economic feasibility, etc.).

In all cases, the phase change temperature of the PCMs will be selected based on the operation temperature range of the CHP plant. This operation interval is fixed by the characteristics of the CHP plant, but it can be slightly adapted to maximize the performance of the system [5]. For instance, in the present work, a 50-65 °C temperature range was selected as the CHP working interval. However, different pairs of temperatures can be tested for each PCM considered, since the relative position of the phase change temperature of the PCM within the operation interval selected influences the discharging time of the LHTES system [5].

Once the PCM(s) selected, the operation temperatures and the maximum acceptable discharging time are defined, all the dimensionless numbers present in the correlation (Eq. 5-29) can be calculated. The form of the correlation presented in Eq. 5-29 relates the Fo_{95} number as a function of the remaining dimensionless numbers. Therefore, that formula was

combined with Eq. 5-23 and rearranged to achieve an expression that provides the maximum PCM thickness ($e_{PCM\,max}$) that can be used to achieve the discharging time previously defined (Eq. 5-31). This maximizes the storage capacity while assuring the required thermal power output. Note that in Eq. 5-31, the *Bi* number also depends on the PCM thickness and thus an iterative process is required.

$$e_{PCM\,max} \leq \sqrt{t_{95\,max}\,\frac{\alpha_{PCM}}{0.25\,Bi^{-0.10}Ste^{-0.78}\,\Psi^{0.89}\,\Psi_{pc}^{-0.67}}} \qquad \text{Eq. 5-31}$$

The plate thickness (e_p) will be comprised by the sum of the maximum PCM thickness ($e_{PCM\,max}$) calculated by Eq. 5-31 and the plate wall thickness (e_w) multiplied by 2 (the PCM is contained in the rectangular boxes with a certain wall thickness). Since the plates are built from extruded commercial rectangular hollow profiles, the dimensions have to be adapted to the values on the market (see Appendix B or ref. [112]). The selected plate thickness (e_p) will be the minimum value on offer that ensures a suitable plate mechanical behavior without compromising the manufacturing. The chosen plate thickness (e_p) will correspond to the commercial hollow profile with the largest available thickness while ensuring that this value is lower than the sum of the maximum PCM thickness ($e_{PCM\,max}$) plus two times the plate wall thickness (e_w), as shown in Eq. 5-32.

$$e_p \leq e_{PCM\,max} + 2 \cdot e_w \qquad \text{Eq. 5-32}$$

To finish with this step, the height of the plate has to be defined. Due to the assumed one-dimensional nature of the heat transfer problem involved (Section 3.3.1), the plates height was not included as a variable in the correlation because it was foreseen to have non-significant influence on the discharging rate (Section 2.1.1.3). Since commercial hollow profiles will be used, as it can be seen in Appendix B, only certain height values are available for each thickness. Accordingly, in order to minimize the manufacturing labor, the maximum available height for the plate thickness selected has to be employed.

3.4.2. Determination of the number of plates in parallel

When the plate thickness, the plate height and the wall thickness are defined, the number of plates to be placed in parallel is calculated. This is an iterative process that depends on the maximum width available for the prototype (600 mm in the present case) and on the laminar flow requirement.

An initial value for the HTF channel thickness has to be first defined. In order to maximize the PCM amount included in the system, the heat transfer rate and to minimize the pressure drop, the minimum HTF thickness value that can be achieved without compromising the fabrication of the system has to be selected [5]. As an example, in the present work (Chapter 6) a value of 2 mm was considered suitable. Note that, in the present study, this was considered a fixed value; however, it could be treated as a variable if considered necessary for a defined case.

Once the HTF channel thickness is fixed, the number of plates in parallel can be estimated based on the calculated plate thickness (e_p), the HTF channel thickness (e_c) and the maximum width available for the LHTES system (e_{LHTES} = 600 mm), as shown in Eq. 5-33. Note that the number of channels must be equal to the number of plates in parallel minus one (Eq. 5-34), because two plates are in contact with the lateral sides of the enclosure. Thus, the final number of plates will be that maximum integer number that fulfills the condition presented in Eq. 5-35.

$$n_p \cdot e_p + n_c \cdot e_c \leq e_{LHTES}(600\ mm) \quad \text{Eq. 5-33}$$

$$n_c = n_p - 1 \quad \text{Eq. 5-34}$$

$$n_p \leq \frac{e_{LHTES} + e_c}{e_p + e_c} \quad \text{Eq. 5-35}$$

The obtained number of plates has to ensure that the HTF moves through the channels on a laminar flow regime. Accordingly, since the total mass flow rate of the system is imposed by the CHP unit, the flow must be divided into a minimum number of channels that assure a laminar flow through each channel. Accordingly, the Reynolds number of the HTF (Re_{HTF}) should remain below 2300 [109], as shown in Eq. 5-36. There, $\overline{v}_{HTF}$ accounts for the average

velocity of the HTF inside the channel. Substituting Eq. 5-34 into Eq. 5-36 and rearranging the velocity term as a function of the channel thickness, Eq. 5-37 is attained.

If the minimum number of plates ($n_{p\,min}$) achieved by Eq. 5-37 is higher than the actual number of plates in parallel determined by Eq. 5-35 (n_p), then the thickness of plates has to be reduced in order to be able to include more plates in the system until the laminar flow condition is met. Otherwise, the number of plates in parallel can be considered suitable and the last design step can be faced, explained next.

$$Re_{HTF} = \frac{\rho_{HTF} \cdot \overline{v}_{HTF} \cdot 2e_c}{\mu_{HTF}} \leq 2300 \qquad \text{Eq. 5-36}$$

$$n_{p\,min} = \frac{2 \cdot \rho_{HTF} \cdot \dot{Q}_{HTF}}{2300 \cdot \mu_{HTF} \cdot h_{conv}} + 1 \qquad \text{Eq. 5-37}$$

3.4.3. Determination of the length and/or number of plates in series

Finally, depending on the space available for the LHTES system, the length of the plates (and the number of plates in series) is determined. In the present case, the maximum available plate length is limited to the maximum length of the system (600 mm). Considering the available commercial sizes, the maximum height of the plates will be noticeably lower than the height available for the prototype; as a result, a configuration with several plates placed height wise and connected in series is preferred.

For instance, with the dimensions assumed in this chapter (around 210 mm of plate height vs 850 mm available for the system), four plate levels could be arranged heightwise. Thus, an equivalent length of 4 x 600 mm = 2400 mm would be achieved.

In any case, the final configuration will also be delimited by the presence of ancillary systems, such as heat exchangers or others that could require being included in the system.

With the final dimensions and the properties of the materials, the total energy storage capacity of the system will be calculated. The cost can also be estimated in order to perform an economic analysis. The process has to be performed for each PCM available in order to decide the configuration that optimizes the behavior and profitability of the plant.

Note finally that, in the present case, one of the starting constraints was the maximum volume available for the system due to the domestic nature of the application. This rendered a methodology with the objective to maximize the storage capacity of a system that fits into the defined volume. However, the process could be performed on the opposite direction: starting from a specific storage capacity, the minimum volume to achieve that storage capacity would be calculated. The way of applying the methodology depends on the objectives of each case and the application where the LHTES system will be included.

The sizing procedure herein developed will be applied in Chapter 6 to design the full-scale LHTES prototype to be constructed and tested. A complete thermal and economical study of the prototype will be also included.

4. Conclusions of the chapter

The main goal of this Chapter was the development of a fast and systematic calculation tool for the sizing and optimization of plate-based LHTES systems. The main conclusions attained are summarized next.

Conclusions regarding the simulations performed to understand the discharging behavior of the system as a function of the plate thickness, as well as the influence of natural convection on the system:

- The charging time of the system as a function of the plate thickness shows a linear trend, which opens the possibility of developing a simplified correlation to model the melting behavior of plate-based LHTES systems upon melting. Conversely, the discharging time shows a parabolic tendency in relation to the plate thickness
- Neglecting convection upon melting is an unacceptable modeling approach for the operation conditions herein involved
- Upon solidification, the influence of natural convection is noticeably lower than on melting. As a result, the natural convection on the discharging stage can be neglected on the models depending on the degree of accuracy needed for the work
- The well-known requirement for PCMs that states that any PCM has to present a phase change temperature comprised within the operation temperatures of the application is not sufficient for design purposes. The optimum relative position of the phase change temperature within the interval depends noticeably on the influence of

natural convection (amongst others). Further studies are required to investigate this effect

The development of a simplified correlation that links the discharging time with the plate thickness, the PCM properties and the operation constraints of the application was faced.

- A dimensionless number proposed, Fo_{95}, can be used for the calculation of the discharging time as a function of several dimensionless groups (*Bi*, *Ste*, Ψ and Ψ_{pc}). These groups depend in turn on the plate thickness, the materials properties and the plant operation parameters
- The results of 86 CFD simulations were adjusted by means of a multiple linear regression analysis to develop the correlation. A good fit for the aims sought was obtained, with an adjusted Pearson's R of, 0.976. The discharging time obtained by means of the correlation was compared with those obtained by means of the original CFD simulations. The average error of the correlation with respect to the CFD simulations was 3.5 %
- An additional expression was developed that covered discharging ratios from 85 % to 98 % by the adjustment of 258 data. The expression showed a high adjusted Pearson´s R: 0.972, suitable for design purpose
- The Fo_{95} correlation was validated against 5 virtual PCMs. The discharging times obtained by CFD and by means of the simplified correlation were compared. The average error was 2.38 %. Consequently, the developed correlation can be employed confidently for design purposes to determine the discharging time of plate based LHTES systems that operate within the Fo_{95} number ranges previously defined

The work was completed with the development of an overall design method for plate based LHTES systems for CHP applications. This method consists of 3 simple steps and produces a complete sizing of the system without the need of simulations. Besides, with small modifications, it could be easily extended to other applications. The procedure noticeably simplifies the design process of LHTES systems and decreases the time needed to size them.

CHAPTER 6: Design, construction and evaluation of a full-scale plate-based LHTES prototype for domestic CHP applications

ABSTRACT

In the present chapter, a full-scale plate-based LHTES prototype is designed, built and evaluated within a micro-CHP plant under representative conditions. The methodology proposed in the previous Chapter 5 is applied to design it. A fabrication procedure will be proposed for each component of the prototype. The chapter includes also an integrity test of the components, in order to check the suitable behavior of seals and welds.

The LHTES prototype will be coupled to the micro-CHP plant and tested. The results will be analyzed in terms of energy capacity and time needed for charging and discharging. Finally, an economic study is performed to evaluate the actual feasibility of the system. The PCM employed in the pilot-plant experiments will be RT60; however, the economical study will include the assessment of the LHTES system using the PCMs developed along chapters 2, 3 and 4 as well the fatty acids previously characterized in Chapter 5.

This way, an overall picture of the feasibility of the LHTES system together with the materials developed is attained. This study will be also employed to evaluate further improvements of the system and reduce its cost.

1. Introduction

The thermal and economic aspects of the behavior of the LHTES system involved in this work were previously evaluated by Campos-Celador [5]. The conclusions of his PhD dissertation suggested that the system can be economically competitive against the traditional water storage tanks for heating and DHW applications. In addition, the storage volume required was reduced to the half. However, the features of the system were studied theoretically and by means of a laboratory-scale small prototype while no full-scale-prototype was manufactured and evaluated. Thus, the full-scale or the industrial design and fabrication of the system were not comprehensively studied.

It is well known that in every engineering application there is an important gap between the conceptual design of a system and its production and full-scale behavior. The extent of this gap depends on several factors such as the level of detail included in the previous theoretical studies or the state of the art of the available manufacturing technologies, amongst others. Accordingly, the present chapter deals with these aspects in order to gain knowledge about the actual economic feasibility of plate based LHTES systems in general and of the herein proposed system in particular.

When recently published literature review articles about the behavior of LHTES systems are consulted [16,17,25,130,131], it can be derived that most of the works deal with the shell-and-tube and double pipe heat exchangers. As a result, a reasonable amount of information about full-scale experimental prototypes using these configurations is available [132,133]. On the opposite situation, the information about plate based systems is really scarce and, unfortunately, the information about LHTES systems with cylindrical or spherical configurations is not useful for rectangular shapes, due to the singularities of this arrangement.

Amongst those works dealing with rectangular shapes, most of them focus on the numerical optimization of the system [134–137]. Some of these articles also include experimental tests with small-scale prototypes [135], exclusively developed for the validation of the numerical results. Therefore, these articles do not include significant details about the design or the manufacturing procedures.

The articles that include experimental work with full-scale prototypes, reviewed in [130], are mostly focused on the air-PCM heat exchange. Relevant articles such as [138–140] deal with PCMs encapsulated within rectangular slabs; however, the design and construction of these systems noticeably differ from the LHTES systems using water as a HTF in terms of sizing and manufacturing processes.

Among those works dealing with water-PCM exchange, Medrano et al [141] researched the heat transfer process during the charging and discharging of five small commercial heat exchangers, working as LHTES systems. To do that, one side of the heat exchanger was filled with the commercial paraffin RT35, used as a PCM, while water circulated through the other side, as the HTF. One of the heat exchanger types included in the study was a plate and frame heat exchanger with PCM in half of the passages. The conclusions reported on the article stated that the plate heat exchanger was not adequate as a LHTES system due to the extremely low ratio of PCM heat capacity over the empty heat exchanger heat capacity. Besides, the high weight of the device was pointed out as an additional drawback. These conclusions agree with the fact that the heat exchanger was used without any modification from the original product to adapt its use with PCMs, and as a result the PCM ratio was not significant in relation to the total capacity of the system.

More recently, Dannemand et al. published a series of articles [32,142,143] about the performance of a LHTES system based on plates, using sodium acetate trihydrate as a PCM. The system employed water as a HTF; therefore, it can be considered of a similar type to the herein developed system. Some design considerations were discussed in the articles together with the potential solutions and the obtained experimental results. However, the plate arrangement of the system was horizontal and the design was constrained by the requirement of maintaining the PCM in a supercooled state. Besides, the system was developed for seasonal heat storage. Accordingly, the information available could not be directly employed for the application herein considered.

As a general conclusion from the reviewed literature, it can be inferred that the research of LHTES systems integrated into heating and DHW plants is in an early development. Only the higher temperature systems have reached a more advanced technology development [144,145] due to their industrial interest. The information available about the development and experimental evaluation of full-scale plants is very scarce, especially for the plate based

configuration. Most of the studies dealing with LHTES systems focus on the heat transfer enhancement at a laboratory scale. While the information of these tests is valuable, the objectives pursued are in most cases different from full-scale evaluations, since they do not focus on the thermal power stored and released, or on the thermal capacity.

Furthermore, most articles do not deal (not even marginally) with aspects related to the design and fabrication of full-scale systems, or to the associated economic issues. The materials employed for the construction of the heat exchangers on the reported works are often expensive and heavy, such as copper or stainless steel. These are adequate for testing purposes, but the cost of the system might become too expensive for their implementation in commercial applications. As an example, no article was found dealing with aluminum as a construction material as it is herein proposed.

As a result, based on the current state-of-the-art, this chapter of the thesis seeks to determine the following three main objectives:

- To evaluate the performance of a full-scale plate-based LHTES system and compare its thermal behavior and economic aspects with other state-of-the-art prototypes
- To gain knowledge on the practical aspects concerning the design and fabrication processes in order to further improve the system and to reduce its costs
- To validate the design procedure for the LHTES systems proposed in Chapter 5 by means of experimental full-scale data

In order to achieve the objectives, a prototype was designed, built and evaluated within a real micro-cogeneration plant under representative conditions. First, a systematic procedure was applied to design the LHTES system, which included the mechanical testing of the most critical components such as seals and welds. Then, the full-scale prototype was constructed and assembled. Those fabrication operations that involved cutting of pieces or welding were performed by the company TSM S.L [122], a producer of steel and aluminum solutions for the industry. They also helped with some of the design aspects of the prototype. The produced LHTES prototype was incorporated to the micro-CHP plant, where it was tested under service conditions. The results were analyzed in terms of energy capacity and time needed for charging and discharging. Finally, the economic implications were assessed.

The reader will notice that this chapter is more descriptive than the previous ones due to the nature of its content. Accordingly, its structure also presents some differences. It is also important to remark that the previous experience gained with the laboratory scale prototype developed within the PhD thesis of Campos-Celador [5], showed that achieving tightness is a crucial factor that strongly influences the design of this kind of LHTES systems. In spite of its importance, this issue is usually omitted in the related literature. As a consequence, the following sections will not spare the details related with tightness.

2. Design and construction of the prototype

A systematic approach was embraced for the design and production of the LHTES prototype. Since the shape and fabrication of each component influenced the selection of the material and vice versa, the process had to be iterative. The steps comprising the procedure are listed next, accompanied by the corresponding section where they will be discussed:

1) Identification of the functions and constraints to be met by the components (Section 2.1)
2) Selection of the material (Section 2.2)
3) Added constraints to the design and sizing of the prototype (Section 2.3)
4) Detailed design of each component and manufacturing process. (Sections 2.4 and 2.5.1)
5) Fabrication and testing of the critical elements of the design (Section 3)
6) Redesign the elements that do not pass the integrity test (if needed) (Section 2.5.2)
7) Final assembly of the prototype (Section 2.6)

Several design options were considered and sketched along the research, but most of them were discarded after subsequent filtering steps. For the sake of brevity, only those design options that reached the final evaluation stage will be detailed herein. As listed above, all the steps will be sequentially detailed throughout the present Section 2, except for the step 5 (integrity tests), which will be discussed separately in Section 3.

2.1. Constraints and functions of the LHTES system and its components

As a remainder, the conceptual design proposed in the PhD thesis of Campos-Celador [5] consists of a plate-based system where the PCM is enclosed. The slabs are placed vertically and arranged in parallel and in-series to form a modular LHTES system. The HTF flows in between them, exchanging heat with the plates' largest surfaces.

Based on that concept, the storage system elements can be grouped on 3 different types: the plates; the outer shell and the ancillary elements. The design started with the definition of the functions and constraints that each component has to fulfill. The constraints were classified into two levels: essential constraints and desirable constraints. The boundary conditions for the use of the system in a domestic CHP plant (provided in Chapters 1 and 5) were also considered, as well as the pilot plant characteristics (see Section 4.2 for more details). All of them are summarized in Table 6-1.

Group	Functions	Essential constraints	Desirable constraints
Whole system	• Store heat from a CHP domestic plant and release it when required	• Maximum volume ~ the size of a domestic appliance (a washing machine): ○ 500-600 mm deep; 600-650 mm wide and 850 mm high • 2mm channel thickness • Laminar flow regime • Suitable discharging power in relation to the user profile • Maximum discharging time of 1.5 h	• Modularity • Economical competitiveness • Compactness
PCM	• Store and release sensible and latent heat in order to increase the effectiveness of the storage system	• Melting temperature between 50 and 90 °C (DHW and heating temperature range) • Stability in relation to the thermal cycling and easy handling (i.e.: no phase segregation; no thermal degradation and non-hygroscopic behavior) • High thermal conductivity to provide a low thermal resistance between the HTF and the PCM.	• Reasonable price: < 6 €/kg • Suitable effective energy storage capacity for the temperature range involved: > 150 kJ/kg • Highest possible thermal conductivity • Well known PCM
Plates	• Contain the PCM guaranteeing no leakage • Transfer the heat from the PCM to the HTF and vice versa	• Suitable mechanical behavior (stiffness and strength) at the working temperatures in order to contain the PCM without deformation or shape modification • Minimum wall thickness of plates of 2 mm to avoid manufacturing problems • Tightness to avoid any PCM leakage from the interior and to prevent any water inclusion • The design requires to include some filling system for the PCM • The plates have to form the HTF channels, with an optimum thickness of 2mm • Chemical compatibility with the PCM, the HTF and the material of the shell. (i.e.: no corrosion)	• Reduced weight and cost • Effortless filling system for the PCM • Easy draining and refilling of the PCM • Design based on commercial products
Shell	• Gathering the plates together • Contain the HTF flow under the required regime and pressure • Defines the dimensions of the heat exchanger • Promote a good hydraulic distribution	• Sufficient mechanical strength and stiffness at the working conditions: temperature up to 90 ºC; gauge pressure 1.5 bar; able to deal with the weight of the PCM plates • Chemical compatibility with the HTF and with the materials of the plates (i.e.: no corrosion) • Tightness in order to avoid any water leakage • Allow an easy access to the PCM plates in order to insert and extract them, and to facilitate maintenance tasks and the solution of potential problems • The PCM plates have to remain on the original position during use and also whenever operations are required (transport, installation, maintenance, others)	• Modularity • Effortless access to the PCM plates • Low weight • Cost-effective manufacturing • Suitable design for mass-production
Ancillary elements (hydraulic connections)	• Allow the HFT entrance and exit • Allow the purge of the air inside the system	• Allow the accommodation of temperature probes • Tightness • Easy insertion and extraction of HTF connection hoses	• Low cost • Design based on commercial products
Ancillary elements (Insulation)	• Minimize the heat loss to the exterior • Avoid potential burns	• Low thermal conductivity • The insulation has to allow the access to the plates and hydraulic connections	• Low cost

Table 6-1: Functions and constraints of the LHTES components

2.2. Selection of the material and the PCM

A selection of materials that meet the constraints defined in Table 6-1 was performed. They are shown in Table 6-2. Plastic materials were discarded due to low thermal conductivity and insufficient stiffness at the working temperatures. Thus, all the candidates were metallic materials. Uncommon options, such as nickel or titanium alloys, were not considered as candidates due to their high price.

Amongst the listed candidates, carbon steel was dismissed due to potential corrosion. However, it is worth mentioning that, according to the economic analysis presented in Section 4.4, plain carbon steel will be considered in future versions of the LHTES in order to reduce costs. Further research to avoid corrosion by means of the use of galvanic coatings or sacrifice anodes should be performed though. Copper alloys were discarded due to their high price and low specific stiffness (modulus of elasticity divided by the density).

Material	Density (kg/m^3)	Modulus of Elasticity (GPa)	Yield strength (MPa)	Cp (kJ/kg·K)	Thermal conductivity (W/m·K)	Weldability	Resistance to corrosion	Price (€/kg)
Low Carbon steel	7850	200-215	250-400	0.45-0.50	49-54	Easy	Low	0.5-1
Medium Carbon Steel	7850	200-216	300-900	0,45-0,50	45-55	Easy	Low	0.5-1
Stainless steel	7800-8100	190-210	170-1000	0.40-0.60	11-36	Medium-to-Difficult	High	4-6
Aluminum alloys	2600-2800	69-80	30-610	0.85-1.10	120-240	Difficult-Limited	High	2-2.3
Copper alloys	8800-8940	112-150	30-350	0.36-0.42	160-390	Easy	High	5.8-7.5

Table 6-2: Main mechanical and thermal properties of the metallic candidates considered for the LHTES system [146]

Aluminum alloys and stainless steel were considered suitable candidates. Some preliminary design sketches of the prototype were produced using them. The use of commercially available manufactured products that could be suitable to fulfill the functions of the component was prioritized. Preliminary calculations rendered an estimated weight of the prototype (when filled with water and PCM) of 500 kg for stainless steel and 250 kg for aluminum[18].

The weight difference was owed to the density of the materials: 7800 kg/m^3 for stainless steel and 2700 kg/m^3 for aluminum alloys. Even though a system made of stainless steel could

[18] Note that this weight differs from that finally calculated in Section 4.1, because the final design was not yet attained. However, this estimation was accurate enough for the selection of the material (note that the design is an iterative procedure).

(theoretically) be produced with thinner plates due its higher *Young's modulus* (thus reducing the weight and the final cost), a minimum wall thickness of 2 mm was considered necessary to avoid potential problems emerging from bonding or welding processes (Table 6-1). Thus, the optimization potential in terms of thickness was limited.

According to the materials price given in Table 6-2 and to the estimated weight, the cost of the raw material[19] to produce the prototype would rise to 1900 € for stainless steel and 650 € for aluminum. As a result of the lower cost and weight, aluminum was selected to construct the prototype plates and shell.

The PCM selected was RT60. It meets the constraints presented in Table 6-1, especially in terms of stability against thermal cycling and easy handling.

2.3. Preliminary size of the full-scale prototype and added constraints

Once the materials were selected, a preliminary estimation of the dimensions required for the storage device was performed by means of the procedure developed in Chapter 5. As a remainder, the flowchart of the procedure is illustrated in Figure 6-1. The constraints considered were already defined in Table 6-1; however, they are summarized next to facilitate the reading:

- Operating temperatures: 50-65 °C
- PCM selected: RT60 (see properties in Chapter 5-Section 2.4)
- Discharging time: 1.5 h (selected according to typical demand profiles)
- Maximum volume availability: (500-600 mm deep; 600-650 mm wide and 850 mm height)
- Nominal mass flow rate: 5 lit/min (typical values for domestic applications, see Section 4.2)

Two extra constraints were added to this list:

[19] This cost refers only to the metallic material; the PCM is not included

- The plate design would be based on extruded hollow rectangular profiles available in the market to optimize costs (see Section 2.4.1 for more details)
- The prototype would be divided into 6 stacks connected in series to gain modularity and to reduce the potential fabrication problems

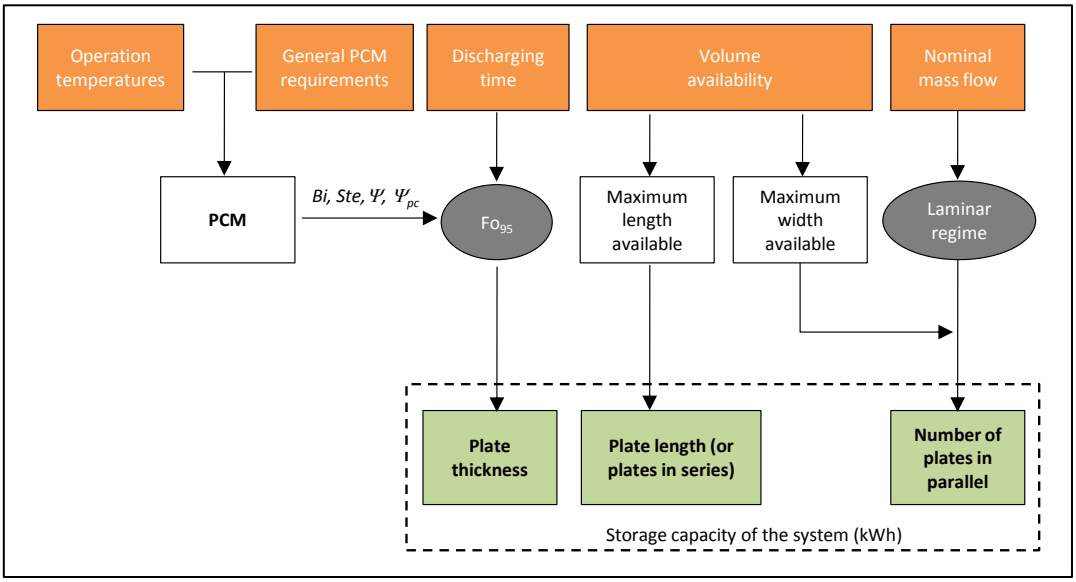

Figure 6-1: Flowchart of the sizing process of LHTES systems developed in Chapter 5

The sizing process consisted of three main steps (Figure 6-1):

1) Plate thickness estimation:
    - Based on the maximum discharging time (1.5 h), on the operating temperatures and on the selected PCM properties, the Fourier number was calculated using the correlation developed in Chapter 5 - Section 3.3 (Eq. 5-27). The maximum PCM thickness to be used ($e_{PCM\ max}$) was estimated by Eq. 5-31. The results rendered a value of 22 mm, as shown in Table 6-3
    - According to the characteristics of the commercially available profiles (see Section 2.4.1), 20 mm thickness plates were selected, with an aluminum wall thickness of 2 mm. The maximum height of the commercially available profiles was selected, 120 mm

PCM thickness (mm)	Calculated Fourier number	Calculated discharging time (h)	Plate thickness to be used assuming a wall thickness of 2mm on each side
23	1.36	1.57	27
22	1.37	1.44	26
16	1.41	0.79	20

Table 6-3: Maximum plate-thickness allowance in a LHTES system with RT60 for a discharging time of 1.5 h

2) Plate length:

- The dimensions of each of the six stacks were defined first according to the maximum volume availability for the whole system. Accordingly, each stack has a minimum size of 310 mm width and a 600 mm length (outer dimensions). A 145 mm height is defined based on the height of the commercial plates selected above. Two stacks are placed widthwise and three stacks vertically. The six stacks form a prototype of approximately 620 x 600 x 450 mm total dimensions. The height is slightly lower than that defined as a constraint; however, it was considered enough at this stage of the research. A sketch of this conceptual prototype is shown in Figure 6-2
- According to the defined volume of each stack, the maximum length of the plates is 600 mm

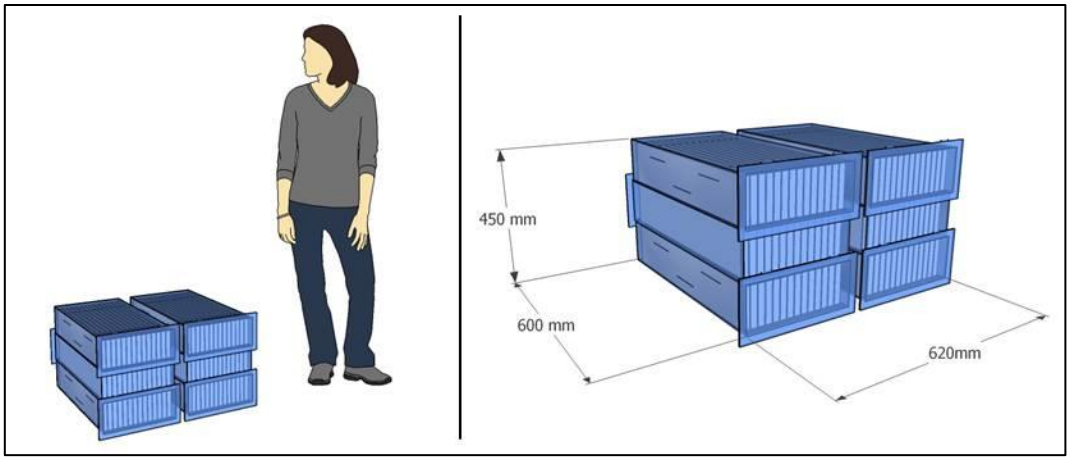

Figure 6-2: Overview of the LHTES prototype design divided into 6 stacks

3) Number of plates in parallel:

- Considering the width of one stack (310 mm) and the thickness of the plates (20 mm) a maximum number of 14 plates per stack was calculated
- With this value and the above defined flow rate of 5 lit/min, a Reynolds number of 284 was achieved, which guaranteed the required laminar flow regime

These are approximated dimensions that were used to face the detailed design and the manufacturing process of the plates and the shell (Sections 2.4 and 2.5, respectively). The final dimensions were slightly different due to production requirements, as it will be detailed in the corresponding sections.

2.4. Design and construction of the plates

Before facing the detailed design of the plates, a literature survey was performed based on literature reviews [13,33] and on several websites of PCM suppliers. The results of the search, shown in Table 6-4, demonstrated that currently there is no commercial product (PCM plates) able to fulfill the requirements presented in Table 6-1. Accordingly, it was necessary to develop own-designed plates. Their design also included the definition of the HTF channels, which will be discussed later in this section.

Manufacturer	Do they provide plate-shaped encapsulated PCMs?	Description of the PCM	Remarks
Rubitherm (www.rubitherm.de)	Yes	They provide metallic rectangular plates with PCMs inside them (CSM modules). Up to 200mm thick.	Discarded because they can't be placed vertically. Besides, the sealings are not prepared to work above 60 °C.
Cristopia (www.cristopia.com)	No, they only provide spherical products.	–	–
Teap (www.teappcm.com)	Yes	Various shapes, including plates within polymeric enclosures.	Discarded due to a low thermal conductivity of the envelope.
Doerken (www.doerken.de)	No, apparently they do not provide any PCM anymore.	–	–
Mitsubishi Chemical (www.mfc.co.jp)	No, apparently they do not provide any PCM anymore.	–	–
Climator (www.climator.com)	Yes	They offer PCMs enclosed into a metallic-polymer bag (Climsel),	Discarded due to a lack of stiffness.
EPS Ltd (PCM Products) (http://www.pcmproducts.net/)	Yes	Seemingly they can provide several encapsulated products, with different shapes and materials.	The information about metallic plates is no longer available.
DatumPCM (http://www.datumphasechange.com)	No. They only provide constructive solutions with PCMs for ceilings.	–	–
PureTemp (entropy solutions) (http://www.puretemp.com)	No. They do not provide encapsulated products.	–	–
Salca (http://www.salcabv.nl/)	Yes	They provide PCMs within bags,	Discarded due to a lack of stiffness.
Phasechange energy solutions (http://www.phasechange.com)	No, they only have a product called Thermastix: an aluminum squared tube.	–	–

Table 6-4: Commercial PCM plates/slabs available in the market

2.4.1. Design and production of the plates

The design consisted of aluminum extruded hollow rectangular profiles readily available in the market. They are offered on a wide range of shape factors and thus, they meet the defined desirable criteria of cost optimization, modularity and adaptability (Table 6-1). Commercial

profiles are available in thicknesses ranging from 10 to 80 mm. According to the simulations performed in Chapter 5, these values are suitable to provide discharging time that range from 30 minutes to 30 hours with typical PCMs. Furthermore, since the profiles are obtained by extrusion, a die with the desired dimensions could be produced to extrude profiles on demand in a future industrialization stage.

The plates manufacturing process is simple and straightforward when using these profiles: the profiles are selected according to the desired thickness and cut to the required length. Then, a lid is welded on each end of the hollow profile to close the body, thus forming a tight system. The PCM is placed inside this body through two small holes that are subsequently produced and sealed. A sketch of the plate design can be seen in Figure 6-3. The details are discussed next.

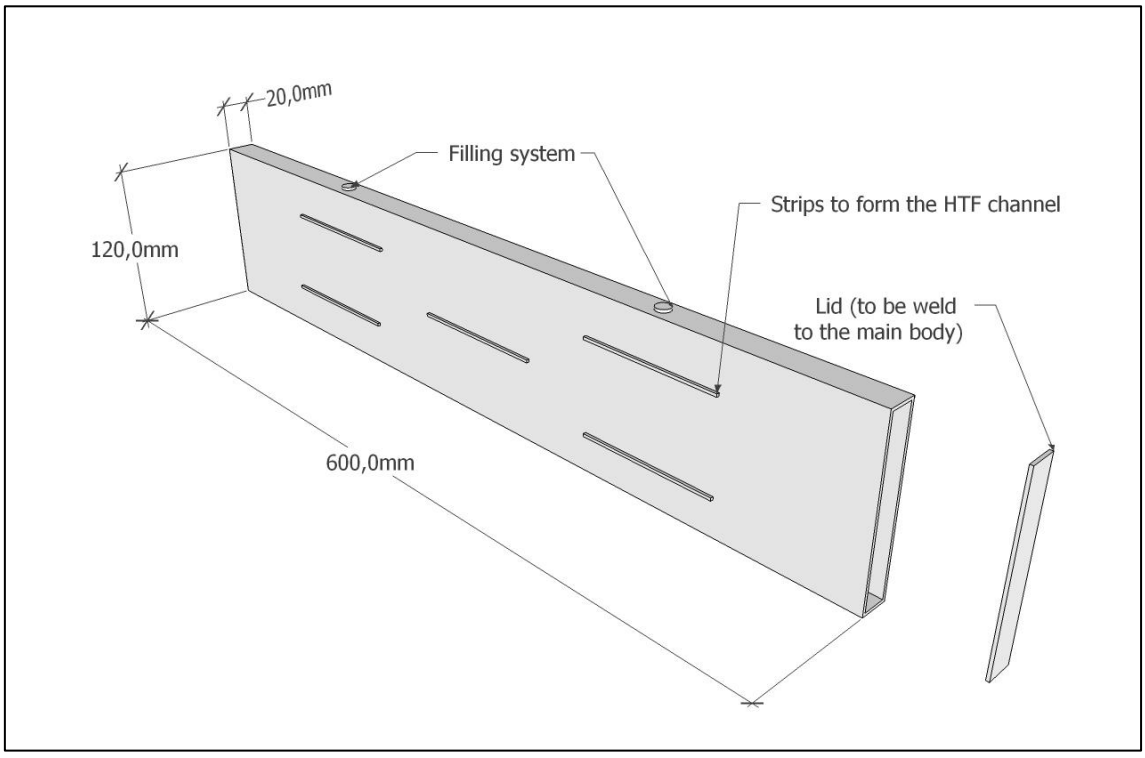

Figure 6-3: Sketch of the PCM plates

The main design constraint is the internal cavity thickness, which should be narrower than 22 mm (Table 6-3). According to the commercial availability (the characteristics and dimensions of several aluminum profiles can be checked in Appendix B.1), hollow profiles of extruded aluminium alloy EN AW 6063-T5 were selected, supplied by Alu-Stock S.A. [112]. They consist of long profiles of simple rectangular hollow section of 20x120 mm^2 (external dimensions, as

shown in Figure 6-3). Among the available options with a 20 mm thickness, the largest possible height (120 mm) was selected in order to optimize construction costs. The wall thickness was 2 mm. The profiles were 6 m long, so they had to be cut to the desired length (600 mm).

The lids needed to close the profile ends were produced by laser cutting from 2 mm thick aluminum flat sheets (alloy EN AW-6082-T6). This process is simple and optimizes the use of material. The lids were welded to the open ends of the profiles to ensure tightness (electrode welding process).

To introduce the PCM into the plates, a filling system was required to be designed. Different options were considered, detailed in Section 3.1 together with the description and the outcomes of a tightness test performed to evaluate their performance. The results showed that the use of aluminum headed plugs including Viton® O-rings were the best option. The thread needed to accommodate them was performed by a thermal drilling technique. A detail of the employed plugs is shown in Figure 6-4.

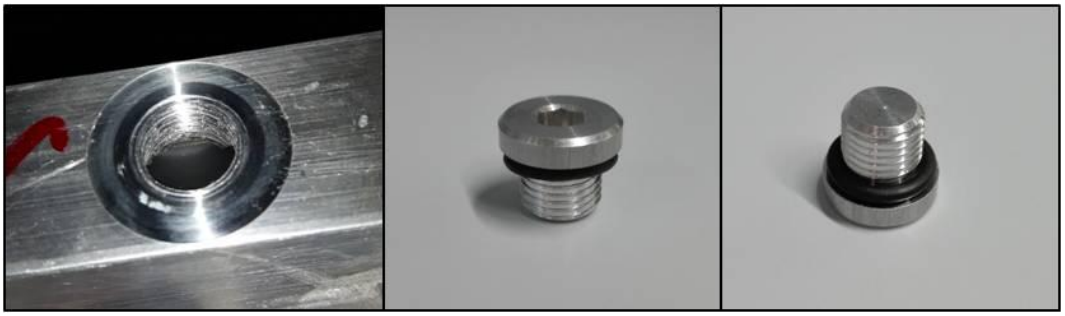

Figure 6-4: Threaded bushing created by thermal drilling (left) and aluminum plugs with Viton O-rings employed for closing the plate filling holes (center and right)

2.4.2. Design of the HTF channels

The design to form the HTF channels was a delicate task due to the reduced thickness required for the channels: 2mm (Table 6-1). Different configurations were proposed and sketched. The simplest solution consisted of the use of separation strips attached to one of the lateral faces of each plate, as depicted in Figure 6-3.

These separation strips were produced by laser cutting from the same aluminum flat sheets previously used for the production of the lids. They were fixed to one of the large sides of each

plate in the longitudinal direction using an epoxy resin adhesive, Pattex Nural 21 [147], which is suitable to join metallic surfaces[20]. The preparation procedure required the roughening of both surfaces to be bonded with sandpaper; cleaning and drying, applying the adhesive on the strips and finally proceeding to their placement. The curing time is 48 hours.

The plates with the adhered strips were tested by means of a thermal cycling test in order to check the good bonding previous to form the stack. The results were adequate, as detailed in Section 3.3.

Each empty plate was weighed, filled in with the molten PCM, left to solidify, and weighed again (on a scale OHAUS Ranger, ± 0.5 g accuracy). Plugs and gaskets were installed afterwards. The weight of the plates is presented in Section 4.1, along with the rest of the components forming the LHTES prototype. The final appearance of the plates can be appreciated in Figure 6-5, while their final dimensions are provided in Table 6-5.

	Plate length	Plate height	Plate thickness	Plate wall thickness
Value (mm)	600	120	20	2

Table 6-5: Plate dimensions

2.5. Shell design and construction

As above described, the LHTES prototype is formed by 6 stacks connected in series. The targeted dimensions for each stack were 310 mm width, 600 mm length and 145 mm height. Two stacks are placed widthwise and three stacks vertically (previously shown in Figure 6-2).

According to that configuration, a detailed design and a manufacturing route for the outer shell were devised, detailed next. However, the design did not pass the integrity tests (detailed in Section 3.3). Accordingly, modifications were included to the design, which will be discussed in the subsequent Section 2.5.2.

[20] The strips were initially welded to the plate, but overheating deformed them.

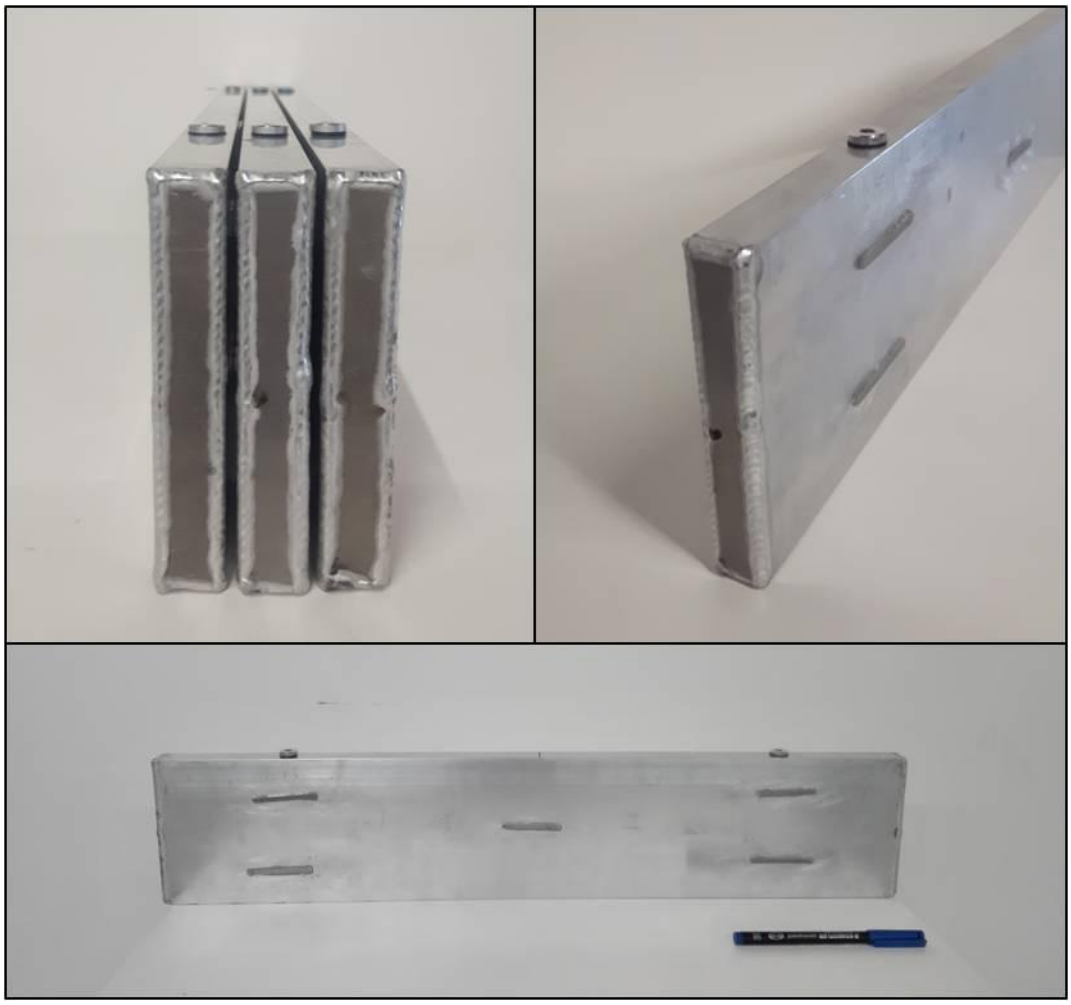

Figure 6-5: Overview of the final design of the plates

2.5.1. Original design

The shell of the each stack defines the dimensions of the heat exchanger. Based on the constraints presented in Table 6-1, the design of each shell was composed by a prismatic body and two screwed lids. The main prismatic body was comprised by two aluminum sheets folded at 90 ^{o} angle and welded together, forming a hollow body of rectangle cross-section.

On each opened side a bridle was formed by welding a thick aluminum fringe to the perimeter. The lids were attached to the bridles by means of 18 screws in order to ensure an easy insertion and extraction of the plates inside the shell. Tightness was attained by means of rubber gaskets placed in between the bridles and the lids. Each lid had a bar attached to their inner side to hold the plates in a fixed position. The dimensions of the shell components are presented in Table 6-6. The design details can be appreciated in Figure 6-6, where the interior of the lid can also be visualized.

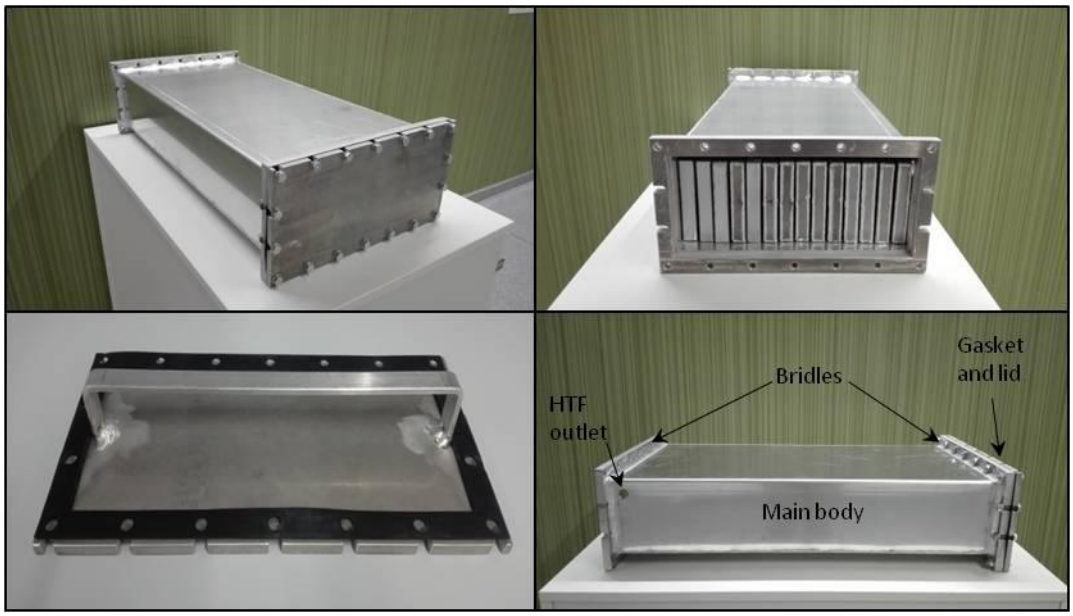

Figure 6-6: Overview of: closed stack shell (upper left corner and lower right corner); opened stack shell, showing the plates contained in it (upper right corner); Inner part of one lid, including the rubber gasket (lower left corner)

To promote a good HTF distribution, 5 cm empty space was left at the front and at the rear parts of the shell body, which acted as a collector. To help the flow homogenization, the HTF entry was placed on one of the sides of the front part, while the HTF exit was located on the opposite side on the rear part. In this way, the HTF travels the same distance inside the heat exchanger independently of the channel. Moreover, the water inlet was at a lower level than the outlet to aid natural convection. The appropriateness of this solution was reinforced with the results attained on a Master thesis carried out within the ENEDI research team (UPV/EHU) [148], where 4 different alternative hydraulic-distribution solutions were investigated by means of CFD.

The shell integrity was evaluated by means of the measurements discussed in Section 3.3. The results showed insufficient stiffness and strength under operation conditions. This was attributed to the use of an alloy EN AW-1050 o/H111 instead of the EN AW-6082-T6 series initially defined, due to manufacturer constraints. As a consequence, the prototype needed modifications. They are detailed next.

	Total length	Body length	Lid thickness	Gasket thickness	Bridle thickness	Body thickness	Body height	Body width	Lid height	Lid width
Value (mm)	750	696	10	2	15	4	145	330	190	367

Table 6-6: Dimensions of the original shell design

2.5.2. Modifications and final shell design for the LHTES prototype

The design and production of a new shell would unacceptably delay the research; therefore, a metallic armor was devised to strengthen it. It was based on the use of reinforcements on the outer part of the shell. In this way, the integrity of the shell would be guaranteed and the LHTES could be tested under real conditions.

The armor was comprised of fourteen U-shaped carbon steel profiles. The profiles were placed on the upper and bottom surfaces joined with through bolts, as depicted in Figure 6-7. Aluminum plates were also placed on the sides of the prototype. The dimensions of the used U-profiles are shown in Table 6-7. The performed integrity tests (see Section 3.3) showed a suitable behavior.

	Profile length	Profile height	Profile width	Profile thickness
Value (mm)	400	40	80	4

Table 6-7: Dimensions of the U-shaped carbon steel profiles used as shell reinforcement

It is important to remark that this configuration is not suitable for a commercial product; it has to be considered as an emergency set-up applied in order to be able to test the thermal behavior of the LHTES system with the resources and time available for this PhD project.

Due to the use of the steel armor, it was not possible to produce the whole LHTES prototype, formed by 6 stacks, even though the remainder five shells and their plates had already been built. Accordingly, the thermal measurements were performed with one stack only. Additional details of the tests are given in Section 4.

2.6. Ancillary elements and final assembly

There are 3 hydraulic devices installed in the LHTES system: the water inlet, the water outlet and the purge.

The hydraulic connections installed in the water inlet and the water outlet consisted of commercial devices made of stainless steel and nickel-brass, as shown in Figure 6-8. They included a “T” type fitting to insert a temperature probe (see Section 4.2 for more details). They were attached to the box by means of an adhesive Loctite 510 [149]. The HTF inlet connection can be visualized in Figure 6-8 (right). A commercial petcock was installed on the upper side of the shell in order to purge the air from the system.

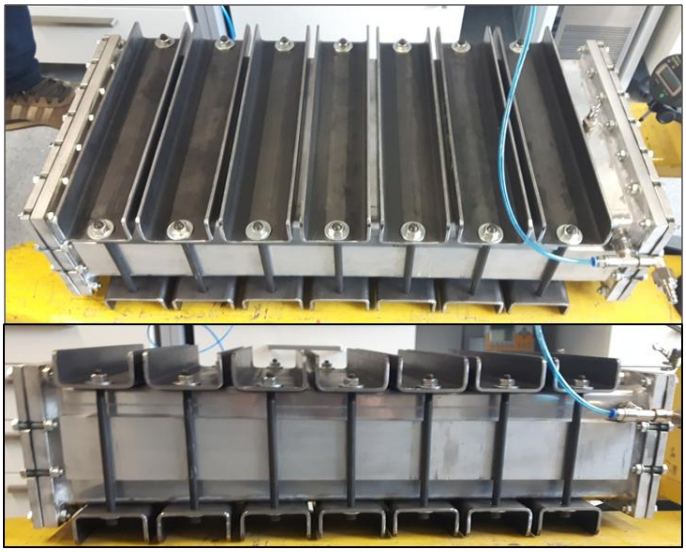

Figure 6-7: LHTES shell reinforced with the steel "armor" (finally tested configuration)

The shell was insulated to minimize the heat loss to the exterior. As the box and armor had an irregular surface, the free spaces were sprayed in with commercial polyurethane foam (Soudal [150]). Then, the outer surface was covered by 4.5 cm thick EDPM (ethylene propylene diene monomer M-class rubber) flexible boards, fastened by means of Velcro strips. The thermal conductivity of the polyurethane foam is 0.2 W/mK, while that of the EPDM is 0.55 W/mK. The final appearance of the system can be observed in Figure 6-8 (left).

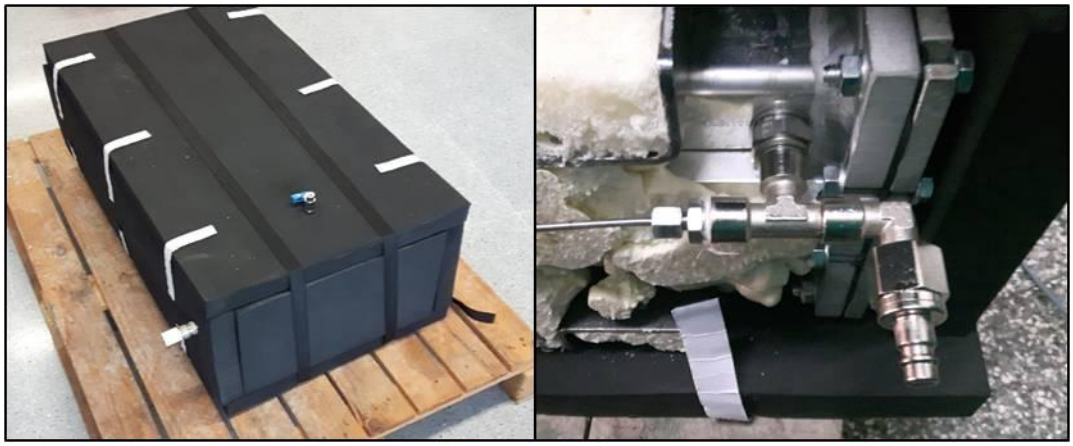

Figure 6-8: Outer aspect of the tested LHTES prototype with the insulation (left) and detail of the HTF inlet hydraulic connection (right)

3. Evaluation of the system integrity

Tightness and mechanical integrity are essential constraints to be fulfilled by the PCM plates and the shell. For that reason, tests were performed to evaluate them.

The Section is organized as follows:

- Experiments performed to determine the tightness of the devised solutions developed for filling-in the plates with the PCM, as well as the tightness of the welds: Section 3.1
- Preliminary thermal cycling to assess the integrity and the sealings of the plates when they were exposed to operation temperatures: Section 3.2 (This test also served to evaluate the reproducibility of the PCM thermal behavior)
- Experiments performed to evaluate the ability of the shell to handle the operational pressure level: Section 3.3

3.1. Testing the welds and the inlet-plugs of the plates for airtightness

To introduce the PCM inside the plates, different filling systems were designed according to the constraints presented in Table 6-1. Based on general recommendations about tightness [151], the use of threaded plugs was considered the best option. However, since the plate wall thickness is limited to 2 mm, the inclusion of threads into the plate was not feasible. Thus, two different solutions were devised to form the threads, the use of rivet nuts and a thermal drilling procedure:

- Rivet nuts (or threaded inserts) are one-piece internally threaded and counter-bored tubular rivets that can be entirely anchored from one side of the plate with a rivet gun. This process is straightforward and economic. A gasket is included in order to ensure tightness. The threaded plug can be accommodated inside it. The system can be visualized in Figure 6-9
- The thermal drilling technique is characterized by the use of a special drilling tool (a bit) that works generating frictional heat. The metal becomes into a "super-plastic" state, allowing the tool to displace the material and form a bushing [152] onto the surface. The height of the bushing is 3 to 4 times the original wall thickness. A common tap can be employed to thread the desired screw on the bushed hole. A scheme of the procedure is shown in Figure 6-10

Figure 6-9: a) Rivet gun; b) Plate with a rivet nut inserted; c) Plate with a river nut inserted and closed with a threaded screw

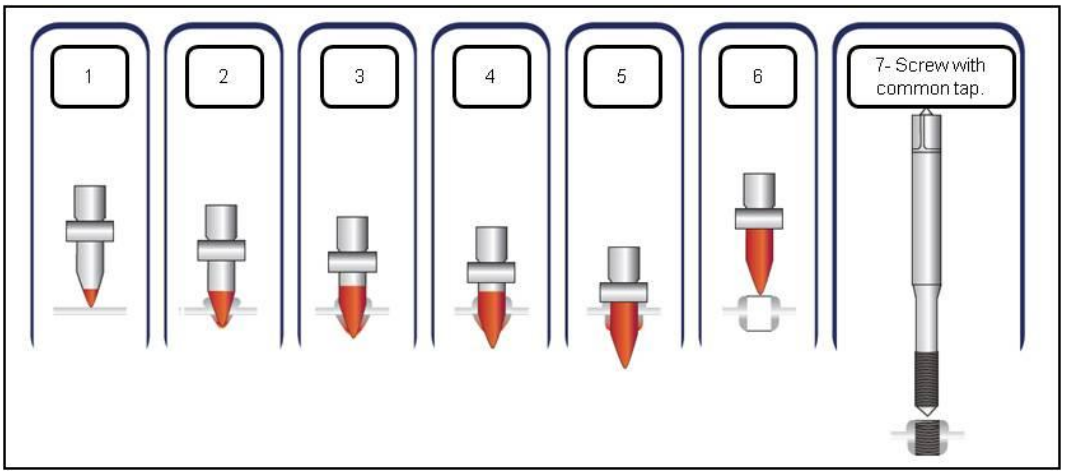

Figure 6-10: Procedure to create the thread by means of thermal drilling [153]

Different types of threaded plugs were tested coupled with both inlet-types. All the plugs were 1/8" gas size. Table 6-8 gathers the different combinations evaluated, along with their description, main characteristics, obtained results and additional remarks. An image of the different options evaluated is provided in Figure 6-11.

Plug accommodation technique	Plug	Material of the plug	Plug sealing type	Airtight?	PCM tight? [a]	Cost	Remarks
Rivet nuts (no gasket)	Headed plug	Carbon steel	Viton O-ring gasket	No	–	++	The plug was airtight, but leakage occurred between the rivet nut and the plate.
Rivet nuts with Viton O-ring gasket	Headed plug	Carbon steel	Viton O-ring gasket	Yes*	–	++	*It is easy to damage the rivet nut gasket on the anchoring operation.
Rivet nuts with copper washer	Headed plug	Carbon steel	Viton O-ring gasket	Yes*	–	++	*It is easy to damage the rivet nut gasket on the anchoring operation.
Thread formed by thermal drilling + tap	Headed plug	Aluminum	Viton O-ring gasket	Yes	Yes	++	Really easy installation. The plugs can be opened and closed repeatedly yet maintaining tightness.
Thread formed by thermal drilling + tap	Headed plug	Stainless steel	Viton O-ring gasket	Yes	–	+++	Really easy installation. The plugs can be opened and closed repeatedly yet maintaining tightness.
Thread formed by thermal drilling + tap	Headed plug	Brass	Viton O-ring gasket	Yes	–	+	Really easy installation. The plugs can be opened and closed repeatedly yet maintaining tightness.
Thread formed by thermal drilling + tap	Headed plug	Aluminum	Flat paper gasket	Yes	No	+	Airtight but permeable to PCM.
Thread formed by thermal drilling + tap	Non-headed plug	Stainless steel	Thread sealant [b]	Yes*	–	+	*The tightness depends on the quality of the application of the sealant. System prone to defective pieces.
Thread formed by thermal drilling + tap	Non-headed plug	Brass	Thread sealant [b]	Yes*	–	+	* The tightness depends on the quality of the application of the sealant. System prone to defective pieces.
Thread formed by thermal drilling + tap	Non-headed plug	Brass	None (just the thread)	No	–	+	

Table 6-8: Different tested types of closure combinations for the plate filling cavities (the underscore symbol means that the solution was not tested with PCM). [a] See Section 3.2 for the PCM permeability tests. [b] Loctite 542 sealant [149]

Figure 6-11: Some types of the tested threaded plugs. From left to right: aluminum headed plug with flat paper gasket; stainless steel headed plug with Viton O-ring gasket; brass headed plug with Viton O-ring gasket, brass non-headed plug and stainless steel non-headed plug

The experiments to assess the tightness consisted of introducing compressed air at a gauge pressure of 1 bar into the plates and immersing them into water. The air was inserted through one of the filling holes while the other hole was closed with the corresponding closing system to be evaluated. Henceforth, the pressure remained at 1 bar during the immersion and if any leakage occurred, clearly perceptible bubbles were produced. The experimental arrangement

is depicted in Figure 6-12 (right top and bottom). A preliminary version of the plates was used for these tests, with reduced size. An overview of the assessed plates with the different closing mechanisms is shown in Figure 6-12 (left). A comparison of an airtight plate vs. one showing leakage is presented in Figure 6-13.

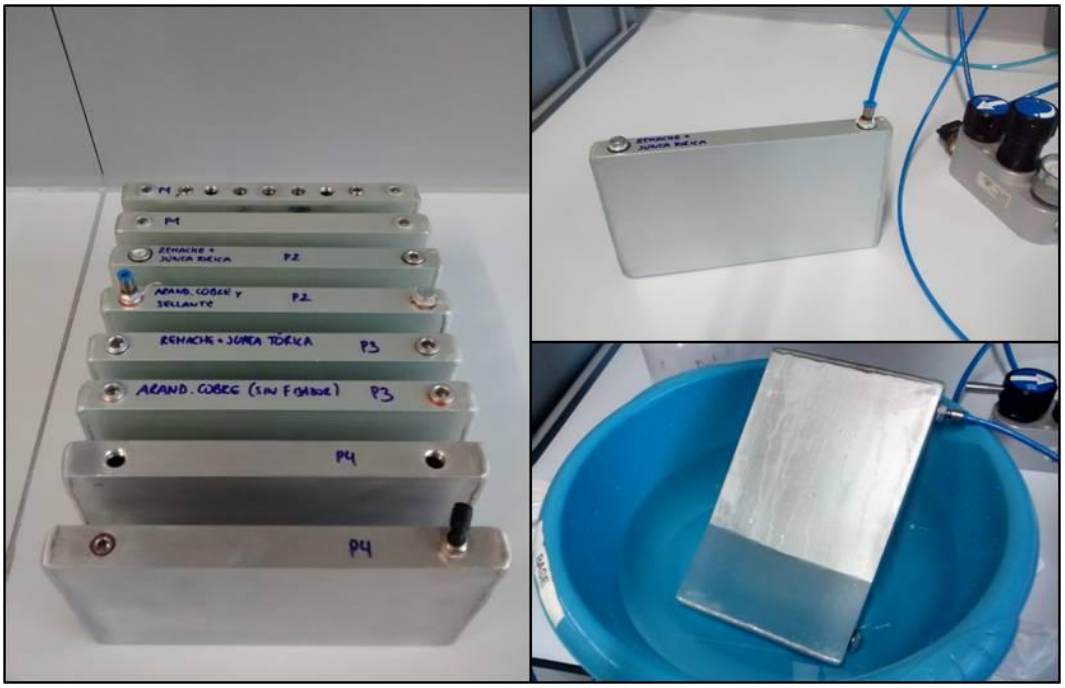

Figure 6-12: Overview of several tested plates with different closing options (left) and experimental arrangement employed for airtightness test (right, top and bottom)

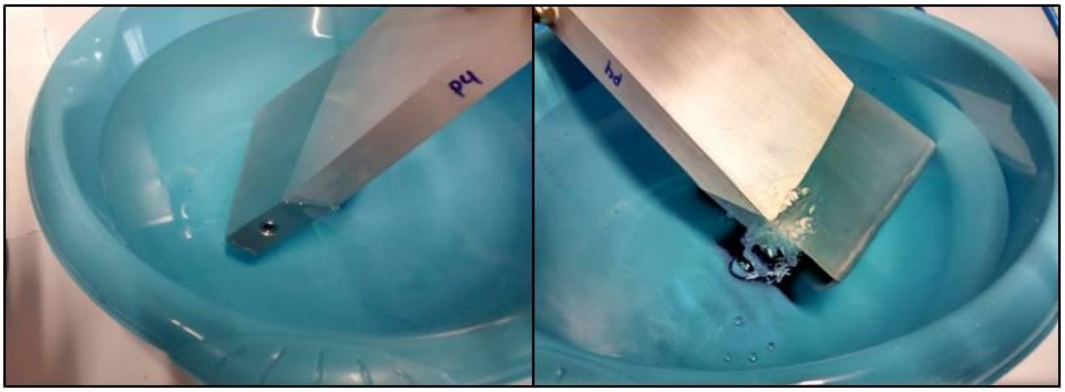

Figure 6-13: Bubbling produced in a closing system with a leak (right) vs. a suitable airtight plate (left)

Concerning the plug accommodation technique, the creation of a thread by thermal drilling was preferred over the rivet nuts. Theoretically, the installation of rivet nuts is easier, but the experiments showed high chances of damaging the gasket when the rivet nut was anchored (see Table 6-8). This depended on the quality of the workforce, which adds difficulty to

guarantee the quality of the production process. Hence, the thermal drilling process was finally selected as the best choice.

Amongst the closing options based on a thread created by thermal drilling and a tap, the use of non-headed plugs with sealant showed airtightness. However, their performance depended on the quality of the labor for applying the liquid sealant, as occurred with the river nuts. Besides, replacing or removing the plug from the plate required breaking the sealant, and new sealant should be applied for the subsequent closing. Therefore, the solution was discarded because of the added complexities.

The most suitable solution was the combination of thermal drilling with threaded plugs and gaskets. It ensured airtightness and was easy to assemble. Closing the plugs manually was good enough to guarantee an airtight system and, hence, the system allowed a fast and repeated opening and closing process.

Several gasket types were tested. The flat paper gaskets were airtight but showed permeability to the PCM during the subsequent thermal cycling test performed (see Section 3.2.1). Conversely, the Viton-O rings demonstrated a suitable performance and were chosen for the production of the prototype. Finally, plugs made of aluminum were selected to minimize potential problems caused by the different volumetric thermal expansion upon heating and cooling when different materials are used.

The tests also served to check the airtightness of the welds between the lids and the plates. The reduced version of the plates did not show any leakage during the first tests. The process was repeated when the first batch of plates with the real length (600 mm) was received from the manufacturer. On that time, 2 out of 3 plates showed leakage. Upon further visual inspection it was appreciated that the finishing of most welds showed imperfections (Figure 6-14). As a consequence, the plates were sent back to the supplier where the welding and finishing was improved.

The 14 plates of the prototype were tested afterwards, and none of them showed leakage. This suggests that the welding of the plate is complex due to the use of aluminum, but a good welding procedure can minimize the odds of defective pieces. Thus, a suitable quality control would be essential in a potential mass-production process of the system. Further research to optimize the production process is therefore advisable on this aspect.

Figure 6-14: Leak produced by deficient welding

3.2. Testing the integrity of the PCM plates under operation temperatures

In order to identify integrity problems that could arise under operation temperature conditions, the PCM filled-in-plates were submitted to a preliminary thermal cycling test performed into a climatic chamber (Section 3.2.1). The test also served to gain knowledge on the thermal behavior of the PCM under bulk conditions (Section 3.2.2). It is noteworthy that the climatic chamber uses air as HTF instead of water; thus, the heat transfer is less effective. However, this was considered enough to fulfill the objectives aimed through these tests. The test conditions are presented in Table 6-9. The plates were inspected periodically in order to detect potential deficiencies.

Climatic chamber model	Melting segment	Solidification segment	Number of thermal cycles (melting and solidification)
CCLP 150L, Ineltec S.L [154]	3h 30 min at 100 ºC	5h 30 min at 20 ºC	20

Table 6-9: Testing conditions of the thermal cycling experiments

The arrangement consisted of three plates emulating the positioning in an actual LHTES system (it was not possible to test more than three plates at a time due to the limited space available inside the climatic chamber). The plates were clenched by clamp-screws to ensure the proper distance between them (2mm). The plate located in the middle was placed facing up with the PCM filling inlets unplugged. Two T-type thermocouples were inserted through these holes into the PCM, each at a different height: one at 1.5 cm from the top of the plate and the other one at 1.5 cm from the bottom of the plate. They were connected to a data acquisition system (Agilent 34972A [155]). The other two plates were placed upside down, closed with the plugs.

In this way a potential PCM leakage trough the plugs and/or into the welds could be observed. The set-up of the plates can be observed in Figure 6-15.

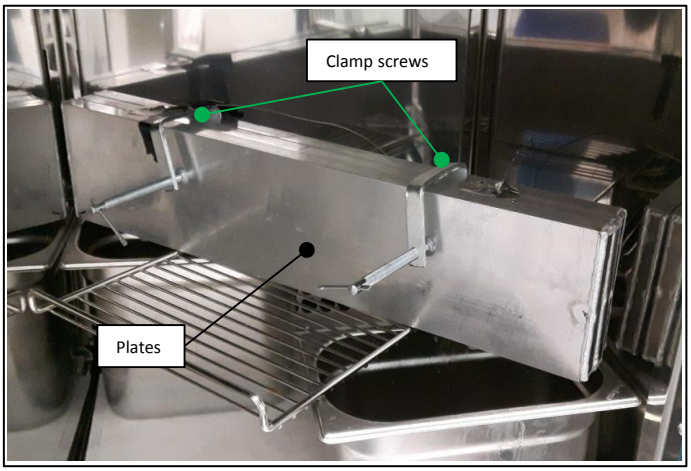

Figure 6-15: Configuration of the plates inside the climatic chamber

3.2.1. *Integrity of the plates, welds and separation strips upon thermal cycling*

The initial tests to determine the potential PCM leakage were conducted using threaded plugs with flat paper gaskets (Table 6). Eight plates (16 plugs) were tested and 2 plugs leaked, as it can be appreciated in Figure 6-16. The rest of the plugs showed no perceptible leak (no dripping). However, the plugs were soaked when the plates were removed from the chamber. The gaskets easily fractured when the plugs were unscrewed. Thus, it was concluded that even though they were airtight, the gaskets were permeable to the employed PCM, and thus unsuitable for the purposes aimed.

Plugs with Viton O-ring gaskets were also evaluated. Seven plates (14 plugs) were submitted to the same test previously performed. None of the plugs leaked during or after the tests. Besides, no relevant elasticity or brittleness changes took place when the plugs were unscrewed. As a result, this type of gaskets was suitable to be used repeatedly and considered to be adequate for the purposes aimed.

None of the welds showed any sign of leakage or damage along the tests performed. Thus, they can be regarded as suitable.

The integrity of the bonds between the strips and the plates was also tested. During the tests, only one strip out of 75 separation strips (15 plates tested with 5 strips per plate) fell down.

This could be associated with an insufficient quantity of adhesive applied, with a poor surface cleaning prior to gluing or with an insufficient surface roughness for a correct attachment. Considering that only 1 out of 75 strips failed, the method can be considered adequate to be applied. Nevertheless, it has to be remarked that, due to its nature, this process is highly influenced by the skills of the worker performing the task. Therefore, quality control procedures must be defined to ensure the required quality.

In addition to the herein described preliminary studies, the deformation of the plates due to the PCM expansion and contraction was studied by Ms Laura Quant as a part of a Master thesis performed within the ENEDI research group [156]. Flatness was measured in all plates prior and after the aforementioned thermal cycling tests by means of an experimental arrangement using a thickness gauge and a dial gauge. The results, which can be consulted in [156], proved that the dimensional stability of the plates was correct after 20 accelerated thermal cycles.

Figure 6-16: Leakage due to the permeability of paper gaskets to paraffin

3.2.2. PCM thermal behavior under thermal cycling

The temperature evolution inside the PCM during one thermal cycle is depicted in Figure 6-17. The zones with steeper slopes on the PCM temperature evolution curve correspond to the sensible heating and cooling of the PCM. The phase change can be identified by a flattened slope that occurred approximately between 50 and 62 °C (the regions between the two vertical dotted blue lines depicted in Figure 6-17).

A different behavior occurs upon melting and upon solidification, due to the PCM hysteresis and to the inertia of the material while bearing dynamic temperature changes. This effect is also appreciable in the DSC measurements of the PCM (Chapter 5). However, the solid-solid transitions observed on those DSC analyses (see Chapter 5 – Section 2.4) were not perceptible in these experiments, performed with a large PCM volume.

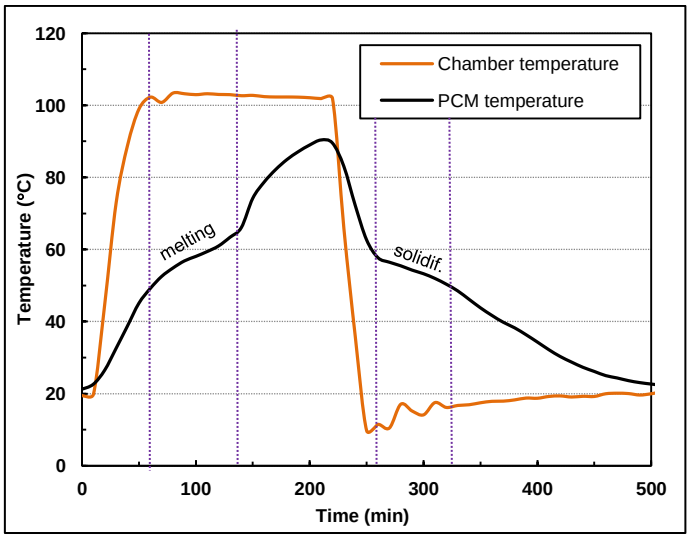

Figure 6-17: Evolution of the PCM temperature on one thermal cycle

The temperatures registered inside the PCM along the 20 cycles rendered a reproducible thermal behavior, as it can be appreciated in Figure 6-18. The PCM melted and solidified in the same temperature ranges along every cycle. No undesired processes, such as degradation or supercooling, were noticed.

The herein performed thermal cycling test, as well as the mechanical test carried out in [156], only comprised 20 cycles, which were considered valid for the purpose of this stage of the research. Nevertheless, longer thermal cycling tests under real operation conditions are required to reach a positive conclusion about the integrity and reliability of the system, which is foreseen to be in use for a period longer than 10 years.

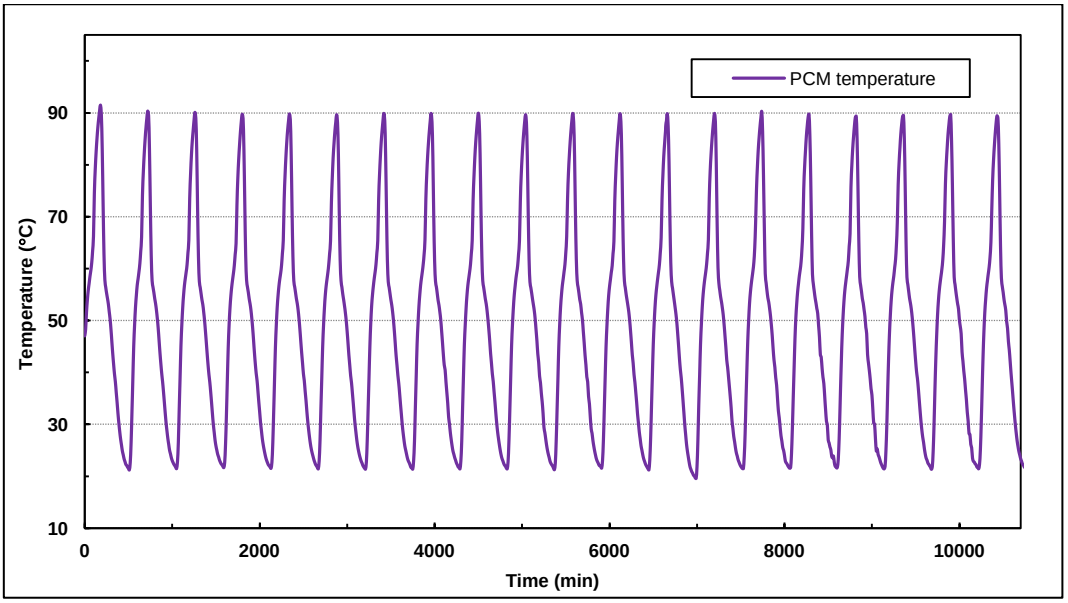

Figure 6-18: Evolution of the PCM temperature inside the plates for 20 thermal cycles (thermocouple located 1.5 cm from the bottom of the plate)

3.3. Testing the shell integrity and stability; modifications to the original design

A test consisting of the introduction of compressed air into the closed shell, at a gauge pressure of 1.5 bar, was devised to evaluate the integrity of the shell: the pressurized vessel should be monitored for 10 min where the pressure should remain unchanged. The foreseen minor deformations (due to the case elastic deformation under pressure) would be measured by means of a dial-gauge. Water and soap would be applied on the areas prone to leak (welds, water inlet and outlet and petcock). By means of this simple test it is possible to determine the mechanical integrity of the shell, as well as the lack of leaking points. The experimental arrangement is shown in Figure 6-19.

The shell initially designed (design and characteristics in Section 2.5.1) was submitted to the test defined on the former paragraph. However, a large unforeseen deformation occurred before reaching the 1.5 bar gauge pressure. The test had to be immediately stopped for safety reasons. Subsequently, tests were performed at lower pressures. It could be clearly seen that the side surfaces imploded inwardly while the upper and lower surfaces deformed outwardly. After releasing the pressure, the case remained permanently deformed. At that point the test was finished because the deformation demonstrated that the mechanical design of the system was not suitable to handle the normal operation pressures.

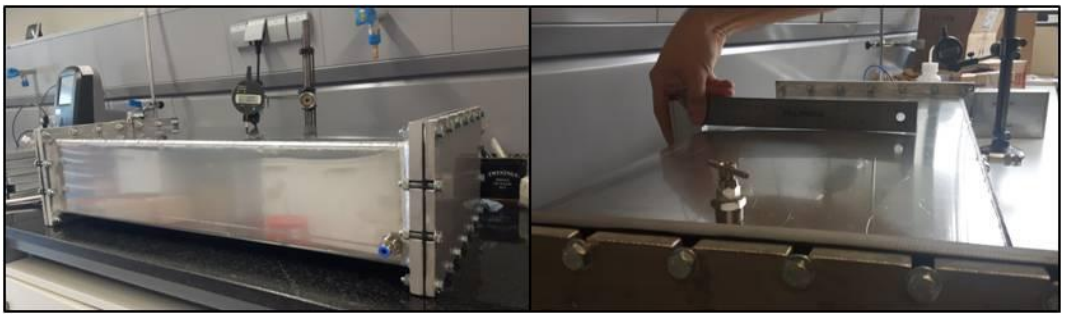

Figure 6-19: Experimental arrangement for testing the shell integrity (left) and plastic deformation attained after the test (right)

Even though a mechanical analysis of the design was not carried out on the design stage, the small pressure to be used in the system did not point towards any potential strength/deformation occurrence. The main reason for this unforeseen behavior was the change of material for the production of the shell. The material selected for the production of the shell was an aluminum alloy of 6082 series (thermally treated T6). However, the manufacturer proposed an alloy change due to welding problems. The alloy EN AW-1050 o/H111 was used instead of the initially selected alloy. The mechanical properties of this alloy are too low to withstand the conditions of the shell (Table 6-10). Nevertheless, the herein reported problem evidenced the need to produce a meaningful mechanical analysis of the system before producing a new shell, in order to ensure beforehand its integrity under operation.

Material	Yield strength (MPa)	Young's modulus (GPa)
EN AW-1050 o/H111 (actually used)	33-37	69-72
EN AW-6082-T6 (initially proposed)	240-290	70-74

Table 6-10: Main mechanical characteristics of the two aluminum alloys for the production of the shell (selected alloy, and finally used alloy) [146]

The devised armor based on U-shaped carbon steel profiles as reinforcements (described in Section 2.5.2) was installed on the shell and tested on the manufacturer facilities under the above mentioned conditions. The results showed negligible deformation of the reinforced shell (lower than 1mm). Besides, no air leakage occurred during these tests. Therefore, the joints of the lids and the welds proved to be hermetic. As a result, the shell, armored with U-shaped steel profiles, was considered suitable to produce the in-service testing of the LHTES prototype.

4. Full-scale performance evaluation

The full-scale performance evaluation of the LHTES prototype under real conditions is one of the main objectives of this chapter. Due to the problems mentioned on the former sections, the testing of the complete system comprised by 6 modules was unfeasible within the period of the PhD project. Consequently, one module was evaluated. The measurements were performed under nominal charging and discharging conditions.

This change should not affect noticeably the outcomes of the tests since the charging and discharging time is mainly dependent on the thickness of the plates, as demonstrated in Chapter 5. The storage capacity of the tested prototype was lower than the originally intended; however, this parameter can be directly scaled up. Thus, the obtained results can be considered representative of a full-scale LHTES system. Further experimental evaluation of the whole system, based on real user demand profiles, is aimed to be done in the near future, after new shells are produced.

4.1. LHTES prototype; characteristics and theoretical storage capacity

The actual weight and the calculated storage capacity of the different components forming the LHTES prototype are presented in Table 6-11, which gathers the data of the produced components and prototype (steel armor included) as well as those of the originally proposed prototype (according to Section 2.5.1). The following features are the main numbers to be highlighted:

- Average PCM amount included inside each plate: 0.84 kg
- Mean weight of the plates, including PCM, plugs and separation strips: 1.81 kg
- Total mass of PCM in the prototype: 11.76 kg
- Total weight of the 14 plates, PCM included: 25.38 kg
- Total weight of the final prototype (armor and insulation included): 82.9 kg
- Total weight of the originally proposed system: 49.3 kg (this substantial difference is due to the high density of the steel armor)

The storage capacity will be discussed in Section 4.3. Additional economic implications of the values gathered on Table 7 will be discussed in Section 4.4.

	Weight				Storage capacity					
	Theoretical prototype		Actual prototype		Theoretical prototype			Actual prototype		
	kg	%	kg	%	kJ	kWh	%	kJ	kWh	%
PCM	11.8	24 %	11.8	14 %	1972.5	0.55	66 %	1972.5	0.55	61 %
Aluminum plates	13.6	28 %	13.6	16 %	179.6	0.05	6 %	179.6	0.05	6 %
Aluminum shell	13.5	27 %	13.5	16 %	178.2	0.05	6 %	178.2	0.05	5 %
Water	10.4	21 %	10.4	13 %	652.6	0.18	22 %	652.6	0.18	20 %
Aluminum (reinforcement armor)	0.0	0 %	4.1	5 %	0.0	0.00	0 %	54.1	0.02	2 %
Steel (reinforcement armor)	0.0	0 %	29.6	36 %	0.0	0.00	0 %	203.9	0.06	6 %
Total	**49.3**	**100 %**	**82.9**	**100 %**	**2982.9**	**0.83**	**100 %**	**3241.0**	**0.90**	**100 %**

Table 6-11: Weight and storage capacity (temperature range from 50 to 65 °C) of the LHTES prototype: breakdown by components

4.2. Description of the micro-CHP pilot plant and the operating conditions

4.2.1. Pilot plant

The tests were carried out in the Laboratory for the Quality Control in Buildings of the Basque Government (*Laboratorio de Control de Calidad en la Edificación del Gobierno Vasco-LCCE)* located in Vitoria, Spain, where a pilot plant ready to test thermal storage systems is available. The plant-arrangement basically consists of a heat production loop, a heat release loop and the LHTES measuring loop. A detailed scheme can be seen in Figure 6-20.

The heart of the heat production loop is a Stirling engine (Remeha eVita model [157]) used as a micro-CHP unit, its main characteristics under normal operating conditions are:

- Electrical output: 1 kWe
- Thermal output: 4.5 – 5.2 kW
- Water flow rate: 5-15 l/min
- Water pressure: 1.2-1.5 bar
- Produced water temperature: nearby 65 °C
- The main element of the heat release loop is a fan coil unit (Sedical-Rhoss, Yardi HP model). The nominal maximum cooling power is 42.8 kW for a water inlet temperature of 70 °C
- Both, the heat production loop and the heat release loop are connected by a hydraulic compensator that acts as a buffer. The plant is controlled by 2 PID loops that act over two 3-way valves with the aim of adjusting the temperature entering the LHTES system

to the set-point specified by the user. Several A-class Pt-100 temperature probes and flow-meters are used to control and monitor the plant

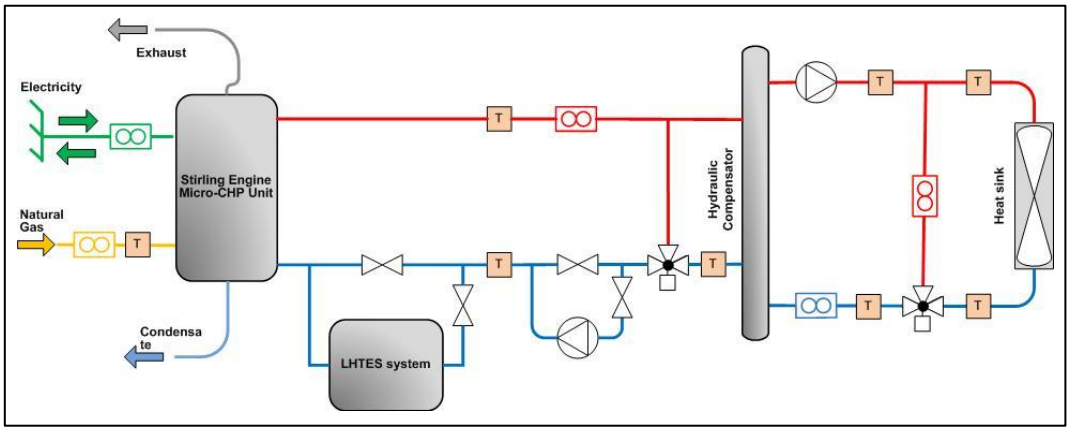

Figure 6-20: Pilot plant set-up for the full-scale evaluation

The LHTES is incorporated into the LHTES loop. Monitoring recommendations defined in the ANSI/ASHRAE standard 94.1-2002 [158] were followed. A-class Pt-100 temperature probes (± 0.2 °C accuracy) were placed in the water inlet and outlet. The probes, protected by 150 mm length - 3 mm diameter stainless steel sheaths, were introduced in the fittings up to 3 cm depth in order to ensure a good contact with the HTF. A data acquisition system (Agilent 34972A [155]) was employed to record the temperature data. The HTF flow rate was measured by means of an electromagnetic flow-meter (MJK Magflux 7100; < 0.1 % uncertainty). Both, temperature and flow rate were registered each 10 s. An overview of the experimental arrangement is depicted in Figure 6-21.

4.2.2. Test operating conditions

The initial step of the tests consisted of circulating water at 50 °C through the system until isothermal conditions were achieved along the circuit. It was considered that isothermal conditions had been met when the difference between the LHTES inlet and outlet temperatures remained within ± 0.2 °C interval for (at least) 1.5 h.

After isothermal conditions are met, the test starts. To study the charging process, the set-point of the pilot plant control probe is set to 65 °C. The inlet temperature is maintained constant until the inlet and the outlet temperatures of the LHTES system reach isothermal conditions again. At that point, the charging process is considered completed.

In order to start the discharging test, the set-point is dropped down to 50 °C. This segment lasts until both, the inlet and the outlet LHTES temperatures achieve isothermal conditions again.

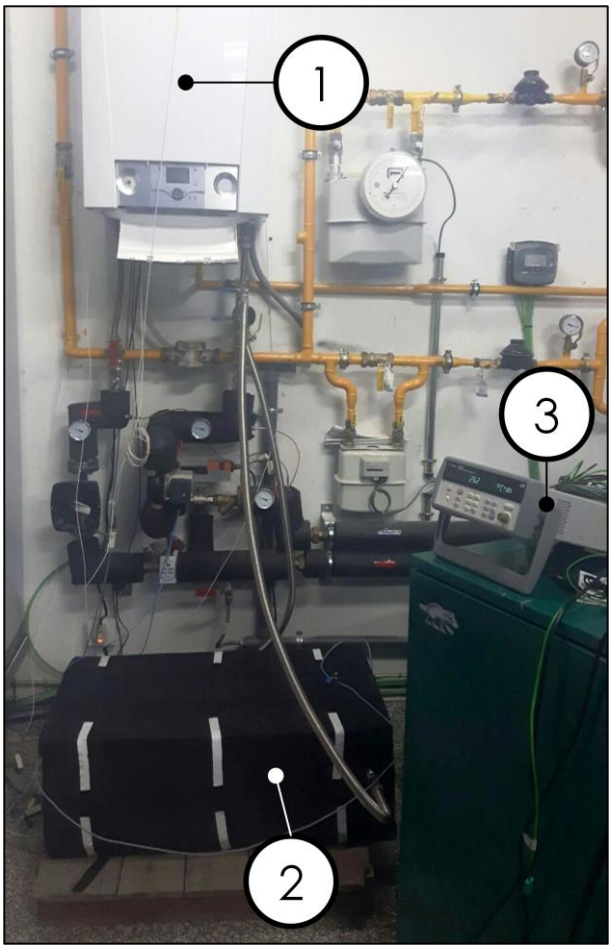

Figure 6-21: Part of the pilot plant showing: 1) CHP unit; 2) LHTES system and 3) data acquisition system

The pumps of the loop are adjusted to provide a HTF flow rate of 5 lit/min (300 lit/h). The actual temperature and flow rate registered throughout the process are shown in Figure 6-22, along with the LHTES temperature. The temperature evolution of the second discharging cycle as a function of time can be appreciated in Figure 6-23.

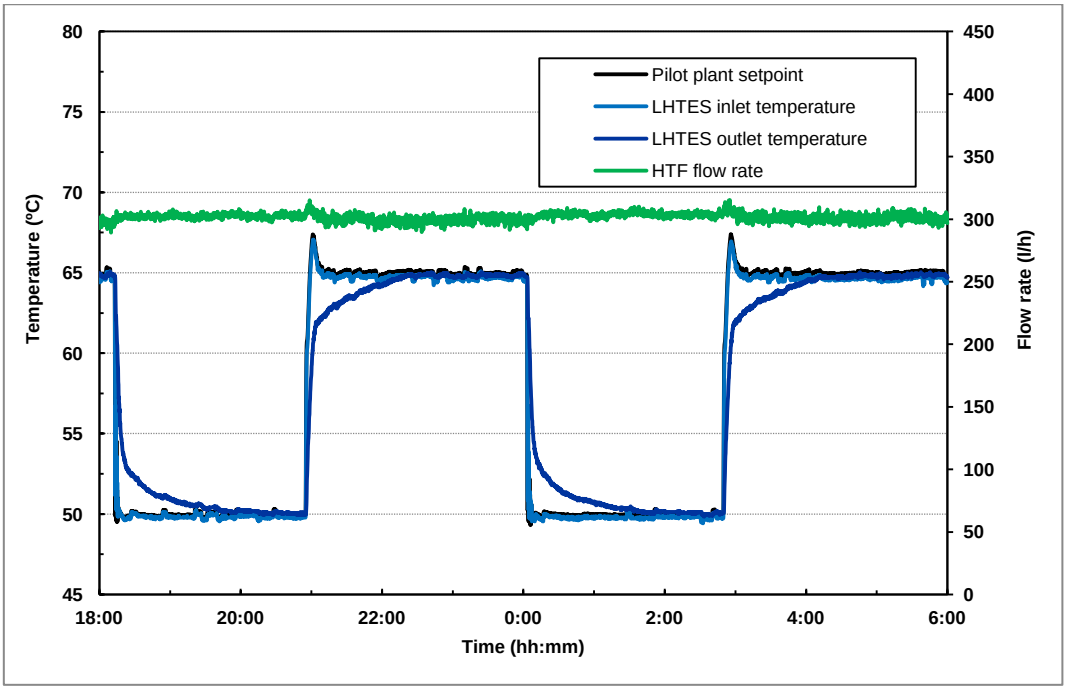

Figure 6-22: Temperature evolution and flow rate evolution of two successive charging and discharging cycles

4.3. Charging and discharging behavior. Storage capacity of the system

For the appraisal of the behavior of the system, the data corresponding to the second charging and discharging cycles were employed. The temperature evolution was used to calculate the heat stored and released by the prototype. To do it, the system energy losses ($\dot{Q}_{loss}$) during the test were first estimated by means of Eq. 6-1. The average difference between the system inlet and outlet temperatures (T_{inlet} and T_{outlet}, respectively) when isothermal conditions are attained was used for that purpose.

The results rendered heat losses of 0.095 kW at 50 °C and 0.14 kW at 65 °C. The heat loss occurring within the 50-65 ºC temperature range was considered linear. Accordingly, the heat-loss during the tests was calculated by the interpolation of the values.

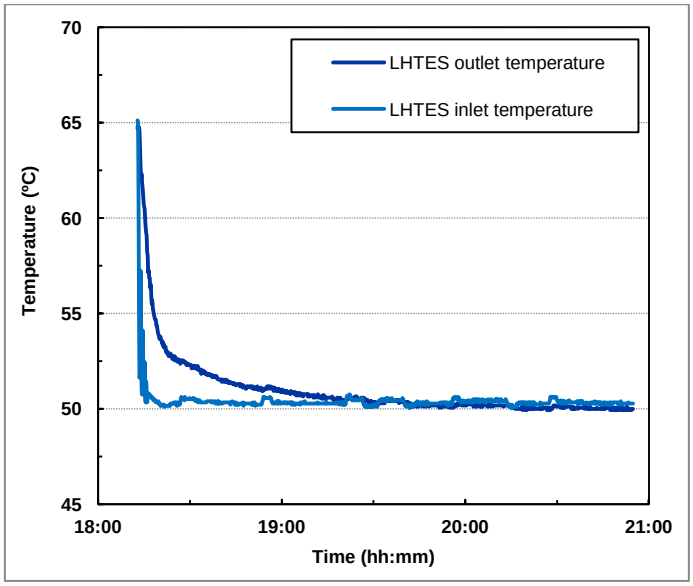

Figure 6-23: Temperature evolution of one discharging cycle

Afterwards, the calculation of the energy stored/ released at each time step ($Q_{time\ step}$) was carried out using Eq. 6-2. The C_p and the density (the latter was used to determine the mass flow rate) were considered temperature dependent. They were calculated for each time step as a function of the inlet and outlet average temperature (T_{inlet} and T_{outlet}, respectively). With the energy stored/released at each time step, the accumulated energy was determined. The charging/ discharging ratio was finally determined for each time step dividing the accumulated stored energy by the total stored/ released energy. The evolution of the charging/ discharging ratio is shown in Figure 6-24, where the asymptotic trend can be appreciated.

$$\dot{Q}_{\ loss}[kW] = \dot{m}C_p(T_{outlet} - T_{inlet})_{steady} \qquad \text{Eq. 6-1}$$

$$Q_{time\ step}[kJ] = \left(\dot{m}C_p(T_{outlet} - T_{inlet}) - \dot{Q}_{\ loss}\right)\Delta t_{\ time\ step} \qquad \text{Eq. 6-2}$$

The total energy stored upon melting was 3021 kJ, whilst 3155 kJ were released on solidification. The difference between these two experimental values is attributed to the sum of uncertainties of the different experimental components, as well as to a possible overestimation of the heat loss. The average of these two values was adopted as the experimental thermal storage capacity value, 3088 kJ. The calculated theoretical energy storage capacity of the prototype was 3232 kJ (Table 6-11). A mismatch of 4.5 % exists

between this experimental value and the theoretically estimated one. This difference is considered acceptable for the purposes aimed.

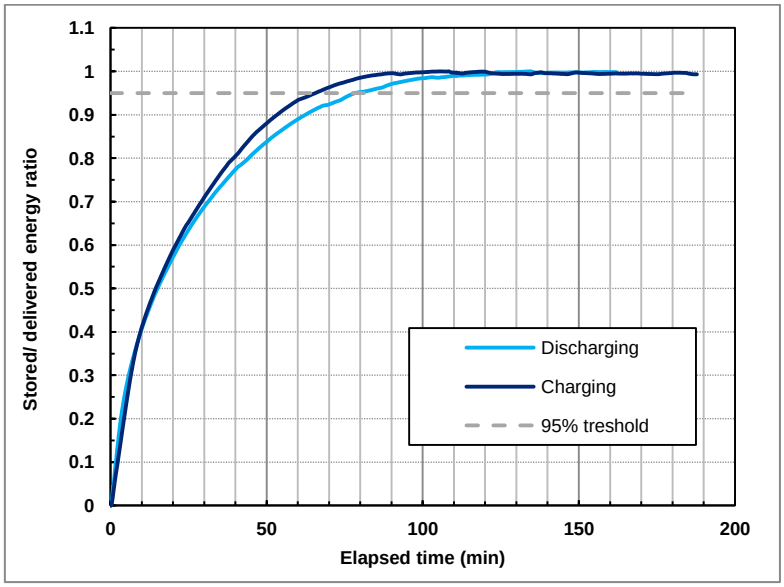

Figure 6-24: Evolution of the stored/ delivered energy ratio versus time, during charging and discharging

Considering the total volume of the tested prototype (armor and insulation included, 0.040m^3), and the storage capacity of 3088 kJ, the density storage rendered by the LHTES prototype was 21.64 kWh/m^3. Considering the typical energy storage capacity of a water tank: 16.5 kWh/m^3, it was deduced that the LHTES prototype was capable of storing 32 % more energy than the traditional sensible heat storage devices.

The discharging power is considered to be an important performance indicator. It was calculated for each time step by means of Eq. 6-3. The evolution of the discharging power can be visualized in Figure 6-25. The average power during the discharging process (calculated until a 95 % discharging ratio was achieved) was 0.65 kW, with a maximum value of 4.49 kW at the beginning of the process.

$$\dot{Q}[kW] = \dot{m} C_p (T_{outlet} - T_{inlet}) \qquad \text{Eq. 6-3}$$

Regarding the average temperature, the mean outlet temperature during discharging was 51.8 °C, while a value of 62.4 °C was attained upon charging. It has to be admitted that, based on the solidification onset temperature of the RT60, 60.0 °C and the performed preliminary tests (See Chapter 5 - Section 2.4 for DSC values or Figure 6-17 for the bulk temperature of the PCM

during the thermal cycling), a higher HTF average temperature was foreseen to be attained during the solidification. Further research is required to gain knowledge on this result because it could denote that the actual heat exchange between the HTF and the PCM is poorer than initially considered.

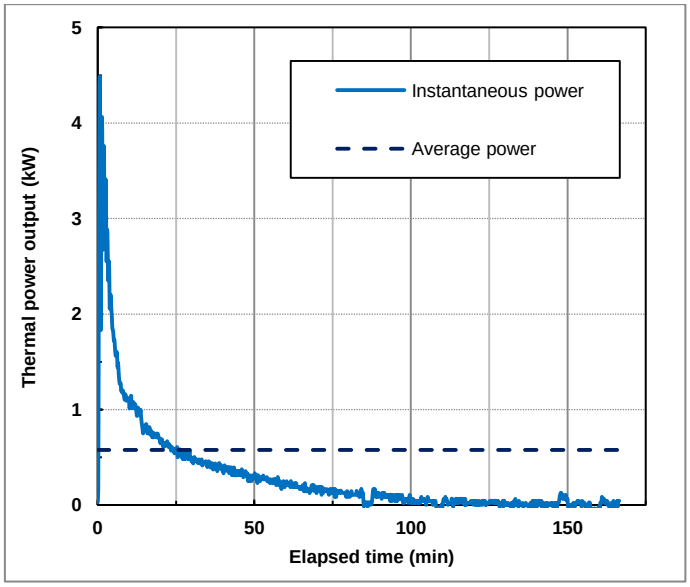

Figure 6-25: Evolution of the LHTES output thermal power during discharging

Finally, analyzing the evolution of the energy ratio, the time needed to charge/ discharge the 95 % of the energy was determined. The results showed that 78 min are needed for discharging the system, while 65 min are required for charging it (they can be inferred from Figure 6-24). Melting was 13 % faster than solidification, which reinforces the hypothesis that the influence of natural convection upon charging is a relevant feature that must be considered to design the system, as discussed in Chapter 5 - Section 3.2.

The design correlation developed in Chapter 5 was employed to estimate the system discharging time using the properties of the RT60 and a PCM thickness of 16mm. According to the correlation, the discharging time should be 47 min (considering solely the energy stored in the PCM). Therefore, a difference of 31 min was attained in comparison with the experimental value. However, in this case the system has a considerable amount of other materials, like the aluminium plates and shell, and the steel profiles, which store a large amount of energy as sensible heat. Indeed, in the present case the PCM represents 61 % of the total energy stored (Table 6-11).

Accordingly, an adjustment was applied to the calculation. The actual total storage value of the system was used as an input for the correlation, instead of the storage capacity of the PCM. The results then rendered a theoretical discharging value of 74 min, which is close to the experimental value of 78 min. This suggests that the correlation can be used under this approach; however, more case studies are necessary to confirm the reliability of this correlation. Further research should consider extending the validity of the correlation to different scenarios where the PCM does not comprise the 100 % of the storage capacity.

4.4. Economic analysis

In order to evaluate the feasibility of the manufactured prototype an economic analysis was performed. The assessment was based on the work published by Rathgeber et al. [159] within the framework of the Task 42/ Annex 29 of the IEA [160]. The study analyzed the economic feasibility of several existing storage systems by means of questionnaires, which were distributed amongst the participants of the Task 42/ Annex 29 that gathered the main technical parameters and costs of several TES prototypes. The research included sensible heat storage, latent heat storage via PCM and thermochemical heat storage, including sorption storage. The procedure is summarized next.

4.4.1. Approach employed for the economic assessment

The procedure consists of the calculation of a *maximum acceptable storage capacity cost* (abbreviated as SCC_{acc} and hereinafter referred to as *acceptable cost* in the text) that is taken as a reference. The detailed calculation procedure to estimate the acceptable cost can be consulted in [159]. As shown in Eq. 6-4, it is determined from the number of storage cycles per year, N_{cycles}, a *substituted reference energy cost*, REC and a *present value annuity factor*, ANF. The *present value annuity factor* (ANF) is obtained from the *discount rate of storage capital* (*i*) and the *payback period of the investment* (*n*), as presented in Eq. 6-5.

$$SCC_{acc}\left[{}^{€}/_{kWh}\right] = {}^{REC \cdot N_{cycle}}/_{ANF} \qquad \text{Eq. 6-4}$$

$$ANF\ [years^{-1}] = {}^{(i+1)^n \cdot i}\Big/_{(i+1)^n - 1} \qquad \text{Eq. 6-5}$$

The *acceptable cost* (SCC_{acc}) is calculated as a function of the number of storage cycles per year for three different scenarios defined: (i) acceptable cost for the industry; (ii) acceptable cost for the building sector and (iii) acceptable cost for a situation termed as "enthusiastic", which gathers the investments that can be afforded when ecological or political reasons are involved.

The *acceptable cost* values are then compared with the *realized storage capacity cost* (abbreviated as SCC_{real}, and hereinafter referred to as *realized cost*). This *realized cost* is determined dividing the *investment costs of the system* (INC) by the *installed storage capacity* (SC), as shown in Eq. 6-6.

$$SCC_{real}\left[{}^{€}/_{kWh}\right] = {}^{INC}/_{SC} \qquad \text{Eq. 6-6}$$

4.4.2. Economic feasibility of the developed LHTES system

To proceed with the study, the *realized cost* of the produced LHTES prototype was first estimated. A breakdown of the cost is presented in Table 6-12. The total *investment* (INC) was 1357 € per storage stack. Considering the energy *storage capacity* (SC) of 0.83 kWh per stack calculated in Section 4.1, the *realized cost* is 1640 €/kWh. It must be remarked that these values correspond to the originally proposed configuration (Section 2.5)[21] without the steel armor detailed in Section 2.5.1.

[21] Although the originally proposed configuration was mechanically unsuitable under normal operation pressure, it can be assumed that a simple reinforcement solution based on aluminum stiffening elements will be developed in the near future and thus, the economic analysis of this configuration will not significantly differ from the herein performed calculation.

	Cost (€)	Cost ratio (%)
14 aluminum plates (without PCM)	**956**	**70 %**
Cost of material	41	
Workforce	915	
Shell	**281**	**21 %**
Cost of material	40	
Workforce	241	
PCM	**71**	**5 %**
Cost of material	71	
Insulation and ancillary elements	**50**	**4 %**
Cost of material	50	
Total	**1357**	**100 %**

Table 6-12: Cost Breakdown of the different elements forming the LHTES prototype

The *realized cost* was compared with the *acceptable cost* for the different scenarios described above. To do it, 300 charging/ discharging cycles per year were assumed. The results are shown in Figure 6-26.

As observed, the *realized cost* of the current LHTES prototype is higher than the maximum *acceptable cost* under the "enthusiastic" scenario. It can be inferred from Figure 6-26 that the highest *acceptable cost* for the building sector and for the defined number of cycles is around 350 €/kWh. Accordingly, the *realized cost* should be reduced 4.5 times in order to reach competitive levels. The prototype is in an early stage of research and thus, it can be foreseen that the current *realized cost* presents a high decrease potential; however, a 4.5 times drop is a noticeable requirement. Henceforth, a deeper study was performed in order to gain knowledge about the actual feasibility of such a drop.

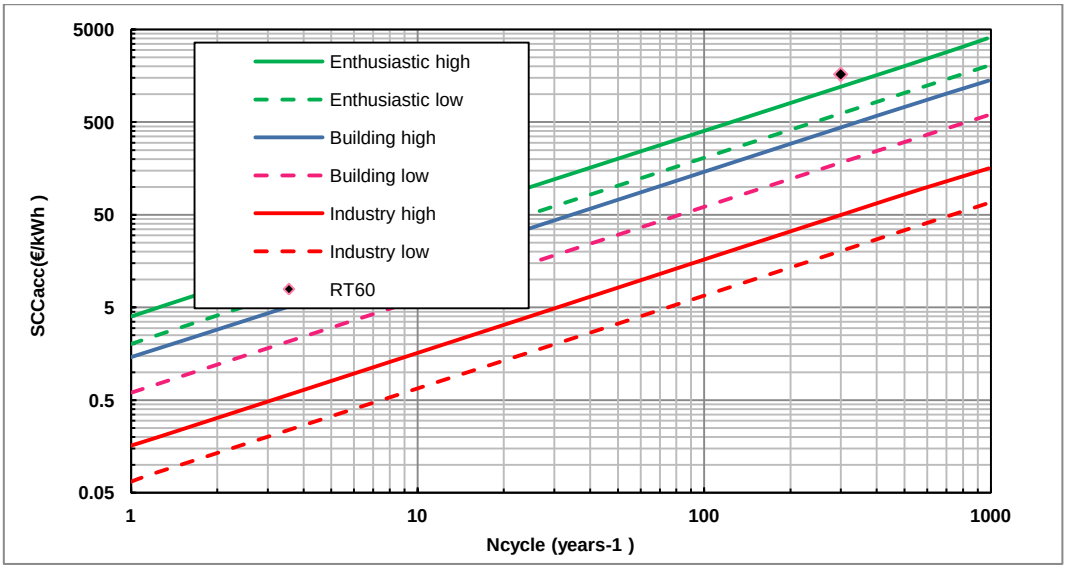

Figure 6-26: Maximum *acceptable storage capacity* (SCC_{acc}) as a function of the number of cycles for the different scenarios considered. The *realized cost* (SCC_{real}) of the LHTES developed system is also shown (denoted as RT60)

4.4.3. Potential solutions to increase the economic competitiveness of the developed system

4.4.3.1. Use of PCMs with increased energy storage density

The use of PCMs with higher storage ability is a potential alternative to lift the *realized cost* (SCC_{real}) because this increases the *installed capacity* (SC). Accordingly, the *realized cost* of the LHTES system including the following PCMs involved in the present PhD thesis were assessed (only at a theoretical basis):

- Commercial stearic and palmitic acids characterized in Chapter 5
- Erythritol-xylitol eutectic mixture (Chapter 2)
- Urea-sodium nitrate eutectic mixture (Chapter 3)
- Urea-erythritol eutectic mixture (Chapter 4)

It is needed to remark that, as discussed in the corresponding chapters, the latter 3 PCMs cannot be considered ready for use at their current stage; however, their inclusion in the economic analysis was considered interesting in order to gain knowledge on their potential as TES materials. The outcomes will also help to ascertain if it is worth to invest further efforts and money in their development.

To perform the calculation, the design procedure developed in Chapter 5 (and used in Section 2.3 of the present chapter) was employed. First, the correlation obtained in that chapter was used to estimate the maximum PCM thickness inside the plates for a maximum discharging time of 1.5 h (this constraint was used for the design of the current prototype). Due to the higher PCM melting temperatures of the analyzed systems, the operation temperatures of the CHP system had to be adapted in certain cases, but a temperature difference of 15 °C was maintained in all of them. The results rendered a thickness value of 20 mm for every PCM[22], as occurred with the RT60. Consequently, the number of plates to be used per stack remained to be 14. Based on this result, the theoretical cost and storage capability of systems using the mentioned PCMs were estimated. The results are shown in Table 6-13.

As it can be appreciated, the *investment cost* of the system (INC) was maintained in the same level for all the cases, even though the price of the various PCMs is noticeably different from one another. This is due to the fact that the cost of the PCM represents a low percentage (1-7 %) of the overall investment.

PCM	Chapter of the thesis where they were studied	Density	PCM amount in 14 plates (20mm thick)	Energy capacity of the PCM for ΔT = 15 ºC	Total energy stored by the LHTES system		Price of the PCM	Investment cost of the LHTES system *(INC)*		PCM cost/ system cost
		kg/m^3	kg	kJ/kg	KJ	kWh	€/kg	€	€/kWh	%
RT60	5	782	11.8	167.7	1972.29	0.83	6.0	1357.3	1640.4	5 %
Stearic acid	5	850	12.8	203.8	2605.10	1.00	1.9	1311.0	1306.9	2 %
Palmitic acid	5	852	12.8	196.3	2515.13	0.98	1.5	1305.8	1334.9	1 %
Urea-NaNO3	3	1420	21.4	200.0	4270.90	1.47	1.0	1308.1	892.3	2 %
Urea-Erythritol	4	1282	19.3	278.0	5359.61	1.77	2.5	1334.9	754.9	4 %
Erythritol-Xylitol	2	1300[23]	19.5	278.7	5448.55	1.79	5.2	1388.4	774.3	7 %

Table 6-13: Main characteristics considered for the economic analysis of the LHTES system including several PCMs

As a result of a similar total cost in all cases, the systems including PCMs with increased storage capacity, such as the eutectic mixtures, presented a *realized cost* (SCC_{real}) nearby 2 times lower than the original prototype due to the increased *storage capacity* (SC).

[22] For some PCMs a value of 30mm thickness could have been employed; however, for the sake of clarity and due to the fact that this is an approximated estimation, the use of 20 mm thickness for every PCM was considered more suitable.

[23] Obtained from [162]. The remainder values of the table were taken from the previous chapters of the thesis.

Although the cost reduction was not large enough to descend below the barrier of 350 €/kWh, considered the *acceptable cost* for the conditions involved, this is a significant drop in comparison with the current version of the system with RT60 as a PCM. These results reinforce the need of further research on PCMs with enhanced storage capacity. Furthermore, they encourage future investigations focused on the enhancement of the PCMs already developed in the present PhD thesis.

4.4.3.2. Reduction of the number of plates to be used by the use of PCM composites with enhanced thermal conductivity

Another potential solution to decrease the high *realized cost* of the system (SCC_{real}) would involve the reduction of the *investment costs* (INC). As shown in Table 6-12 and Table 6-13, the price of the PCM per stack in the developed system represents merely 1 to 7 % of the total *investment cost*. This is low compared with the estimations provided in the PhD thesis of Campos-Celador [5] and the literature [159], where values above 10 % of the total cost are suggested. Thus, considering that the price of the employed PCMs is at a reasonable level (all below 6 €/kg), and that the specific manufacture of the plates represents 70 % of the final cost, it can be inferred that the *investment cost* of the system is highly influenced by the price of the plates. Accordingly, further efforts should be focused on the development of a simpler manufacturing process, mainly focused to minimize the labor needed.

A complete redesign of the plates is out of the scope of this thesis; however, a direct decrease in the *realized cost* could be attained by the reduction of the number of plates to be used per stack. This would result in a reduction of the output thermal power; thus, an increase of the heat exchange rate between the PCM and the HFT should be attained in order to compensate for it.

The original version of the LHTES system developed in the work of Campos-Celador [5] included fins to enhance the thermal conductivity. Their manufacturing was too expensive and therefore they were discarded from the design in the present work. Instead of this expensive solution, recent literature studies demonstrate that the use of composite materials with increased thermal conductivity can be economically competitive, as follows:

- Karthik et al. [92] developed a composite based on a low-cost expanded graphite foam (EG) used as a heat conductive matrix. This matrix was combined with erythritol to create a form-stable PCM of 75 % (w/w) erythritol. The thermal conductivity of the composite was 5 times larger than that of pristine erythritol (3.77 W/mK vs. 0.72 W/mK). The cost of the graphite foam was 3 €/kg; thus, the cost of the composite PCM only rose from 1.5 €/kg to 2 €/kg
- Mantilla et al. [161] developed a composite PCM formed by RT60 and expanded graphite by means of a simple method based on the use of an autoclave. Their results showed that a material comprised by a 75 % (w/w) of RT60 achieved a thermal conductivity of 1.33 W/m·K. They also reported that the cost of the composite was maintained low, although they did not provide any specific value

Attending to these articles, the use of composite PCMs with higher thermal conductivities can be nowadays economically competitive. Thus, the aforementioned data were used to estimate the performance and cost of plate-based LHTES systems combined with expanded graphite. The PCMs selected were RT60 and the erythritol-xylitol eutectic mixture, in order to be able to extrapolate the data found in refs [92,161]. Since erythritol was combined with the EG foam in [92], it was assumed that the EG foam could be used with the erythritol-xylitol eutectic mixture, rendering a thermal conductivity 5 times higher than the pristine material. Regarding the RT60, those properties provided in [161] were directly applied.

The numbers were inserted in the design correlation developed in Chapter 5. The maximum plate thickness that could be used to achieve the same discharging time of the pristine materials was then calculated. They are shown in Table 6-14. It can be appreciated that the value rose noticeably when the composite was employed: 2.4 times for the erythritol-xylitol + EG composite and 2.8 times for the RT60 + EG combination.

PCM	Thermal conductivity (W/m·K)	Energy capacity of the PCM for ΔT = 15 ºC (kJ/kg)	Discharging time by the correlation (h)	PCM thickness (mm)	Number of plates to be used
Erythritol-xylitol	0.38 [a]	278.70	0.64	16	14
75 % Erythritol-xylitol + EG	1.90 [b]	209.03	0.64	39	6
RT60	0.20	167.71	0.79	16	14
75 % RT60 + EG	1.33 [c]	125.78	0.78	45	6

Table 6-14: Determination of the maximum plate thickness to be used with the expanded graphite composite PCMs.[a] Obtained from [162]. [b] Estimated from the data published in [92].[c] Obtained from [161].

The maximum thickness values were used to estimate the weight and storing capacity of the LHTES system including the PCM-EG composites. The rest of the constraints, such as the length of the plates and the stack dimensions remained unchanged. The results are shown in Table 6-15 and Table 6-16, broken down by components.

A first observation at both tables indicates that the overall capacity of the two systems with EG decreased slightly, as could be expected from the fact that the composites only include 75 % (w/w) of PCM. However, the overall storage capacity dropped less than the 25 % because the reduction in the number of plates allows increasing the total volume occupied by the PCM-composite in relation to the HTF. Accordingly, the capacity of the RT60 + EG system was 90 % of the original system, while the system employing the erythritol-xylitol + EG system maintained the 80 % of its initial capacity.

	RT60					RT60 + EG				
	Weight		Storage capacity			Weight		Storage capacity		
	kg	%	kJ	kWh	%	Kg	%	kJ	kWh	%
PCM	11.8	23.9 %	1972.5	0.55	66.2 %	10.8	24.8 %	1804.4	0.50	67.2 %
Aluminum plates	13.6	27.6 %	177.6	0.05	6.0 %	8.5	19.6 %	111.1	0.03	4.1 %
Aluminum shell	13.5	27.4 %	176.2	0.05	5.9 %	13.5	31.1 %	176.2	0.05	6.6 %
Water	10.4	21.1 %	652.6	0.18	21.9 %	9.0	20.6 %	561.8	0.16	20.9 %
Graphite	0.0	0.0 %	0.0	0.00	0.0 %	1.7	4.0 %	30.2	0.01	1.1 %
Total	**49.3**	**100.0 %**	**2978.9**	**0.83**	**100.0 %**	**43.5**	**100.0 %**	**2683.7**	**0.75**	**100.0 %**

Table 6-15: Weight and storage capacity of the different LHTES elements: comparison between RT60 and RT60 +EG

Finally, the *installed storage capacity* and the weight were employed to calculate the *investment cost* (INC) of the system. There are presented in Table 6-17, itemized by components. A comparison between the *realized costs* of the systems with and without EG can be ultimately observed in Table 6-18.

	Erythritol-xylitol					Erythritol-xylitol + EG				
	Weight		Storage capacity			Weight		Storage capacity		
	kg	%	kJ	kWh	%	kg	%	kJ	kWh	%
PCM	19.8	34.6 %	5528.3	1.54	84.6 %	16.1	31.9 %	4499.9	1.25	81.7 %
Aluminum plates	13.7	23.8 %	178.1	0.05	2.7 %	8.2	16.3 %	107.3	0.03	1.9 %
Aluminum shell	13.5	23.5 %	176.2	0.05	2.7 %	13.5	26.7 %	176.2	0.05	3.2 %
Water	10.4	18.1 %	652.6	0.18	10.0 %	11.1	22.0 %	698.1	0.19	12.7 %
Graphite	0.0	0.0 %	0.0	0.00	0.0 %	1.5	3.0 %	26.9	0.01	0.5 %
Total	**57.4**	**100.0 %**	**6535.3**	**1.82**	**100.0 %**	**50.5**	**100.0 %**	**5508.4**	**1.53**	**100.0 %**

Table 6-16: Weight and storage capacity of the different LHTES elements: comparison between erythritol-xylitol and erythritol-xylitol + EG

	RT60 + EG		Erythritol-xylitol + EG	
	Cost (€)	Cost ratio (%)	Cost (€)	Cost ratio (%)
6 aluminum plates	**418**	**51 %**	**417**	**49 %**
Cost of material	26	3 %	25	3 %
Workforce	392	48 %	392	46 %
Shell	**281**	**34 %**	**281**	**33 %**
Cost of material	41	5 %	41	5 %
Workforce	241	29 %	241	28 %
PCM	**65**	**8 %**	**97**	**11 %**
Cost of material	65	8 %	97	11 %
Graphite	**5**	**1 %**	**5**	**1 %**
Cost of material	5	1 %	5	1 %
Insulation and ancillary elements	**50**	**6 %**	**50**	**6 %**
Cost of material	50	6 %	50	6 %
Total	**819**	**100 %**	**849**	**100 %**

Table 6-17: Costs of theoretical LHTES systems with RT60 + EG and erythritol-xylitol +EG, itemized by elements

PCM	RT60	RT60 + EG	Erythritol-xylitol	Erythritol-xylitol + EG
Cost (€)	1357	819	1390	836
***Storage capacity* (kWh)**	0.83	0.75	1.82	1.53
***Realized cost* of the system (€/kWh)**	**1640**	**1098**	**766**	**547**

Table 6-18: Realized costs of LHTES system with and without PCM composites for thermal conductivity enhancement

When comparing the *realized costs* of the systems produced with composites and those with pristine PCMs, a reduction of 33 % was achieved for the RT60 + EG system, while a 28 % drop was reached for the erythritol-xylitol + EG case. In absolute terms, both values are still above the 350 €/kWh threshold. However, a system using erythritol-xylitol + EG would be close to it. Accordingly, it can be concluded that the use of PCM composites with enhanced thermal conductivity would increase the economic competitiveness of the LHTES system. Further research oriented towards this direction is therefore commendable.

Furthermore, this solution could help in solving the problem of the low average discharging temperature (see Section 4.3) if further tests would actually confirm the poor heat exchange (between the PCM and the HTF) being the main reason for this low temperature.

4.4.3.3. Additional potential improvements of the system

Additional investment cost reductions could be targeted on the manufacturing process. It has to be noticed that workforce computes for 90 % of the total cost of the plates and the shell, even if the number of plates is reduced (Table 6-17). Henceforth, a significant cost-reduction is still feasible to be attained if the production processes are optimized.

It can be inferred that the manufacturing of the plates and the shell is highly influenced by the complexity of the aluminum welding. Therefore, the use of carbon steel as the main material of the system should be considered as an alternative, because its welding procedure is noticeably easier than aluminum and/or stainless steel.

The use of carbon steel was initially discarded in the present thesis project due to potential corrosion problems and to the higher weight than aluminum (Section 2.2). However, according to the attained results, its use should be considered as a realistic alternative in forthcoming steps of the research. The corrosion problems could be avoided by the use of galvanic protection (zinc coating, sacrifice anodes, imprinted current) or by others methods (paints, corrosion inhibitors in the water, etc.).

Other cost reduction could involve the use of one big stack for the whole prototype (although only one stack was herein evaluated, a full-scale prototype would comprise 6 stacks). Besides, bearing in mind that the EG foam is a highly stiff material, a new plate design could be approached: the enclosure would not require being stiff anymore; a tight but flexible envelope could now be used. This opens the door to the use of low cost bag-like wraps, made of metallic films or similar. The cost of the system could drop down to a competitive level. All these challenges will be faced in further research.

5. Conclusions of the chapter and further work

A plate-based LHTES full-scale prototype was designed, built and evaluated under real operation conditions. The system is based in 3 different types of elements: the plates; the shell and the ancillary elements. The material chosen for the production of the plates and the shell

was an aluminum alloy due to its low cost and weight. The produced LHTES prototype was coupled to a micro-CHP pilot plant and was tested. The results were analyzed in terms of the thermal behavior and the economic performance. The main conclusions of the chapter are detailed next.

5.1. Conclusions related to the design and manufacturing of the LHTES system

According to the performed literature review, no suitable plates are currently commercialized for the aimed purpose, which demonstrates the lack of available market products.

The plate design is based in the use of commercially available extruded rectangular profiles, cut to the desired length and closed with two welded lids to fulfill the functions required. The plates' mechanical integrity and stability was verified after 20 accelerated thermal cycles. Longer period evaluation is required in the near future in order to ensure that the plates show a proper lifespan behavior.

Some welds showed leakage to air due to an improper finishing of the welding. The problem was fixed with additional visual control of the pieces after the reception. This suggests that the welding of the plates is complex due to the use of aluminum, but that a good welding procedure combined with a suitable quality control can render a feasible production process of the plates.

Several tests were carried out in all the elements to determine any tightness failure and, especially, to determine suitable closure options of the inlet-holes introduced on the plates to fill–them-in with the PCM. A reliable and simple closure identified comprises the combination of a thread, formed by thermal drilling, with threaded plugs that included Viton O-ring gaskets. The same closure using paper gaskets was air-tightened but permeable to the RT60 PCM.

The use of separation strips attached to one side of the plates represents a simple and successful solution to form the HTF channels. The behavior of the selected adhesive under a thermal cycling test was adequate.

The designed shell could not be produced with the originally selected alloy (aluminium alloy AA6082) because the manufacturer could not guarantee defect-free welds on the large case. Instead, it was made of an aluminium alloy AA1050. This alloy was unsuitable to handle the

normal operation pressures of the system. A thorough evaluation of the mechanical and manufacturing aspects of the design should be faced in the near future to develop a suitable shell. This will include the simulation of different design options and materials in a mechanical modeling software (SolidWorks, others) and its further validation by producing a new shell and prototype.

An "armor-like" interim solution was used to evaluate the thermal behavior of the produced prototype without compromising the physical integrity of the system under the operating conditions. This solution showed an adequate mechanical behavior although the configuration is unsuitable for a commercial product. The use of the steel armor, and the associated changes, prevented to test the total LHTES prototype, formed by 6 stacked shells. Accordingly, the thermal measurements were performed only with one stack. However, the results are still representative of a full-scale LHTES prototype.

5.2. Conclusions related to the thermal behavior of the LHTES system

The thermal cycling tests of the PCM plates into a climatic chamber proved that the thermal behavior of the PCM was reproducible along 20 cycles. The PCM melted and solidified in the same temperature ranges along every cycle. No variations due to undesired effects such as degradation or supercooling occurred.

The tests carried out in the pilot plant rendered an energy density storage of 25.75 kWh/m^3 for the produced prototype. Subtracting the calculated storage capacity of the steel armor, a final storage density of 21.64 kWh/m^3 was achieved for the original design. This storage capacity is 31 % higher than a water tank with the same volume and temperature operation conditions.

The mean outlet temperatures during charging and discharging were lower than foreseen according to the PCM solidification onset temperature. Further research is required to gain knowledge on this effect because it could denote that the actual heat transfer to the PCM is poorer than initially considered.

The discharging time estimated by means of the correlation developed in Chapter 5 showed a difference of 40 % in relation to the actual value. The difference was attributed to the fact that the PCM represented merely 61 % of the total energy to be stored in the present case. After including an adjustment to the correlation, the difference between the experimental and the

theoretical values was limited to 5 %. Further research is required to confirm the validity of the modified correlation.

5.3. Conclusions regarding the economic aspects

An economic analysis of the LHTES system was performed, based on the work by Rathgeber et al. ([159]) within the Task 42/ Annex 29 of the IEA [160]. The *realized storage capacity cost* [159] of the produced prototype was 1640 €/kWh. This cost is 4.5 times higher than the *maximum acceptable costs* for the building sector. The cost is even higher than the *acceptable costs* under the "enthusiastic" scenario defined in [159].

The same LHTES system including PCMs with increased thermal storage capacity, such as the eutectic mixtures developed in this thesis, would reduce the *realized costs* to nearby 2 times lower. This reduction is not enough to achieve the threshold of 350 €/kWh considered competitive for buildings, but the drop is significant and straightforward. These results reinforce the need of further research on PCMs with enhanced storage capacity. Moreover, they encourage future investigations focused on the improvement of the PCMs already developed in the present PhD thesis.

The use of composite PCMs with enhanced thermal conductivity can be a solution to increase the economic competitiveness because the number of plates could be noticeably reduced to achieve the same thermal power output. A theoretical analysis of the LHTES system using erythritol-xylitol + EG would present a *realized cost* of 547 €/kWh, close to the 350 €/kWh considered as the limit cost for the building sector, and 3 times lower than the current cost of the prototype. Further research oriented towards the use of PCM composites with enhanced thermal conductivity is therefore recommended.

The use of carbon steel as the main material for the production of the plates and the shell should be considered as an alternative option to aluminium alloys because the cost is lower and its weldability is noticeably higher and easier than aluminum alloys. The corrosion problems that prevented the selection of carbon steel to produce the prototype developed in this project could be avoided by means of galvanic protection (coatings or sacrifice anodes).

CHAPTER 7: Conclusions and further work

ABSTRACT

As closing remarks to this thesis, all the conclusions and contributions obtained from the work are summarized in this chapter. A dissemination plan for the results is provided and the future research lines are described.

1. Introduction

The main objective of this PhD thesis was the development of a plate-based LHTES system based on a basic configuration defined on a former research thesis [5]. According to the system's characteristics and constraints indentified in [5], the search of solutions was herein divided into three main research lines:

- Development of new, cost-effective PCMs for the temperature range 50 – 90 °C, based on eutectic mixtures of materials
- Research on simplified design procedures for plate-based LHTES systems for heating and DHW applications
- Design and construction of a full-scale plate-based LHTES prototype and its evaluation on a domestic CHP pilot plant

The conclusions attained for each of these research items are described on the following sections, followed by the performed dissemination of the results. The chapter is closed with a plan for future research and the main concluding remarks.

2. Conclusions related to the development of new, cost-effective eutectic PCMs for the 50-90 ºC temperature range

Five eutectic mixtures of eutectic PCMs were studied and evaluated in order to develop new, cost-effective PCMs for the temperature range involved. They are summarized in Table 7-1, together with the characterized main properties. All of them showed good potential as a PCM for the intended applications; however, drawbacks were also indentified. The main conclusions are presented next, divided into groups of materials.

2.1. Binary mixtures of sugar alcohols

Three new binary mixtures of sugar alcohols were studied. The mixtures comprise erythritol, sorbitol and xylitol. The solid–liquid phase diagrams of the systems were established, and each of them corresponded to a simple eutectic system. The polymorphism and solidification behavior of the pristine materials and of the mixtures were also assessed.

Component 1	Component 2	Eutectic composition (% w/w) (% of component 1)	Experimental eutectic temperature (ºC)	Experimental melting enthalpy (kJ/kg)	Density (g/cm3)	Price (€/kg)
Erythritol	Xylitol	21.0	83.9	248.7	1.3 (95 ºC)	5.2
Erythritol	Sorbitol	22.0	86.6	172.8	_	1.5
Xylitol	Sorbitol	47.0	74.6	169.6	_	3
Urea	Sodium Nitrate	71.3	85.0	172.0	1.42 (89 ºC)	<1
Urea	Erythritol	45.1	81.1	248.0	1.28 (95 ºC)	2.5

Table 7-1: Eutectic mixtures developed in the thesis project and their main properties

Regarding melting temperature, storage capacity and market price, the mixtures studied are suitable for the intended purpose. Even though the three mixtures were considered interesting for TES purposes, the erythritol–xylitol eutectic composition showed the highest potential due to its superior heat storage ability.

Experimental measurements showed that the mixtures presented a low crystallization rate, which limits their use in short-term LHTES systems like that herein developed. Additionally, the materials show polymorphism and tend to form metastable amorphous states. As a result, further research is needed to enhance the crystallization behavior of the mixtures to be used as PCMs for the intended applications.

2.2. Sodium nitrate-urea binary mixture

The binary system composed of sodium nitrate and urea was also studied. The solid–liquid equilibrium of the system was determined by using several complementary techniques.

The experimental measurements demonstrated that the system is a eutectic type. The volumetric energy density of the eutectic composition is close to the storage capacities of stearic or palmitic acid and is larger than the values for paraffins in the considered temperature level. The influence of the water uptake on the melting and solidification behaviour was also characterized.

Due to the known thermal degradation of urea above 133 °C, the thermal stability of the eutectic mixture was evaluated using an accelerated thermal cycling test. Under the applied experimental conditions, the mixture underwent irrelevant changes after 210 cycles, while HPLC tests showed a minor presence of degradation by-products. It was deduced that the thermal stability of the proposed eutectic PCM at its potential operation range (below 90 °C) is clearly improved in comparison to that of the pure urea at its melting temperature (133 °C).

As a main conclusion, the proposed sodium nitrate-urea eutectic mixture shows potential for use as a PCM for LHTES systems at the heating and DHW temperature range, especially due to its highly competitive price. Further research is required to evaluate the mixture thermal stability for the long-term use under conditions representative of actual applications.

2.3. Erythritol-urea binary mixture

The binary system formed by erythritol and urea was studied for its use as a PCM. The attained experimental results showed that the binary system forms a simple eutectic phase diagram. According to the energy storage capacity, melting temperature and price, the studied PCM is suitable for TES purposes at the intended temperature level.

Preliminary thermal cycling tests showed that after 85 thermal cycles the enthalpy of the eutectic mixture was reduced 3.6 % in relation to the original melting enthalpy. This fact reinforced the idea that the thermal degradation of urea is greatly dependent on the temperature. Thus, its decomposition rate will be significantly lower when forming part of a molten eutectic PCM operating at temperatures below 100 °C than when pure urea is operating at around its melting temperature (133 °C).

As occurred with the urea-sodium nitrate mixture, further works are required before it is confirmed that it can be employed as a PCM. These works should be specifically focused to evaluate the stability of the mixture on longer usage-periods.

2.4. Methodologies for the development of new eutectic PCMs and their characterization

The need to develop suitable characterization methods is highlighted in the literature. An extra objective of this work was to gain knowledge on the determination of phase diagrams and thermophysical properties of PCMs by means of different complementary techniques, and eventually to develop new techniques and new procedures to determine thermophysical parameters.

The modeling of phase diagrams was approached by a thermodynamics–based approach suitable to predict solid–liquid equilibrium of binary systems involving organic materials. This approach was employed for the determination of the phase diagrams of mixtures between sugar alcohols and also between urea and erythritol. Equilibrium melting temperatures and

melting enthalpies obtained from simulations were in good agreement with the experimental results.

The experimental determination of phase diagrams required the use of several complementary techniques for the research of the new eutectic materials. Some of them are rarely used in the TES field, such as the hot–stage microscopy and the contact preparation method. Detailed information of the employed methodologies was deliberately provided in each chapter. As a result, this document can be used as a consultation reference for methodologies suitable for the determination of new eutectic PCMs for TES purposes.

The combined use of some of these techniques was included as a sequential methodology employed to evaluate the suitability of the urea-erythritol mixture as a PCM. This procedure started using fast techniques to achieve an initial estimation of the potential of the eutectic composition as a PCM. After that, the results were refined with more precise techniques, such as DSC, the synthetic visual method and XRD. The methodology employed has proven to be adequate for the development of new eutectic PCMs.

3. Conclusions on the development of simplified design procedures for plate-based LHTES systems for heating and DHW applications

A fast and systematic calculation tool for the sizing and optimization of plate-based LHTES systems was developed.

A dimensionless number, Fo_{95}, was proposed for the calculation of the discharging time as a function of several dimensionless groups (*Bi*, *Ste*, Ψ and Ψ_{pc}). In turn, these groups depend on the plate thickness, the materials properties and the plant operation parameters.

The results of 86 CFD simulations were adjusted by means of a multiple linear regression to develop the correlation. A good fit for the sought aims was obtained, with an adjusted Pearson's R of, 0.976. The discharging time obtained by means of the correlation was compared with those obtained by means of the original CFD simulations. The average error of the correlation was 3.5 %.

The Fo_{95} correlation was validated against 5 additional PCMs. The discharging times obtained by CFD and by means of the simplified correlation were compared. The average error was 2.38

%. Consequently, the correlation developed can be confidently employed for design purposes to determine the discharging time of plate based LHTES systems that operate within the above mentioned Fo_{95} number ranges.

Combining the correlation and the remaining constraints of the system, an overall design method was developed for plate based LHTES systems for CHP applications. The objective of the methodology is to maximize the storage capacity of a system constrained to a specified volume, able to provide the required thermal power to achieve a discharging time defined by the user demand profile.

The method consists of 3 simple steps: To estimate the plate thickness, to calculate the number of plates in-parallel and to determine the plate length (or the number of plates in-series). This renders a complete sizing of the system without the need of simulations. Besides, with small modifications, it could be easily extended to other applications rather than CHP plants. This procedure noticeably simplifies the design process of LHTES systems and decreases the time needed to size them.

4. Conclusions on the design and construction of a full-scale plate-based LHTES prototype and its evaluation on a domestic CHP pilot plant

A plate-based LHTES full-scale prototype was designed, built and evaluated under nominal operation conditions. The produced LHTES prototype was coupled to a micro-CHP pilot plant and was tested. The results were analyzed in terms of the thermal behavior and the economic performance.

4.1. Conclusions related to the design and manufacturing of the LHTES system

The proposed plate design is based on the use of commercially available extruded rectangular profiles made of aluminum alloys. It fulfilled the required functions. The plates´ tightness and the mechanical integrity were verified after 20 accelerated thermal cycles. Longer period evaluation is required in the near future in order to ensure that the plates show a proper lifespan.

The produced outer shell of the prototype was unable to handle the normal operation pressures. An “armor-like” interim solution was used to evaluate the thermal behavior of the produced prototype without compromising the physical integrity of the system under the operating conditions. A thorough evaluation of the mechanical and manufacturing aspects of the design should be faced in the near future to develop a suitable shell.

4.2. Thermal behavior of the LHTES system

The tests carried out on the pilot plant rendered an energy density storage 31 % higher than a water tank with the same volume and temperature operation conditions.

The mean outlet temperatures during charging and discharging were lower than foreseen according to the PCM solidification onset temperature. Further research is required to gain knowledge on the reasons for this behavior because it could denote that the actual heat transfer to the PCM is poorer than initially considered.

The discharging time estimated by means of the correlation developed in Chapter 5 showed a difference of 40 % in relation to the actual value. The difference was attributed to the fact that the PCM represented merely 61 % of the total energy stored in the prototype. After including the required adjustment to the correlation, the difference between the experimental and the theoretical values was limited to 5 %. Further research is required to confirm the validity of the modified correlation.

4.3. Economic aspects of the LHTES system

An economic analysis of the LHTES system was performed. The results showed that the cost of the produced prototype was 4.5 times higher than the *maximum acceptable cost* for the building sector.

Additional calculations performed showed that the same LHTES system including PCMs with increased thermal storage capacity, such as the eutectic mixtures developed along the previous chapters of the thesis (Table 7-1), would reduce the *realized costs* to nearby 2 times lower. These results reinforce the need of further research on PCMs with enhanced storage capacity. Moreover, they encourage future investigations focused on the enhancement of the PCMs already developed in the present PhD thesis.

The use of composite PCMs with enhanced thermal conductivity can be a solution to increase the economic competitiveness because the number of plates could be noticeably reduced to achieve the same thermal power output. Further research oriented towards the use of PCM composites with enhanced thermal conductivity is therefore recommended.

The use of carbon steel as the main material for the production of the plates and the shell should be considered as an alternative option to aluminium alloys because of its lower cost and easier weldability in comparison with aluminum alloys. The corrosion problems that prevented the selection of carbon steel to produce the prototype developed in this project could be avoided by means of galvanic protection (coatings or sacrifice anodes).

5. Dissemination of the thesis outcomes

Many results attained in this thesis have already been disseminated by means of the activities presented in Table 7-2. The scientific articles published so far in international journals correspond to the work related with materials development because that work was performed at the initial period of the thesis project.

Two additional articles are in progress: one about the design procedure for LHTES systems developed in Chapter 5 and another one about the design and behavior of the LHTES constructed (and tested) prototype (Chapter 6).

The latter results, related with Chapters 5 and 6, will presumably be presented in international conferences about TES during the years 2017 and 2018, such as the forthcoming SHC 2017 conference in Abu Dhabi or the Stock Series conference to be held in Adana, Turkey in 2018.

Besides, the results of the thesis will be disseminated in the SHC Task 58/ ECES Annex 33 of the IEA, where the author of the thesis will take part. This coordination program deals with advanced materials for latent and chemical thermal energy storage and will last from January 2017 to December 2019.

Research topic	Journal articles in international journals	Conference papers
Sugar alcohol eutectic mixtures as PCMs for heating and DHW LHTES systems	• G. Diarce, I. Gandarias, A. Campos-Celador, A. García-Romero, J.M. Sala, Eutectic mixtures of sugar alcohols for thermal energy storage in the 50-90 °C temperature range, Solar Energy Materials and Solar Cells, 134 (2015) 215-226.	• G. Diarce, A. Campos-Celador, A. García-Romero, J.M. Sala, Eutectic mixtures of sugar alcohols as PCMs for heating and DHW applications: phase diagrams and crystallization behavior, Greenstock 2015, Beijing, 2015. • G. Diarce, I. Gandarias, S. Gómez, A. Campos-Celador, A. García-Romero, J.M. Sala, Sugar alcohol eutectic mixtures for thermal energy storage in a temperature range of 60-90 ºC, Eurosun 2014, Aix-Les Bains, 2014. • G. Diarce, I. Gandarias, S. Gómez, A. Garcia-Romero, J.M. Sala, Determination of the solid-liquid equilibrium of mixtures of sugar alcohols for their use as phase change materials, Thermam 2014, Çesme, 2014. • G. Diarce, U. J. Griesser, A. Garcia-Romero, Crystallization rate of eutectic mixtures of erythritol and xylitol for thermal energy storage applications, ISC 2014, Granada, 2014.
The sodium nitrate-urea eutectic mixture as a PCM for heating and DHW LHTES systems	• G. Diarce, E. Corro-Martínez, L. Quant, Á. Campos-Celador, A. García-Romero, The sodium nitrate- urea binary mixture as a phase change material for medium temperature thermal energy storage. Part I: Determination of the phase diagram and main thermal properties, Sol. Energy Mater. Sol. Cells. 157 (2016) 1065–1075. • G. Diarce, E. Corro-Martínez, A. Campos-Celador, A. García-Romero, J.M. Sala, The sodium nitrate- urea eutectic binary mixture as a phase change material for medium temperature thermal energy storage. Part II: Accelerated thermal cycling test and water uptake behavior of the material, Sol. Energy Mater. Sol. Cells. 157 (2016) 1076–1083.	• S. Gómez, G. Diarce, A. Campos-Celador, A. García-Romero, J.M. Sala, Thermal reliability of an urea based eutectic mixture for thermal energy storage, Eurosun 2014, Aix-Les Bains, 2014. • S. Gómez, G. Diarce, A. Campos-Celador, A. Garcia-Romero, J.M. Sala, Thermophysical Characterization of a Urea Based Eutectic Mixture for Thermal Energy Storage, Thermam 2014, Çesme, 2014.
The erythritol-urea eutectic mixtures as a PCM for heating and DHW LHTES systems	• G. Diarce, L. Quant, Campos-Celador, J.M. Sala, A. García-Romero, Determination of the phase diagram and main thermophysical properties of the erythritol-urea eutectic mixture for its use as a phase change material, Sol. Energy Mater. Sol. Cells. 157 (2016) 894–906.	
Modeling and characterization of eutectic mixtures for the development of new PCMs		• G. Diarce, A. Campos-Celador, A. García-Romero, J.M. Sala Practical guidelines for the development of new eutectic mixtures of phase change materials based on equilibrium thermodynamics, Greenstock 2015, Beijing, 2015. • G. Diarce, A. Campos-Celador, I. González-Pino, E. Pérez-Iribarren, J. Terés-Zubiaga. Modelado termodinámico de sistemas eutécticos sólido-liquido para el estudio de nuevos materiales de cambio de fase, 9CNIT, Cartagena, 2015.
Modeling and simulation of plate-based LHTES systems/ development of simplified design procedures		• G. Diarce, A. Campos-Celador, A. García-Romero, J.M. Sala, CFD modeling of a plate based LHTES system: evaluation of the plate thickness on its performance and development of a simplified method for design purposes. Greenstock 2015, Beijing, 2015. • G. Diarce, A. Campos-Celador, A. García-Romero, J.M. Sala. Procedimiento general para el diseño de sistemas de almacenamiento térmico latente de placas en base a simulaciones detalladas de CFD, 9CNIT, Cartagena, 2015.
Evaluation of the behavior of plate-based LHTES systems for heating and DHW applications		• G. Diarce, A. Campos-Celador, S. Gómez, A. García-Romero, J.M. Sala, Evaluation of the thermal and economical performance of a modular TES system for domestic applications: comparison between paraffinic and fatty acid based PCMs, Eurosun 2014, Aix-les Bains, 2014.

Table 7-2: Published scientific articles and contributions to conferences directly linked to the thesis project

In addition to the research performed on the thesis project, further research related with LHTES was performed during the four years of the thesis. The covered topics include the development of characterization methodologies for PCMs, the use of PCMs on building

façades and structures or the study of LHTES systems for concentrated solar thermal plants. The dissemination activities related with those topics are presented in Table 7-3.

Journal articles in international journals	Conference papers
• A. Ristić, S. Furbo, C. Moser, H. Schranzhofer, A. Lazaro, M. Delgado, G. Diarce et al., IEA SHC Task 42 / ECES Annex 29 WG A1: Engineering and Processing of PCMs, TCMs and Sorption Materials, Energy Procedia. 91 (2016) 207–217. doi:10.1016/j.egypro.2016.06.205. • S.S.M. Tehrani, R.A. Taylor, P. Saberi, G. Diarce, Design and feasibility of high temperature shell and tube latent heat thermal energy storage system for solar thermal power plants, Renew. Energy. 96 (2016) 120–136. doi:10.1016/j.renene.2016.04.036. • W. van Helden, M. Yamaha, C. Rathgeber, A. Hauer, F. Huaylla, N. Le Pierrès, G. Diarce et al., IEA SHC Task 42 / ECES Annex 29 – Working Group B: Applications of Compact Thermal Energy Storage, Energy Procedia. 91 (2016) 231–245. doi:10.1016/j.egypro.2016.06.210. • A. Campos-Celador, G. Diarce, J. Terés-Zubiaga, T. Bandos, A. García-Romero, L.M. López, J.M. Sala, Design of a Finned Plate Latent Heat Thermal Energy Storage System for Domestic Applications, Energy Procedia, 48 (2014) 300 - 308. • A. Campos-Celador, G. Diarce, I. González-Pino, J.M. Sala, Development and comparative analysis of the modeling of an innovative finned-plate latent heat thermal energy storage system, Energy, 58 (2013) 438-447. • A. Lazaro, C. Peñalosa, A. Solé, G. Diarce, T. Haussmann, M. Fois, B. Zalba, S. Gshwander, L. F. Cabeza, Intercomparative tests on phase change materials characterization with differential scanning calorimeter, Applied Energy, 109 (2013) 415-420. • G. Diarce, A. Campos-Celador, K. Martin, A. Urresti, A. García-Romero, J.M. Sala, A comparative study of the CFD modeling of a ventilated active façade including phase change materials, Applied Energy, 126 (2014) 307-317. • G. Diarce, A. Urresti, A. García-Romero, A. Delgado, A. Erkoreka, C. Escudero, A. Campos-Celador, Ventilated active façades with PCM, Applied Energy, 109 (2013) 530-537.	• S.Saeed Mostafavi Tehrani, Gonzalo Diarce, Robert A. Taylor, Pouya Saberi, Ardalan Shafiei Ghazani, Geometric Optimization Of High Temperature Shell And Tube Latent Heat Thermal Energy Storage, 20th International Conference on Mechanical and Aerospace Engineering ICMAE, Sydney, Australia, 15th April 2016. • S. Gschwander, T. Haussmann, G. Hagelstein, A. Solé, L. Cabeza, G. Diarce, W. Hohenauer, D. Lager, A. Ristic, C. Rathgeber, P. Hennemann, H. Mehling, C. Peñalosa, A. Lázaro, Standardization of PCM characterization via DSC, Greenstock 2015, Beijing, 2015. • S. Gschwander, T. Haussmann, G. Hagelstein, C. Barreneche, L. Cabeza, G. Diarce, et al., Standardization of PCM characterization via DSC, IEA SHC Task 42/ECES Annex 29, SHC2015, Istambul, 2015. • A. Lazaro, C. Peñalosa, A. Solé, G. Diarce, T. Haussmann, M. Fois, B. Zalba, S. Gshwander, L. F. Cabeza, Round robin test for DSC characterization of PCM, SESB Conference, Dublin, 2013. • G. Diarce, K. Martin, A. Campos-Celador, A. Urresti, A. García-Romero, J.M. Sala, CFD modeling of a ventilated active façade including PCM, SESB Conference, Dublin, 2013.

Table 7-3: Published scientific articles and contributions to conferences related to PCMs and LHTES for applications different than heating and DHW

6. Future research lines and concluding remarks

Based on the attained main conclusions, the forthcoming research activities will be focused on two main research lines: The first line targets the improvement of the developed PCMs in order to maximize their thermal characteristics and to ensure their long-term stability. The second research line targets the evolution of the LHTES design and manufacturing procedure to increase the economic competitiveness of the plate-based LHTES system.

6.1. Further research related with the development of suitable PCMs for the application involved

The two urea-based eutectic mixtures investigated showed potential as a PCM for the application involved. However, since urea undergoes a thermal decomposition, further research is required to evaluate the thermal stability of the eutectic mixtures for long periods of use under conditions representative of actual applications.

Accordingly, the degradation kinetics of the two mixtures will be studied. This study consists of submitting prepared samples to a controlled degradation process under isothermal conditions at different temperatures and for different time periods. Each sample will be analyzed by means of HLPC following a procedure already defined. The results will be analyzed in order to determine the degradation kinetics. This study will be complemented with accelerated thermal cycling tests by means of DSC that will comprise at least 1000 thermal cycles. The comparison between both techniques will additionally serve to gain knowledge on the use of different technologies for the study of the lifespan behavior of PCMs. This work will also include the assessment of the atmosphere-influence on the PCMs behavior (specifically, the presence of oxygen and humidity), and the use of different sealed/ unsealed recipients.

In the specific case of the urea-erythritol mixture, the potential thermal degradation of erythritol should also be taken into consideration. Besides, solutions to the complex crystallization behavior of erythritol should also be developed before the material can be used in commercial systems.

In the case of the sodium nitrate-urea eutectic mixture, the possibility that phase segregation upon thermal cycling could take place (even when using the eutectic composition) due to the density difference of the two pristine materials, is an additional issue that will be researched.

In addition to the degradation studies, a thorough study of the supercooling should be performed. In the present thesis that effect was only succinctly studied. If the behavior of any of the mixtures is positive, further evaluation on the full-scale LHTES prototype will be embraced.

These studies will be performed under the framework of the projects: “Almacenamiento térmico latente con mezclas eutécticas base urea”, sponsored by the Ramon Areces Foundation, and “EkimProVe”, funded by the Spanish government (MINECO). Besides, they will be carried out in cooperation with Ms Laura Quant as a part of her incipient PhD thesis project, which will be performed within the ENEDI research group and in cooperation with the University of Pau, as well as the University of the Basque Country.

The development of the erythritol-xylitol mixture, although considered motivating, is not a priority. Recent research by Dr. Palomo et al. has demonstrated the feasibility of the use of a

bubbling-based technique to promote the fast crystallization of this system´s eutectic mixture. However, the implementation of such as technique in the herein developed LHTES system should need a significant modification of the design. Since the approach of the forthcoming investigations aims at developing materials that can be combined with the herein proposed LHTES system, this mixture will not be on the focus of the forthcoming research works.

On a broad sense, searching for new PCM materials for LHTES will continue on the coming future. The knowledge generated in this thesis about the methodologies and the characterization of mixture-based PCMs will be employed, and eventually improved, since it can be very helpful to develop new mixture-based PCMs. Regarding phase diagram modeling, the employed methodology will be developed into more complex models that can predict the behavior of inorganic materials such as sodium nitrate, and into models able to simulate systems different from eutectic mixtures. This will be complemented with research on PCM's characterization, task to be performed under the framework of the above mentioned SHC Task 58/ ECES Annex 33 of the IEA.

6.2. Further research related with the cost reduction of the developed plate-based LHTES system

Design modifications should be implemented on the prototype in order to reduce its cost. The most urgent task involves a thorough analysis of the mechanical and manufacturing aspects of the shell in order to develop a suitable configuration without additional "armors". This will include the simulation of different design options and materials in a mechanical modeling software (SolidWorks, others) and its further validation by producing a new shell and prototype.

Subsequently, a large cost reduction can be attained by means of the use of composites with enhanced thermal conductivity, and therefore the development of these materials will be faced. The cost-effective EG foam used for the calculations in Chapter 5, was developed in the near CIC Energigune research center. Presently, CIC Energigune has confirmed their interest in a future cooperation to research the use of their EG foams in the developed LHTES system.

Some additional contacts with research groups that work in composite foams are already in progress. The main objective is to form a consortium for the development of new materials for

TES in order to prepare a project proposal in the framework of the *Elkartek 2018* call funded by Government of the Basque Country.

If the application of EG foams is successful, a complete redesign of the PCM plates will be faced, since the use of stiff metallic plates could not be necessary anymore.

An additional objective comprises the further optimization of the system by using PCMs with different melting temperatures, placed in series. The modeling skills that have been achieved during the development of the present thesis will be essential to face this task. This objective will only be faced after the evaluation of the use of composite foams is performed.

All the above mentioned forthcoming research tasks are specifically related with the topics covered by the thesis. However, since the completion of the PhD thesis is the conclusion of the first important career stage for any researcher, this is the moment to think about potential new research topics and lines. The use of TES in applications different from those herein considered, such as waste heat recovery and/or industrial applications should be included as part of that reflection.

Such a deliberation should also involve a broader reflection about the direction to head to, both professionally and personally. As a researcher in energy efficiency, the main objective is to perform research that is able to produce sustainable technologies. Although LHTES systems can be considered promising, this is the moment to pause and evaluate whether they can really contribute to achieve the main pursued goal. All these factors should be considered in order to decide the next steps to take.

References

[1] 2016 Key World Energy Statistics - International Energy Agency (IEA), n.d. https://www.iea.org/publications/freepublications/publication/key-world-energy-statistics.html.

[2] Directive 2010/31/EU of the European Parliament and of the Council of 19 May 2010 on the energy performance of buildings, n.d. http://eur-lex.europa.eu/legal-content/EN/ALL/;ELX_SESSIONID=FZMjThLLzfxmmMCQGp2Y1s2d3TjwtD8QS3pqdkhXZbwqGwlgY9KN!2064651424?uri=CELEX:32010L0031.

[3] Combined Heat and Power: Evaluating the benefits of greater global investment - International Energy Agency (IEA), 2008. https://www.iea.org/chp/.

[4] Directive 2012/27/EU of the European Parliament and of the Council of 25 October 2012 on energy efficiency, n.d. http://eur-lex.europa.eu/legal-content/EN/TXT/?qid=1399375464230&uri=CELEX:32012L0027.

[5] Á. Campos-Celador, Integration of latent thermal energy storage systems in the design and operation of residential cogeneration plants, a novel finned plate based LHTES system, University of the Basque Country UPV/EHU, 2012.

[6] Análisis del Potencial de Cogeneración de Alta Eficiencia en España 2010-2015-2020 - IDAE, n.d. http://www.idae.es/index.php.

[7] A. Campos Celador, A. Erkoreka, K. Martin Escudero, J.M. Sala, Feasibility of small-scale gas engine-based residential cogeneration in Spain, Energy Policy. 39 (2011) 3813–3821. doi:10.1016/j.enpol.2011.04.011.

[8] J. de Wit, Heat Storages for CHP Optimisation, in: PowerGen Eur., 2007.

[9] A. Abhat, Low temperature latent heat thermal energy storage: Heat storage materials, Sol. Energy. 30 (1983) 313–332. doi:10.1016/0038-092X(83)90186-X.

[10] A. Gil, M. Medrano, I. Martorell, A. Lázaro, P. Dolado, B. Zalba, et al., State of the art on high temperature thermal energy storage for power generation. Part 1—Concepts, materials and modellization, Renew. Sustain. Energy Rev. 14 (2010) 31–55.

doi:10.1016/j.rser.2009.07.035.

[11] I. Dincer, M.A. Rosen, Thermal Energy Storage: Systems and Applications, 2nd ed., John Wiley & Sons, Ltd, 2010.

[12] K. Pielichowska, K. Pielichowski, Phase change materials for thermal energy storage, Prog. Mater. Sci. 65 (2014) 67–123. doi:10.1016/j.pmatsci.2014.03.005.

[13] B. Zalba, J.M. Marín, L.F. Cabeza, H. Mehling, Review on thermal energy storage with phase change: materials, heat transfer analysis and applications, Appl. Therm. Eng. 23 (2003) 251–283. doi:10.1016/S1359-4311(02)00192-8.

[14] M.M. Farid, A.M. Khudhair, S.A.K. Razack, S. Al-Hallaj, A review on phase change energy storage: materials and applications, Energy Convers. Manag. 45 (2004) 1597–1615. doi:10.1016/j.enconman.2003.09.015.

[15] R. Baetens, B.P. Jelle, A. Gustavsen, Phase change materials for building applications: A state-of-the-art review, Energy Build. 42 (2010) 1361–1368. doi:10.1016/j.enbuild.2010.03.026.

[16] Y. Dutil, D.R. Rousse, N. Ben Salah, S. Lassue, L. Zalewski, A review on phase-change materials: Mathematical modeling and simulations, Renew. Sustain. Energy Rev. 15 (2011) 112–130. doi:10.1016/j.rser.2010.06.011.

[17] F. Agyenim, N. Hewitt, P. Eames, M. Smyth, A review of materials, heat transfer and phase change problem formulation for latent heat thermal energy storage systems (LHTESS), Renew. Sustain. Energy Rev. 14 (2010) 615–628. doi:10.1016/j.rser.2009.10.015.

[18] N.R. Jankowski, F.P. McCluskey, A review of phase change materials for vehicle component thermal buffering, Appl. Energy. 113 (2014) 1525–1561. doi:10.1016/j.apenergy.2013.08.026.

[19] A. Sharma, V.V. Tyagi, C.R. Chen, D. Buddhi, Review on thermal energy storage with phase change materials and applications, Renew. Sustain. Energy Rev. 13 (2009) 318–345. doi:10.1016/j.rser.2007.10.005.

[20] H. Mehling, L.F. Cabeza, Heat and cold storage with PCM, 1st ed., Springer-Verlag Berlin Heidelberg, 2008. doi:10.1007/978-3-540-68557-9.

[21] Á. Campos-Celador, G. Diarce, J.T. Zubiaga, T. V. Bandos, A.M. García-Romero, L.M. López, et al., Design of a Finned Plate Latent Heat Thermal Energy Storage System for Domestic Applications, Energy Procedia. 48 (2014) 300–308. doi:10.1016/j.egypro.2014.02.035.

[22] L. Fan, J.M. Khodadadi, Thermal conductivity enhancement of phase change materials for thermal energy storage: A review, Renew. Sustain. Energy Rev. 15 (2011) 24–46. doi:10.1016/j.rser.2010.08.007.

[23] M. Liu, W. Saman, F. Bruno, Review on storage materials and thermal performance enhancement techniques for high temperature phase change thermal storage systems, Renew. Sustain. Energy Rev. 16 (2012) 2118–2132. doi:10.1016/j.rser.2012.01.020.

[24] Rubitherm GmbH, (n.d.). http://www.rubitherm.de/english/index.htm (accessed April 19, 2016).

[25] M. Kenisarin, K. Mahkamov, Solar energy storage using phase change materials, Renew. Sustain. Energy Rev. 11 (2007) 1913–1965. doi:10.1016/j.rser.2006.05.005.

[26] M.M. Kenisarin, Thermophysical properties of some organic phase change materials for latent heat storage. A review, Sol. Energy. 107 (2014) 553–575. doi:10.1016/j.solener.2014.05.001.

[27] B. Xu, P. Li, C. Chan, Application of phase change materials for thermal energy storage in concentrated solar thermal power plants: A review to recent developments, Appl. Energy. 160 (2015) 286–307. doi:10.1016/j.apenergy.2015.09.016.

[28] R.O.K. Resse, C. Gmbh, F. Main, H.E.W. Agner, K. Ag, Barium and Barium Compounds, (1878). doi:10.1002/14356007.a03.

[29] Y. Yuan, N. Zhang, W. Tao, X. Cao, Y. He, Fatty acids as phase change materials: A review, Renew. Sustain. Energy Rev. 29 (2014) 482–498. doi:10.1016/j.rser.2013.08.107.

[30] Loba Chemie Pvt. Ltd., (n.d.). http://www.lobachemie.com/ (accessed April 19, 2016).

[31] S D Fine-Chem Ltd., (n.d.). http://www.sdfine.com/home.aspx (accessed April 19, 2016).

[32] M. Dannemand, J.M. Schultz, J.B. Johansen, S. Furbo, Long term thermal energy storage with stable supercooled sodium acetate trihydrate, Appl. Therm. Eng. 91 (2015) 671–678. doi:10.1016/j.applthermaleng.2015.08.055.

[33] L.F. Cabeza, a. Castell, C. Barreneche, a. de Gracia, a. I. Fernández, Materials used as PCM in thermal energy storage in buildings: A review, Renew. Sustain. Energy Rev. 15 (2011) 1675–1695. doi:10.1016/j.rser.2010.11.018.

[34] M. Dannemand, J.B. Johansen, S. Furbo, Solidification behavior and thermal conductivity of bulk sodium acetate trihydrate composites with thickening agents and graphite, Sol. Energy Mater. Sol. Cells. 145 (2016) 287–295. doi:10.1016/j.solmat.2015.10.038.

[35] L.F. Cabeza, G. Svensson, S. Hiebler, H. Mehling, Thermal performance of sodium acetate trihydrate thickened with different materials as phase change energy storage material, Appl. Therm. Eng. 23 (2003) 1697–1704. doi:10.1016/S1359-4311(03)00107-8.

[36] P. Hu, D.-J. Lu, X.-Y. Fan, X. Zhou, Z.-S. Chen, Phase change performance of sodium acetate trihydrate with AlN nanoparticles and CMC, Sol. Energy Mater. Sol. Cells. 95 (2011) 2645–2649. doi:10.1016/j.solmat.2011.05.025.

[37] B.M.L. Garay Ramirez, C. Glorieux, E. San Martin Martinez, J.J. a. Flores Cuautle, Tuning of thermal properties of sodium acetate trihydrate by blending with polymer and silver nanoparticles, Appl. Therm. Eng. 62 (2014) 838–844. doi:10.1016/j.applthermaleng.2013.09.049.

[38] A. Solé, H. Neumann, S. Niedermaier, I. Martorell, P. Schossig, L.F. Cabeza, Stability of sugar alcohols as PCM for thermal energy storage, Sol. Energy Mater. Sol. Cells. 126 (2014) 125–134. doi:10.1016/j.solmat.2014.03.020.

[39] C. Barreneche, A. Gil, F. Sheth, A. In??s Fern??ndez, L.F. Cabeza, Effect of d-mannitol

polymorphism in its thermal energy storage capacity when it is used as PCM, Sol. Energy. 94 (2013) 344–351. doi:10.1016/j.solener.2013.05.023.

[40] A. Nezzal, L. Aerts, M. Verspaille, G. Henderickx, A. Redl, Polymorphism of sorbitol, J. Cryst. Growth. 311 (2009) 3863–3870. doi:10.1016/j.jcrysgro.2009.06.003.

[41] A. García-Romero, G. Diarce, J. Ibarretxe, A. Urresti, J.M. Sala, Influence of the experimental conditions on the subcooling of Glauber's salt when used as PCM, Sol. Energy Mater. Sol. Cells. 102 (2012) 189–195. doi:10.1016/j.solmat.2012.03.003.

[42] N.R. Jankowski, F.P. McCluskey, Electrical Supercooling Mitigation in Erythritol, in: 2010 14th Int. Heat Transf. Conf. Vol. 7, 2010: pp. 409–416. doi:10.1115/IHTC14-22306.

[43] D.Q.M. Craig, M. Reading, eds., Thermal Analysis of Pharmaceuticals, 1st ed., CRC Press, Boca Raton FL, 2006.

[44] J.M. Smith, H.C. Van Ness, M.M. Abbott, Introduction to Chemical Engineering Thermodynamics, seventh, McGraw-Hill, New York, 2005.

[45] J. Gmehling, J. Li, M. Schiller, A Modified UNIFAC model. 2. Present parameter matrix and results for different thermodynamic properties., Ind. Eng. Chem. Res. 32 (1993) 178–193. doi:10.1021/ie00013a024.

[46] The MathWorks, Inc., (n.d.). https://www.mathworks.com/products/matlab.html (accessed January 3, 2017).

[47] G. Höhne, W.F. Hemminger, H.-J. Flammersheim, Differential Scanning Calorimetry, 2nd ed., Springer-Verlag Berlin Heidelberg, 2003. doi:10.1007/978-3-662-06710-9.

[48] T. Kousksou, a. Jamil, Y. Zeraouli, J.P. Dumas, Equilibrium liquidus temperatures of binary mixtures from differential scanning calorimetry, Chem. Eng. Sci. 62 (2007) 6516–6523. doi:10.1016/j.ces.2007.07.008.

[49] A.J. Lopes Jesus, S.C.C. Nunes, M. Ramos Silva, A. Matos Beja, J.S. Redinha, Erythritol: crystal growth from the melt., Int. J. Pharm. 388 (2010) 129–35. doi:10.1016/j.ijpharm.2009.12.043.

[50] H.S. Kim, G. a. Jeffrey, The crystal structure of xylitol, Acta Crystallogr. Sect. B Struct. Crystallogr. Cryst. Chem. 25 (1969) 2607–2613. doi:10.1107/S0567740869006133.

[51] P. Perkkalainen, H. Halttunen, I. Pitkgnen, thermochimica acta Solid state co-crystallization of sugar alcohols measured with differential scanning calorimetry *, 270 (1995) 351–359.

[52] A. Seppälä, A. Meriläinen, L. Wikström, P. Kauranen, The effect of additives on the speed of the crystallization front of xylitol with various degrees of supercooling, Exp. Therm. Fluid Sci. 34 (2010) 523–527. doi:10.1016/j.expthermflusci.2009.11.005.

[53] H. Niedermaier, Sophia Neumann, M. Duquesne, A. Godin, P. Palomo del Barrio, Elena Schossig, Characterization of Sugar Alcohols as Phase Change Materials (PCM) for Medium Temperature Storage Applications, in: Greenstock 2015, 13th Int. Conf. Energy Storage, 2015.

[54] W.C. Winegard, S. Majka, B.M. Thall, B. Chalmers, Eutectic Solidification in Metals, Can. J. Chem. 29 (1950) 320–327.

[55] L. Chen, H.-R. Li, R.-J. Xu, Y. Xiong, T. Xu, B.-Y. Huang, et al., Solidification Behavior of the Hydrazine Nitrate-Nitroguanidine Eutectic System, Propellants, Explos. Pyrotech. 39 (2014) 217–223. doi:10.1002/prep.201300030.

[56] R.P. Rastogi, P.S. Bassi, Mechanism of eutectic crystallization, J. Phys. Chem. 68 (1964) 2398–2406. doi:10.1021/j100791a003.

[57] P. Gupta, T. Agrawal, S.S. Das, N.B. Singh, Phase equilibria and molecular interaction studies on (naphthols + vanillin) systems, J. Chem. Thermodyn. 48 (2012) 291–299. doi:10.1016/j.jct.2012.01.001.

[58] A. Sari, K. Kaygusuz, Thermal performance of palmitic acid as a phase change energy storage material, Energy Convers. Manag. 43 (2002) 863–876. doi:10.1016/S0196-8904(01)00071-1.

[59] Z. Liu, X. Sun, C. Ma, Experimental study of the characteristics of solidification of stearic acid in an annulus and its thermal conductivity enhancement, Energy Convers. Manag.

46 (2005) 971–984. doi:10.1016/j.enconman.2004.05.011.

[60] T. Wada, R. Yamamoto, Y. Matsuo, Heat storage capacity of sodium acetate trihydrate during thermal cycling, Sol. Energy. 33 (1984) 373–375.

[61] S. Furbo, J. Fan, E. Andersen, Z. Chen, B. Perers, Development of Seasonal Heat Storage based on Stable Supercooling of a Sodium Acetate Water Mixture, Energy Procedia. 30 (2012) 260–269. doi:10.1016/j.egypro.2012.11.031.

[62] J.H. Meesen, Urea, Ullmanns Encycl. Ind. Chem. (2012) 1–46. doi:10.1002/14356007.a27.

[63] D. Haillot, T. Bauer, U. Kröner, R. Tamme, Thermal analysis of phase change materials in the temperature range 120–150°C, Thermochim. Acta. 513 (2011) 49–59. doi:10.1016/j.tca.2010.11.011.

[64] Quimidroga, s.a., (n.d.). http://quimidroga.com/ (accessed November 10, 2015).

[65] ICIS price index, (n.d.). http://www.icis.com/ (accessed November 10, 2015).

[66] P.M. Schaber, J. Colson, S. Higgins, D. Thielen, B. Anspach, J. Brauer, Thermal decomposition (pyrolysis) of urea in an open reaction vessel, Thermochim. Acta. 424 (2004) 131–142. doi:10.1016/j.tca.2004.05.018.

[67] H.L. Fang, H.F.M. DaCosta, Urea thermolysis and NOx reduction with and without SCR catalysts, Appl. Catal. B Environ. 46 (2003) 17–34. doi:10.1016/S0926-3373(03)00177-2.

[68] A.M. Bernhard, D. Peitz, M. Elsener, A. Wokaun, O. Kröcher, Hydrolysis and thermolysis of urea and its decomposition byproducts biuret, cyanuric acid and melamine over anatase TiO2, Appl. Catal. B Environ. 115–116 (2012) 129–137. doi:10.1016/j.apcatb.2011.12.013.

[69] A. Sharma, S.D. Sharma, D. Buddhi, R.L. Sawhney, Thermal cycle test of urea for latent heat storage applications, Int. J. Energy Res. 468 (2001) 465–468.

[70] M. Kamimoto, R. Sakamoto, Y. Takahashi, K. Kanari, T. Ozawa, Investigation of latent heat-thermal energy storage materials. II. Thermoanalytical evaluation of urea,

Thermochim. Acta. 74 (1984) 281–290.

[71] K. Kauffman, I. Gruntfest, Congruently Melting Materials for Thermal Energy Storage - NCEMP-20 report, Philadelphia, 1973.

[72] G.J. Janz, C.B. Allen, N.P. Bansal, R.M. Murphy, R.P. Tomkins, Physical Properties Data Compilations Relevant to Energy Storage. II. Molten Salts: Data on Single and Multi-Component Systems, 1979. http://www.nist.gov/srd/nsrds.cfm.

[73] A. Lomonaco, D. Haillot, E. Pernot, E. Franquet, J.-P. Bédécarrats, Sodium nitrate thermal behavior in latent heat thermal energy storage: A study of the impact of sodium nitrite on melting temperature and enthalpy, Sol. Energy Mater. Sol. Cells. 149 (2016) 81–87. doi:10.1016/j.solmat.2015.12.043.

[74] T. Bauer, D. Laing, R. Tamme, Characterization of sodium nitrate as phase change material, Int. J. Thermophys. 33 (2012) 91–104. doi:10.1007/s10765-011-1113-9.

[75] M. Gambino, P. Gaune, M. Nabavian, M. Gaune-Escard, P. Bros, Enthalpie de fusion de l uree et de quelques melanges eutectiques a base d'uree, Thermochim. Acta. 111 (1987) 37–47. doi:http://dx.doi.org/10.1016/0040-6031(87)88032-2.

[76] S. Sebelius, T.T. Le, L.J. Pettersson, H. Lind, Identification of urea decomposition from an SCR perspective; A combination of experimental work and molecular modeling, Chem. Eng. J. 231 (2013) 220–226. doi:10.1016/j.cej.2013.06.124.

[77] A.M. Bernhard, I. Czekaj, M. Elsener, O. Kröcher, Adsorption and catalytic thermolysis of gaseous urea on anatase TiO2 studied by HPLC analysis, DRIFT spectroscopy and DFT calculations, Appl. Catal. B Environ. 134–135 (2013) 316–323. doi:10.1016/j.apcatb.2013.01.009.

[78] Zhao J C, ed., Methods for Phase Diagram Determination, 1st ed., Elsevier, 2007.

[79] E. Palomo del Barrio, R. Cadoret, J. Daranlot, F. Achchaq, Infrared thermography method for fast estimation of phase diagrams, Thermochim. Acta. 625 (2015) 9–19. doi:10.1016/j.tca.2015.12.010.

[80] A. Jakob, R. Joh, C. Rose, J. Gmehling, Solid-liquid equilibria in binary mixtures of

organic compounds, Fluid Phase Equilib. 113 (1995) 117–126.

[81] M.L.P. Mostefa, H. Muhr, Determination of the solid–liquid phase diagram of the binary system acrylic acid+ propionic acid, J. Chem. Eng. Data. 57 (2012) 1209–1212. http://pubs.acs.org/doi/abs/10.1021/je201193d.

[82] L. Rycerz, Practical remarks concerning phase diagrams determination on the basis of differential scanning calorimetry measurements, J. Therm. Anal. Calorim. 113 (2013) 231–238. doi:10.1007/s10973-013-3097-0.

[83] J. Guenet, Contributions of phase diagrams to the understanding of organized polymer-solvent systems, Thermochim. Acta. 284 (1996) 67–83. doi:10.1016/0040-6031(96)02892-4.

[84] Y. Waseda, E. Matsubara, K. Shinoda, X-Ray Diffraction Crystallography Introduction, Examples and Solved Problems, Springer-Verlag, 2011.

[85] H.M. Rietveld, A profile refinement method for nuclear and magnetic structures, J. Appl. Crystallogr. 2 (1969) 65–71. doi:10.1107/S0021889869006558.

[86] S. Gschwander, T. Haussmann, G. Hagelstein, A. Solé, L. Cabeza, G. Diarce, et al., Standard to determine the heat storage capacity of PCM using hf-DSC with constant heating/cooling rate (dynamic mode)-ANNEX 29: A technical report of subtask A2.1 of IEA, 2015.

[87] A. Lazaro, C. Peñalosa, A. Solé, G. Diarce, T. Haussmann, M. Fois, et al., Intercomparative tests on phase change materials characterisation with differential scanning calorimeter, Appl. Energy. 109 (2013) 415–420. doi:10.1016/j.apenergy.2012.11.045.

[88] G. Diarce, I. Gandarias, Á. Campos-Celador, A. García-Romero, U.J. Griesser, Eutectic mixtures of sugar alcohols for thermal energy storage in the 50–90°C temperature range, Sol. Energy Mater. Sol. Cells. 134 (2015) 215–226. doi:10.1016/j.solmat.2014.11.050.

[89] C.Y. Zhao, Z.G. Wu, Thermal property characterization of a low melting-temperature

ternary nitrate salt mixture for thermal energy storage systems, Sol. Energy Mater. Sol. Cells. 95 (2011) 3341–3346. doi:10.1016/j.solmat.2011.07.029.

[90] A. Campos-Celador, G. Diarce, I. González-Pino, J.M. Sala, Development and comparative analysis of the modeling of an innovative finned-plate latent heat thermal energy storage system, Energy. 58 (2013) 438–447. doi:10.1016/j.energy.2013.06.032.

[91] M. Kenisarin, K. Mahkamov, Salt hydrates as latent heat storage materials:Thermophysical properties and costs, Sol. Energy Mater. Sol. Cells. 145 (2016) 255–286. doi:10.1016/j.solmat.2015.10.029.

[92] M. Karthik, A. Faik, P. Blanco-Rodríguez, J. Rodríguez-Aseguinolaza, B. D'Aguanno, Preparation of erythritol–graphite foam phase change composite with enhanced thermal conductivity for thermal energy storage applications, Carbon N. Y. 94 (2015) 266–276. doi:10.1016/j.carbon.2015.06.075.

[93] F. Agyenim, P. Eames, M. Smyth, Experimental study on the melting and solidification behaviour of a medium temperature phase change storage material (Erythritol) system augmented with fins to power a LiBr/H2O absorption cooling system, Renew. Energy. 36 (2011) 108–117. doi:10.1016/j.renene.2010.06.005.

[94] E.P. Ona, X. Zhang, K. Kyaw, F. Watanabe, H. Matsuda, H. Kakiuchi, et al., Relaxation of supercooling of erythritol for latent heat storage, J. Chem. Eng. Japan. 34 (2001) 376–382.

[95] T. Oya, T. Nomura, N. Okinaka, T. Akiyama, Phase change composite based on porous nickel and erythritol, Appl. Therm. Eng. 40 (2012) 373–377. doi:10.1016/j.applthermaleng.2012.02.033.

[96] N.A. Puschin, M. Dezelic, Das Gleichgewicht in bin iren Systemen mit Erythrit als Komponente, Monatshefte Für Chemie. 60 (1932) 431–437.

[97] T. Kousksou, P. Bruel, A. Jamil, T. El Rhafiki, Y. Zeraouli, Energy storage: Applications and challenges, Sol. Energy Mater. Sol. Cells. 120 (2014) 59–80. doi:10.1016/j.solmat.2013.08.015.

[98] C. Rathgeber, L. Miró, L.F. Cabeza, S. Hiebler, Measurement of enthalpy curves of phase change materials via DSC and T-History: When are both methods needed to estimate the behaviour of the bulk material in applications?, Thermochim. Acta. 596 (2014) 79–88. doi:10.1016/j.tca.2014.09.022.

[99] G. Diarce, E. Corro Martínez, L. Quant, Á. Campos-Celador, A. García-Romero, The sodium nitrate-urea binary mixture as a phase change material for medium temperature thermal energy storage. Part I: Determination of the phase diagram and main thermal properties., Sol. Energy Mater. Sol. Cells. (2016). doi:10.1016/j.solmat.2016.04.042.

[100] A. Diedrichs, J. Gmehling, Solubility calculation of active pharmaceutical ingredients in alkanes, alcohols, water and their mixtures using various activity coefficient models, Ind. Eng. Chem. Res. 50 (2011) 1757–1769. doi:10.1021/ie101373k.

[101] S.A. Febra, Implementation and evaluation of two models for solubility of active pharmaceutical ingredients (APIs). Master Thesis, Instituto Superior Tecnico Lisboa, 2013.

[102] N.D.D. Carareto, A.O. Dos Santos, M.P. Rolemberg, L.P. Cardoso, M.C. Costa, A.J.A. Meirelles, On the solid-liquid phase diagrams of binary mixtures of even saturated fatty alcohols: Systems exhibiting peritectic reaction, Thermochim. Acta. 589 (2014) 137–147. doi:10.1016/j.tca.2014.05.022.

[103] M. Kuhnert-Brandstätter, Thermomicroscopy of Organic Compounds, in: G. Svehla (Ed.), Wilson Wilson's Compr. Anal. Chem. Vol XVI, Elsevier, Amsterdam, 1982.

[104] G. Diarce, E. Corro Martínez, Á. Campos-Celador, A. García-Romero, J.M. Sala, The sodium nitrate-urea eutectic binary mixture as a phase change material for medium temperature thermal energy storage. Part II: Accelerated thermal cycling test and water uptake behavior of the material., Sol. Energy Mater. Sol. Cells. (2016). doi:http://dx.doi.org/10.1016/j.solmat.2016.04.020i.

[105] PCM Products Ltd., (n.d.). http://www.pcmproducts.net/ (accessed April 19, 2016).

[106] H.S. Carslaw, J.C. Jaeger, Conduction of heat in solids, 2nd ed., Clarendon Press,

Oxford, 1959.

[107] W.R. Humphries, E.I. Griggs, A design handbook for phase change thermal control and energy storage devices, 1977. https://ntrs.nasa.gov/search.jsp?R=19780007491.

[108] Y.A. Çengel, J.M. Cimbala, Fluid Mechanics: Fundamentals and Applications, 2nd ed., McGraw-Hill, New York, 2010.

[109] Y.A. Çengel, A.J. Ghajar, Heat and Mass Transfer: Fundamentals and Applications, 4th ed., McGraw-Hill, New York, 2011.

[110] ANSYS Inc., PA, USA, (n.d.). http://www.ansys.com/ (accessed September 19, 2016).

[111] UNSW Wikispaces - Leonardi Engineering Research Cluster, (n.d.). http://leonardi.unsw.wikispaces.net/ (accessed October 10, 2016).

[112] Alu-Stock S.A., (n.d.). http://www.alu-stock.es/es/ (accessed February 1, 2017).

[113] B.M. Berkovsky, V.K. Polevikov, Numerical study of problems on high-intensive free convection, in: D.B. Spalding, N. Afgan (Eds.), Heat Transf. Turbul. Buoyant Convect., Hemisphere, Washington. DC, 1977: pp. 443–445.

[114] Dikoin S.L., (n.d.). http://dikoin.com/ (accessed December 16, 2016).

[115] R.K.J. Brent A.D, Voller V. R., Enthalpy-Porosity Technique for Modelling Convection-Difusion Change Application To the Melting of a Pure Metal.Pdf, Numer. Heat Transf. 13 (1988) 297–318.

[116] V.R. Voller, C. Prakash, A Fixed-Grid Numerical Modeling Methodology for Convection-Diffusion Mushy Region Phase-Change Problems, Int. J. Heat Mass Transf. 30 (1987) 1709–1720.

[117] K. Kumarasamy, J. An, J. Yang, E.H. Yang, Numerical techniques to model conduction dominant phase change systems: A CFD approach and validation with DSC curve, Energy Build. 118 (2016) 240–248. doi:10.1016/j.enbuild.2016.02.040.

[118] G. Diarce, Á. Campos-Celador, K. Martin, A. Urresti, A. García-Romero, J.M. Sala, A comparative study of the CFD modeling of a ventilated active façade including phase

change materials, Appl. Energy. 126 (2014) 307–317. doi:10.1016/j.apenergy.2014.03.080.

[119] F. Fornarelli, S.M. Camporeale, B. Fortunato, M. Torresi, P. Oresta, L. Magliocchetti, et al., CFD analysis of melting process in a shell-and-tube latent heat storage for concentrated solar power plants, Appl. Energy. 164 (2016) 711–722. doi:10.1016/j.apenergy.2015.11.106.

[120] P.M. Gresho, R.L. Lee, R.L. Sani, On the Time-Dependent Solution of the Incompressible Navier-Stokes Equations in Two and Three Dimensions, in: Recent Adv. Numer. Methods Fluids, Pineridge Press, Swansea, U.K, 1980.

[121] Sigma Aldrich Co. LLC., (n.d.). http://www.sigmaaldrich.com/spain.html (accessed December 12, 2016).

[122] TSM, S.L., (n.d.). http://www.tsmsl.es/ (accessed December 27, 2016).

[123] I.B. Celik, U. Ghia, R.P. J, C.J. Freitas, H. Coleman, P.E. Raad, Procedure for estimation and reporting of uncertainty due to discretization in CFD applications, J. Fluids Eng. 130 (2008) 78001-1-78001–4. doi:10.1115/1.2960953.

[124] R. Xu, N.G. F, Controlled interface acceleration in unidirectional solidification, Int. J. Heat Mass Transf. 47 (2004) 4821–4832.

[125] M. Farid, a Kanzawa, Thermal performance of heat storage module\rusing PCM s with different melting temperatures: Mathematical modelling, J. Sol. Energy Eng. Trans. ASME. 111 (1989) 152–157.

[126] E.M. Sparrow, T.A. Myrum, Experiments on natural convection in complex enclosed spaces containing either two fluids or a single fluid, Int. J. Heat Mass Transf. 30 (1987) 1247–1258. doi:10.1016/0017-9310(87)90158-X.

[127] I. Dincer, M.A. Rosen, Exergy Analysis of Thermal Energy Storage Systems, in: Exergy, Elsevier, 2013: pp. 133–166. doi:10.1016/B978-0-08-097089-9.00009-7.

[128] A. Bastani, F. Haghighat, J. Kozinski, Designing building envelope with PCM wallboards: Design tool development, Renew. Sustain. Energy Rev. 31 (2014) 554–562.

doi:10.1016/j.rser.2013.12.031.

[129] C. Pérez López, Estadística aplicada a través de Excel, Prentice Hall, Madrid, 2002.

[130] M.K.A. Sharif, a. a. Al-Abidi, S. Mat, K. Sopian, M.H. Ruslan, M.Y. Sulaiman, et al., Review of the application of phase change material for heating and domestic hot water systems, Renew. Sustain. Energy Rev. 42 (2015) 557–568. doi:10.1016/j.rser.2014.09.034.

[131] N. Dhaidan, J.M. Khodadadi, Melting and convection of phase change materials in different shape containers: A review, Renew. Sustain. Energy …. 43 (2015) 449–477. doi:10.1016/j.rser.2014.11.017.

[132] O. Kurata, N. Iki, T. Matsunuma, T. Maeda, S. Hirano, K. Kadoguchi, et al., Micro gas turbine cogeneration system with latent heat storage at the University: Part I: Plan and energy flow test, Appl. Therm. Eng. 65 (2014) 513–523. doi:10.1016/j.applthermaleng.2014.01.033.

[133] A. López-Navarro, J. Biosca-Taronger, J.M. Corberán, C. Peñalosa, A. Lázaro, P. Dolado, et al., Performance characterization of a PCM storage tank, Appl. Energy. 119 (2014) 151–162. doi:10.1016/j.apenergy.2013.12.041.

[134] E. Halawa, W. Saman, Thermal performance analysis of a phase change thermal storage unit for space heating, Renew. Energy. 36 (2011) 259–264. doi:10.1016/j.renene.2010.06.029.

[135] U. Stritih, An experimental study of enhanced heat transfer in rectangular PCM thermal storage, Int. J. Heat Mass Transf. 47 (2004) 2841–2847. doi:10.1016/j.ijheatmasstransfer.2004.02.001.

[136] M. Liu, W. Saman, F. Bruno, Validation of a mathematical model for encapsulated phase change material flat slabs for cooling applications, Appl. Therm. Eng. 31 (2011) 2340–2347. doi:10.1016/j.applthermaleng.2011.03.034.

[137] P. Silva, L. Goncalves, L. Pires, Transient behaviour of a latent-heat thermal-energy store: numerical and experimental studies, Appl. Energy. 73 (2002) 83–98.

http://www.sciencedirect.com/science/article/pii/S0306261902000600 (accessed January 7, 2015).

[138] P. Charvát, L. Klimeš, M. Ostrý, Numerical and experimental investigation of a PCM-based thermal storage unit for solar air systems, Energy Build. 68 (2014) 488–497. doi:10.1016/j.enbuild.2013.10.011.

[139] P. Dolado, A. Lazaro, J.M. Marin, B. Zalba, Characterization of melting and solidification in a real-scale PCM-air heat exchanger: Experimental results and empirical model, Renew. Energy. 36 (2011) 2906–2917. doi:10.1016/j.renene.2011.04.008.

[140] M. Labat, J. Virgone, D. David, F. Kuznik, Experimental assessment of a PCM to air heat exchanger storage system for building ventilation application, Appl. Therm. Eng. 66 (2014) 375–382. doi:10.1016/j.applthermaleng.2014.02.025.

[141] M. Medrano, M.O. Yilmaz, M. Nogués, I. Martorell, J. Roca, L.F. Cabeza, Experimental evaluation of commercial heat exchangers for use as PCM thermal storage systems, Appl. Energy. 86 (2009) 2047–2055. doi:10.1016/j.apenergy.2009.01.014.

[142] M. Dannemand, J. Dragsted, J. Fan, J.B. Johansen, W. Kong, S. Furbo, Experimental investigations on prototype heat storage units utilizing stable supercooling of sodium acetate trihydrate mixtures, Appl. Energy. 169 (2016) 72–80. doi:10.1016/j.apenergy.2016.02.038.

[143] M. Dannemand, W. Kong, J. Fan, J.B. Johansen, S. Furbo, Laboratory Test of a Prototype Heat Storage Module Based on Stable Supercooling of Sodium Acetate Trihydrate, Energy Procedia. 70 (2015) 172–181. doi:10.1016/j.egypro.2015.02.113.

[144] M. Johnson, M. Fiss, T. Klemm, M. Eck, Test and analysis of a flat plate latent heat storage design, Energy Procedia. 57 (2014) 662–671. doi:10.1016/j.egypro.2014.10.221.

[145] J. Vogel, J. Felbinger, M. Johnson, Natural convection in high temperature flat plate latent heat thermal energy storage systems, Appl. Energy. 184 (2016) 184–196. doi:10.1016/j.apenergy.2016.10.001.

[146] CES EduPack, (n.d.). http://www.grantadesign.com/education/edupack/ (accessed

February 1, 2017).

[147] Pattex (Nural 21), (n.d.). http://www.pattex.es/pagina-de-inicio/productos/bicomponentes/para-el-profesional/metal/nural-21.html (accessed January 3, 2016).

[148] P. García-Álvarez, Master´s thesis - CFD evaluation of the hydraulic distribution inside a LHTES system, UPV/EHU, 2016.

[149] Henkel Ltd., (n.d.). http://www.loctite.co.uk/homepage.htm (accessed December 20, 2016).

[150] Soudal N.V., (n.d.). http://www.soudalgroup.com/global-gateway/ (accessed December 15, 2016).

[151] J.M. Mateo Solé, Introducción a la estanqueidad industrial : principios, conceptos, aplicaciones, casos prácticos, 2nd ed., Visión Libros, Madrid, 2004.

[152] Formdrill thermal drilling, (n.d.). http://www.formdrill.com/english/formdrill.htm (accessed January 3, 2017).

[153] Celesa S.A. (Blue Master), (n.d.). http://www.bluemaster.es/en-GB/Contenido/Index/Novedades (accessed January 3, 2016).

[154] Ineltec S.L., (n.d.). http://www.ineltec.es/en/ (accessed December 27, 2016).

[155] Agilent Technlogies, (n.d.). http://www.agilent.com/home (accessed December 27, 2016).

[156] L. Quant, Master´s Thesis - Full Scale Performance Evaluation of a LHTES System, UPV/ EHU, 2015.

[157] Remeha B.V., (n.d.). http://www.remeha.com/products/micro-chp/ (accessed January 3, 2017).

[158] ANSI/ ASHRAE Standard 94.1-2002 (RA 2006), Method of testing active latent-heat storage devices based on thermal performance., in: Atlanta, 2006.

[159] C. Rathgeber, S. Hiebler, E. Lävemann, P. Dolado, A. Lazaro, J. Gasia, et al., IEA SHC Task 42 / ECES Annex 29 – A simple tool for the economic evaluation of thermal energy storages, SHC 2015 , Int. Conf. Sol. Heat. Cool. Build. Ind. 91 (2015) 197–206. doi:10.1016/j.egypro.2016.06.203.

[160] M. Rommel, A. Hauer, W. van Helden, IEA SHC Task 42 / ECES Annex 29 Compact Thermal Energy Storage, Energy Procedia. 91 (2016) 226–230. doi:10.1016/j.egypro.2016.06.208.

[161] P. Mantilla Gilart, Á. Yedra Martínez, M. González Barriuso, C. Manteca Martínez, Development of PCM/carbon-based composite materials, Sol. Energy Mater. Sol. Cells. 107 (2012) 205–211. doi:10.1016/j.solmat.2012.06.014.

[162] E.P. del Barrio, A. Godin, M. Duquesne, J. Daranlot, J. Jolly, W. Alshaer, et al., Characterization of different sugar alcohols as phase change materials for thermal energy storage applications, Sol. Energy Mater. Sol. Cells. 159 (2017) 560–569. doi:10.1016/j.solmat.2016.10.009.

[163] J. Gmehling, Present status and potential of group contribution methods for process development, J. Chem. Thermodyn. 41 (2009) 731–747. doi:10.1016/j.jct.2008.12.007.

[164] G. Diarce, I. Gandarias, S. Gómez, A. García-Romero, J.M. Sala, Determination of the solid-liquid equilibrium of mixtures of sugar alcohols for their use as phase change materials, in: Thermam 2014, n.d.

[165] A. Paul, L. Shi, C.W. Bielawski, A eutectic mixture of galactitol and mannitol as a phase change material for latent heat storage, Energy Convers. Manag. 103 (2015) 139–146. doi:10.1016/j.enconman.2015.06.013.

[166] E. Palomo Del Barrio, R. Cadoret, J. Daranlot, F. Achchaq, New sugar alcohols mixtures for long-term thermal energy storage applications at temperatures between 70°C and 100°C, Sol. Energy Mater. Sol. Cells. 155 (2016) 454–468. doi:10.1016/j.solmat.2016.06.048.

[167] Samssa (Sugar Alcohol based Materials for Seasonal Storage Applications) FP7 EU funded project, (n.d.). http://www.samssa.eu/ (accessed November 10, 2015).

Appendix A: Model employed for the determination of the solid-liquid equilibrium for phase diagrams

According to theory [44], the basis of the solid–liquid equilibrium of a mixture can be defined by Eq. A - 1. Here, $\hat{f}$ represents the fugacity of each *i* compound for the solid (*s*) and the liquid (*l*) phases in equilibrium.

$$\hat{f}_i^l = \hat{f}_i^s \qquad \text{Eq. A - 1}$$

Using activity coefficients, Eq. A - 1 can be rearranged, resulting in Eq. A - 2. Here, γ^l and γ^s are the activity coefficients in the liquid and solid phases, respectively, and they denote the deviation from an ideal mixture; *x* is the mole fraction in the liquid phase and *z* is the mole fraction in the solid phase. Finally, *f* represents the fugacity of the pure compounds for the solid (*s*) and the liquid (*l*) phases. The subscript *i* accounts for each compound in the system.

$$x_i \gamma_i^l f_i^l = z_i \gamma_i^s f_i^s \qquad \text{Eq. A - 2}$$

It can be demonstrated [44] that the relationship between the fugacities of the pure compounds in the liquid and solid states, denoted by ψ in Eq. A - 3, can be defined as shown in Eq. A - 4. Here, ΔH^{sl} represents the enthalpy of fusion of each *i* pure compound; T_m is the melting temperature of the pure substance; *T* is the temperature of the system; ΔC_{pi}^{sl} is the difference between the specific heat of the liquid and solid phases, evaluated at T_m (ΔH^{sl} is evaluated at this temperature as well) and *R* is the ideal gas constant. The term *I* is a second order term related to the variation of the specific heat with temperature, which can be neglected. In the same way, the difference between specific heats of the solid and liquid phases was found to be negligible in the present study. Therefore, combining Eq. A - 2, Eq. A - 3 and Eq. A - 4, the expressions shown in Eq. A - 5 and Eq. A - 6 are reached.

$$\psi_i = f_i^s / f_i^l \qquad \text{Eq. A - 3}$$

$$\psi_i = exp\left((\Delta H_i^{sl}/RT_{mi})\ ((T - T_{mi})/T)\right) + \left(\Delta C_{pi}^{sl}/R\right)\left(ln\ (T/T_m) - ((T - T_{mi})/T)\right) + I \qquad \text{Eq. A - 4}$$

$$x_i\gamma_i^l = z_i\gamma_i^s\psi_i \qquad \text{Eq. A - 5}$$

$$x_i\gamma_i^l/z_i\gamma_i^s = exp\left((\Delta H_i^{sl}/RT_{mi})\ ((T - T_{mi})/T)\right) \qquad \text{Eq. A - 6}$$

For a eutectic system, where the compounds are immiscible in the solid phase, the molar fraction of each solid composition, z_i, is equal to unity. Additionally, it can be assumed that the solid activity coefficients are also equal to unity. Consequently, Eq. A - 7 is reached.

$$z_i\gamma_i^s = 1 \qquad \text{Eq. A - 7}$$

As a result, from Eq. A - 6 and Eq. A - 7, Eq. A - 8 is obtained. Here, the remaining unknown variables are the composition, equilibrium temperature and activity coefficients of the liquid state. For a binary mixture, only two equations are available, one for each compound of the mixture. Therefore, an additional method is required to evaluate the activity coefficients of the liquid phases.

$$x_i\gamma_i^l = exp\left((\Delta H_i^{sl}/RT_{mi})\ ((T - T_{mi})/T)\right) \qquad \text{Eq. A - 8}$$

In the present study, two options were adopted to evaluate the activity coefficients. On the one hand, systems were assumed to form an ideal mixture. For those cases, the activity coefficient equals unity. The compounds herein modeled present similar structures, so it can be a suitable assumption.

On the other hand, an approach based on group contribution methods was adopted to predict activity coefficients. As explained in Ref. [163], this method assumes the system does not consist of molecules but of functional groups. An advantage of group contribution methods is that the number of functional groups is much smaller than the number of possible molecules. Therefore, when parameters are adjusted for certain functional groups, the activity coefficient of different molecules formed by different combinations of those functional groups can be predicted. Two specific procedures were used: the Modified UNIFAC model (Chapter 2) [45] and the Pharma Modified UNIFAC model (Chapter 4) [100]. The equations involved are the same in both approaches, but the values of the parameters used are different.

The activity coefficient consists of two parts, as shown in Eq. A - 9: a combinatorial contribution, γ^C, mostly dependent on differences in molecular size and shape and the residual contribution, γ^R, mainly arising from differences in intermolecular forces of attraction. For component *i* of a multi-component solution, the combinatorial contribution can be calculated from Eq. A - 10.

$$ln\,\gamma_i = ln\,\gamma_i^C + ln\,\gamma_i^R \qquad \text{Eq. A - 9}$$

$$ln\,\gamma_i^C = 1 - V_i' + lnV_i' - 5q_i(1 - V_i/F_i + ln(V_i/F_i)) \qquad \text{Eq. A - 10}$$

The parameters V_i', $V_i$and F_i can be calculated from Eq. A - 11, Eq. A - 12 and Eq. A - 13, where *x* accounts for the molar fraction of the component *j* and pure-component parameters r_i and q_i are, respectively, measures of molecular (Van der Waals) volumes and surface areas. These, in turn, are given by group contributions R_k and Q_k according to Eq. A - 14 and Eq. A - 15. Here, $v_k^{(i)}$ is always an integer and is the number of groups of type *k* in molecule *i*.

$$V_i' = r_i^{3/4} \Big/ \sum_j x_j r_j^{3/4} \qquad \text{Eq. A - 11}$$

$$V_i = r_i \Big/ \sum_j x_j r_j \qquad \text{Eq. A - 12}$$

$$F_i = q_i \Big/ \sum_j x_j q_j \qquad \text{Eq. A - 13}$$

$$r_i = \sum v_k^{(i)} R_k \qquad \text{Eq. A - 14}$$

$$q_i = \sum v_k^{(i)} Q_k \qquad \text{Eq. A - 15}$$

The residual part of the activity coefficient can be obtained by using Eq. A - 16 and Eq. A - 17, whereby the group area fraction, θ_m, and the group mole fraction, X_m, are given by Eq. A - 18 and Eq. A - 19. The group interaction parameter, Ψ_{nm}, is given by Eq. A - 20. Here, *T* is the equilibrium temperature from Eq. A - 8, and *a*, *b* and *c* are temperature-dependent parameters

systematically evaluated from a large body of equilibrium data. These parameters, as the group contribution, R_k and Q_k, can be found in refs. [45,100].

$$ln\,\gamma_i^R = \sum_k v_k^{(i)}\left(ln\Gamma_k - ln\Gamma_k^{(i)}\right) \quad \text{Eq. A - 16}$$

$$n(\Gamma_k) = Q_k\left(1 - ln\left(\sum_m \theta_m\Psi_{mk}\right) - \sum_m\left(\theta_m\Psi_{km}\Big/\sum_n \theta_n\Psi_{nm}\right)\right) \quad \text{Eq. A - 17}$$

$$\theta_m = Q_m X_m\Big/\sum_n Q_n X_n \quad \text{Eq. A - 18}$$

$$X_m = \sum_j v_m^{(j)} x_j\Big/\sum_j\sum_n v_n^{(j)} x_j \quad \text{Eq. A - 19}$$

$$\Psi_{nm} = exp(-(a_{nm} + b_{nm}T + c_{nm}\,T^2)/T) \quad \text{Eq. A - 20}$$

In a similar way, the excess enthalpy of a mixture can be used to predict the resultant melting enthalpy of a mixture (Note that the model to predict the enthalpies was exclusively used in Chapter 2). As shown in Eq. A - 21, the enthalpy of a mixture (H^{mix}) comprises the sum of the excess enthalpy (H^{e}) and the enthalpy of an ideal mixture (H^{ideal}).

$$H^{mix} = H^e + H^{ideal} \quad \text{Eq. A - 21}$$

The results of solid–liquid equilibrium showed that the studied mixtures can be considered ideal. Therefore, the term related to the excess enthalpy can be neglected. As a result, the melting enthalpy of the mixture can be modeled as an ideal melting enthalpy, as shown in Eq. A - 22. Here, *x* is the molar fraction of each compound *i* and ΔH^{sl} is the melting enthalpy of that pure compound *i*. However, Eq. A - 22 allows evaluating the melting enthalpy of the mixture, ΔH_{mix}^{sl}, at an ideal temperature, T_{ideal}, which is different from the eutectic temperature T_{eut}.

$$\Delta H_{mix}^{sl\,(T\,ideal)} = \sum_i x_i \Delta H_i^{sl} \quad \text{Eq. A - 22}$$

To be able to evaluate the melting enthalpy at the eutectic temperature, $\Delta H_{mix}^{sl\,(T\,eut)}$, the formula has to be corrected, using the specific heats of the pure compounds. As a result, Eq. A - 23 is obtained. Here, *x* is the molar fraction; ΔH^{sl} is the melting enthalpy of the pure compound; ΔC_p^{sl} is the difference between the specific heat of the solid and the liquid state; T_m is the melting temperature of the pure compound and T_{eut} is the predicted eutectic temperature of the system. The subscript *i* accounts for each compound in the system. This was the relation used in the present work to predict the melting enthalpies of the eutectic compositions determined.

$$\Delta H_{mix}^{sl\,(T\,eut)} = \sum_i x_i(\Delta H_i^{sl} + \Delta C_{p\,i}^{sl}\,(T_{m\,i} - T_{eut})) \qquad \text{Eq. A - 23}$$

Appendix B: Information of the different elements comprising the LHTES prototype

B.1. Different dimensions of aluminum commercial extruded profiles from Alu-Stock S.A. *[112]*

TUBOS RECTANGULARES DE ALUMINIO

TABLAS DETALLADAS

b x h mm	e mm	Peso kg/m	Mlx cm⁴	Mly cm⁴	Wx cm³	Wy cm³	SIMAGALTOK 60/63 6060/6063	SIMAGALTOK 82 6082
80 x 20	1,50	0,824	2,181	20,658	2,181	5,164	▣	–
80 x 20	2,00	1,089	26,803	2,739	6,701	2,739	□	–
80 x 30	2,00	1,202	32,889	6,869	8,222	4,579	□	–
80 x 40	1,50	0,995	29,902	10,164	7,476	5,082	□	–
80 x 40	2,00	1,315	38,974	13,118	9,743	6,559	□	–
80 x 40	3,00	1,937	55,853	18,429	13,963	9,215	□	–
80 x 40	4,00	2,540	71,134	23,006	17,783	11,503	□	–
80 x 40	5,00	3,119	84,917	26,917	21,229	13,458	□	–
80 x 50	3,00	2,107	64,701	30,803	16,188	12,321	□	–
80 x 60	2,00	1,542	32,777	51,145	10,926	12,786	□	–
80 x 60	4,00	2,994	59,635	94,259	19,878	23,565	□	–
100 x 20	2,00	1,315	3,390	48,702	3,390	9,740	□	–
100 x 25	1,70	1,172	4,908	46,076	3,927	9,215	□	–
100 x 30	3,00	2,107	11,671	83,883	7,781	16,777	□	–
100 x 40	1,50	1,164	12,389	51,926	6,194	10,385	▣	–
100 x 40	2,00	1,542	16,009	67,913	8,004	13,583	□	–
100 x 40	4,00	2,994	28,211	125,683	14,106	25,137	□	–
100 x 45	1,70	1,365	17,985	62,505	7,993	12,501	▣	–
100 x 45	2,00	1,598	20,801	72,715	9,245	14,543	□	–
100 x 50	2,00	1,656	26,298	77,518	10,519	15,504	□	–
100 x 50	2,50	2,055	32,026	95,151	12,810	19,030	□	–
100 x 50	3,00	2,449	37,440	112,120	14,976	22,424	□	–
100 x 50	4,00	3,221	47,366	144,126	18,946	28,825	□	–
100 x 50	5,00	3,965	56,167	173,667	22,467	34,733	□	–
100 x 50	6,00	4,691	63,927	200,867	25,571	40,173	▣	–
100 x 50	8,00	6,073	76,654	248,734	30,662	49,747	–	▣
100 x 60	2,00	1,767	39,507	87,123	13,169	17,425	□	–
100 x 60	4,00	3,447	72,201	162,596	24,067	32,514	□	–
100 x 80	3,00	2,957	109,241	154,473	27,310	30,895	▣	–
120 x 20	2,00	1,542	4,041	79,681	4,041	13,313	□	–
120 x 40	1,50	1,334	14,613	82,169	7,307	13,695	□	–
120 x 40	2,00	1,769	18,899	107,731	9,450	17,955	□	–
120 x 40	4,00	3,447	33,417	201,353	16,708	33,559	□	–
120 x 50	2,00	1,882	30,909	121,657	12,363	20,276	□	–
120 x 50	3,00	2,787	44,075	176,767	17,630	29,461	▣	–
120 x 50	4,00	3,674	55,851	228,275	22,340	38,046	▣	–
120 x 60	2,00	1,996	46,238	135,582	15,413	22,597	□	–
120 x 60	4,00	3,901	84,766	255,198	28,255	42,533	□	–
120 x 60	5,00	4,815	101,417	309,417	33,806	51,569	▣	–
120 x 60	6,00	5,710	116,467	360,115	38,822	60,019	▣	–

B.2. Dimensions of the aluminum threaded plugs employed to close the filling holes in the PCM plates

TEI

HEX. SOCKET HEAD PLUGS

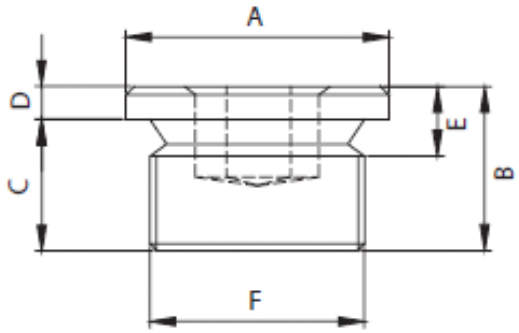

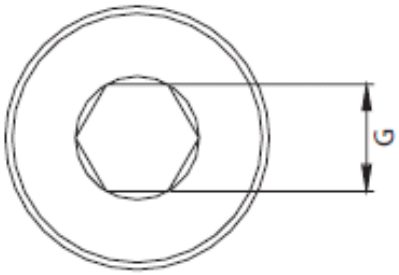

The hexagon socket head plug is useful when good tightening torque is required while avoiding protrusions.
- Body in aluminium alloy D11S.
- Oilproof gasket.

GAS TYPE	F	A	B	C	D	E	G
TEI 1/8"	1/8" GAS	14	11	8	3	5	5
TEI 1/4"	1/4" GAS	18	15	12	3	7	6
TEI 3/8"	3/8" GAS	22	15	12	3	7,5	8
TEI 1/2"	1/2" GAS	26	18	14	4	7,5	10
TEI 3/4"	3/4" GAS	32	20	16	4	9	12
TEI 1"	1" GAS	40	21	16	5	9	17

B.3. Characteristics of the Viton O-rings employed coupled to the aluminum plugs used in the PCM plates.

RS PRO

Datasheet

ENGLISH

Stock No: 129-044

RS Pro Fluorocarbon Elastomer O-Ring, 9.25mm Bore, 12.7mm O.D , -20 → +200°C

Product Details

Viton™ 'O' Rings, Imperial sizes

- High temperature & oil resistance
- Temperature range -15°C to +200°C
- Excellent resistance to flame, weather, oxidation and ozone

'O' Rings

'O' ring seals available in a choice of three materials to suit different applications. All 'O' rings are supplied in bags of 50.,The Nitrile 'O' rings are available in both Metric and Imperial sizes. Imperial sizes are to BS1806, Metric sizes are to BS4518.